Structure-function relationship of mitochondrial cytochrome *c* oxidase: redox centres, proton pathways and isozymes

Raksha Jagdish Dodia

Structural Molecular Biology

University College London

Submitted for the Degree of Doctor of Philosophy

2014

Supervisor: Prof. Peter R. Rich
Internal examiner: Dr. Joanne Santini
External examiner: Prof. Peter J. Nixon

Signed declaration

I Raksha J. Dodia confirm that the work presented in this thesis is my own. Where information has been derived from other sources, I confirm that this has been indicated in the thesis.

_____

_____

Abstract

Cytochrome *c* oxidase (C*c*O) reduces O_2 to water with four electrons from cytochromes c^{2+} and four matrix protons. The energy released is conserved in the protonmotive force by translocation of four additional protons into the intermembrane space. Electrons are transferred via Cu_A, haem *a*, to the binuclear centre; haem a_3 and Cu_B, where O_2 is reduced. Four major aspects of its structure/function have been investigated in this study.

Mid-infrared (IR) spectroscopy has been used to probe redox-induced structural changes. By using electrochemically-poised samples of cyanide- and carbon monoxide-ligated bovine C*c*O these redox-linked IR changes were shown to be linked primarily with Cu_A and haem *a* metal centre transitions with fewer changes associated with transitions in haem a_3 and Cu_B.

C*c*O contains a cross-linked Tyr-His which is believed to form a Tyr radical in the P_M intermediate. In this work, electrochemical conditions to induce Tyr-His model compound radicals have been combined with IR spectroscopy to record IR reference spectra. This has aided tentative assignment of IR bands at 1572 cm^{-1} or 1555 cm^{-1} to *v*8a(C-C), 1519 cm^{-1} to *v*7a(C-O$^{\bullet}$) to the phenoxyl radical and at 1336 cm^{-1} to a His ring stretch of the cross-linked structure in the P_M state of bovine C*c*O.

There is strong evidence from mutagenesis studies in bacterial C*c*Os that the well-conserved D channel is the proton translocation pathway. However, mutagenesis studies in a human/bovine hybrid C*c*O of an extensive hydrophilic H channel suggest that it fulfils this function, at least in mammalian C*c*Os. A structural model of *Saccharomyces cerevisiae* C*c*O produced by homology modelling indicates that it also contains an H channel (Maréchal, A., Meunier, B., Lee, D., Orengo, C. and Rich, P. R. (2012) Biochim. Biophys. Acta. **1817**, 620-628). However, measurements of the H^+/e^- stoichiometry of a yeast H channel mutant (Q411L/Q413L/S458A/S455A) suggest it is not critical for proton translocation in yeast C*c*O.

The nuclear-encoded subunit 5 of yeast C*c*O has two isoforms, 5A and 5B. *COX5A* is expressed aerobically and *COX5B* below 1 µM O_2. They are reported to alter core catalytic activity; however comparisons were not strictly controlled. Here mutants were constructed where *COX5B* expression was controlled by the *COX5A* promoter yielding wild type levels of aerobically expressed 5B isozyme. Interestingly, this 5B isozyme exhibits the same catalytic activity and oxygen affinity as the 5A isozyme and the previously observed elevated activity must arise from a secondary effect.

Contents

Acknowledgements

I would like to take this opportunity to express my gratitude to everyone who has supported me throughout the course of this Ph.D. First and foremost I thank my supervisor, Prof. Peter R. Rich, for his wealth of knowledge, patience and encouragement, moreover, for always being available to offer insightful discussions and endless support; from writing this thesis to presentations at conferences and with laboratory experiments.

I am thankful to my secondary supervisor, Dr. Katherine Holt for providing excellent supervision during the Tyr-His project, for providing constructive feedback, testing questions and friendly advice at the thesis committee meetings. Moreover, for establishing collaboration with Dr. Tom Sheppard and Rachel Lanigan, to whom I am also grateful for chemically synthesising Tyr-His structures, without those, the project could not have been extended. I thank Dr. Tom Varley, Mohammed Haque and Meetal Hirani for their help and guidance with cyclic voltammetry.

My thesis committee chair, Dr. Christopher W. M. Kay, for invaluable feedback, and for his expertise over the past few months in the statistical analysis that was necessary for the preparation of the 5A/5B manuscript.

Dr. Brigitte Meunier, for welcoming me to undertake an enjoyable and educational three week placement in her laboratory to work on the 5A/5B project, and for constructing the yeast mutant strains described in this thesis.

Dr. Amandine Maréchal, for the critical scientific discussions that challenged me to always evaluate my work rigorously. For kindly offering her time and support in tutoring me on key aspects of my Ph.D. including FTIR spectroscopy, UV/visible spectroscopy and protein purification.

I acknowledge Prof. Shelagh Ferguson-Miller, Prof. Marten Wikström and Dr. Jelena Ostojić for kindly sharing protocols. Dr. Susanne Arnold, who agreed to conduct mass spectrometry experiments and Prof. Bernard Guiard for providing yeast cyts *c*.

I express my gratitude to Talha Arooz for his positivity and excellent research assistance and for always going that extra mile and most of all for the advice and support. For outstanding technical support, I thank Santi Garcia who has built the ATR compatible electrochemical and perfusion devices described in this thesis. I am grateful to my Ph.D. administrator Dr. Carolyn Moores, who offered great advice and guidance.

I acknowledge former group members, Tomas Warelow, Dr. Simona Bettini and Hongorzul Davaapil for contributing to the development of various projects.

To my fellow group members, Katie Oliver and Liberty Foreman, for support with the use of Gaussian03 and to Liberty for help with script writing. Most of all for the laughter and joy we have shared over many lunch breaks and also for being there during the difficult times. To my fellow Ph.D. cohort in particular Liz Rodriguez, for her friendship and who has without doubt made my time here at UCL over the past four years an enjoyable experience.

I gratefully acknowledge the Biotechnology and Biological Sciences Research Council (BBSRC) (grant code; BB/F016948/1) for funding this Ph.D.

Lastly, I express my deepest gratitude to my family and friends for their love and encouragement. To my sister, Krishna Dodia, my brother, Milan Dodia, and my best friend Dilly Kabarwal, for their unconditional support, patience and always believing in me. To my parents for always supporting me in all my pursuits throughout my life.

Publications

1 Dodia, R., Holt, K., Sheppard, T., Lanigan, R. and Rich, P. R. (2014) Electrochemical and IR properties of radicals related to the tyrosine-histidine redox cofactor of bovine cytochrome *c* oxidase. *In preparation*

2 Dodia, R., Meunier, B., Kay, C. W. M. and Rich, P. R. (2014) Comparisons of subunit 5A and 5B isozymes of yeast cytochrome *c* oxidase. *In press.* Biochem. J. doi:10.1042/BJ20140732

3 Dodia, R., Maréchal, A., Bettini, S., Iwaki, M. and Rich, P. R. (2013) IR signatures of the metal centres of bovine cytochrome *c* oxidase: assignments and redox-linkage. Biochem. Soc. Trans. **41**, 1242-1248

Abbreviations and nomenclature

A	absorbance	Mb	myoglobin
Å	angstrom	Mitos	mitochondrial membrane fragments
ATP	adenosine triphosphate	mV	milli volts
ATR	attenuated total reflection	NADH	reduced nicotinamide adenine dinucleotide
Au	gold	nm	nanometre
bc_1	complex III of respiratory chain	ORF	open reading frame
BDD	boron doped diamond	PDB	protein data bank
BNC	binuclear centre	PMF	protonmotive force
CCCP	carbonyl cyanide m-chlorophenylhydrazone	Pt	platinum
C*c*O	cytochrome *c* oxidase	RCR	respiratory control ratio
cm^{-1}	wavenumber	RPM	revolutions per minute
CN	cyanide	SHE	standard hydrogen electrode
CO	carbon monoxide	TBP	2,4,6-tri-tert-butylphenol
COVs	cytochrome *c* oxidase vesicles	TMP	2,6-di-tert-butylmethoxyphenol
Cu	Copper	TMPD	N,N,N',N'-tetramethyl-p-phenylenediamine dihydrochloride
CV	cyclic voltammetry	UQ/UQH_2	ubiquinone/ubiquinol
cyt *c*	cytochrome *c*	UV	ultraviolet
Da	Dalton	*v*	stretching vibrational mode
DDM	n-dodecyl-β-D-maltoside	V/s	volts per second
$e.s^{-1}.CcO^{-1}$	electrons per second per C*c*O	v/v	volume to volume percent
E_m	midpoint potential	V_{max}	maximum velocity
E_p^{ox}	oxidation peak potential	vs.	versus
EPR	electron paramagnetic resonance	w/v	weight to volume percent
ETC	electron transport chain	WT	wild type
$FADH_2$	reduced flavin adenine dinucleotide	YPGal	1 % (w/v) yeast extract, 2 % (w/v) peptone, 2 % (w/v) galactose
Fe-S	iron sulphur cluster	δ	bending vibrational mode
FMN	flavin mononucleotide	ε	extinction coefficient
FPLC	Fast protein liquid chromatography		
FTIR	Fourier transform infrared	<u>Nomenclature of C*c*O forms</u>	
GC	glassy carbon	O	fully oxidised (Cu_A^{2+}, a^{3+}, Cu_B^{2+}, a_3^{3+})
IMS	intermembrane space	FR	fully reduced (Cu_A^{1+}, a^{2+}, Cu_B^{1+}, a_3^{2+})
i_p^a	anodic peak current	O-CN	fully oxidised, cyanide-ligated (Cu_A^{2+}, a^{3+}, Cu_B^{2+}, a_3^{3+}-CN)
i_p^c	cathodic peak current	MV-CN	mixed-valence, cyanide-ligated (Cu_A^{1+}, a^{2+}, Cu_B^{1+}, a_3^{3+}-CN)
IR	infrared	MV-CO	mixed-valence, CO-ligated (Cu_A^{2+}, a^{3+}, Cu_B^{1+}, a_3^{2+}-CO)
K_m	Michaelis Menten constant	FR-CO	fully reduced, CO-ligated (Cu_A^{1+}, a^{2+}, Cu_B^{1+}, a_3^{2+}-CO)
KPi	potassium phosphate	P_M	oxyferryl associated radical (Cu_A^{2+}, a^{3+}, Cu_B^{2+}, a_3^{4+}=O^{2-})

List of figures

List of tables

1 Introduction

1.1 Electron transport chain

The majority of energy-requiring cellular processes take place by utilising the energy released from ATP (adenosine triphosphate) hydrolysis. ATP is the molecular entity in which living organisms store energy from catabolic metabolism. Thus it is often described as the universal energy currency of the cell. In the cytoplasm, ATP is synthesised during glycolysis by phosphoglycerate kinase and pyruvate kinase. However, the bulk of its synthesis from ADP and phosphate is catalysed by the mitochondrial inner membrane protein, ATP synthase [1]. ATP synthase is indirectly driven by the proton translocating functions of the electron transport chain (ETC) embedded in the mitochondrial inner membrane and is depicted in Figure 1-1. In prokaryotes it is located on the cytoplasmic membrane.

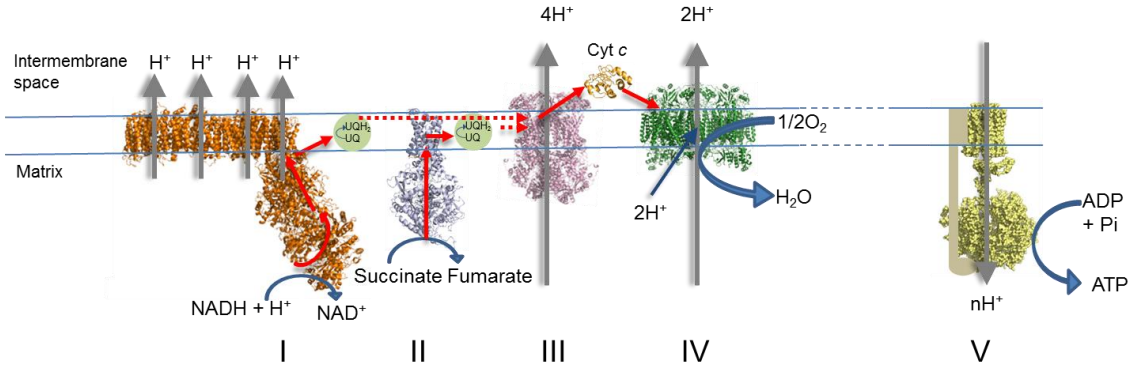

***Figure 1-1. Mitochondrial respiratory chain and ATP synthase**.*
Electron transfer (red arrows) and proton transfer (grey arrows) routes are shown. Structures of the complexes are taken from different species; complex I is from Thermus thermophilus (protein data bank accession number (PDB):4HEA); complex II is from porcine heart (PDB:1ZOY); complexes III, cyt c and complex IV are from bovine heart (PDB:1BGY), (PDB:2B4Z) and (PDB:2Y69) respectively, and ATP synthase is from yeast (PDB:1QO1). Figure is not drawn to scale.

The ETC is composed of four principal membrane protein complexes termed nicotinamide adenine dinucleotide:ubiquinone (NADH:UQ) oxidoreductase (complex I), succinate dehydrogenase (complex II), cytochrome bc_1 complex (complex III), and cytochrome *c* oxidase (C*c*O) (complex IV). Rapid intraprotein electron transfer is facilitated by the presence of redox active prosthetic groups that include flavin mononucleotide (FMN), iron-sulphur (Fe-S) clusters, flavin adenine dinucleotide (FAD), copper (Cu) and/or haem groups whose midpoint potentials are tightly controlled by the protein complex. Interprotein transfer is mediated by ubiquinone (UQ) and cyt *c*. Complex I is the largest member of the ETC; the bovine complex I is ~1 MDa and is composed of 45 different subunits [2]. The crystal structure of its 536 kDa bacterial homologue from *Thermus thermophilus* is comprised of 16 subunits and has recently been solved to 3.30 Å (Figure 1-2) [3].

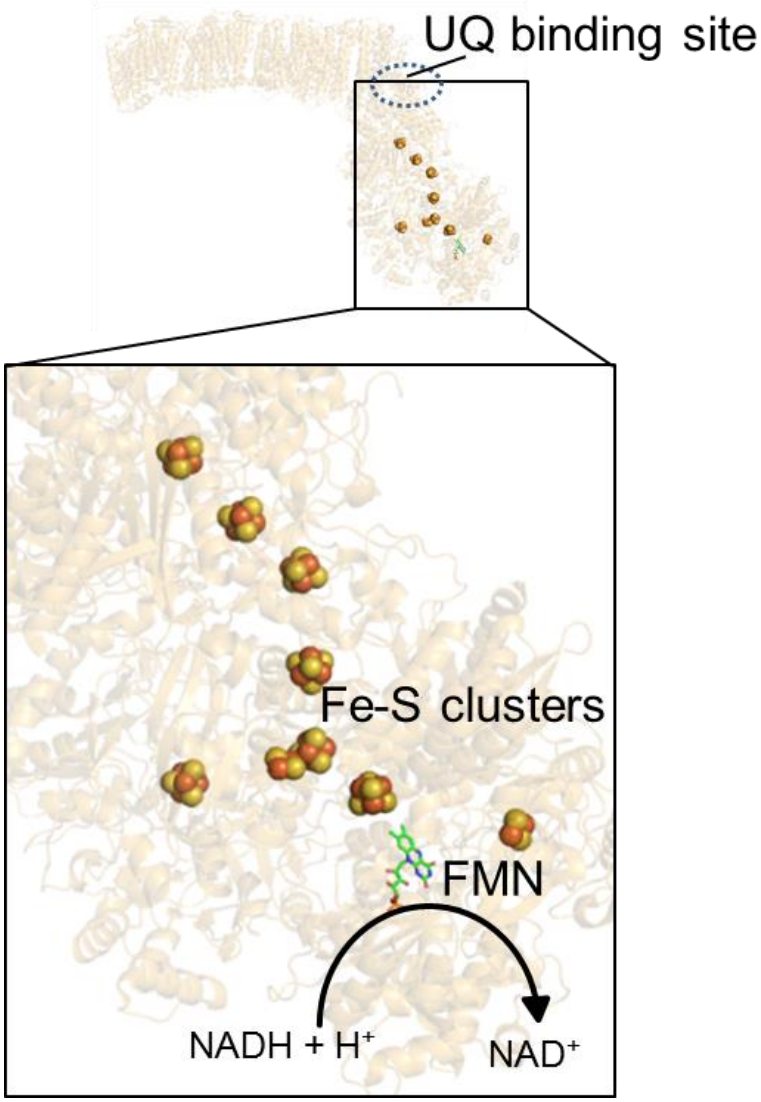

Figure 1-2. Expansion of complex I from T. thermophilus showing buried redox centres (PDB:4HEA).
Fe-S clusters are shown as spheres, sulphur atoms are in yellow, Fe atoms are in orange. Flavin mononucleotide (FMN) is shown as a stick representation and the approximate ubiquinone (UQ) binding region is highlighted.

Subunit I provides an entry site for electrons from NADH that is produced in the matrix by the citric acid cycle or fatty acid oxidation. Cytosolic NADH indirectly supplies electrons to complex I via a malate-aspartate shuttle system. Malate is translocated into the matrix via a malate-α-ketoglutarate transporter and is used by malate dehydrogenase to reduce NAD^+_{matrix} to NADH. The subsequent oxaloacetate is converted to aspartate by aspartate aminotransferase before it is transported into the cytosol via a glutamate-aspartate transporter [1]. Complex I transfers electrons from NADH to a mobile electron carrier UQ via FMN and seven Fe-S centres. Although *T. thermophilus* complex I contains nine Fe-S centres (Figure 1-2) [3], only seven transfer electrons from FMN to UQ buried in the hydrophilic matrix domain [2]. In contrast to

mammalian mitochondria, the respiratory chain of *Saccharomyces cerevisiae* (yeast) lacks complex I. Instead it contains a single subunit peripheral membrane NADH dehydrogenase (Ndi1) facing the matrix and another that faces the IMS (Nde). They are not capable of proton translocation but provide the main electron entry site into the ETC [4-7].

Complex II is a member of the citric acid cycle enzymes and catalyses the conversion of succinate to fumarate. Mitochondrial and bacterial complex II is the smallest member of the ETC (e.g. porcine complex II; 124 kDa) and is composed of 4 subunits (Figure 1-3) [8].

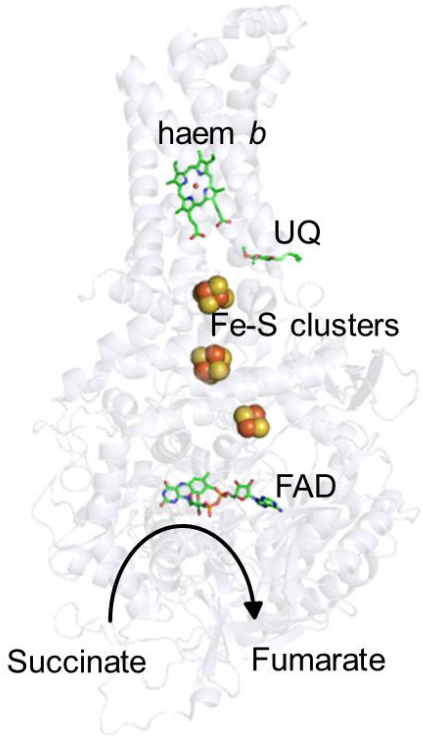

Figure 1-3. Expansion of complex II from porcine heart showing buried redox centres (PDB:1ZOY).
Fe-S clusters are shown as spheres, sulphur atoms are in yellow, Fe atoms are in orange. Flavin adenine dinucleotide (FAD), haem b and bound UQ are shown as a stick representation.

Electrons are transferred from succinate via FAD, and 3 Fe-S clusters buried in the hydrophilic subunits to ubiquinone bound to the integral membrane subunits. These subunits also ligate a haem B on the proximal and distal sides by histidines (one is replaced by a cysteine in yeast). Haem B is both close to the UQ binding site and the third Fe-S cluster. The role of haem *b* is unclear since its midpoint potential (-185 mV vs. a standard hydrogen electrode in bovine [9] and +36 mV in *Escherichia coli* [10]) is less than the third Fe-S cluster (+60 mV bovine [11]; +65 mV *E. coli* [10]) and UQ (+70 mV in ethanol [12]), and so, it is favourable for electron transfer to bypass haem *b*. Yeast mutants of haem *b* ligating residues show that it is not essential for assembly and UQ reduction. However, they exhibit decreased turnover activity [13]. Haem *b* has been proposed to stabilise the enzyme by preventing the leakage of reactive oxygen species [10] and/or provide an alternative electron transfer pathway during high electron flux [13,14].

The reduced form of UQ (ubiquinol, UQH_2) carries 2 electrons and 2 protons. The electrons are transferred to complex III which is a dimer. Each monomer of bovine complex III is ~240 kDa and composed of 11 subunits (Figure 1-4) [15].

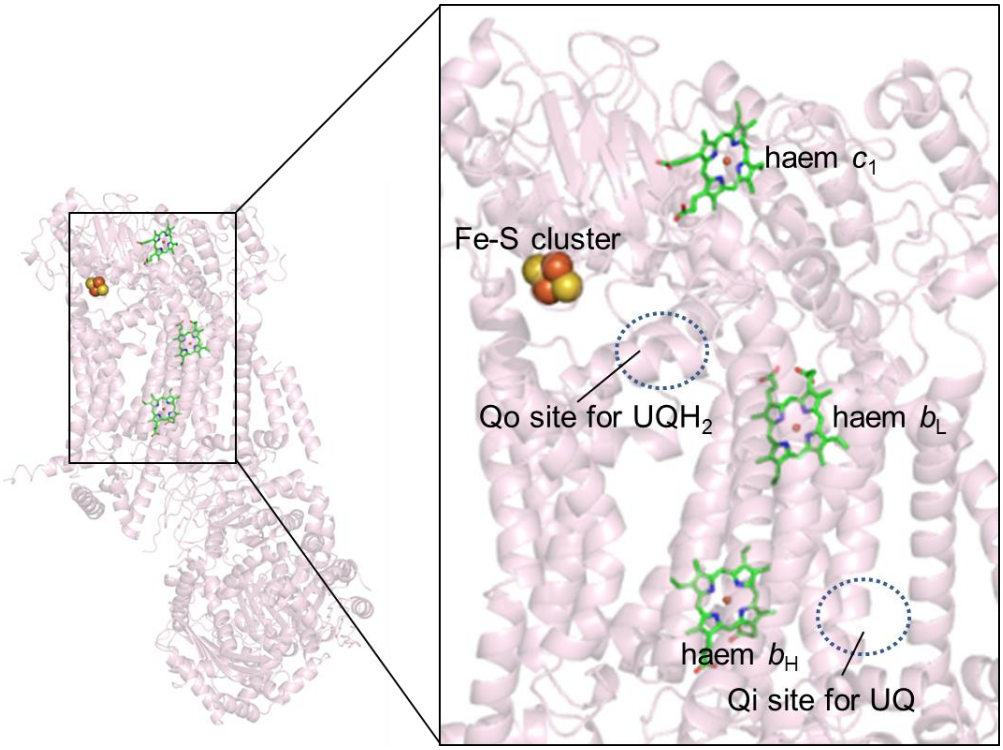

Figure 1-4. Expansion of monomeric complex III from bovine heart showing buried redox centres (PDB:1BGY).
Fe-S clusters are shown as spheres, sulphur atoms are in yellow, Fe atoms are in orange. Haems b_L, b_H and c_1 are shown as a stick representation. The approximate binding regions of UQ are highlighted.

A bacterial (*Rhodobacter Rba. sphaeroides*) homologue consists of 3 conserved subunits; Fe-S protein, cytochrome c_1 and a cytochrome *b* that contains haem b_L close to the IMS and another haem b_H close to the matrix [16]. A Q-cycle mechanism has been proposed by Peter Mitchell [17]. Upon UQH_2 binding to the Q_o site, one of the two electrons is transferred to soluble cyt *c* in the IMS via the Fe-S centre and cyt c_1. The other electron is transferred to another UQ at a second Q_i site via haems b_L and b_H. The net result is that from the oxidation of 2 UQH_2, 2 electrons are transferred to 2 cyts *c*, and 1 UQ is reduced. This process releases four protons into the IMS and collects 2 protons from the matrix.

Finally, a total of 4 reduced cyts *c* deliver four electrons from complex III to the terminal electron acceptor, complex IV (C*c*O) that catalyses the reduction of oxygen to water [18] (discussed below).

1.2 Protonmotive force

Overall, electrons are transferred from a low redox potential electron donor (NADH E_m -320 mV vs. SHE at pH 7.0 [1] and FAD, E_m -79 mV vs. SHE at pH 7.0 [11]) through to finally a high potential electron acceptor, O_2 (+816 mV [1]). These electron transfer processes are exergonic. Complexes I, III and IV have developed unique mechanisms to conserve the energy released from the exergonic electron transfer processes by coupling them to proton/charge transfer across the mitochondrial inner membrane or, in prokaryotes, across the cell membrane into the periplasmic space. Complex I translocates 4 protons from the oxidation of one NADH to NAD^+ [1]. Complex III releases 4 protons into the IMS from the oxidation of 2 UQH_2 and consumes 2 protons from the matrix due to reduction of 1 UQ [17]. Complex IV proton translocation mechanism is summarised in section 1.3 and discussed in detail in sections 1.11 to 1.15. This results in the generation of a protonmotive force (PMF) across the membrane. The PMF is a combination of both a pH gradient (ΔpH) generated from the proton concentration gradient and an electric field component (ΔΨ) generated from the charge gradient [19]. It is defined by the following equation;

$$\Delta G = 2.3RT\Delta pH + F\,\Delta\Psi$$

ΔG = Gibbs free energy change for the creation of an electrochemical gradient, R = gas constant (8.314 J/K mol), T = temperature (K), $\Delta pH = pH_{(matrix/negative\ side)} - pH_{(IMS/\ positive\ side)}$, $\Delta\Psi$ = transmembrane difference in electrical potential (V), F = Faradays constant (96.5 kJ/V).

This form of energy conservation was first described by Peter Mitchell as the chemiosmotic theory, in which energy conserving processes of the ETC, are indirectly linked to energy requiring processes [20].

ATP synthase utilises the energy conserved in the PMF, by providing a route for the translocated protons to move down their concentration/charge gradients into the matrix (Figure 1-5). As they do so, they induce a 360^o rotation of the stalk domain and the membrane domain that is composed of a ring of c subunits. Each 360^O rotation induces a series of conformational states in the three catalytic domains that can each bind ADP and phosphate. This allows 3 ADP and 3 phosphates to bind optimally to form a high energy phosphate bond and subsequently be released as 3 ATP. The number of protons required to produce 3 ATP is equal to the number of c subunits present. Crystal structures have shown the yeast mitochondrial ATP synthase has 10 c-subunits and so requires 10 H^+ to produce 3 ATP [21]. The crystal structure of the bovine mammalian ATP synthase has 8 c-subunits [22]. Thus, it is proposed that the

bioenergetic cost to produce 1 ATP in mammalian systems is less than in bacteria or yeast [22], where the c-subunits range from 10 to 14 [21,23,24].

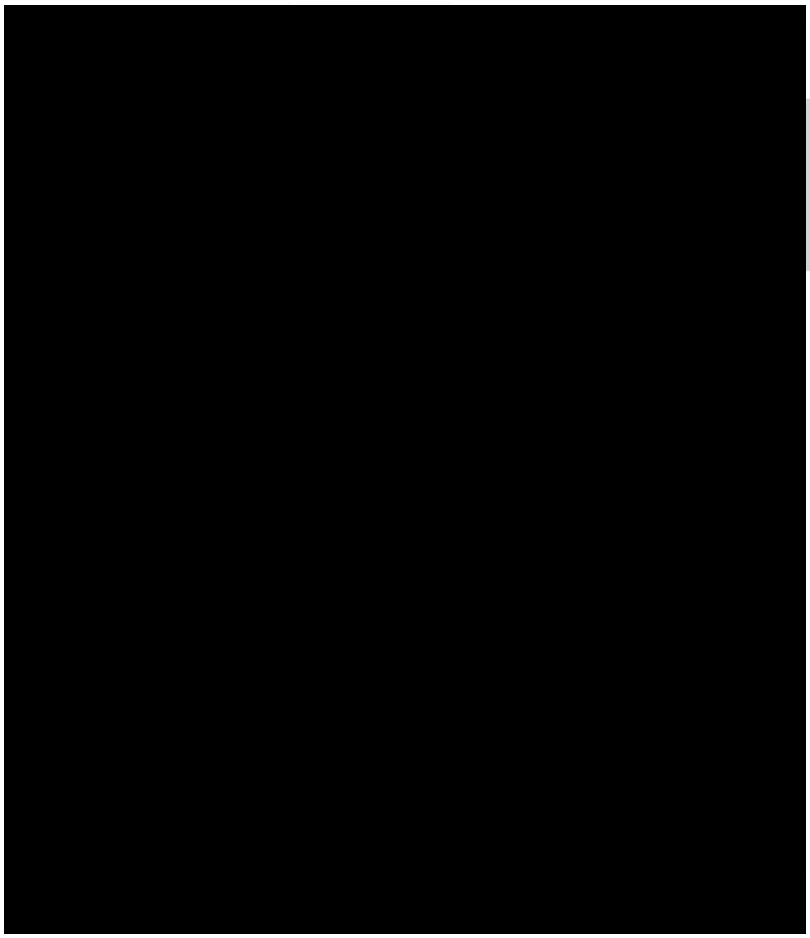

Figure 1-5. Illustration of ATP synthase structure highlighting the position of the c subunits, the stalk domain and the site for ATP synthesis.
Image is adapted from [25].

This introduction will focus on the structure and functions of C*c*O, with attention on the role of a cross-linked Tyr-His feature in the reaction P (peroxy) intermediate of C*c*O, functional groups involved in the coupling of proton transfer with electron transfer, and the roles of the possible proton pathways. It will also focus on the role of a nuclear-encoded supernumerary subunit 5 in yeast C*c*O, that is homologous to subunit IV in mammalian C*c*O [26], and is thought to be a key regulatory subunit of C*c*O [27,28].

1.3 Cytochrome c oxidase function

The terminal electron acceptor of the mitochondrial and some bacterial respiratory chains during aerobic respiration is oxygen. C*c*O catalyses the reduction of oxygen to water with 4 electrons provided by 4 reduced cyts *c* and 4 protons from the mitochondrial matrix. This oxygen reduction reaction is a PMF–generating reaction, as it consumes 4 matrix protons for water formation, but the electrons are delivered by 4

cyts *c* from the IMS [19]. However, a large further part of the released energy is conserved in the PMF, by the translocation of 4 additional matrix protons across the mitochondrial inner membrane into the IMS [29]. The overall reaction is summarised below:-

$$4\ cyt\ c^{2+}\ (IMS) + O_2 + 8\ H^+\ (matrix) \rightarrow 4\ cyt\ c^{3+}(IMS) + 2\ H_2O + 4\ H^+\ (IMS)$$

1.4 Cytochrome c oxidase structure

X-ray crystal structures of several bacterial forms of C*c*O have been solved. *Paraccocus denitrificans* aa_3 C*c*O (protein data bank accession number (PDB); 1QLE) [30], *Rba. sphaeroides* aa_3 C*c*O (1M56) [31], *T. thermophilus* ba_3 C*c*O (1XME) [32], *E. coli* bo_3-quinol oxidase that oxidises quinol rather than cyt *c* (1FFT) [33] and mitochondrial bovine aa_3 C*c*O structure has been solved to 2.8 Å resolution (1OCC) [34], that was later improved to 1.9 Å resolution (2EIJ) [35]. C*c*O belongs to a large superfamily of haem-copper terminal oxidases. They have been classified into 3 major classes of type A (mitochondrial-like oxidases), type B (ba_3-like oxidases) and type C (cbb_3-type oxidases), (italic letters represent haem types present in each structure) [36]. The classification was achieved by consideration of available sequence information, X-ray structures of primarily subunits I and II (a common feature in all forms of C*c*O), and residues implicated in the proton transfer processes [36]. The type A C*c*Os have been further divided into type A1 and A2, based primarily on the sequence motif at the end of a D channel (a proton transfer pathway-see below), that is conserved in type A C*c*Os. Type A1 contains a conserved glutamic residue in a sequence motif of –XGHPEV-, and is thought to have evolved from type A2 which instead contains a serine and a tyrosine residue in a sequence motif of -YSHPXV-. Bacteria contain all three classes of C*c*O where types A and B are most common. *P. denitrificans* aa_3 C*c*O, *Rba. sphaeroides* aa_3 C*c*O and *E. coli* bo_3 belong to the type A1 and *T. thermophilus* ba_3 C*c*O belongs to the type B and is lacking a D channel, but maintains a K channel that is common in all classes. All mitochondrial forms of C*c*O belong to the type A1, and this form of C*c*O will be the focus of this introduction.

Bovine C*c*O crystallises as a homodimer (Figure 1-6); each monomer is ~200 kDa and is composed of 13 different subunits [34], whereas for the yeast C*c*O, it is composed of 11 different subunits [37]. Subunits I, II and III are encoded by the mitochondrial genome and constitute the essential catalytic core, where the metal centres; Cu_A (subunit II), haem *a*, haem a_3 and Cu_B (subunit I), the hydrophilic pathways for proton transfer (subunit I), and the possible oxygen entrance pathway

(subunit III) are located. These subunits are conserved across all eukaryotic and most prokaryotic homologues of C*c*Os. The remaining subunits are encoded by the nuclear genome and are the supernumerary subunits.

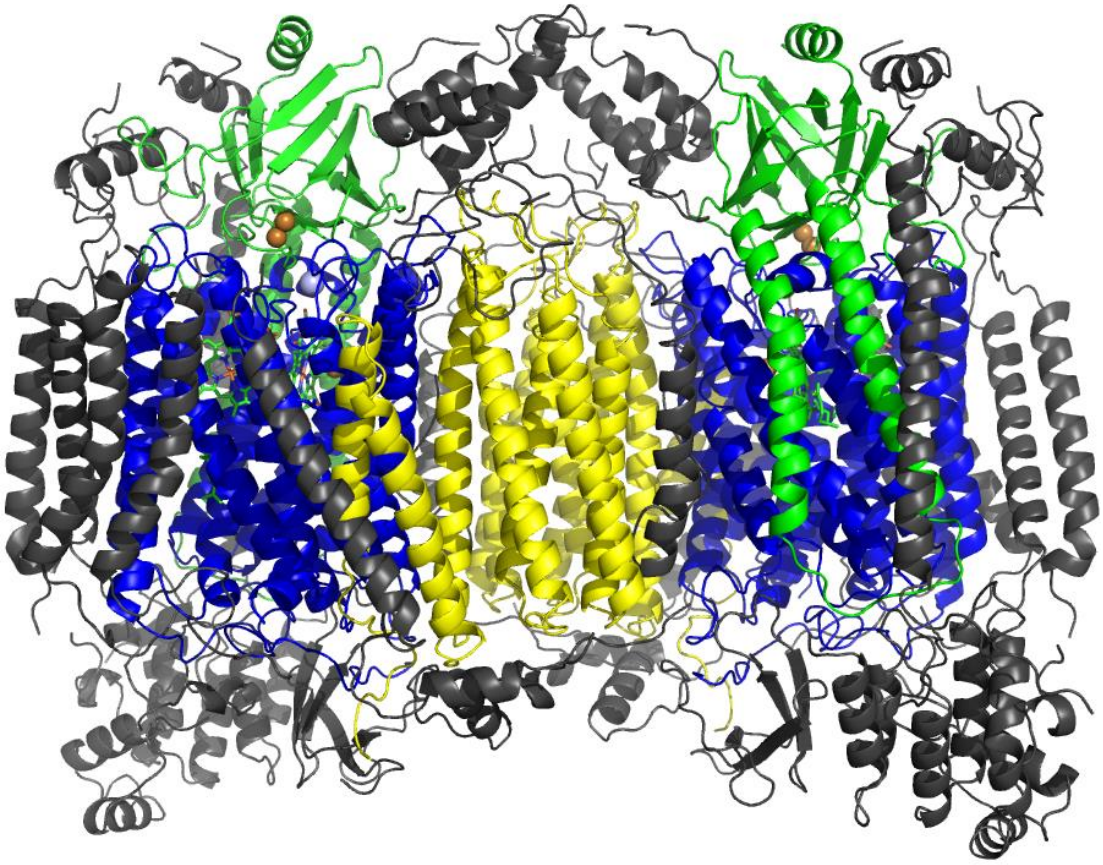

Figure 1-6. Structure of bovine CcO to 1.95 Å resolution (PDB: 2Y69).
Subunits I, II and III are coloured blue, green and yellow respectively, those in grey are supernumerary subunits.

1.5 Overview of the electron transfer route

The electron transfer pathway is shown in Figure 1-7. Electrons from cyt c^{2+} are delivered in a stepwise manner to dinuclear Cu_A. Electrons are transferred from Cu_A to haem *a* (16 Å to haem edge) and then to the binuclear centre (BNC) (~8 Å haem edge–edge) composed of haem a_3 and Cu_B which is the catalytic site that reduces oxygen to water [38].

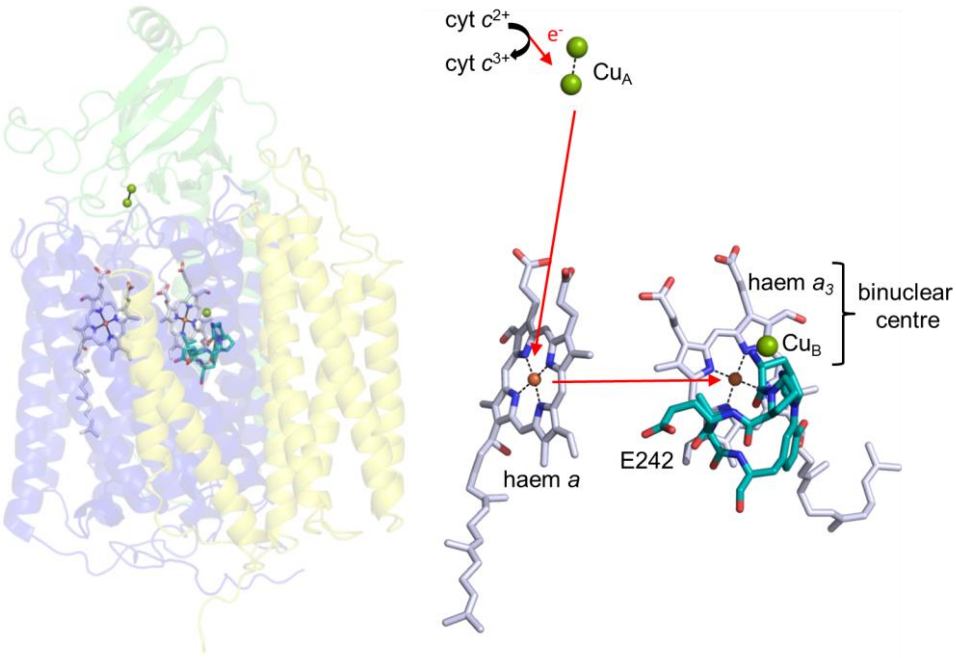

Figure 1-7. Structure of subunits I II and III of bovine CcO and its redox centres (PDB:2Y69).
Subunits I, II and III are coloured blue, green and yellow respectively. Electron transfer route (red arrows), redox centres (Cu_A, haem a, haem a_3, and Cu_B) and the conserved pentameric ring of amino acids (blue sticks) are shown with the presence of a glutamic acid at its centre.

1.6 Subunit I structure

The largest subunit is subunit I, it is composed of twelve membrane-spanning α-helices arranged in three bundles of four helices. Haem *a* is ligated on the distal and proximal sides by histidines, and provides electrons very rapidly to the binuclear centre (BNC), aided by the short (~8 Å) distance between the haem edges (Figure 1-8). The proximal ligand of haem a_3 is also a histidine, but the sixth ligand position faces the distal pocket. The haem iron is separated by 5 Å from Cu_B and provides the oxygen binding site. A further three histidines are ligands of Cu_B, intriguingly one of them (H240) (all numbering refers to the bovine C*c*O sequence numbering) is covalently bound by its Nτ (nitrogen to the ortho ring carbon of tyrosine Y244 (Figure 1-8). This creates a pentameric ring of amino acids, H240-P-E242-V-Y244 [34,38].

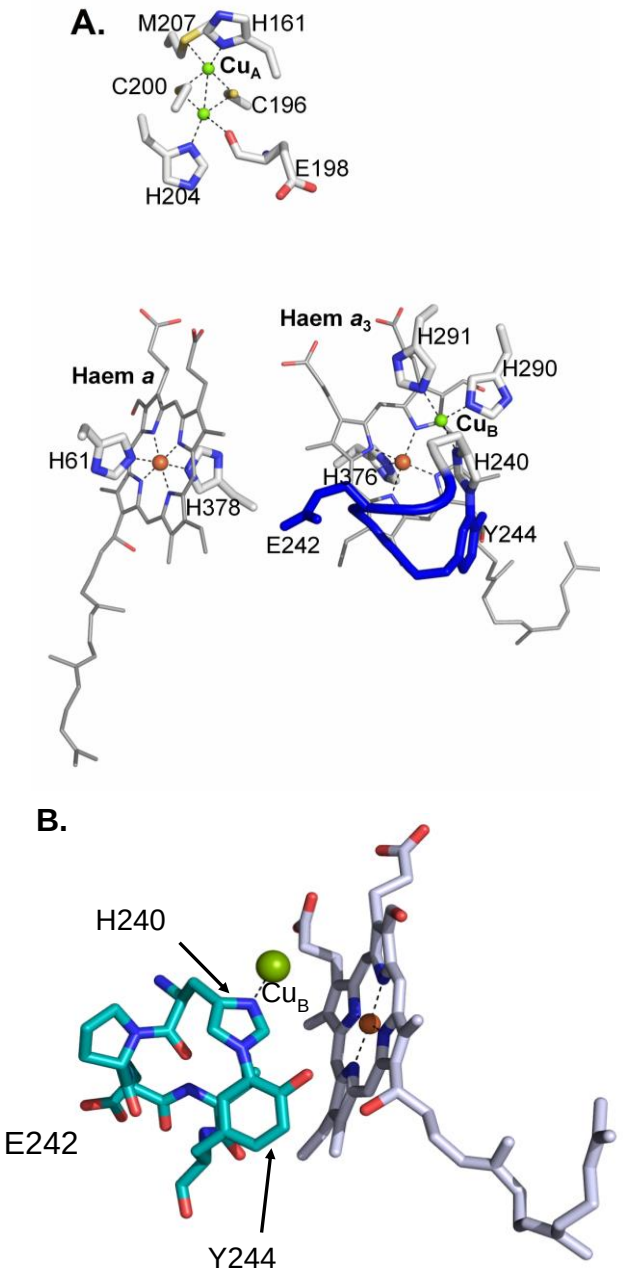

Figure 1-8. (A) Ligands of redox-active metal centres of bovine CcO. (B) Close up of the covalent linkage between ortho carbon of the phenol group of Y244 and Nτ nitrogen of the imidazole group of H240. H240 is also the ligand of Cu_B (PDB;1V54).

This structural feature is conserved in type A C*c*Os and, in type A1 bovine C*c*O, the centre of the ring is occupied by a functionally important glutamic acid, E242 (Figure 1-7). The E242 is positioned approximately 10 Å from haems *a* and a_3, and is also the residue located at the end of the D channel. The D channel is a proton channel

composed of a hydrogen bond network of hydrophilic amino acids and waters, named after D91 at its matrix side entrance. A second possible proton pathway, the K channel, named after a lysine (K319) located in the middle of the pathway, also leads from the matrix side to the cross-linked Y244 at the BNC. X-ray crystallographic data of bovine C*c*O has revealed a third pathway termed the H channel. In contrast to the others, this forms a possible continuous hydrophilic route for protons leading from the matrix to the IMS that runs beside haem *a* [38-40]. The homology model of yeast C*c*O, also revealed a continuous H channel in the equivalent location, however, some of the amino acids are not conserved [41]. The structures of all three pathways in the yeast C*c*O and bovine C*c*O are overlaid in Figure 1-9.

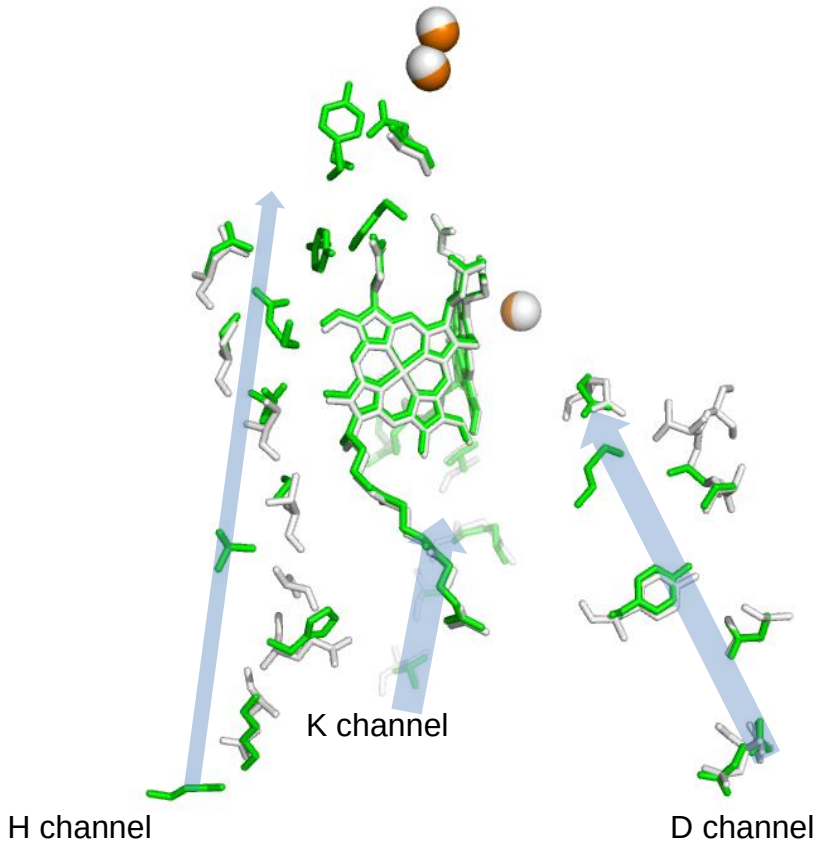

Figure 1-9. The D, K and H channels of bovine CcO and of the homology model of yeast CcO [41] are superimposed.
The pathways of the bovine CcO (PDB:2Y69) are shown in green and the yeast CcO are shown in white. This structure has been rotated horizontally 90^{o} anti-clockwise.

1.7 Subunit II and III structure

Subunit II has two membrane spanning α-helices and a globular hydrophilic domain facing the IMS. This subunit is conserved in all types of C*c*O [36]. This provides the binding site for soluble cyt c^{2+}, mediated by electrostatic interactions between the positively charged groups on cyt *c,* and negatively charged groups on C*c*O [42,43]. Subunit III is formed of 7 membrane spanning α-helices, and does not contain metal centres or hydrophilic pathways [34]. Removal of subunit III from purified *Rba. sphaeroides* C*c*O, by incubation with triton X-100 detergent, resulted in 'suicide inactivation' after reaction with oxygen under steady state conditions [44]. Hence it was proposed to be essential in maintaining the stability of the BNC, via long range interactions. In the crystal structure of bovine C*c*O, it provides an interaction point between the two monomers (Figure 1-7). The transmembrane helixes are oriented such that they form a V-shaped cleft leading to the BNC. Hence, a hydrophobic channel in subunit III of *P. denitrificans* C*c*O, has been proposed for oxygen diffusion to the active site from the lipid bilayer [45]. To further define an oxygen pathway, X-ray structures have been solved of *T. thermophilus* C*c*O, here, crystals were pressurized with xenon gas that acted as an oxygen analogue and bound to hydrophobic cavities [46,47]. *T. thermophilus* C*c*O lacks subunit III; nevertheless, a Y shaped channel in subunit I, lined with hydrophobic residues leading from the lipid bilayer to the BNC (18–20 Å in length) has been identified as an oxygen diffusion pathway in this enzyme. This channel is not entirely conserved in all C*c*Os whose structures have been solved [46,47]. Three possible pathways for oxygen entry are proposed for bovine C*c*O that also has a V-shaped cleft in subunit III [34]. One proposed pathway passes through subunit III shown in Figure 1-10. Definitive assignment will require solving X-ray structures in the presence of xenon gas as has been carried out for *T. thermophilus* C*c*O [46,47]. The product H_2O is thought to exit the BNC via a hydrophilic route that leads to the IMS. The exact pathway has not been characterised. However, it is proposed to exit via the haem propionates and hydrophilic residues surrounding the Mg^{2+} ion, that is 10 Å from the haem a_3 edge, followed by residues on subunit II [34].

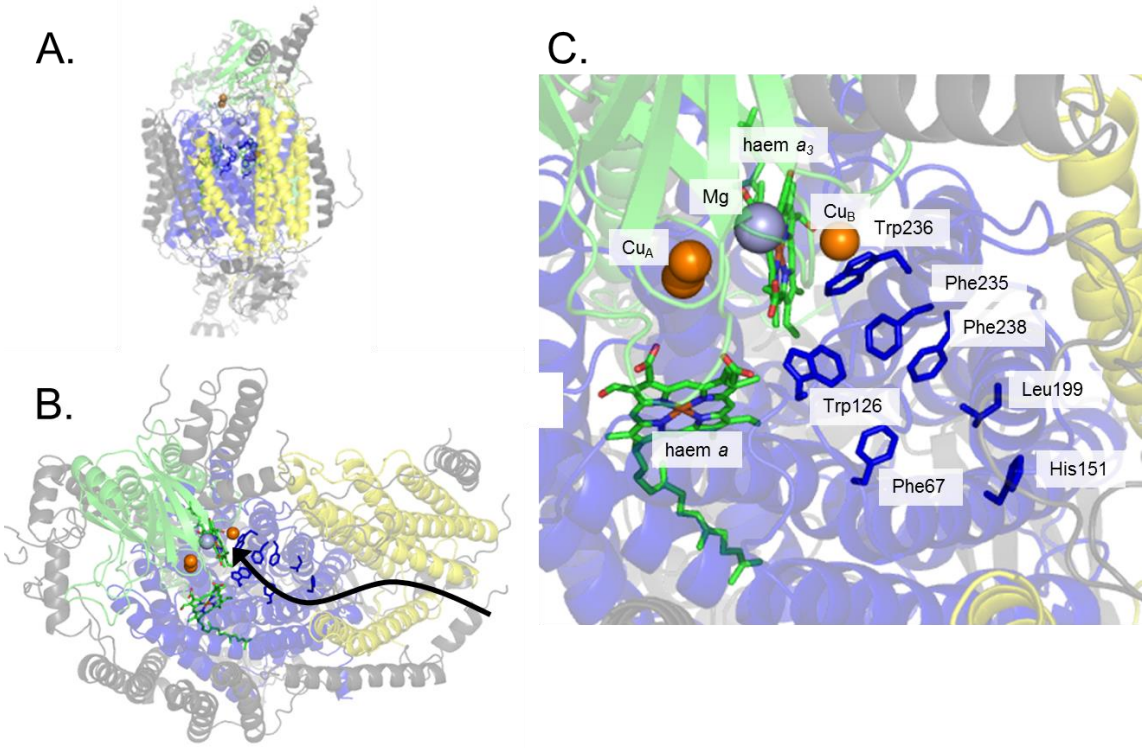

Figure 1-10. Possible oxygen channel in bovine CcO (PDB;2Y69).
A. Subunit III (yellow) forms a V-shaped cleft leading to subunit I (blue). B. A view from the top showing a possible oxygen diffusion pathway from the lipid bilayer (black arrow). C. Hydrophobic residues in subunit I proposed by [34] to provide a pathway for oxygen to the BNC. Subunit II is shown in green and supernumerary subunits are coloured in grey.

1.8 Reaction mechanism

Figure 1-11 shows the overall reaction cycle of C*c*O based on [18]. Some of the protonation states of ligands, e.g. hydroxide versus water, remain controversial. Every electron transfer is associated with the uptake of a substrate proton, of which there are four. When the enzyme is fully reduced (FR - Cu_A^{1+}, a^{2+}, Cu_B^{1+}, a_3^{2+}), the distal pocket of haem a_3 becomes available for oxygen to bind (A). The reduction of oxygen to produce two oxide products requires four electrons. To avoid reactive oxygen species being released into the mitochondria, it is proposed that these four electrons are supplied from the immediate vicinity of the BNC. One is proposed to come from the covalently linked Y244 of the pentameric ring, because it is positioned such that it is close to and faces the oxygen binding site. As a result, it is proposed to form a neutral tyrosine radical (see below) [38,48,49]. The second two electrons are from haem a_3 which forms a high oxidation state ferryl species (P - Cu_A^{2+}, a^{3+}, Cu_B^{2+}, a_3^{4+}=O^{2-} plus protein associated radical) and the fourth is from a cuprous/cupric Cu_B transition. To return to FR, four electrons are supplied one at a time from ferrocyt *c,* via Cu_A and haem *a* to the BNC, to reduce the four BNC sites that donated an electron. The first

electron is thought to reduce the tyrosine radical, which is also associated with the uptake of a substrate proton (F - Cu_A^{2+}, a^{3+}, Cu_B^{2+}, a_3^{4+}=O^{2-}). The second electron transfer and associated substrate proton, reduces haem a_3^{4+} to haem a_3^{3+} to form the O state (oxidised state - Cu_A^{2+}, a^{3+}, Cu_B^{2+}, a_3^{3+}). The third (E) and fourth electron and proton transfers into the BNC centre reduce Cu_B and haem a_3, respectively, with the release of two water molecules to form the FR state, where the site becomes available for the next oxygen to bind.

Figure 1-11. Reaction cycle for oxygen reduction.
CcO steps through a series of catalytic intermediates, out of these, steps O (oxidised) → E, E → FR (reduced), P (peroxy) → F (oxyferryl) and F → O are associated with the uptake of an electron and a substrate proton, these steps are also coupled with the translocation of a proton into the IMS (not shown). Figure is taken from Figure 11 in ref [19].

1.9 P and F transient intermediates

The P and F transient intermediates of the reaction cycle are characterised by a distinct visible absorption maximum at 607 nm of the P state, and at 580 nm of the F state [50,51]. Meanwhile, their Soret band positions are the same 428 nm [52].

Although the major principles of how oxygen reduction occurs are understood, the precise structures (including sites involved in de/protonation) and chemical properties of the transient P and F intermediates are still under question [53-55]. Oxygen enters and binds to the distal pocket of haem a_3 when the BNC is reduced [56]. The name of

P (peroxy) was given since it was originally proposed to have a peroxide structure [50]. However resonance Raman spectroscopy data now show that the O-O bond is already broken in the P state from a band at 803 cm^{-1} attributed to the $Fe^{4+}=O^{2-}$ stretch of an oxyferryl structure of haem a_3 [57-59]. This was also supported by mass spectrometry data of $H_2{}^{18}O$ that is released into the bulk solution when $^{18}O_2$ reacts with C*c*O to form the P_M state [60]. The conversion from FR to A to P is fast (10 µs and ~200 µs [55]) and, although it requires 4 reducing equivalents, it takes place in a single measurable step. Hence the electrons must be donated by the BNC as described above. One of these electrons is suggested to come from Y244 that would form a radical [38,48,49].

Visible absorbance spectra of the P and F states, rule out the possibility that the fourth electron comes from the haem a_3 macrocycle, which would result in a porphyrin π-cation radical ($haem^{\cdot+}$ a_3 ($Fe^{4+}=O^{2-}$)), as occurs in some peroxidases. This is concluded because the Soret band (400-430 nm) of a porphyrin radical associated ferryl intermediate, is expected to have the same peak position as the ferric state, and a smaller extinction coefficient as is observed, for example, in horseradish peroxidase [61,62]. However the Soret band of the P and F states are red shifted and equivalent in intensity to the ferric state. This behaviour is consistent with the ferryl haem only in both species, with any radical in the P state being located instead on an amino acid, as is observed, for example, in compound I (an electronic equivalent of the P state) of cytochrome *c* peroxidase [63].

1.9.1 Experimentally induced P and F states

P and F are catalytic transient intermediates that can be experimentally induced in a manner that last for several minutes to permit analysis. These artificially generated forms have been given names that refer to the conditions used to induce them (P_M/P_R/F/ $F^{\cdot}$ (F dot)) [54,55]. Figure 1-12 summarises how the various forms of P and F states differ.

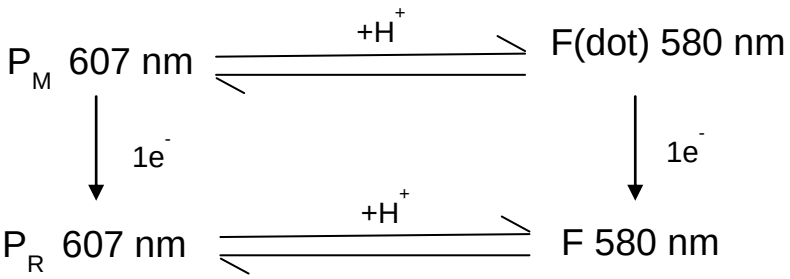

Figure 1-12. Schematic showing how the various P and F states differ in their protonation state and electron status, together with the position of their visible absorption band.
See main text for how each state is experimentally generated.

1.9.1.1 P_M

The P_M state can be formed with two different approaches. In the first, fully oxidised C*c*O is reacted with CO/O_2 at alkaline pH. CO donates two reducing equivalents and two protons to reduce only the BNC where it is released as CO_2. This forms a mixed-valence state that binds and reacts with O_2 to form A that spontaneously decays to form the P_M state (Figure 1-13) [64,65]. In the second approach, fully oxidised C*c*O is reacted with stoichiometric levels of H_2O_2 at alkaline pH [52]. H_2O_2 reacts with the BNC to form P_M and H_2O is released. In both reactions, Cu_A and haem *a* remain oxidised. Hence P_M will be an oxyferryl species with an associated radical, equivalent to the P state with a visible absorption peak at 607 nm.

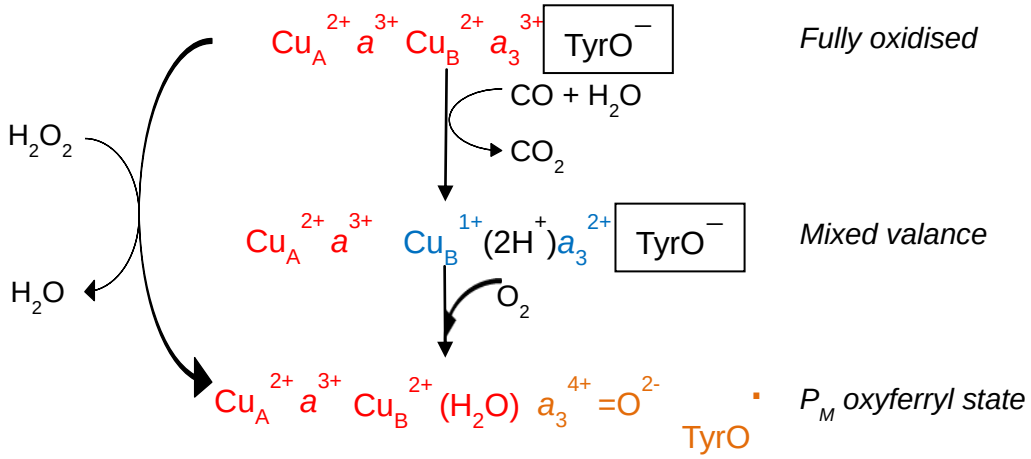

Figure 1-13. Reaction mechanisms of fully oxidised CcO with CO/O_2 or stoichiometric levels of H_2O_2, at alkaline pH to form P_M state.
The protonation state of tyrosine within the BNC is not definitively established.

1.9.1.2 P_R

The P_R state is a transient state that forms when the same CO/O_2 reaction occurs with the fully reduced enzyme at alkaline pH. Therefore it can only be observed at low temperatures (-90 ^oC) [66]. Here the BNC contains one more electron than the P_M state that is provided haem *a*. However, the visible spectrum of P_R is the same as P_M with a peak at 607 nm [66]. This transient P_R state forms the F state with the uptake of a proton.

1.9.1.3 F

The F state can be formed when fully oxidised C*c*O is reacted with an excess of H_2O_2 at alkaline pH. Initially, the P_M state is formed as described above. However, this reacts with a second H_2O_2 that donates a third electron and a proton (and is released as a superoxide O_2^- or hydrogen superoxide $HO_2^{\cdot}$) to reduce the radical species in P_M and so form a stable F state.

The ratios of P_M and F states generated by the H_2O_2 reaction in the steady state are dependent on the relative amount of H_2O_2 reacted and the pH [67,68]. At low pH the F state is favoured and at high pH with equal ratios of H_2O_2 and C*c*O, the P_M state is favoured [52].

1.9.1.4 $F^{\cdot}$ (F dot)

An $F^{\cdot}$ state is formed by reaction of oxidised C*c*O with stoichiometric levels of H_2O_2 at low pH [69]. This state is also formed by lowering the pH of a sample of C*c*O in the P_M state that has been prepared at alkaline pH with either CO/O_2 or stoichiometric levels of H_2O_2 [69,70]. $F^{\cdot}$ is isoelectronic with P_M, but its visible spectrum is similar to the F state with an absorption maximum at 580 nm instead of 607 nm. Since it is isoelectronic with P_M, the $F^{\cdot}$ state must also have a radical amino acid. The shift from a 607 nm (P_M and P_R) to a 580 nm (F and Fdot) species is most likely the result of protonation of a site within P_M or P_R, rather than an effect on the haem a_3 spectrum of an amino acid radical [54]. For example, the 607 nm peak is present in the P_R and P_M states even though only P_M contains a radical species.

1.9.2 Detection of a radical species in P_M

EPR spectroscopy has in fact detected one or sometimes two radicals in C*c*O when it reacts with H_2O_2 [52-54,71]. The broad and narrow EPR signals detected were dependent on the pH conditions used. At alkaline pH (8.0) the P_M state exhibits a narrow signal attributed to a tyrosine (Y244 [53]) or a porphyrin cation radical [54]. At low pH (6-6.5) $F^{\bullet}$ has a broad signal that was attributed to the migration of the radical to a nearby tryptophan [54,70] or another Y129 [53,72]. Intriguingly the same broad signal was detected by Budiman, *et al.* [73] in *P. denitrificans* C*c*O but was independent of pH and, through mutagenesis (Y167F), it was assigned to Y167, a residue 10-13 Å away from the haem a_3-Fe (equivalent to Y129 in bovine C*c*O). In all cases, there has not always been a direct correlation between the amount of the radical species and specific intermediates of the reaction cycle. The radicals have been suggested to arise from a side reaction after H_2O_2 has reacted with the BNC, and subsequent migration of the radical to other sites [54,55]. For example, the background narrow EPR signal of a porphyrin radical was detected in P_M, $F^{\bullet}$ and also in the F intermediate that should not contain a radical [54]. Non-specific side reactions can also occur from the toxic by-products, superoxide $O_2^{\bullet-}$ or hydrogen superoxide $HO_2^{\bullet}$, of this reaction.

In contrast, in the P_M state generated by the less damaging reaction of oxidised C*c*O with CO/O_2 at alkaline pH, no EPR signal attributable to a tyrosine, tryptophan radical or porphyrin cation radical was detected [52,54,70]. The absence of an EPR signal was proposed to be due to the spin coupling of the true cross-linked Y244(-H240) radical (S=1/2) with paramagnetic Cu_B^{2+} (S=1/2) because the Cu_B distance from Tyrosine-OH group is 5.7 Å and Cu_B is a ligand of H240 [38,54,70,74,75].

Radioactive iodide labelling of the P_M state (bovine C*c*O) prepared using the CO/O_2 method followed by peptide cleavage and detection of labelled residues has located the radical site to be on Y244 [76]. Resonance Raman spectroscopy has detected a band at 1489 cm^{-1} that was tentatively assigned to a C-O$^{\bullet}$ stretch of a tyrosine radical of the P_M state of *E. coli* C*c*O [77] but its definitive assignment still requires isotope labelling.

IR spectroscopy can also offer a means to detect a protein associated radical and this has been explored in Results Chapter 5 with the aid of model compounds that have provided reference spectra.

1.10 Route for substrate protons

The K and D channels provide the substrate protons to the BNC (reviewed in [78-81]. The role of the K channel in providing substrate protons has been investigated in purified C*c*O. This has been achieved by site-directed mutagenesis of conserved residues and following absorbance changes of a pH indicator dye (measuring proton uptake/release) and haem redox states (measuring electron transfer) [82-84]. K channel mutants of *Rba. sphaeroides* C*c*O had diminished turnover activity in which K362M (K319-bovine numbering) had turnover activity that was 2 % of wild type and T359A (T326-bovine numbering), ~35 % of wild type [83]. The FR states of these mutants were able to bind and react with O_2 and become oxidised, and the proton uptake that is associated with the oxidation of C*c*O [85] was not affected in these K channel mutants. However, the proton uptake that is associated with reduction of the oxidised BNC [85] was impaired, suggesting the K channel is involved in proton uptake only during the reduction of C*c*O [83]. E286 (E242-bovine) of *Rba. sphaeroides* C*c*O is situated at the top of the D channel. A E286Q mutant of *Rba. sphaeroides* C*c*O exhibited the opposite behaviour. The reaction of oxygen with the FR state was impaired and so was the proton uptake. However, proton uptake associated with the reduction of the BNC was unaffected [84]. Therefore, the first 1 or 2 substrate protons are delivered by the K channel and are associated with the reductive phase of the reaction cycle (O to E to R) and the second 3/2 substrate protons are transferred by the D channel and are associated with the oxidative part of the cycle (R to P to F to O) [80,81]. The slow and only partial reduction of the oxidised BNC (electron transfer from haem *a* to a_3) in the K362M mutant of *Rba. sphaeroides* C*c*O (also observed by Jünemann, *et al.* [86]) led to the proposal of an alternative role of the K channel as a dielectric well/channel whose role would be to increase the dielectric strength around the BNC to allow transiently charged intermediates to exist, before they are charge compensated by protonation [78,86]. Either function would be consistent with the observation that the reduction phase (O to E to R), takes up 2 charge compensating protons to the BNC [85].

1.11 Route for translocated protons

There is sufficient evidence in literature that the route for translocated protons in bacterial C*c*Os is provided by the D channel (see below). However the presence of an extensive H channel in bovine C*c*O, has led to the proposal that the H channel provides this route at least in mammalian oxidases reviewed in [87]. Yeast C*c*O also has an extensive H channel as shown in Figure 1-9. Hence, two models have been

proposed for proton translocation in C*c*O which involve either the D channel or the H channel and are discussed below.

1.12 Model for proton translocation via the D pathway

The role of the D channel in providing the route for some substrate protons and all translocated protons has been proposed for both bacterial and mitochondrial C*c*Os reviewed in [19,55,78]. The mechanism involves a functionally important glutamic acid (E242) (Figure 1-7) that is buried in the centre of subunit I, in a region of low dielectric strength. Fourier-transform infrared (FTIR) spectroscopy has been used to determine the pK_a of this residue. This has been achieved by following the IR changes of its protonated carboxyl group in the reduced *minus* oxidised IR difference spectrum of *P. denitrificans* C*c*O at different pHs (4.7-9.0) [88]. Surprisingly the IR band was found to have no pH dependence and so the group must have an unusually high pK_a above 9.0. This is also true for the bovine C*c*O where pH titrations (6.5-8.5) of the FR to FR-CO transition showed no pH dependence of the protonated carboxyl group IR band [89,90]. Mutagenesis of this residue into a glutamine impairs turnover activity in *Rba. sphaeroides* C*c*O, by preventing electron transfer in the oxidative phase of the reaction cycle, hence confirming that it is an essential residue for enzyme activity [84,91,92]. A E286C mutant from *Rba. sphaeroides* C*c*O, that was reconstituted into liposomes, retained electron transfer activity however proton pumping activity was lost [92]. Furthermore, the mutation of an equally conserved asparagine residue located in the D channel of *Rba. sphaeroides* C*c*O resulted in the inhibition of proton pumping but accelerated the electron transfer activity by 150-300 % [93].

The proposed model for translocation, via the D channel, is based on the principle of electroneutrality, which states that each electron arriving at the BNC in a stable manner, must be charge-compensated by a proton [85,94]. This is necessary because the BNC is in a region of low dielectric strength, and it would be energetically unfavourable for charged species to exist. Taking this concept of charge compensating electrostatics into consideration, a model for proton translocation was put forward [19,94]. Figure 1-14, Figure 1-16 and Figure 1-17 show the steps involved for a single proton translocation event (out of four), where each is associated with one of the four electron transfers from haem *a* to the BNC, during the reaction cycle. As an electron is being transferred to the BNC, the proton on glutamic acid is translocated to a so-called 'trap' site where it electrostatically stabilises the negative charge being introduced in the active site. The K channel may facilitate formation of such charge-compensated intermediates, via its possible role as a dielectric channel, by reorganisation of dipoles and charges of its amino acids (see Figure 1-14) [19,86].

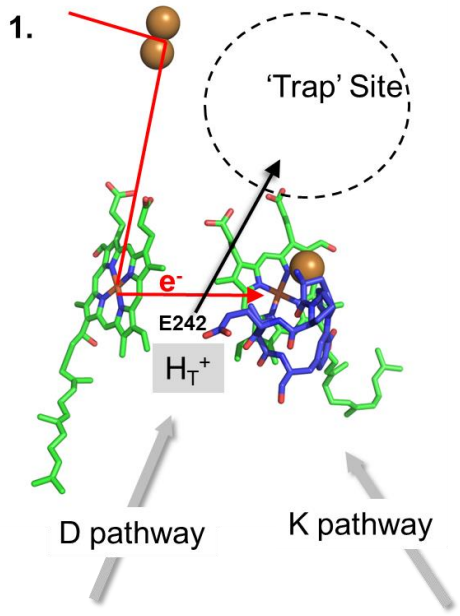

Figure 1-14. Step 1 of 3 of the proton translocation model via the D channel.
Black arrow shows the route of the translocated proton (H_T+) when an electron is being donated to the BNC (red arrow).

The 'trap' site places the proton in a region where it can compensate the BNC charge but cannot be used as a substrate proton. The exact location is unknown but possible candidates near the Mg^{2+} are shown in Figure 1-15. They include haem a_3 A- and D-propionates, arginines/aspartates/glutamic acids or water molecules. Molecular dynamic simulations show changes in the hydrogen bond pattern, and conformational changes in the haem a_3 propionates upon reduction of haem *a* [95]. The change was linked to an estimated pK_a increase from ~7 to 9 of only A-propionate, and so it was proposed that when haem *a* is reduced it enables the proton from E242 to be transferred to A-propionate (the 'trap' site) via water molecules and the D-propionate [95].

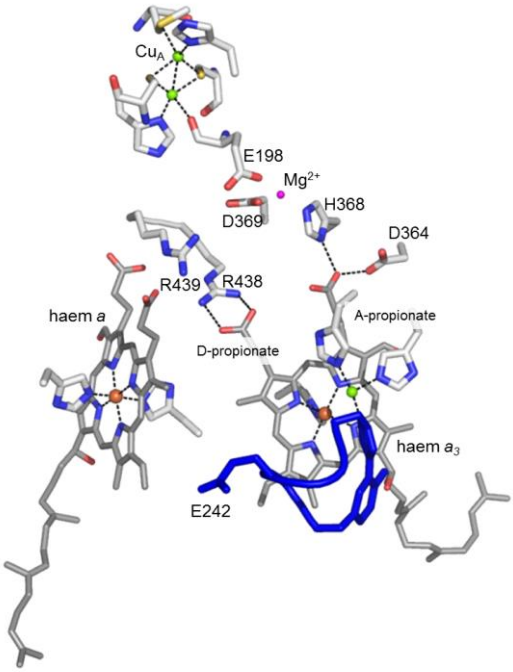

Figure 1-15. Hydrophilic residues that could be possible proton trap sites near the Mg^{2+} ion (purple ball).
Structure is of oxidised bovine CcO (PDB;1V54), the metal centre ligands are also shown.

Since the pK_a of glutamic acid is high [96], it becomes re-protonated via the D channel. The substrate proton is then delivered into the BNC via either the D or the K channel (Figure 1-16) [81].

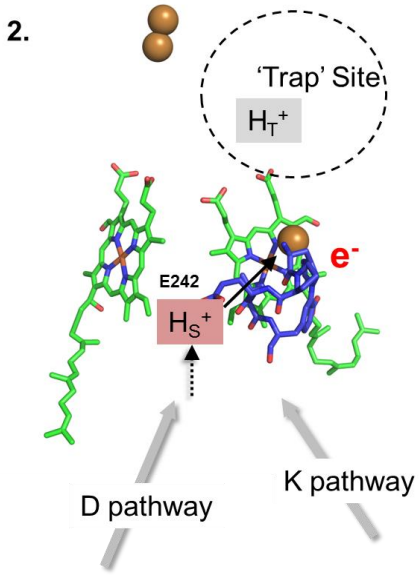

Figure 1-16. Step 2 of 3 of the proton translocation model via the D channel.
H_T^+ is stabilised at the trap site by the negative charge at the BNC. A substrate proton for water formation (H_S^+) re-protonates E242 from the D/K channel and is attracted to the negative charge at the BNC (black arrow).

Once the electron has arrived at the BNC, the proton on glutamic acid is attracted to the negative charge and moves to the BNC, to form the next stable oxygen intermediate of the reaction cycle. As a result, the negative charge has been neutralised and the proton located in the 'trap' site is expelled into the IMS. The glutamic acid finally becomes re-protonated again by a further proton delivered via the D (Figure 1-17).

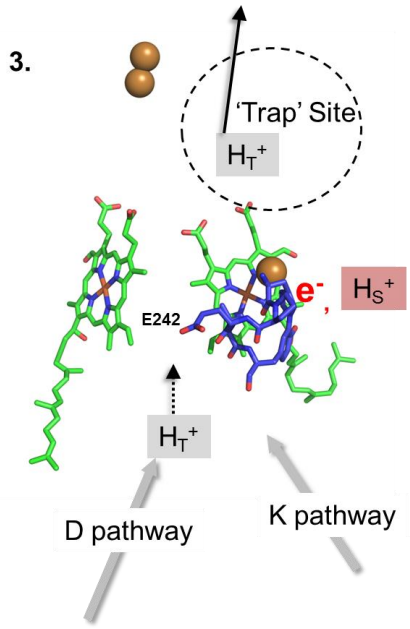

Figure 1-17. Step 3 of 3 of the proton translocation model via the D channel.
H_T^+ is extruded into the IMS as the negative charge at the BNC is neutralised by H_s^+. E242 becomes reprotonated by the next H_T^+ from the D channel.

1.13 Controversial points on the D pathway

Several factors of this model are not well understood. For example, it is not clear how the proton reaches the 'trap' site or the BNC from glutamic acid, because the space between these sites in X-ray crystal structures of C*c*O lacks electron density. A plausible explanation is that the space is filled with dynamic water molecules, which would be undetectable with X-ray crystallography. Indeed, molecular dynamic simulations have been used to model the water molecules in this region of *Rba. sphaeroides* and bovine C*c*O [79,95,97]. Furthermore, FTIR spectroscopy has detected a chain of water molecules in bovine and *P. denitrificans* C*c*O, that have been shown to undergo structural changes in response to ligand (CO) binding/unbinding at the BNC, and to redox changes of the metal centres [98]. Moreover, the spectral signature of the change was similar in both oxidases, suggesting that they have water molecules that undergo a similar change. However, the location of the observed chain of water molecules in the protein structure is unresolved, but the vacant space surrounding the

glutamic acid remains a strong candidate, as it is large enough to accommodate a chain of eight simulated waters [98]. An additional aspect that remains unclear is how the essential gating mechanism could operate in the D channel in order to deliver protons alternately to the proton trap site or the BNC. A chain of water molecules could take on this role by breaking and forming hydrogen bonds, during their reorganisation [98]. Furthermore, it is also unclear how protons are prevented from leaking backwards from the trap site and exit pathway into the matrix side of the membrane. It is suggested that this can be controlled by the transiently changing pK_a values of the amino acids lining the pathway, in response to different redox states of the enzyme during the reaction cycle [19]. Finally, to date a hydrophilic route for proton extrusion from the trap site in to the IMS has not been definitively resolved.

1.14 Model for proton translocation via the H pathway

The second model for the translocation of protons is via the H channel, which was identified as a continuous hydrophilic channel in the X-ray structure of bovine C*c*O [38]. The H channel is composed of two halves. The IMS end is composed of a hydrogen bonded network of predominantly amino acids, the second half is composed of predominantly water molecules and some amino acid side chains leading from the matrix [87].

The H channel is proposed to be functional as the proton translocation pathway in mammalian/mitochondrial C*c*Os [38-40]. X-ray structures of bovine C*c*O in the fully reduced and fully oxidised states revealed redox linked conformational changes (Figure 1-18) [38,39]. The most noticeable change was of an aspartic acid (D51) located at the ‘exit’ of the channel. The nature of the conformational change is such that the residue becomes exposed to the aqueous environment of the IMS when the enzyme is reduced. Hence, it has been suggested that the conformational change is linked with a pK_a change of D51 by approximately 5 units [87], such that D51 becomes deprotonated upon reduction.

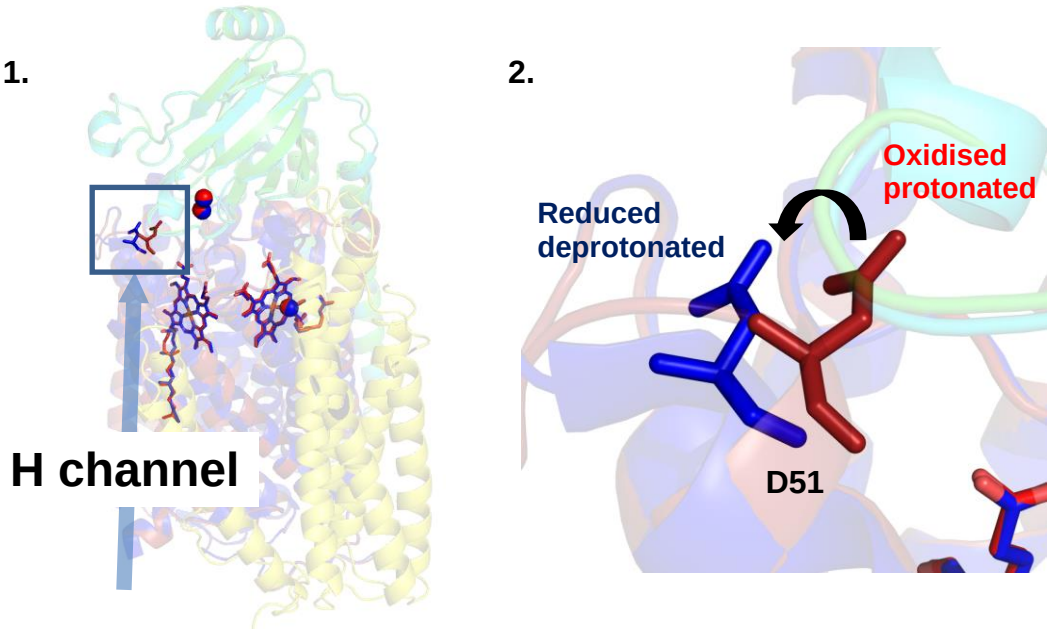

Figure 1-18. Redox-linked conformational change in D51 of bovine CcO.
*The structure of the fully oxidised (red) (PDB:1V54) has been superimposed on the fully reduced CcO (PDB:1V55). '**2.**' is an expansion of '**1.**'*

In order to study the effect of site-directed mutagenesis on D51 of bovine mitochondrial C*c*O, a hybrid expression system was developed by Tsukihara, *et al.* [39]. This was achieved by insertion of vectors in to HeLa cells that express bovine subunit I in the cytosol. This is imported into mitochondria where it competes with the human subunit I and assembles with the remaining human subunits to form a chimeric hybrid C*c*O. The proton pumping activity of a D51N hybrid mutant in mitoplasts (mitochondria without the outer membrane) was lost. However, the oxygen reduction activity was retained and was intriguingly 70 % faster than wild-type.

A peptide bond formed between a tyrosine and a serine (Y440-S441) is located in hydrogen bonding distance of D51 [38] (Figure 1-19), and it is proposed to re-protonate D51 when the enzyme is oxidised [87]. Site-directed mutagenesis of S441 to a proline was also found to abolish proton pumping, without affecting the oxygen reduction activity in the same hybrid expression system described above [99].

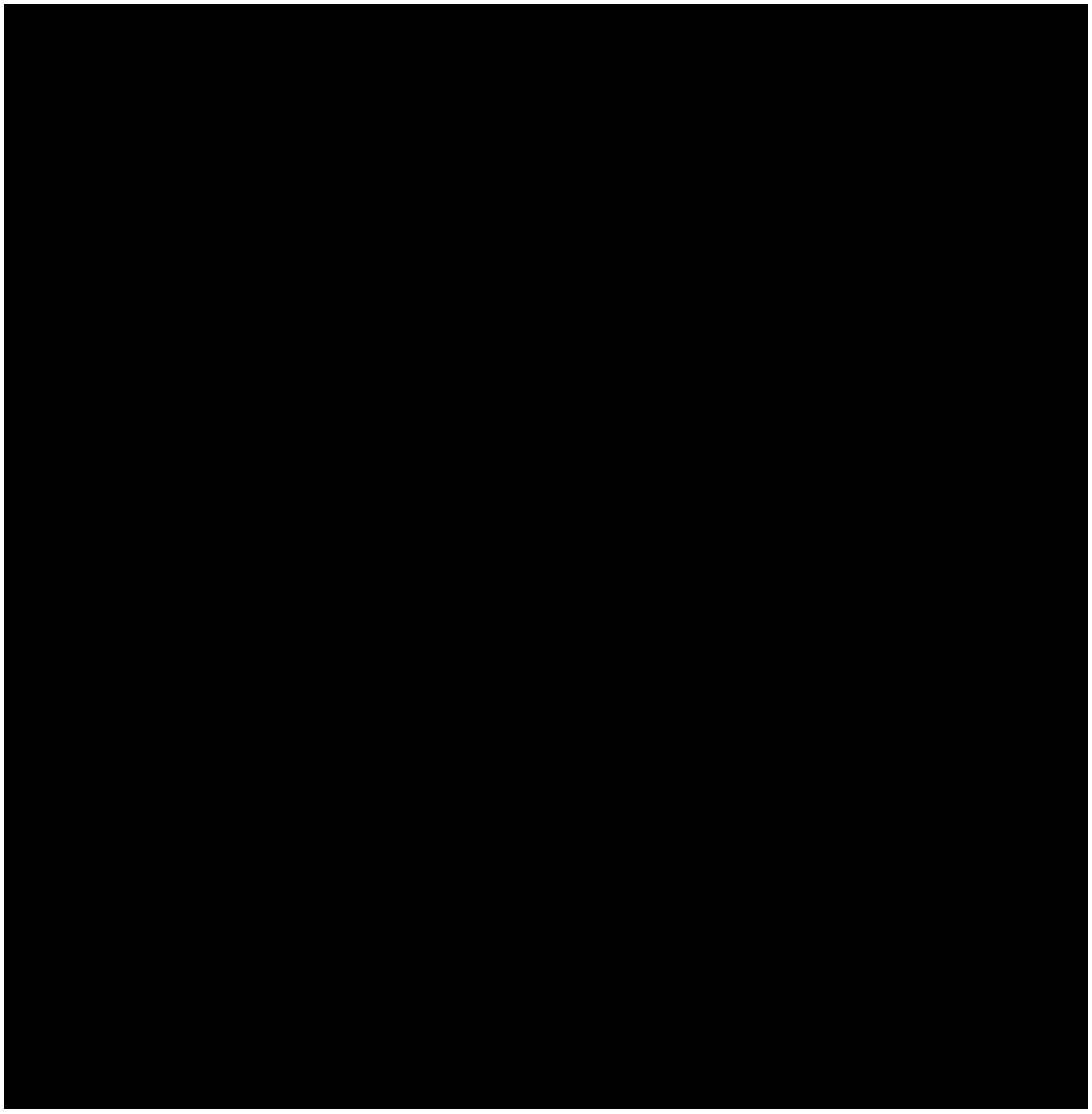

Figure 1-19. A schematic structure of the H Channel in the fully reduced and fully oxidised bovine CcO. Viewed from the left of the structure, facing the haem a plane (black rectangle).
Figure shows the conformational change of D51, the peptide bond between Y440-S441, R38, hydroxyfarnesylethyl group, and shows the water channels (grey rectangles) and water cavities (grey ovals). Fixed water molecules are shown as black circles. Figure is taken from Figure 2 in ref [87].

The hydrogen bond network of the H channel makes connections with porphyrin ring substituents of haem *a*. One of these is between the formyl and an arginine (R38) that leads to the proton-transferring peptide bond of the H channel (Figure 1-19). It is proposed that redox changes in haem *a* provide the driving force for proton pumping through the H channel. This is because, when haem *a* is oxidised, the net positive charge generated drives the proton towards the peptide bond through repulsion, to re-protonate D51. When haem *a* is reduced, the R38 affinity for a proton is restored and extracts protons from the water molecules from the water channel leading towards the matrix end (Figure 1-19) [87].

The hydroxyfarnesylethyl group of haem *a* and helix X of subunit I, protrude into the same water channel of the H channel, and also undergo redox-linked conformational changes (Figure 1-19). Furthermore, the X-ray structure of fully reduced bovine C*c*O ligated to CO, has been solved and should structurally resemble the oxygen bound form of the enzyme [40]. Comparison of reduced and CO-bound reduced structures, show that a region of helix X undergoes the same conformational change as when the enzyme becomes fully oxidised, whilst the conformation of D51 and hydroxyfarnesylethyl groups remain unchanged. This suggests that the helix X conformation is controlled by the redox and ligation state of haem a_3, whilst the D51 and hydroxyfarnesylethyl groups, are controlled by redox changes of haem *a* [40]. The nature of the helix X change is such that the channel becomes 'closed' to the matrix side when the enzyme is ligated or oxidised, which prevents proton back leak.

Based on these redox-linked structural changes, a mechanism has been put forward. When the enzyme is reduced the pathway becomes open to allow the uptake of all four protons into the cavity. Once oxygen binds to the BNC, the channel closes to prevent back leak of the four protons. They are then translocated via R38 to the area surrounding the gating Y440-S441 peptide bond. Possible candidate groups that could accommodate protons are proposed to be serines, arginines, propionates of haem *a* and water molecules. As each electron is transferred from haem *a* to the BNC, a proton is translocated across the Y440-S441 peptide bond to D51, and eventually into the IMS [40,87].

1.15 Controversial points on the H pathway

This model of proton translocation is based primarily on the observed conformational changes of D51, and the H channel. However, this residue is not conserved across all homologues of C*c*O. Bacterial C*c*Os also lack a continuous hydrophilic H channel across the entire subunit, and H channel mutants of C*c*O from *P. denitrificans* [100] or *Rba. sphaeroides* [101], had no effect on the proton translocation activity. The homology model of mitochondrial yeast C*c*O does indeed contain a continuous hydrophilic H channel structure. However, it also lacks an aspartic acid (D51-bovine) at the end of its H channel [41]. Thus it has been suggested that the H channel may only operate in mammalian C*c*Os [87] but at the same time, it is argued that the absence of D51 isn't enough to rule out the function of the H channel as a proton pathway, since other hydrophilic residues in this region may be used [87]. The yeast mitochondrial C*c*O has other polar residues at the H channel exit that may take on this role.

The H channel proposal does not provide a consideration of the electrostatic costs of binding of four protons, nor a clear mechanism of how each of the four protons after entering the hydrogen bond network, are supplied to the peptide bond to be released into the IMS, via D51. More importantly, it does not provide a rationale of how the transiently charged species at the BNC, would be stabilised, if the translocated protons are spatially separated from the oxygen reduction site.

A very recent alternative proposal is that the H channel does not function as a proton pathway, but instead acts as a dielectric channel in all C*c*Os in the same way as the K channel [78,86]. In such a function, the hydrophilic groups reorganise during electron transfer into/out of haem *a*, directing their dipoles to increase the dielectric strength around haem *a,* which would aid rapid electron transfer from Cu_A to the BNC.

1.16 Infrared spectroscopy on functional carboxyl groups

FTIR spectroscopy can allow vibrational structural changes of proteins to be studied. It is particularly useful for large membrane protein complexes, and can be used to complement X-ray and electron microscopy data that provide 3D structural information. IR spectroscopy has been used extensively to probe ligand- [102-105], and redox- [106-109] induced structural changes in C*c*O and related oxidases. ATR-FTIR spectroscopy method allows the sample placed on an ATR prism surface to be accessible from above for manipulation [110]. In this way it has opened up the types of reactions/conditions that can be induced by pH, temperature, perfusion-induced reactions [111], dialysis [112], or electrochemistry [113]. Transmission IR spectroscopy, in which a sample is sandwiched between two optically transparent windows, has been particularly useful in monitoring photolysis induced reactions such as CO photolysis from the FR state of C*c*O [90,103,104]. In all cases, the reaction induced IR changes are always small relative to the large overall background absorbance of the protein and water. For this reason spectra are averaged from repeated cycling between two defined states, and are recorded as difference spectra showing only the reaction induced changes [114]. In this way subtle vibrational changes in individual amino acids and cofactors can be detected. Results Chapter 3 of this thesis has focused on separating those structural changes and linking them with specific metal centre redox transitions. Such IR changes can arise from protonation, conformation or hydrogen bonding environment changes. FTIR studies of bovine C*c*O have revealed redox-induced IR changes of two protonated carboxyl groups at 1749 cm^{-1} and 1737 cm^{-1} [104,115]. The photolysis induced CO binding and unbinding to FR bovine C*c*O

showed a shift in only the first band [90,104]. Similar studies with C*c*O from *P. denitrificans* [116,117], exhibited only one redox-sensitive IR band, equivalent to the first band (1749 cm^{-1}) of bovine C*c*O, and no strong CO-ligation sensitive carboxyl change [105]. The 1749 cm^{-1} band has been assigned to extinction coefficient changes of the conserved functional glutamic acid (E242) [104,115]. This assignment is based on mutagenesis studies of the same residue and H/D exchange experiments in bacterial C*c*Os [88,103,106]. The second band that is only present in bovine C*c*O at 1737 cm^{-1}, has been tentatively assigned to de/protonation changes of D51 [90,104]. However, the actual number of components contributing in the 1760-1710 cm^{-1} protonated carboxyl region of the bovine redox IR spectrum, and their linkage to specific redox centres are not well understood therefore the Results Chapter 4 explores these issues.

1.17 Yeast CcO as a model system

In collaboration with yeast geneticist Brigitte Meunier, we are now able to purify and analyse various yeast WT and mutant forms of C*c*O, with a 6-his tag on the C terminus of a nuclear-encoded supernumerary subunit [41,118]. Yeast is a model system that allows mutations to be introduced into the nuclear and mitochondrially-encoded subunits, that does not depend on a hybrid expression system [39]. Yeast C*c*O is homologous to mammalian bovine C*c*O (see below), and therefore has provided a model system to study the structure and function of a mitochondrial form of C*c*O.

Mutations in the vicinity of the D channel were found to greatly affect the respiratory growth of yeast cells on glycerol medium, highlighting the essential role of the D channel for enzyme activity. Furthermore, a mutant with four mutations along the H channel has been expressed where polar residues have been replaced with non-polar residues (Q411L/Q413L/S458A/S455A). Growth of this mutant on a glycerol medium, was shown to be significantly impaired compared to the WT C*c*O [118]. Result Chapter 6 has therefore focused on the measurement of the proton/electron stoichiometry of this mutant in reconstituted phospholipid vesicles, to determine whether the H channel provides the pathway for translocated protons in the mitochondrial yeast C*c*O, or alternatively may be a dielectric channel [78]. The crystal structure of yeast C*c*O has not yet been solved although a structure based on homology modelling has been produced [41]. Crystallisation trials are underway to refine this model and, eventually, to solve structures in the oxidised or reduced states that will reveal redox linked conformational changes of yeast C*c*O. Such information will allow identification of functionally significant residues in yeast C*c*O and compliment IR data. Recently, redox-induced IR difference spectra of WT yeast C*c*O, have revealed only one IR sensitive

band in the protonated carboxyl region, equivalent to 1749 cm^{-1}. Based on site-directed mutagenesis, this component has been tentatively assigned to E243 (E242-bovine) (personal communication, Amandine Maréchal). The second 1737 cm^{-1} component in bovine C*c*O is absent from yeast C*c*O as is the D51 residue (replaced by S52) which is consistent with the assignment of this band to D51 in bovine C*c*O.

1.18 Supernumerary subunits

The additional supernumerary subunits are unique to eukaryotic C*c*Os and are encoded by the nuclear genome. They have evolved following the endosymbiotic event between a pre-eukaryote (host) and an α-proteobacterium (mitochondrion) [119,120]. They are not directly involved in the reaction mechanism, and their individual functions are still unclear. 8 supernumerary subunits of yeast C*c*O are homologous to 8 of the 10 supernumerary subunits of bovine C*c*O. Their sequence identities are given in Table 1-1 [26,41,121].

Table 1-1. Amino acid sequence identity between yeast CcO subunits and bovine CcO subunits.
The amino acid length of each subunit is shown in brackets. The subunits that have isoforms are highlighted. Although Cox9 has been compared with VIc, VIIb and VIII subunits it is homologous with VIc. Table and values are adapted from [41].

	Saccharomyces cerevisiae CcO subunits (amino acid length)	*Bovine CcO subunits (a.a. length)*	*Amino acid sequence identity % (vs shortest sequence)*
Mitochondrially encoded	Cox1 (534)	I (514)	59 % (303/514)
	Cox2 (236)	II (227)	43 % (98/227)
	Cox3 (269)	III (261)	47 % (122/261)
Nuclear-encoded supernumerary subunits	Cox4 (130)	Vb (98)	35 % (34/98)
	Cox5A (133)	**IV isoform-1**	20 % (26/133)
		IV isoform-2	20 % (26/133)
	Cox5B (134)	**IV isoform-1**	16 % (22/134)
		IV isoform-2	20 % (27/134)
	Cox6 (108)	Va (109)	37 % (40/108)
	Cox7 (59)	**VIIa isoform-1**	22 % (13/59)
		VIIa isoform-2	25 % (15/59)
	Cox8 (47)	VIIc (47)	38 % (18/47)
	Cox9 (55)	VIc (73) VIIb (56)	18 % (10/55) 16 % (9/55)
		VIII isoform-1 **VIII isoform-2**	9 % (4/44) 11 % (5/46)
	Cox12 (82)	**VIb isoform-1**	43 % (35/82)
		VIb isoform-2	39 % (32/82)
	Cox13 (120)	**VIa isoform-1**	33 % (28/85)
		VIa isoform-2	35 % (30/85)

Supernumerary subunits are thought to be involved in the assembly, dimerization or stability of C*c*O, while others are thought to allosterically regulate enzyme activity, for example via ligand-binding [122,123] or phosphorylation sites [124]. Approximately half of the supernumerary subunits of bovine (mammalian) C*c*O have tissue-specific or development related isoforms. In this way the presence of supernumerary subunits provides a means to regulate C*c*O, in different cell types, and in response to changing energy demands [27,125]. The supernumerary subunits may also be involved in the formation of supercomplexes/respirasomes. The *in vivo* arrangement of the individual respiratory chain complexes have been proposed to exist as one entity (solid state model) [126], or as a fluid state model in which the complexes are freely diffusing in the membrane [127]. However, blue-native PAGE gels of digitonin solubilised mitochondria [128] and co-immunoprecipitation [129] experiments revealed high molecular weight bands of respiratory chain complexes (I, II and IV) of defined stoichiometries [130]. In favour of the solid state model, a model was described that involved direct channelling of cyt *c* [130] rather than random collision between complexes. In bovine mitochondria two types of supercomplex with different stoichiometries were isolated ($I_1III_2IV_2$ and

$I_1III_2IV_4$) [130]. In yeast mitochondria that lacks complex I, two distinct supercomplexes were isolated, III_2IV_1 and $IV_1III_2IV_1$. Cardiolipin has also been shown to enhance the stability of these associations [131]. The interactions are thought to have a role in stabilisation of the individual complexes and/or facilitate electron transfer from bc_1 to C*c*O via cyt *c* as it would have a shorter distance to migrate (40 Å [132]) [133]. Cryo electron microscopy structures have also been solved of the supercomplexes isolated from bovine [134] and yeast [135].

1.18.1 Bovine supernumerary subunit IV and yeast subunit 5

Subunit IV of bovine C*c*O is the largest supernumerary subunit (~17 kDa). The structure is superimposed on the homologous subunit 5 of yeast C*c*O shown in Figure 1-20. The hydrophilic C terminal domain projects into the IMS close to the cyt *c* binding site on subunit II, and a hydrophilic N terminal domain projects into the matrix [34]. The single membrane spanning α-helix is closely associated with core subunit I.

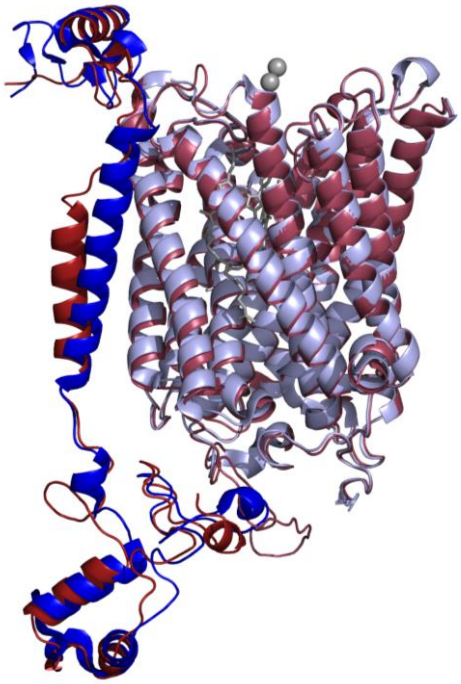

Figure 1-20. Subunit 5 of yeast CcO (red) is in the same structural location as subunit IV (blue) of bovine CcO.
Although the yeast 5A isoform [41] is overlaid with the bovine IV-2 isoform (PDB:1V54), the pairing of specific isoforms (5A with IV-1/IV-2 and 5B with IV-2/IV-1) is not possible based on their modest ~20 % sequence identities [26,41].

Subunit IV of bovine C*c*O has gained interest since it is thought to be a key regulatory subunit that binds ATP (allosteric inhibitor) or ADP (allosteric activator) [122,123], and is part of a negative feedback loop mechanism of respiratory control

[136-138]. Moreover, subunit IV has phosphorylation sites and S58 phosphorylation (only conserved in mammalian C*c*Os), is reported to modulate the respiratory activity by controlling ATP allosteric inhibition [139]. Subunit IV-2 expression is limited to lung, neurons and fetal muscle whilst IV-1 expression occurs across all tissue types [140,141]. Moreover, IV-2 expression is induced by hypoxic conditions under the control of RBPJ, CXXC5 and CHCHD2 transcription factors [142], or by toxins [143].

Yeast C*c*O is a useful model system to study this subunit, since its subunit 5 is homologous to mammalian subunit IV [26], and is the only yeast C*c*O supernumerary subunit to have isoforms (5A and 5B) [144,145]. These are encoded by single copy genes; *COX5A* on chromosome 14 and *COX5B* on chromosome 9. They share 67 % nucleotide (66 % amino acid) identity and are thought to have arisen from gene duplication followed by sequence divergence [145]. One or other polypeptide is essential for C*c*O assembly. As with the mammalian subunit IV isoforms, the expression pattern of subunits 5A and 5B is controlled by oxygen (and haem) concentration [146,147]. *COX5A* is expressed above 1 µM O_2 and *COX5B* under low (<1 µM O_2) oxygen concentrations [148]. The O_2 regulatory pathway of subunit 5 isoform expression is summarised in Figure 1-21. O_2 stimulates haem synthesis that then binds to and activates the transcription inducer Hap2/3/4/5 complex of *COX5A;* haem also activates Hap1 that induces the expression of *ROX1*, a repressor of *COX5B* expression. Under low oxygen levels, haem levels fall and Hap1 and Hap2/3/4/5 are no longer activated. This prevents *COX5A* transcription and loss of *ROX1* transcription allows derepression of a set of hypoxic genes including *COX5B* [149,150].

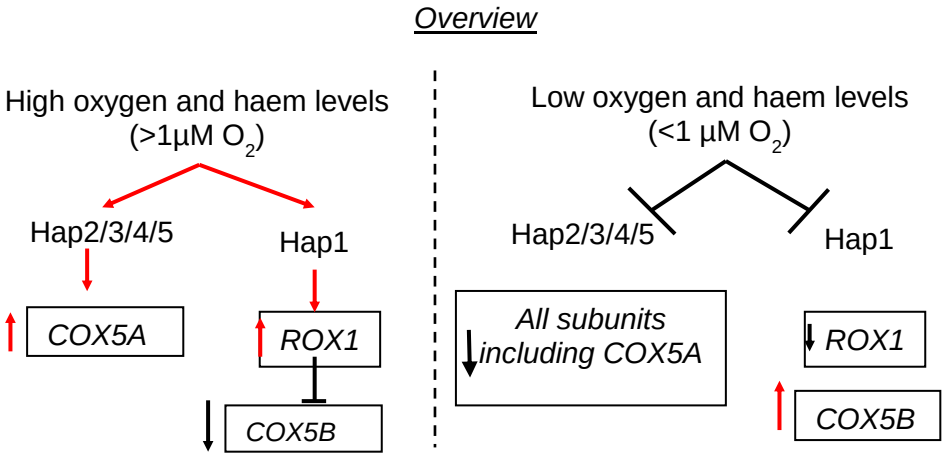

Figure 1-21. The oxygen sensing and regulatory pathway of subunit 5A and 5B of yeast CcO.
COX5A is expressed at high oxygen concentrations (>1 µM) and COX5B is expressed under low oxygen concentrations <1 µM.

To enable *COX5B* to be expressed and subunit 5B to be assembled into C*c*O, under normal growth conditions, the *ROX1* gene was mutated in a *ΔCOX5A*-deleted strain [147]. However, the C*c*O level was lowered by a factor of 2-3 compared to the control *COX5A*-expressing strain. Intriguingly, it was observed that the 5B isozyme had a turnover number that was 2-3 times faster than that of the 5A isozyme [28,151]. Thus subunit 5 isoforms were proposed to have an activity regulating role by allosterically altering the protein environment around haems *a* and a_3 [28]. This effect on core catalytic activity has been explored further in Results Chapter 7.

1.19 Aims

The aims of each of the five results chapters are listed here and are described in detail within each results chapter.

Results Chapter 3.

To associate redox-induced IR changes in the 1700-1000 cm^{-1} IR range in bovine CcO with specific metal centre transitions by exploiting the mixed valence (MV) states of C*c*O ligated with either cyanide (CN) or carbon monoxide (CO) [159,160][161].

Results Chapter 4.

To associate the redox-induced IR changes of functionally significant protonated carboxyl groups in the 1800-1700 cm^{-1} IR range in bovine C*c*O with specific redox groups by exploiting the MV states of C*c*O ligated with CN or CO.

Results Chapter 5.

To electrochemically induce a phenoxyl radical on Tyr-His model compounds designed to resemble the conserved feature in C*c*O and combine the optimal electrochemical conditions with ATR-FTIR spectroscopy to record reduced *minus* oxidised (radical) IR difference spectra. These spectra were used together with published spectra to tentatively assign tyrosine radical and Tyr-His associated IR bands in the P_M (oxyferryl associated radical) *minus* oxidised IR difference spectrum of bovine C*c*O.

Results Chapter 6.

To develop a protocol to reconstitute yeast WT C*c*O into liposomes using bovine C*c*O as a control. This would allow the proton translocation activity of yeast WT CcO to be quantitatively assayed. To then compare the proton/electron stoichiometry to that of the extreme 4H mutant (Q411L/Q413L/S458A/S455A). This would provide a means to assess the possible role of the H channel as a route for translocated protons in yeast mitochondrial C*c*O.

Results Chapter 7.

To investigate the origin of the increased core catalytic activity of 5B isozyme compared to 5A isozyme [147]. In order to do so, mutant strains were constructed by Brigitte Meunier following a BBSRC funded 3 week visit to her laboratory. The mutant strains expressed wholly subunit 5B, by replacing the *COX5A* open reading frame with *COX5B*, so that it was under the control of the *COX5A* promoter. This gene replacement was achieved at the *COX5A* nuclear locus or on a centromeric plasmid (1 copy per cell). Such mutants expressed the 5B isozyme to wild type (5A isozyme) levels under aerobic growth conditions, and without the complication of secondary effects caused by mutation of *ROX1*-encoded transcription factor. This allowed comparison of the catalytic properties of the 5A and 5B isozymes that have been expressed under identical conditions.

2 Materials and methods

2.1 Sources of (bio) chemicals

White spot nitrogen gas (99.998 %) was from BOC Ltd. Carbon monoxide gas (99 %) and ^{18}oxygen-isotope gas (98 %) were from CK Gas products Ltd. Lecithin (α-phosphotidylcholine) type IV-S from soy bean and cardiolipin from bovine heart (98 % purity) were purchased from Sigma-Aldrich. Potassium cholate was prepared by titration of cholic acid (98 % purity) with potassium hydroxide to pH 7.4. N-dodecyl-β-d-maltoside (DDM) (>99.5 %) was purchased from Melford Laboratories Ltd, UK. 0.05 µm alumina paste (Buehler), 0.3 µm alumina powder (MetPrep). Yeast iso-1 cyt *c* and iso-2 cyt *c* were a kind gift from B. Guiard (CGM, CNRS, Gif-sur-Yvette, France). The plasmid pRS415-COX5A containing *COX5A* gene was a kind gift from D. Winge (University of Utah, USA). Tyrosine model compounds, 2,6-di-*tert*-butylmethoxyphenol (TMP) and 2,4,6-tri-*tert*-butylphenol (TBP) were purchased from Sigma-Aldrich. The cross-linked Tyr-His model compounds were chemically-synthesised by Rachel Lanigan (PhD student) and Dr Tom Sheppard, Chemistry, UCL. Unless stated otherwise, all other chemicals were purchased from Sigma-Aldrich.

2.2 Yeast mutant generation

All yeast strains (Table 1) were constructed by Brigitte Meunier from a modified *Saccharomyces cerevisiae* strain W303-1B (Alpha *ade2 HIS3 leu2 trp1 ura3*) that expressed wild type C*c*O (WTCOX5A) with a 6 his tag sequence attached to Cox13 (supernumerary subunit) [118]. Mutations in the mitochondrially-encoded subunit I were introduced on a plasmid vector (pYGT21) encoding subunit I using a quickchange site-directed mutagenesis kit (Stratagene) [152]. Mitochondrial transformation of yeast cells was achieved using biolistic transformation. This approach consists of coating plasmids onto micron-sized particles (tungsten). These particles are placed on a macrocarrier platform which is placed into the biolistic device (biolistic PDS-1000-He particle delivery system (Bio-Rad)). The platform is placed under a tube containing high pressure helium. The particles are ejected at high speeds onto an agar plate with recipient yeast cells [153].

2.3 Construction of 5A or 5B isozymes of yeast CcO

Table 2-1 summarises the strains that were constructed and their genotype.

Table 2-1. Saccharomyces cerevisiae strains constructed and analysed.
All strains were constructed by Brigitte Meunier. Table is adapted from Dodia, R. et al submitted.

Genotype	Description	Strain
COX5A	Expression of *COX5A* under normal aerobic growth conditions.	WTCOX5A
cox5a::URA3	Deletion of *COX5A*	ΔCOX5A
cox5a::URA3, pCOX5A	*COX5A* cloned on a centromeric plasmid under the control of its own promoter. Deletion of genomic *COX5A*.	ΔCOX5ApCOX5A
cox5a::COX5B	Replacement of *COX5A* by *COX5B* downstream of the *COX5A* promoter on the nuclear genome. Expression of *COX5B* under normal aerobic growth conditions.	COX5B
cox5a::URA3, pcox5a::COX5B	*COX5B* cloned downstream of *COX5A* promoter on a centromeric plasmid. Deletion of genomic *COX5A*.	pCOX5B
rox1::kanMX4, cox5a::URA3	Up-regulation of *COX5B* through deletion of its transcription repressor *ROX1* in *COX5A*-deleted background.	ΔROX1ΔCOX5A
rox1::kanMX4, cox5a::URA3, pCOX5A	*COX5A* with its own promoter on a centromeric plasmid. Deletion of *ROX1*, the transcription repressor of *COX5B*.	ΔROX1ΔCOX5A pCOX5A
rox1::kanMX4, cox5a::URA3, pcox5a::COX5B	*COX5B* cloned downstream of the *COX5A* promoter on a centromeric plasmid. Deletion of *ROX1*, the transcription repressor of *COX5B*, in *COX5A*-deleted background.	ΔROX1ΔCOX5A pCOX5B

The WTCOX5A strain carries functional copies of both *COX5A* and *COX5B.* However, under aerobic growth conditions only subunit 5A is assembled into C*c*O. The *COX5B* gene at its genomic locus was not deleted in these mutants since its expression relies on hypoxic conditions, and hence is not expressed under aerobic growth conditions [146,147]. The COX5B strain expressed *COX5B* downstream of the *COX5A* promoter on the nuclear genome. The strain was constructed from a *COX5a::URA3* strain, where the open reading frame (ORF) of *COX5A* was replaced with *URA3. COX5B* replaced the *URA3* ORF by homologous recombination, using a linear PCR construct that had complementary *COX5A* 5' and 3' flanking sequences and the *COX5B* ORF (Figure 2-1). The linear PCR construct was produced using primers that had *COX5A* 5' or 3' flanking sequences and *COX5B* 5' or 3' ORF sequence. They were used to amplify the *COX5B* locus from yeast DNA.

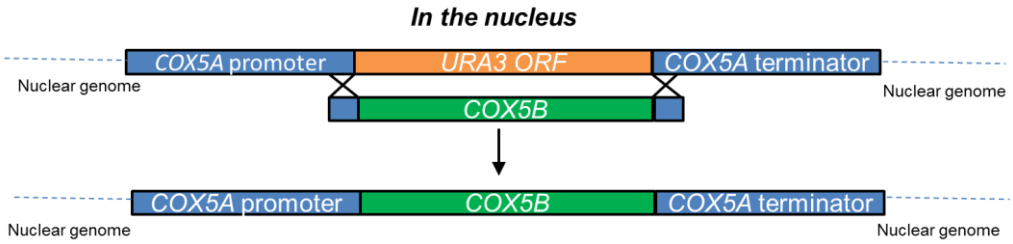

Figure 2-1. Homologous recombination of a linear construct with COX5A flanking sequences and COX5B ORF with the nuclear COX5A locus.

ΔCOX5ApCOX5B strain contained a centromeric plasmid pRS406 that expressed *COX5B* downstream of the *COX5A* promoter. A centromeric plasmid contains a centromere so that its replication pattern is the same as the yeast chromosomes and results in one copy per cell, and it prevents the spontaneous loss of the plasmid from the cell. This strain was constructed by co-transformation of *COX5a::URA3* with both the linear PCR construct, and pRS406 that was carrying a disrupted/non-functional *cox5a* gene, inserted between *BamHI* and *XhoI* restriction sites. This resulted in homologous recombination between the 5' and 3' *COX5A* flanking sequences between the linear PCR construct and the plasmid. Successful transformants were able to grow on respiratory plates that were uracil deficient (*COX5a::URA3*), and that were leucine deficient which selected for pRS406 carrying the LEU gene. ΔROX1ΔCOX5A allowed *COX5B* expression from its nuclear locus since its transcription repressor *rox1* had been deleted. ΔROX1ΔCOX5ApCOX5A expressed *COX5A* on pRS406 and contained a *Δrox1* deletion. ΔROX1ΔCOX5ApCOX5B expressed *COX5B* downstream of the *COX5A* promoter on pRS406 and contained a *Δrox1* deletion. The last two strains, ΔROX1ΔCOX5ApCOX5A and ΔROX1ΔCOX5ApCOX5B, were derived from ΔROX1ΔCOX5A by transformation with pRS406 carrying a functional gene for *COX5A* or *COX5B*-with flanking *COX5A* sequences. The PCR products and gene replacements were confirmed by DNA sequencing (Strategene, Germany).

2.4 Yeast cell growth and mitochondrial preparation

Yeast cell growth and mitochondrial preparation was carried out using the method of Meunier, *et al.* [118]. A yeast colony was inoculated into 7 mL of autoclaved YPGal media (1 % yeast extract, 2 % peptone, 2 % galactose), and incubated with shaking (150 rpm) at 28 ^{o}C. After 24 h, 0.5 mL of culture was diluted into 50 mL of YPGal and incubated overnight at 28 ^{o}C. For large scale purification, 5 mL of culture was diluted into 10 x 500 mL of YPGal and, for small scale mitos (mitochondrial membrane fragments) preparations, into 2/3 x 500 mL of YPGal with shaking at 200 rpm. Cells

were harvested when they reached late log phase. This was determined by comparison of the optical density with a pre-recorded growth curve (logOD versus time). Typically this was when logOD = 0.9-1 with an incubation time of 14-16 h. The cells were pelleted by centrifugation at 6,500 x *g* for 5 min at 4 °C and washed twice in 50 mM KPi pH 7.0 by centrifugation and resuspension. A typical yield was 10-16 g of wet weight cells per litre of culture.

Mitos were prepared by mechanical lysis of cells at 4 ^{o}C using a bead-beater (BioSpec Products, Inc., Bartlesville, OK, USA). For a large scale preparation, a 400 mL capacity bead beater was used; 200 mL of 425-600 µm diameter glass beads and 200 mL (final volume) of 650 mM (D)-mannitol, 50 mM KH_2PO_4/K_2HPO_4 (KPi) and 5 mM ethylenediaminetetracetic acid (EDTA(K^+)) at pH 7.4 containing 80 g wet weight cells. For small scale preparations, an 80 mL capacity bead beater was used; 40 mL of glass beads and 40 mL of the same buffer containing 10-11 g of wet weight cells. Cell disruption was assessed by comparing lysed cells with intact cells under a microscope. Typically 90-95 % cell lysis was achieved in a total of 9-12 mins of bead-beating. The cell debris was separated by centrifugation at 5,600 x *g* (SLA-1500 rotor) for 20 min at 4 °C. The supernatant containing mitos was ultracentrifuged at 120,000 x *g* (T647.5 rotor) for 1 h at 4 °C. The pellet of mitos was washed twice by resuspension and homogenisation (hand held homogeniser) in 50 mM KPi, 100 mM KCl, 5 mM EDTA(K^+) pH 7.4, until the A_{260} (DNA) of supernatant reach <1. The final pellet of mitos was resuspended in a minimal volume (~50 mL, large scale and ~10 mL, small scale preparation) of the same buffer and stored at -80 ^{o}C.

2.5 Determination of protein content in yeast mitos

The mitos protein content was determined so that the amount of detergent to solubilise mitos could be calculated. The protein content was determined by measurement of an ATR-IR absorbance spectrum of 10 µL of non-diluted and 2 fold diluted mitos, in deionised water (MilliQ water at 18 Ω, dH_2O). The size of the protein amide II band ΔA_{II} at 1545-1481 cm^{-1} was compared to a calibration curve of ΔA_{II} of bovine serum albumin (BSA). In order to assess the reliability of using IR spectroscopy to determine protein content in mitos, it was also averaged with the estimates from the conventional Bradford protein assay. The concentrated Bradford reagent was prepared by dissolving 100 mg coomassie brilliant blue G-250 (Bio-Rad) in a mixture of 50 mL ethanol and 100 mL phosphoric acid. This concentrated mixture was diluted in dH_2O to 1 litre, and filtered through Whatman #1 paper giving a brownish colour of the Bradford reagent. 10 µL of non-diluted mitos or 2 fold diluted mitos in 5 mL of Bradford reagent was incubated at room temperature with mixing for ~1 h, before the A_{595} was

measured. The reading was compared to a BSA calibration curve. The protein content estimates were within the same range using each method and are shown in Figure 2-2.

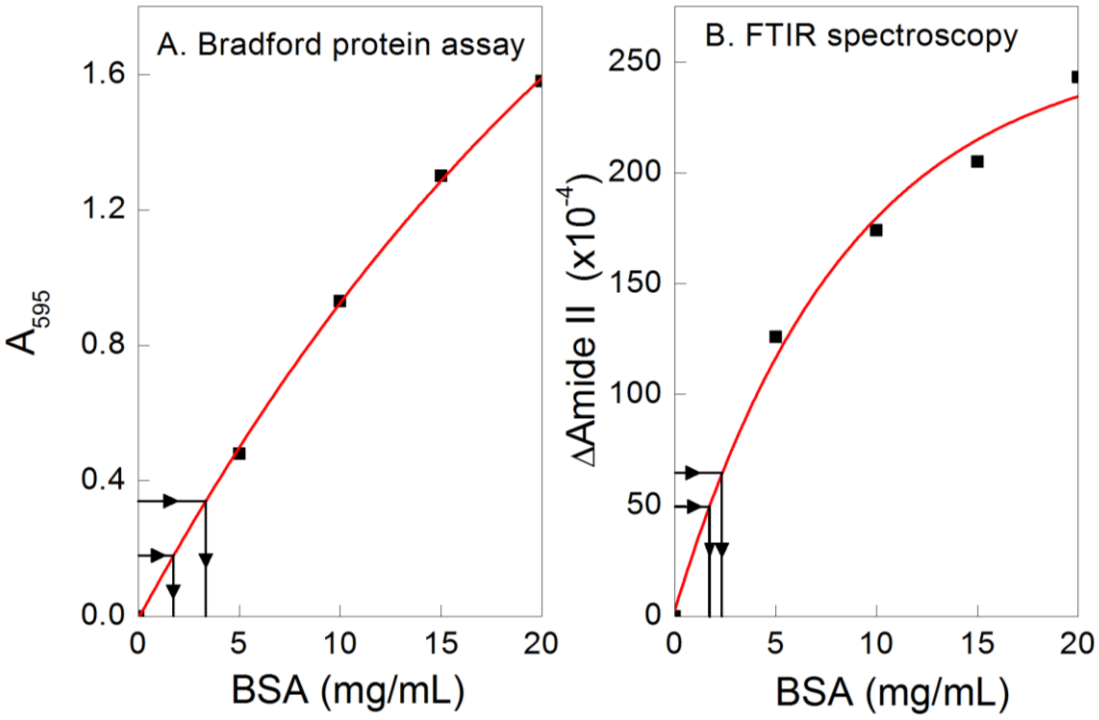

Figure 2-2. BSA calibration curves.
0 – 20 mg/mL BSA samples were prepared in dH_2O for IR measurements and in 50 mM KPi pH 8.5 for the Bradford protein assay. Arrows indicate the level of protein content of typical mitochondrial preparations.

2.6 Purification of yeast CcO

Purification was carried out using the method of Meunier, *et al.* [118]. Based on the determined protein content, the mitos were diluted to give 1.8 mg protein/mL in 2 % (w/v) n-dodecyl-β-D-maltoside (DDM) 50 mM KPi pH 8.0. To ensure complete solubilisation, mitos were stirred at 4 ^{o}C for 1 h. The insoluble debris was removed by ultracentrifugation at 120,000 x *g* at 4 °C for 35 min. 5 mM imidazole was added to the detergent-solubilised supernatant. From this stage the purification method of C*c*O was optimised and three methods are described here. C*c*O prepared from each method was tested for membrane reconstitution.

2.6.1 Purification method 1

Purification was carried out under gravity at room temperature. A 40 x 2 cm column containing 40 mL of nickel-iminodiacetic acid resin (His-bind® resin, Novagen) was equilibrated with 3 column volumes of 50 mM KPi, 0.009 % (w/v) DDM, 5mM imidazole pH 8.0 before the supernatant was loaded manually at 6.7 mL/min. Once loaded, the resin was washed until the eluate A_{280} was <1, typically 5 column volumes of 50 mM

KPi, 0.009 % DDM, 5 mM imidazole, 150 mM KCl pH 8.0. It was then washed with 50 mM KPi, 0.009 % DDM, 10 mM imidazole pH 8.0 until the A_{280}<0.08, typically 3-4 column volumes. C*c*O was eluted with 100 mM imidazole in the same buffer. Dithionite reduced *minus* 'as prepared' (oxidised) visible absorption difference spectra were recorded of eluted fractions in 50 mM KPi, 0.009 % (w/v) DDM pH 8.0. C*c*O content was quantitated based on the intensity of $\Delta A_{605-621}$ using an extinction coefficient (ε) of 26 $mM^{-1}.cm^{-1}$ [154]. The fractions containing the highest C*c*O:bc_1 ratios were pooled together.

The pooled fractions were loaded onto a 40 x 2 cm column containing 40 mL of (diethylaminoethanol) DEAE Sepharose CL-6B (Sigma-Aldrich) equilibrated with 20 column volumes of 50 mM KPi, 0.015 % (w/v) DDM at pH 8.0. The column was washed with 2 column volumes of 50 mM KPi, 0.01 % (w/v) DDM, 50 mM NaCl at pH 8.0. C*c*O was eluted by increasing the salt concentration to 250 mM. C*c*O concentration in eluted fractions was estimated. Purest fractions based on the absence of bc_1 and a '554' species were pooled together. The 554 species is partly cyt c_1 of the bc_1 complex, however, the size of this band in the visible spectra did not change proportionally with the cyt *b* band of bc_1 complex, and so, it may consist of another component or a dissociated bc_1 complex. These were concentrated at 4 ^{o}C using a pressure cell with a 100 kDa cut-off membrane (YM100, Millipore) to a final C*c*O concentration of ~20 µM. Overall from 80 g of wet weight cells, ~120 nmoles of C*c*O was present in the mitos preparation. After column chromatography and concentrating, the final yield of C*c*O was ~31 nmoles i.e. a ~26 % yield. The A_{280}:A_{422} ratio was ~4.

2.6.2 Purification method 2

For the second method the final buffer used to wash the mitos contained 0.1 mM phenylmethylsulfonyl fluoride (PMSF), a serine protease inhibitor. The solubilisation buffer was changed to 2 % (w/v) DDM, 50 mM 4-(2-hydroxyethyl)-1-piperazineethanesulfonic acid (HEPES), 0.1 mM PMSF, 150 mM NaCl at pH 8.0. A typical redox visible difference spectrum of solubilised mitos is shown in Figure 2-3.

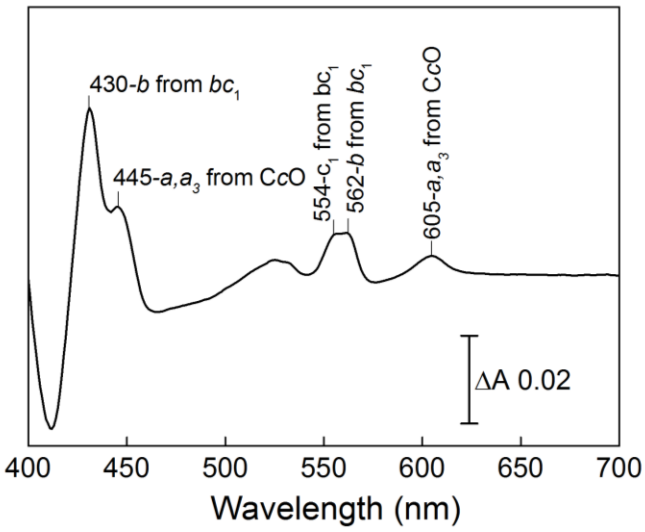

Figure 2-3. A typical reduced minus oxidised visible difference spectrum (400-700 nm) of DDM solubilised mitos.
A baseline was recorded and then a small amount of solid sodium dithionite was added. After reduction was complete a reduced minus oxidised difference spectrum was recorded. Spectrum is of a 2 fold diluted sample in 2 % (w/v) DDM, 0.1 mM PMSF, 50 mM HEPES, 150 mM NaCl at pH 8.0. Visible bands of bc_1 and CcO are indicated.

C*c*O was purified by FPLC at 4 ^{o}C using an Äkta system. A series of 4 x 5 mL pre-packed HisTrap^{TM} HP columns (GE Healthcare) containing Ni-nitrilotriacetic acid (NTA) resin were connected together. They were equilibrated with 4 (80 mL) column volumes of 50 mM HEPES, 0.05 % (w/v) DDM, 10 mM imidazole, 500 mM NaCl pH 8.0 at 5 mL/min. 10 mM imidazole and 350 mM NaCl were added to the solubilised mitos and then they were loaded onto the column. The column was washed with 5 column volumes of the same equilibration buffer until A_{280} <1. C*c*O was then eluted using a gradient with the same buffer containing 200 mM imidazole, in a total volume of 50 mL. Eluted fractions in the central portion of the elution profile were pooled together (Figure 2-4) and concentrated using a centrifugal concentrator (Vivaspin100 kDa cut-off, Fisher Scientific) in a swinging bucket rotor at 4,000 x *g* for 10-15 mins at 4 ^{o}C, to a final concentration of ~20 µM. The redox spectrum showed the presence of primarily yeast C*c*O (Figure 2-5).

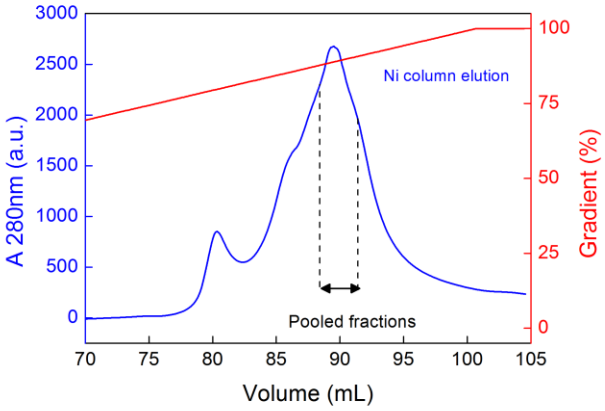

Figure 2-4. A typical elution profile from the Ni affinity column chromatography.
Elution profile is shown in blue and the imidazole concentration gradient from 10 mM (0 %) to 200 mM (100 %) in 50 mL total volume is shown in red.

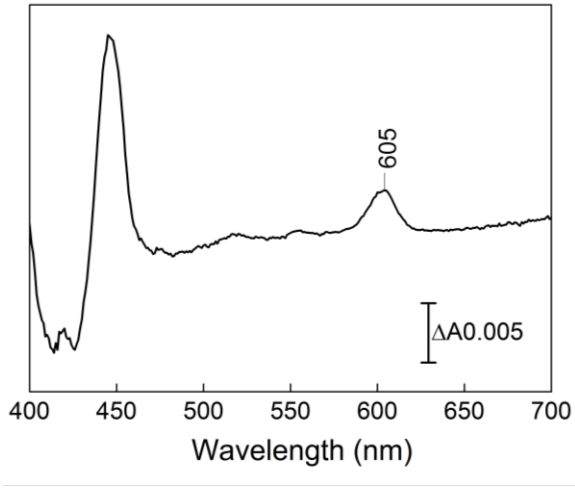

Figure 2-5. A reduced minus oxidised visible difference spectrum (400-700nm) of yeast CcO after Ni affinity column chromatography.
Spectrum was recorded as described in Figure 2-3. Spectrum is of 300 fold diluted CcO in 50 mM HEPES, 500 mM NaCl and 0.05 % (w/v) DDM at pH 7.4.

The pooled sample was loaded onto a 0.8 x 30 cm TSK gel filtration column (TOSOH BioScience) that had been equilibrated with 50 mM HEPES, 500 mM NaCl and 0.05 % (w/v) DDM at pH 7.4. The sample was run in the same buffer. The elution profile, however, displayed an excluded front that overlapped the elution peak containing C*c*O (Figure 2-6). Therefore the fractions of C*c*O were pooled (~24 mL) and concentrated to 500 µL and re-run on the same column to separate out the large front. This front was most likely formed of detergent micelles, lipid and aggregated/multimers of C*c*O. The fractions in the central portion of the second elution profile (~3.5 mL) were concentrated (470 µL) to ~20-30 µM. 20 % (v/v) glycerol was added before storage at -80 ^{o}C. The elution profile of the second run suggested that the concentration step may

have caused further aggregation. Alternatively this aggregation effect may have been time-dependant. This method is part of an ongoing project to produce a more homogeneous preparation of C*c*O.

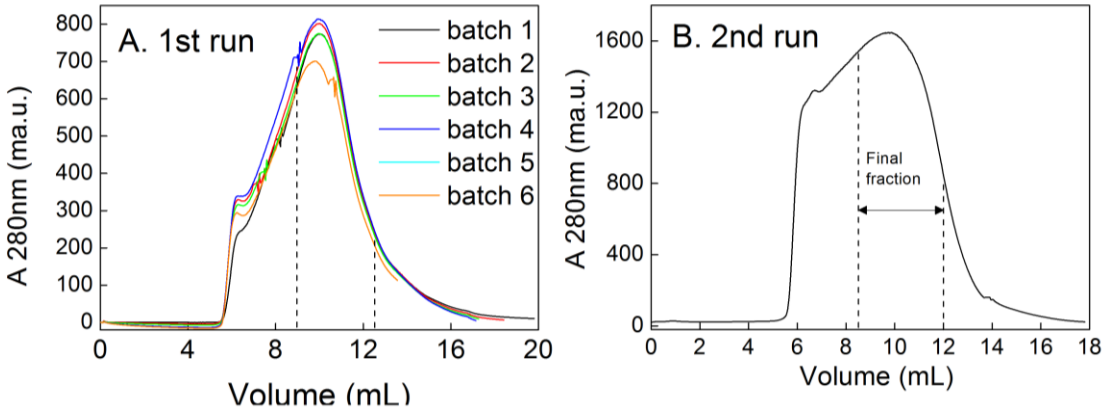

Figure 2-6. Elution profiles of the (A) 1st run and (B) the 2nd run through the gel filtration column.
*(A) Since the column was small, C*c*O was loaded 6 times in 500 µL batches indicated by the multiple profiles shown. Dashed lines indicate the volume of fractions pooled together. These were concentrated from 24 mL total to ~500 µL and passed through the column again (B).*

Overall, when starting with ~130 nmoles of C*c*O (mitos), the yield of purified C*c*O was 20 nmoles i.e. 15 % yield. The A_{280}:A_{422} ratio was ~4.3. A typical redox spectrum of yeast C*c*O purified this way, is compared to a typical redox spectrum of yeast C*c*O purified using method 1, described above (Figure 2-7). It is clear that method 2 was better at separating C*c*O from bc_1 and '554 species' than method 1.

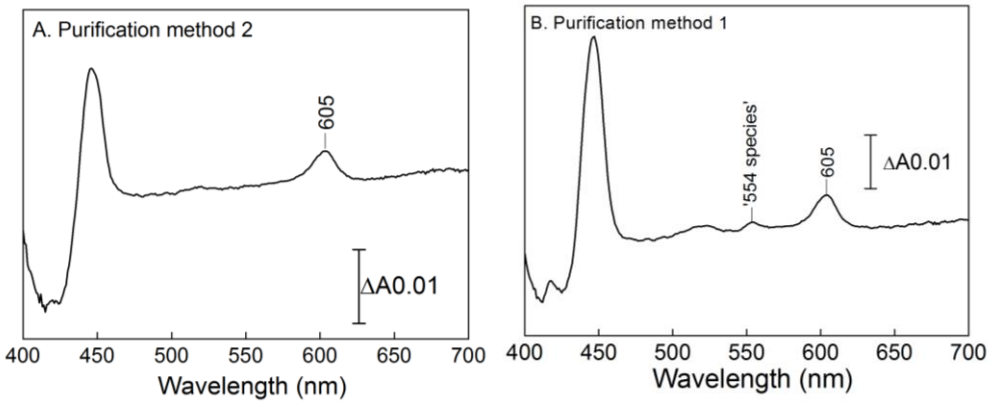

Figure 2-7. A typical reduced minus oxidised visible difference spectrum (400-700nm) of yeast CcO purified using (A) method 2 compared to (B) method 1.
(A) The redox spectrum was recorded as described in Figure 2-3. Spectrum is of 300 fold diluted CcO in 50 mM HEPES, 500 mM NaCl 0.05 % (w/v) DDM at pH 7.4. (B) Spectrum is of 125 fold diluted CcO in 50 mM KPi pH 8.0, 250 mM NaCl, 0.01 % (w/v) DDM.

2.6.3 Purification of yeast CcO in the presence of digitonin

Purification of yeast C*c*O was also repeated using digitonin-solubilised mitos at room temperature. Digitonin is a mild detergent that has been used to isolate supercomplexes of C*c*O:bc_1 [128,135]. Mitos were diluted to 5 mg/mL in 2 % (w/v) digitonin, 50 mM HEPES, 0.1 M PMSF pH 8.0 (personal communication, Jelena Ostojić, CNRS, France). To ensure complete solubilisation, mitos were stirred at 4 ^{o}C for 1 h. The insoluble debris was removed by ultracentrifugation at 120,000 x *g*, for 35 min at 4 °C. 500 mM NaCl and 5 mM imidazole were added to the supernatant. A 40 x 2 cm column containing 40 mL of nickel-iminodiacetic acid resin was equilibrated with 50 mM HEPES, 500 mM NaCl, 5 mM imidazole, 0.01 % (w/v) digitonin, pH 8.0 at 6.7 mL/min. The supernatant was loaded onto the column which was washed with 2 column volumes of the same buffer. The column was then washed with 1 column volume of the same buffer containing 10 mM imidazole. C*c*O was eluted by increasing the imidazole to 100 mM. A redox visible spectrum confirmed that C*c*O co-eluted with bc_1 as a supercomplex (Figure 2-8). Pooled fractions were concentrated using the 100 kDa cut-off centrifugal concentrator to give ~10 µM C*c*O and were stored at -80 ^{o}C. From 90 nmoles of C*c*O in mitos, 15 nmoles of C*c*O were purified giving a yield of 17 %.

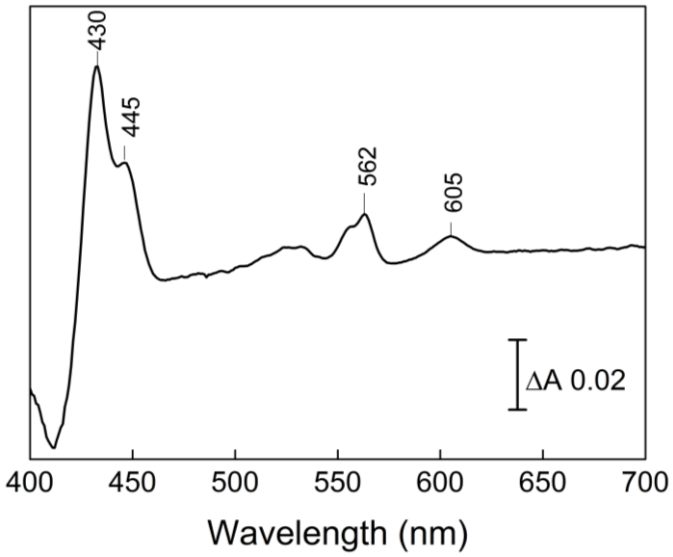

Figure 2-8. A reduced minus oxidised visible difference spectrum (400-700 nm) of yeast CcO purified from digitonin-solubilised mitos after Ni affinity column chromatography.
Spectrum was recorded as described in Figure 2-3. Spectrum is of 60 fold diluted CcO in 50 mM HEPES, 500 mM NaCl, 0.01 % (w/v) digitonin, 5 mM imidazole pH 8.0.

2.7 Purification of bovine CcO

Bovine C*c*O from beef heart was purified by Peter Rich and Tomas Warelow using the method of Moody, *et al.* [155] that had been adapted from the methods of Kuboyama, *et al.* [156] and Keilin, and Hartree, [157]. In general, the meat was blended and the soluble fraction was isolated by pressing the blended meat through a muslin cloth. This was followed by centrifugation (1,368 *x g* for 30 mins at 4 ^{o}C). The supernatant was squeezed through some more muslin, and centrifuged (20,000 *x g* for 1 h, at 4 °C). The pellet containing mitochondria was resuspended and homogenised in 100 mM sodium borate, 100 mM sodium phosphate pH 8.5. This was again centrifuged at 25,654 x *g* for 1 h followed by resuspension and homogenisation of the pellet to produce the final mitochondrial preparation. The preparation was solubilised by dilution to give 20 mg protein/mL in 20 % (w/v) sodium cholate, 100 mM sodium borate, 100 mM sodium phosphate pH 8.5. Bovine C*c*O was purified by a series of ammonium sulphate precipitation, centrifugation and resuspension cycles. The final precipitate was dissolved to give ~0.5 mM bovine C*c*O in 50 mM potassium bicine, 0.1 mM EDTA(K^+), 0.15 % cholate, pH 8.0 and dialysed against the same buffer before storage at -80 ^{o}C. Thus the final preparation was in the same buffer. Concentration of bovine C*c*O was determined based on the size of $\Delta A_{605-621}$ using ε of 25.7 $mM^{-1}.cm^{-1}$ [154]. Figure 2-9 shows a typical reduced *minus* oxidised difference spectrum of purified bovine C*c*O.

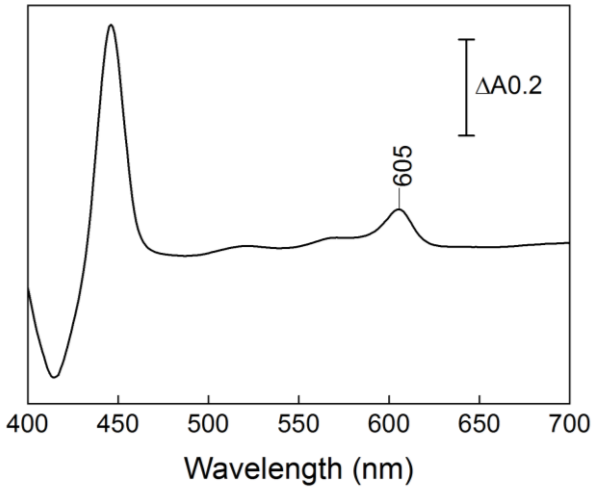

Figure 2-9. A reduced minus oxidised visible difference spectrum (400-700 nm) of purified bovine CcO.
Spectrum was recorded as described in Figure 2-3. Spectrum is of 110 fold diluted CcO in 100 mM KPi 100 mM KCl pH 7.

2.8 ATR-FTIR spectroscopy overview

Mid-IR spectra (4000-900 cm^{-1}) were recorded in ATR mode with a Bruker IFS/66 FTIR spectrophotometer fitted with a liquid nitrogen-cooled mercury cadmium telluride (MCT-A) detector at 4 cm^{-1} resolution, giving ±1 cm^{-1} accuracy of cited frequencies. OPUS6.5 software was used for measurement and processing of IR spectra. In ATR mode, the IR beam is directed through an internal reflection element (IRE) before being directed to the IR detector. The IRE used was a 3 mm diameter silicon prism with three internal reflections (SensIR, Europe). For measurements in the lower frequency region 1800-700 cm^{-1}, a diamond prism was used. An evanescent wave of the internally-reflected beam extends a few microns into the space above the reflection surface. This allows the IR characteristics of a sample placed on the silicon prism surface to be monitored (Figure 2-10). At the same time the sample is accessible for manipulation from above, hence allowing various types of reactions to be induced [110,112].

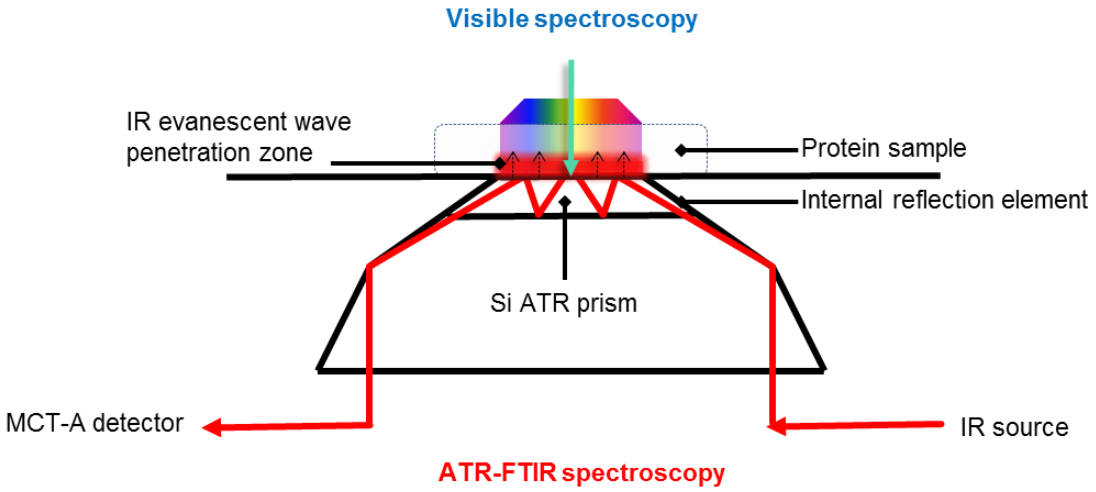

Figure 2-10. Si ATR prism representation.
The IR beam is reflected three times through the silicon internal reflection element (IRE). This creates an evanescent wave (red zone) that penetrates a few microns into the sample. Visible spectra can be recorded at the same time using a fibre optic reflection probe (not shown) directed through the sample from above. The visible light (green arrow) penetrates through the entire sample and is reflected from the prism surface back into the collecting optical fibres.

2.9 Bovine CcO layer preparation for ATR-IR spectroscopy

By depleting bovine C*c*O of detergents and exploiting its hydrophobicity, a layer of C*c*O can be adsorbed onto an attenuated total reflection (ATR) prism surface for IR spectroscopic analysis [110,112]. A minimum of 150 pmol of C*c*O is required to cover the prism surface at an optimal thickness [115]. 'ATR-ready' detergent-depleted bovine C*c*O samples were prepared by a series of washing/ultracentrifugation cycles. 2-3 nmol C*c*O was suspended in 2.5 mL of 20 mM KPi pH 8.5, 0.1 % (w/v) sodium cholate and 0.1 % (w/v) octyl glucoside and ultracentrifuged at 300,000 x *g*, 4 ^{o}C for 1 h. The pellet was resuspended in 20 mM KPi pH 8.5 and ultracentifuged for 20 mins. It was then resuspended in 1 mM KPi pH 8.5 and ultracentifuged for 15 mins. The final pellet was diluted in 10 µL dH_2O and placed onto the prism. Figure 2-11 (black trace) shows a typical IR absorbance spectrum, it consists of primarily a water spectrum. The sample was then dried with a stream of nitrogen gas (Figure 2-11, blue). As a result, the IR spectrum revealed the underlying IR bands of protein that increased in absorbance since the sample become more concentrated and was brought into close contact with the IR prism surface. The spectrum is primarily of amide I and amide II bands at 1650 cm^{-1} and 1539 cm^{-1} and with some contribution of lipid in the 1740 cm^{-1} region. The layer was then rewetted with 10 µL of the buffer of the experiment (buffer conditions are provided in the figure legends within the results chapters). Thus the water bands reappeared (smaller in intensity) and the protein bands decreased with rehydration due to the expansion and equilibration of the layer (Figure 2-11, red). The layer was allowed to stabilise for up to 30 mins at which point the IR absorbance spectrum was constant (not changing) before assembling the electrochemical cell/perfusion cell above the protein layer. The amount of protein deposited was quantitated from the size of the amide II band (ΔA_{II} 1545-1481 cm^{-1}) as indicated in Figure 2-11, it was typically 0.16 to 0.2.

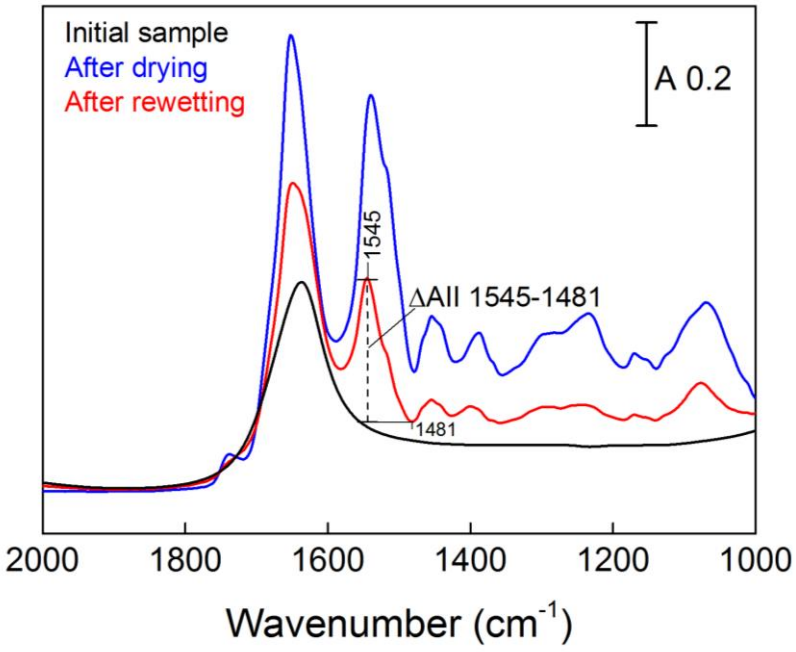

Figure 2-11. IR absorbance spectrum of a detergent depleted bovine CcO sample before (black) and after drying (blue) and after rewetting (red).
The sample of bovine CcO was in 10 µL of dH_2O (black), it was dried with nitrogen gas until absorbance of water bands disappeared (blue). It was rewetted in the buffer (10 µL) of the experiment (red) and allowed to stabilise for 30 mins. Figure shows how the size of ΔA_{II} band in the rewetted spectrum was calculated.

2.10 ATR-FTIR spectroscopy with controlled electrochemistry

An electrochemical cell was assembled above the IR prism surface. The chamber created between the working electrode (platinum mesh or glassy carbon) and the protein layer (100-300 µm distance) was filled with (~80-200 µL) buffer containing appropriate redox mediators (Figure 2-12). Computer control allowed automated switching of potentials for cyclic generation of specific redox states [112,114]. The counter electrode (a platinum sheet) and an Ag/AgCl/KCl reference electrode were connected to the sample chamber by a Vycor frit. All redox potentials are given *versus* the standard hydrogen electrode (SHE) electrode unless stated otherwise. Visible spectra were recorded using a reflection optic fibre probe above the sample which transmitted visible light (450-700 nm) from a stepped dispersive monochromator. The reflected light was collected by fibres in the same probe and directed to a photomultiplier for quantitation. This approach allows sample accessibility for switching between various states whilst recording IR and visible spectra simultaneously.

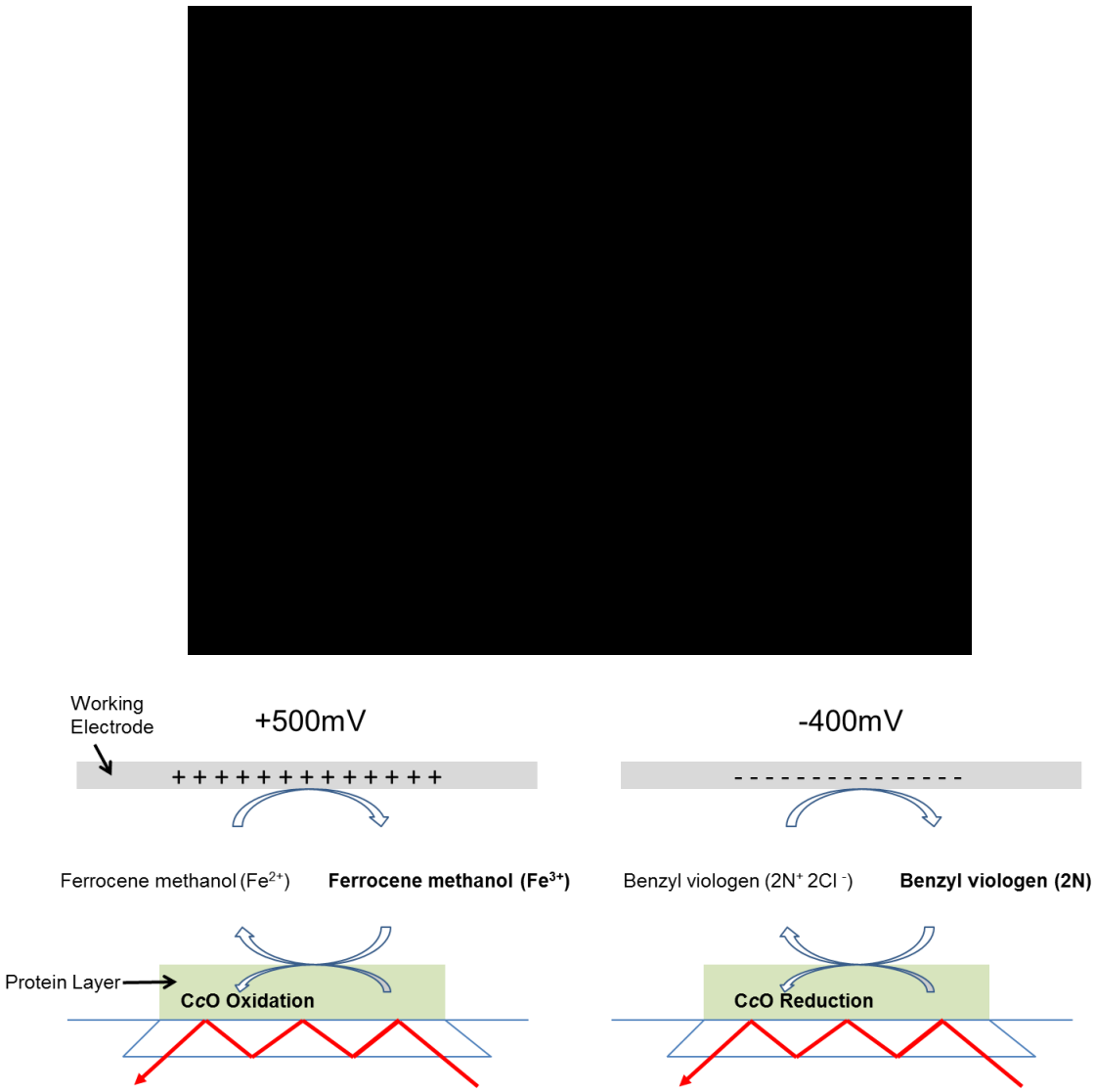

Figure 2-12. Representation of an ATR-FTIR electrochemical cell.
A parafilm gasket coated in vacuum grease was used to create a watertight seal between the ATR and electrochemical devices and sealed the sample within a chamber. This minimised the sample volume and created a small separation (0.1-0.3 mm) between the working electrode and prism surface to achieve redox equilibration times of 5-20 mins. Addition of a fibre optic reflection probe permits the simultaneous acquisition of ATR-FTIR and visible spectra. Potentials are versus SHE. Figure is adapted from figure 1B in ref [158].

2.11 Redox mediators

Redox mediators were used to equilibrate, via diffusion, the applied potential at the working electrode surface and the protein layer [88]. The redox mediators were chosen so that they spanned the redox potential range of the metal centres of C*c*O, and enabled the oxidation and reduction of specific redox centres by control of applied electrochemical potentials. Figure 2-13 shows the E_m values of the redox mediators and of the metal centres of unligated C*c*O, CN-ligated and CO-ligated C*c*O. CN-ligation lowers the E_m of only haem a_3-CN such that the redox transitions of $Cu_{A,}$ haem *a* and Cu_B can be separated from a_3-CN and *vice versa* [159,160]. CO-ligation raises substantially the E_m values of haem a_3 and Cu_B such that the redox transitions of Cu_A and haem *a* can be separated from those of the BNC metals [161].

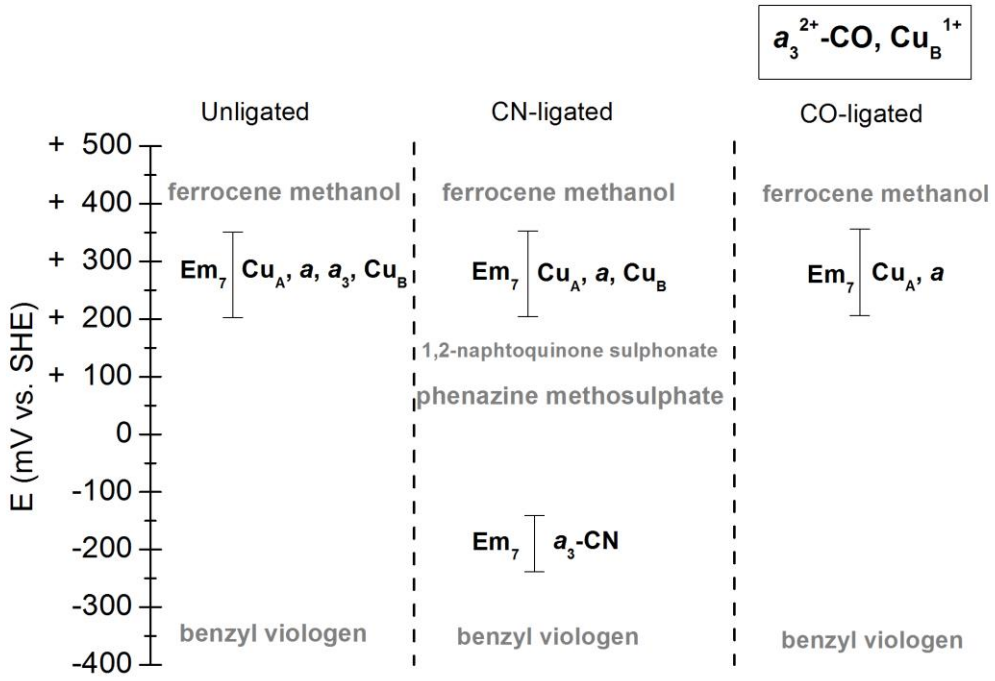

Figure 2-13. E_{m7} values of redox mediators and of the metal centres of unligated CcO, CN-ligated and CO-ligated CcO.
E_m range of unligated CcO is from [159,160]. CN-ligation lowers the E_m of only haem a_3-CN such that the redox transitions of $Cu_{A,}$ a and Cu_B can be separated from a_3-CN and vice versa. CO-ligation holds the binuclear centre in the reduced state such that the redox transitions of Cu_A and haem a can be separated from the BNC [161]. E_m of the redox mediators at pH 7 are; -358 mV benzyl viologen [162], +172 mV 1,2-naphtoquinone sulphonate [163], +80 mV phenazine methosulphate [162], +407 mV ferrocene methanol.

2.12 IR difference spectroscopy

Reaction-induced IR changes are very small and difficult to observe relative to the large overall absorbance background of protein, lipid, water and buffer (Figure 2-14A and B). Therefore IR spectra were plotted/recorded as difference spectra between two defined states (reduced *minus* oxidised) [112,114]. IR difference spectra show only the redox-induced IR band changes and so are easier to interpret. To increase signal to noise the spectra were averaged by cycling between two defined states (for reversible reactions), or by preparation of new protein layers and repeating the measurements.

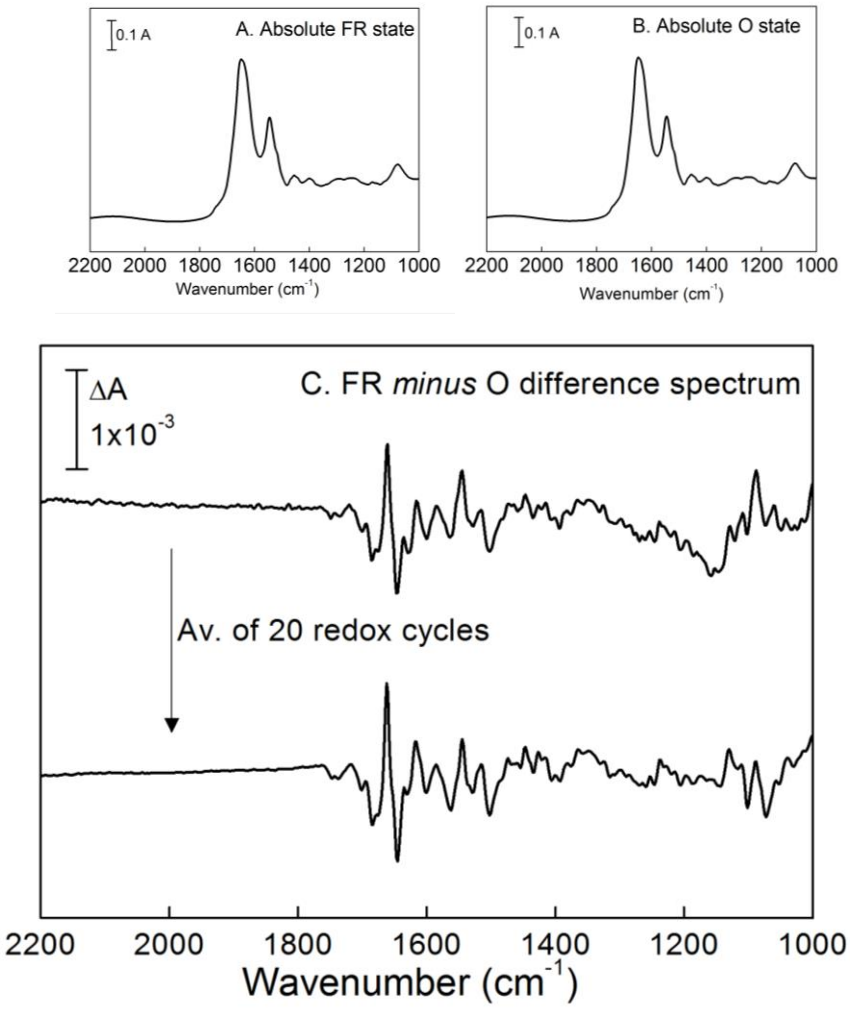

Figure 2-14. Absolute IR absorbance and reduced minus oxidised difference IR spectra of bovine CcO (4000-900 cm^{-1}).
The absolute spectra of (A) fully reduced (FR) and (B) oxidised (O) CcO contain a large overall background of protein/water/buffer absorbance and so subtle redox-linked IR changes cannot be distinguished. However redox linked IR changes can be revealed in the (C) IR difference spectrum.

2.12.1 Measurement of IR difference spectra

Each single spectrum/baseline of intensity (I) vs. frequency (cm^{-1}) was computed from the Fourier transformation of 500 or 1000 averaged interferograms. Absorbance spectra were automatically computed from intensities with the Beer-Lambert law;

$$A = log_{10} (I_{0\ (baseline)}/I_{(sample)})$$

The exact details of redox potentials and buffer conditions are provided in the Figure legends within each chapter. The sequence of events for a typical redox cycle were as follows:- an oxidising potential of typically +500 mV was applied and, after an equilibration time ~10-30 mins, a baseline of the fully oxidised state was recorded. A reductive potential was then applied (typically -400 mV) and, after ~10-30 mins equilibration, a fully reduced (FR) spectrum *versus* the O baseline was recorded. The reaction was complete when consecutive spectra were superimposable in the visible (400-700 nm) and/or IR (2200-1000 cm^{-1}, silicon or 1800-750 cm^{-1}, diamond prism) regions. The sequence of events were then reversed by recording a baseline with the FR state, followed by switching to an oxidative potential (+500 mV) and recording the O *minus* FR difference spectrum after ~10-30 mins. These spectra were averaged as follows:

[(FR *minus* O) – (O *minus* FR)] */ 2 = averaged FR minus O*

This gave an averaged redox spectrum for 1 redox cycle. To produce final spectra presented, such cycles were repeated ~20 times and data were averaged to increase the signal to noise ratio (see Figure 2-14C).

2.12.2 Preparation CN and CO bound CcO for IR measurements

A layer of C*c*O was always prepared in the same way as described above. To prepare CN-ligated bovine C*c*O, the experimental buffer containing 10 mM KCN (details are given in Figure legends) was added to the reaction chamber. To ensure all cyanide was ligated to C*c*O an oxidative potential was applied (+500 mV) for 30 mins. Binding was monitored by the intensity of the CN-ligated band at 2151 cm^{-1}. This frequency is characteristic of CN bound to the fully O state of C*c*O [164]. To prepare CO-ligated bovine C*c*O, 5 mL of the experimental buffer was bubbled with CO gas for 2-5 mins. 200 µL was used to fill the sample chamber and a reductive potential (-400 mV) was applied. CO binding to the FR state was monitored by the intensity of the CO band at 1963 cm^{-1}. This frequency is characteristic of CO bound to the FR state of bovine C*c*O [165].

2.13 Electrochemically induced IR difference spectra of Tyr and Tyr-His model compounds

TMP, TBP and TyrHis(trimethyl) were tested as model structures of tyrosine that could form a stable phenoxyl radical in the oxidised state. 5-10 mM compound dissolved in 50 % (v/v) propan-2-ol, 20 mM KPi, 500 mM KCl, pH 13 was added to the sample chamber. In this case the reaction buffer did not require redox mediators since the compounds interacted electrochemically directly with the working electrode, and were small enough to diffuse between the working electrode and the prism surface. The electrochemical cell contained a glassy carbon working electrode, platinum counter and Ag/AgCl reference electrode (Figure 2-15).

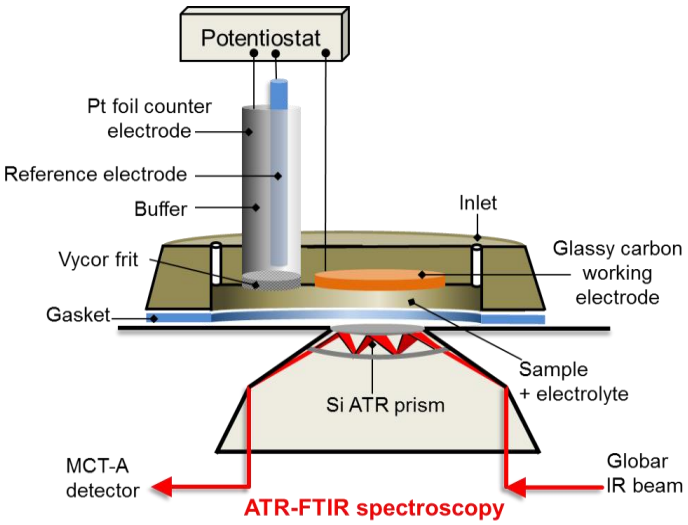

Figure 2-15. Electrochemical cell used for coupled ATR-FTIR spectroscopy of TMP, TBP and Tyr-His model compounds.
Glassy carbon working, Ag/AgCl/KCl reference and a platinum coil counter electrode were used. This electrochemistry cell did not permit in situ acquisition of visible spectra.

IR difference spectra were recorded as described above. Data were averaged from ~5-10 redox cycles. Tyr-His(trimethyl) displayed partial reversible oxidation, and so IR spectra of oxidised versus a reduced baseline were averaged from 10 freshly prepared samples.

2.14 Perfusion-induced IR difference spectroscopy

A perfusion cell was assembled above the protein layer creating a chamber (~3 mm height) (Figure 2-16). This setup permitted the simultaneous acquisition of visible spectra (450-700 nm) allowing the reaction to be monitored. The buffer was delivered into the cell through plastic tubing. A pump controlled the flow rate at 1 mL/min. This

permitted the introduction of ligands or redox mediators into the reaction chamber that could react with the protein layer, and then, be removed by exchanging the buffer [111,112]. This method was used to record a ligated O-CN *minus* unligated O spectrum of bovine C*c*O. It was also used to record a FR *minus* O IR difference spectrum of bovine C*c*O [111]. Lastly it was used to record a P_M state *minus* oxidised IR spectrum of bovine C*c*O [166]. The exact reaction conditions are given in the Figure legends.

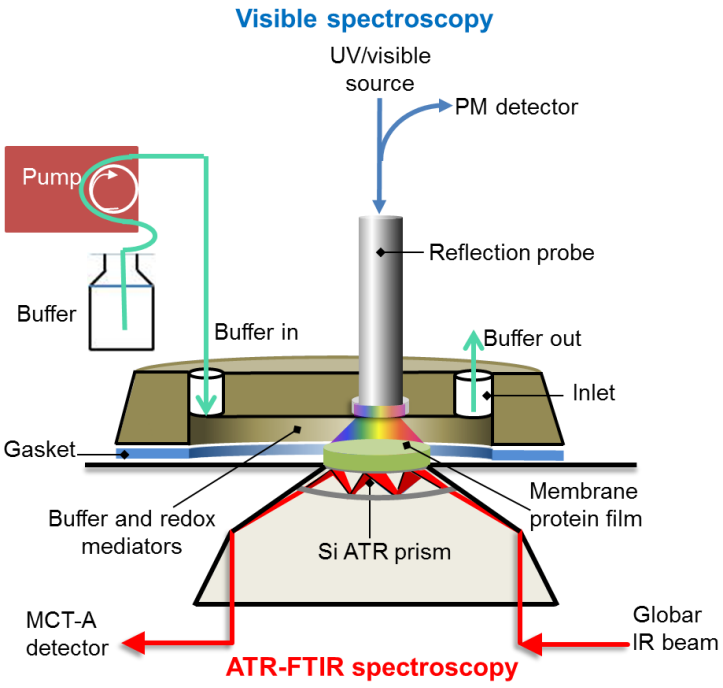

Figure 2-16. Perfusion cell coupled to ATR-FTIR and visible spectroscopy.
Buffers containing different redox mediators or ligands (CN or CO) can be perfused using a peristaltic pump over the protein layer for transition between protein states.

2.15 IR data manipulation

2.15.1 Baseline corrections

All averaged difference spectra were corrected for baseline changes arising from pH, protein layer, buffer, water and water vapour variations. This was achieved by iterative subtraction, performed on OPUS6.5, of pre-recorded IR reference spectra (Figure 2-17). As an example Figure 2-18 shows the sequential correction of a FR *minus* O IR difference spectrum of unligated bovine C*c*O.

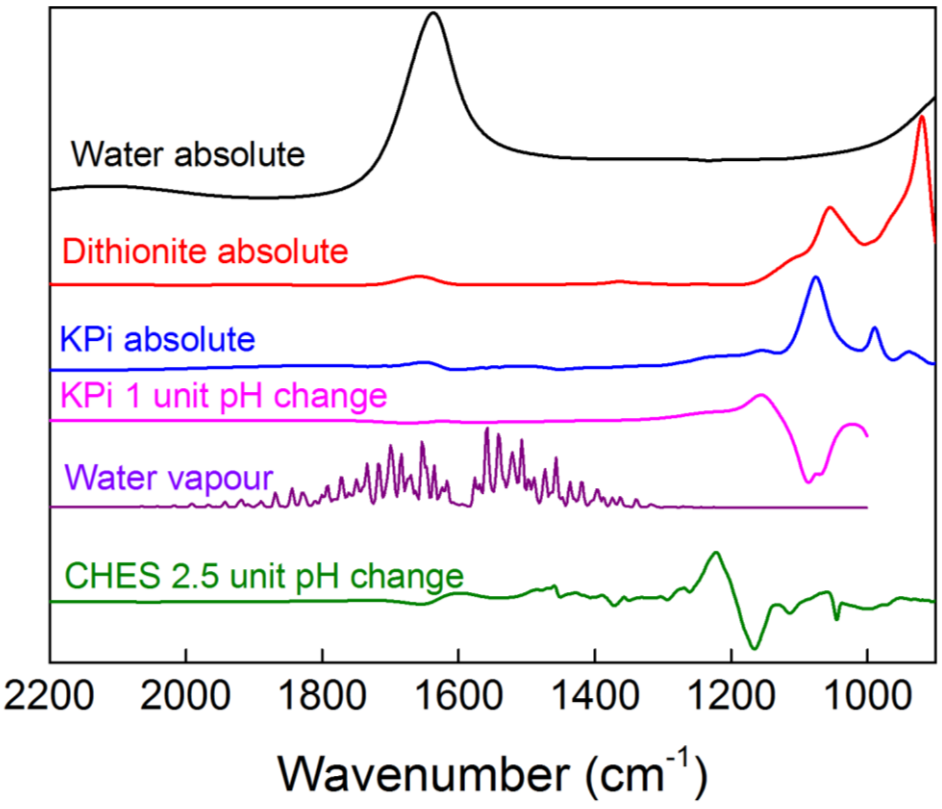

Figure 2-17. Series of IR reference spectra that were used in the correction of experimentally recorded IR difference spectra.
The spectra are not plotted to scale and are only meant for illustrative purpose. The pink and green traces are calculated IR difference spectra of the respective buffer recorded at two different pHs.

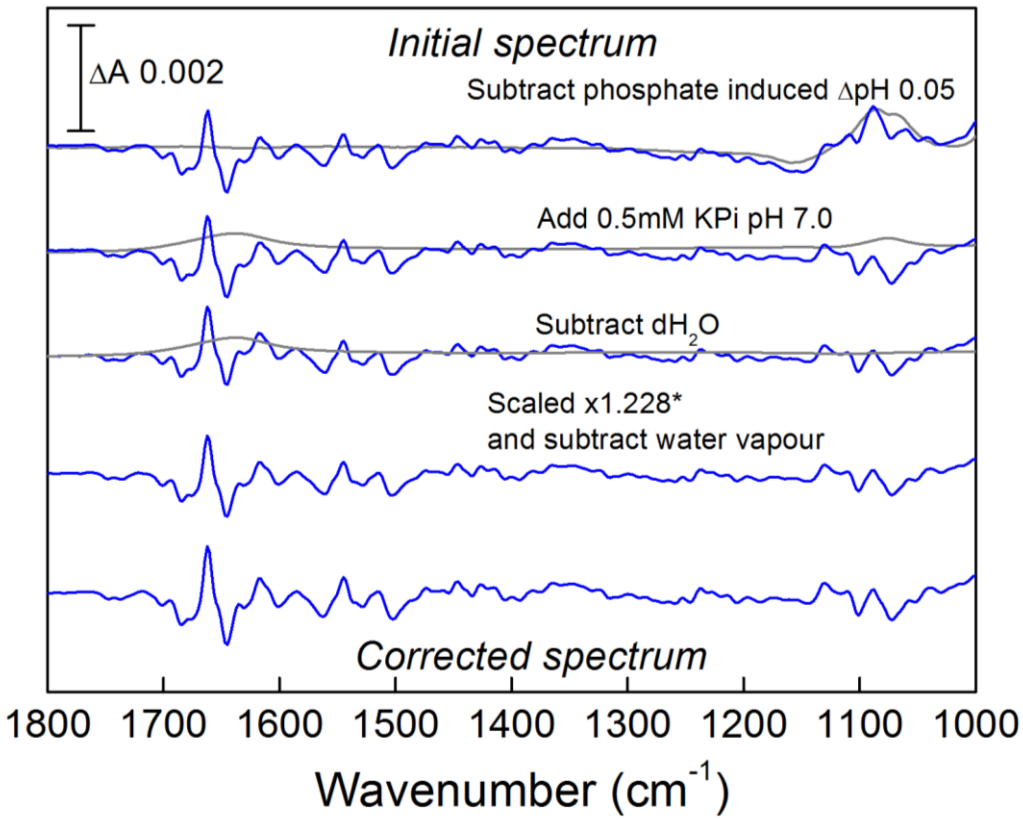

Figure 2-18. Correction of FR minus O IR difference spectrum (1800-1000 cm^{-1}).
Spectra shown in grey were used for subtraction. The spectrum was corrected by subtraction of ΔpH 0.05, water vapour variations (not shown). It was then scaled x1.228 according to the ΔA_{II} size of the absolute spectrum that was used to record the FR-CN minus O-CN IR difference spectrum (see next section for normalisation).

2.16 Normalisation of redox spectra

The IR difference spectra were normalised to total protein to allow direct comparison between individual spectra presented within each results chapter. Total protein was estimated from the size of the amide II (ΔA_{II}) band of the rewetted protein layer in each experiment (see Figure 2-11). All IR difference spectra were then scaled so that their ΔA_{II} bands were the same. For IR experiments with TBP, TMP and TyrHis(trimethyl), the concentrations were known. Hence, the spectra were scaled by a factor so that each spectrum displayed intensities corresponding to 10 mM concentration.

2.17 Gaussian calculated IR absorbance spectra

Theoretical IR absorbance spectra of Tyr-His(trimethyl) in the protonated, neutral and deprotonated state, were calculated using Gaussian03 [167]. Gaussian03 has functions for calculating energy minimised structures, and from these structures, predicting the normal mode vibrational spectra. Geometry optimisation and frequency calculations were performed using the commonly used B3LYP (Becke, three-parameter, Lee-Yang-Parr) [168,169] exchange-correlation functional in conjunction with the 6-31g(d) basis set. Typical input files are shown in Figure 2-19.

A.
%chk=trimethylHYH+H+_opt.chk
#t opt b3lyp 6-31g(d)

Optimisation of TyrHis(trimethyl) structure in the fully protonated state i.e. net charge = +1, multiplicity= 1

1 1

O	0.054	2.621	0.450
N	1.221	0.079	-0.171
N	3.370	0.548	-0.663
C	2.112	0.991	-0.709
C	3.291	-0.702	-0.052
C	1.985	-1.016	0.271
C	-0.202	0.267	-0.072
C	-0.703	1.584	0.284
C	-2.139	1.640	0.413
C	-2.970	0.558	0.162
C	-2.455	-0.695	-0.241
C	-1.060	-0.800	-0.355
C	-3.363	-1.870	-0.532
H	1.778	1.957	-1.039
C	4.519	-1.526	0.205
C	-2.710	2.974	0.818
H	-4.049	0.677	0.265
H	-0.633	-1.741	-0.694
H	-2.796	-2.708	-0.960
H	-4.159	-1.616	-1.249
H	-3.868	-2.253	0.371
H	-2.143	3.783	0.328
H	-2.640	3.089	1.913
H	-3.769	3.032	0.511
H	4.371	-2.137	1.111
H	5.387	-0.860	0.351
H	4.707	-2.188	-0.658
H	1.633	-1.945	-0.213
H	-0.329	3.229	1.287
H	4.004	1.262	-0.107

B.
%chk=trimethylHYH+H+_freq.chk
#t freq b3lyp 6-31g(d)

IR freq calculation of optimised structure i.e. net charge = +1, multiplicity= 1

1 1

O	0.477435	-2.255196	0.123862
N	-1.171481	-0.064341	-0.157564
N	-3.154429	-0.817958	-0.588887
C	-1.846378	-1.034042	-0.783511
C	-3.347132	0.321500	0.183241
C	-2.091841	0.786479	0.451138
C	0.258124	0.093790	-0.108404
C	1.077614	-1.027844	0.066093
C	2.470113	-0.854886	0.162933
C	2.984755	0.438370	0.076464
C	2.177449	1.571812	-0.110698
C	0.800963	1.378689	-0.205352
C	2.787821	2.949275	-0.209221
H	-1.407808	-1.850395	-1.332230
C	-4.696137	0.819190	0.580619
C	3.364306	-2.057027	0.356318
H	4.061949	0.567948	0.148409
H	0.143362	2.226066	-0.376048
H	2.035791	3.706023	-0.450325
H	3.561033	2.986178	-0.984636
H	3.262767	3.239581	0.735534
H	3.273893	-2.773674	-0.471236
H	3.143410	-2.590966	1.291569
H	4.413055	-1.755537	0.406281
H	-4.595372	1.719634	1.190360
H	-5.239755	0.072020	1.169775
H	-5.303273	1.071492	-0.296155
H	-1.770111	1.629812	1.040119
H	1.135117	-2.929945	0.357203
H	-3.890110	-1.412410	-0.952080

Figure 2-19. Example of the (A) input file to Gaussian to optimise the structure of TyrHis(trimethyl) in the fully protonated state, and the (B) input file to compute the IR spectrum.
The charge and multiplicity of the molecule was defined as +1 and 1 respectively, and the initial atomic coordinates were from a drawn structure. The output coordinates after optimisation, were then used in the (B) input file to determine the IR spectrum and normal modes of vibration.

The frequencies (cm^{-1}) of the output IR spectra were scaled by the scale factor of 0.9614 (as defined on Facio 18.6.2 for this method). The starting structures were drawn and evaluated on Facio 18.6.2. Facio 18.6.2 provided a user interface to visualise the normal modes of vibration that give rise to each IR band, so that the IR bands could be assigned. In general a non-linear molecule can have 3*N*-6 normal modes of vibration, where *N* is the number of atoms. Phenol has a well-defined set of normal modes of vibrations that have been given names to describe them, some of which are displayed in Figure 2-20. These were used as a guide to make assignments of IR bands to phenol. All other modes were described as a stretching vibration (*v*) or a bending vibration (δ). For example δ(CH_3) refers to a bending vibration of the -CH_3 group (changing bond angles).

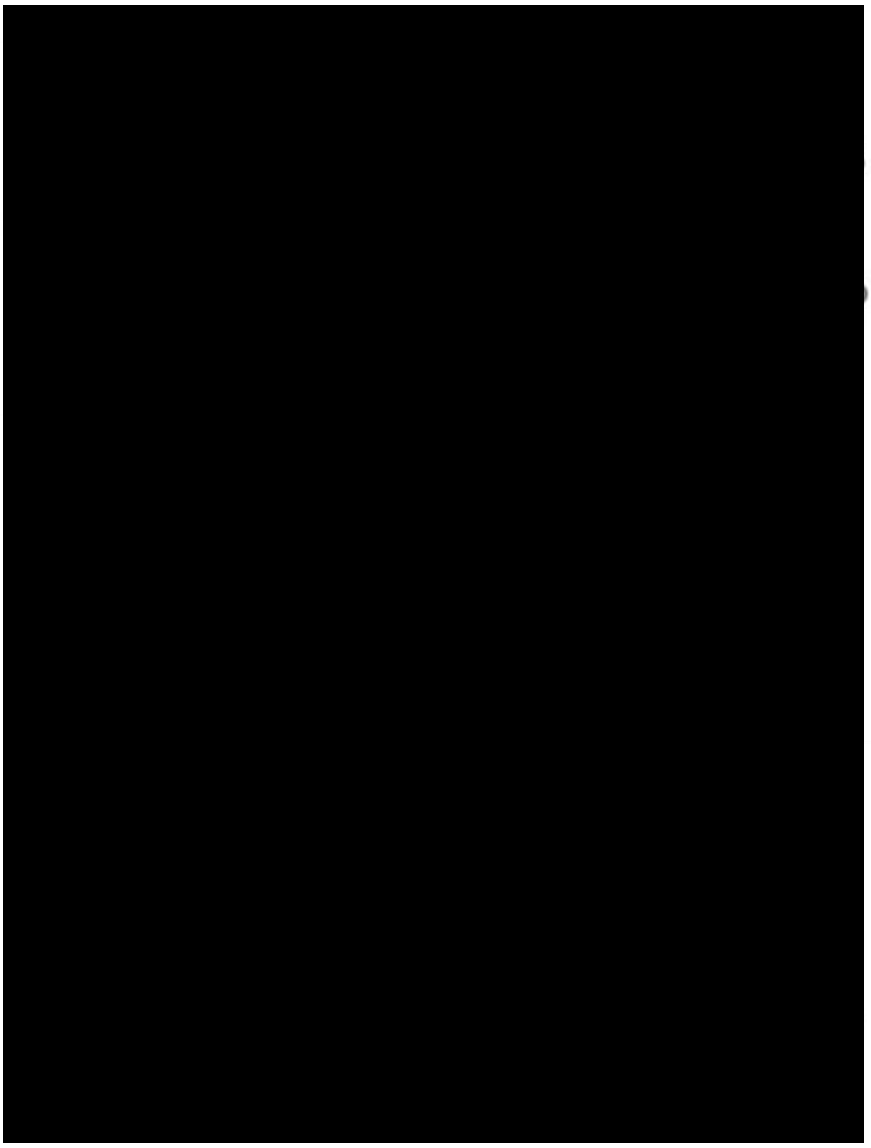

Figure 2-20. Illustration of characterised normal vibrational modes of phenol.
Arrows indicate the displacement vectors of each atom. Figure is adapted from figure 8 in ref [170].

2.18 Determination of pK_a values of Tyr-His(trimethyl)

pK_a values of Tyr-His(trimethyl) were determined by pH titration of its absolute UV/visible spectra (230-430 nm), with an Avantes UV/visible spectrometer. Two pK_a values were fitted using the standard Henderson–Hasselbalch equation.

$$pH = pK_a + \log_{10} (\text{deprotonated/protonated})$$

$$(10^{(x- pKa)}/ 1+10^{(x- pKa)}) * \text{range}) + \text{offset} = y$$

2.19 Oxygen electrode assay to determine turnover number

Steady-state oxygen consumption rates were measured in a stirred reaction chamber of a Clark-type O_2 electrode (Figure 2-21). The temperature was controlled at 25 ^{o}C using a water bath. Whole cell assays were carried out using 12.5 mg/mL yeast cells, giving ~25 nM C*c*O, in 50 mM KPi pH 7.2, 440 mM sucrose, 10 mM lactate, 1 µM valinomycin and 1.8 µM CCCP (carbonyl cyanide m-chlorophenylhydrazone) [171].

Assays with mitos were carried out using membranes containing 2-10 nM C*c*O, in 10 mM KPi pH 6.6, 50 mM KCl, 2 mM sodium ascorbate, 0.05 % (w/v) DDM and 40 µM N,N,N',N'-tetramethyl-p-phenylenediamine dihydrochloride (TMPD), a redox mediator. The reaction scheme of the oxygen electrode is shown in Figure 2-21. Once the baseline had stabilised, the reaction was initiated by addition of 50 µM cyt *c* from horse heart or yeast. Turnover numbers were calculated after subtraction of the baseline rate. The kinetic parameters V_{max} and apparent K_m were determined using non-linear fitting of the Michaelis-Menten equation for single phase kinetics, and with the sum of two Michaelis-Menten terms for plots that displayed biphasic kinetics. Fitting was performed using OriginPro 8.6.

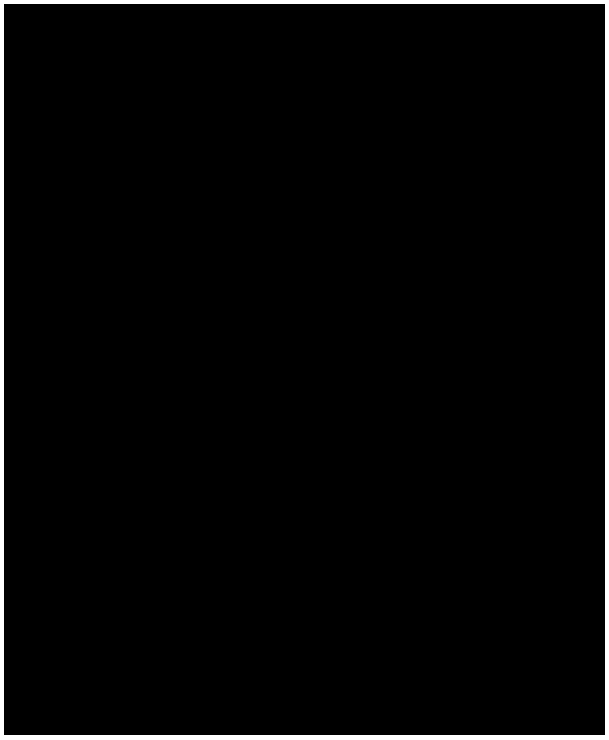

Figure 2-21. Clark-type oxygen electrode.
The working electrode was platinum surrounded by a Ag/AgCl/KCl counter and reference electrode. 3 M KCl was used as the electrolyte between these electrodes, which were separated from the main incubation chamber by an oxygen permeable membrane (image from http://www.rankbrothers.co.uk/prod1.htm).

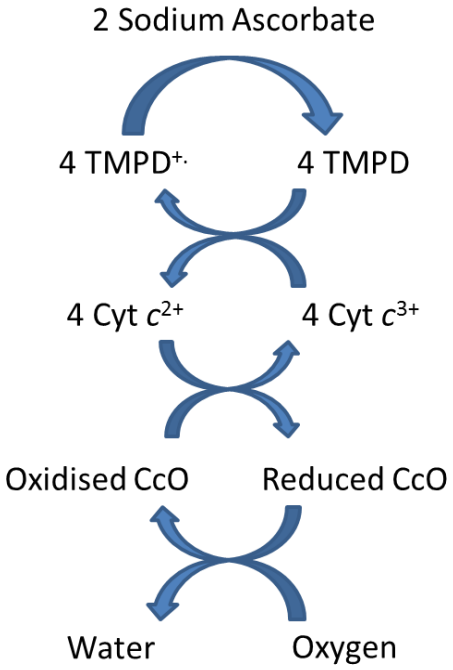

Figure 2-22. Reaction scheme of the oxygen electrode assay.
Cyt c was maintained in the reduced state throughout the assay. This was achieved by addition of sodium ascorbate (E_{m7} +58 mV [162]) that reduced the $TMPD^{\cdot+}$/TMPD (E_{m7} +260mV [172]) which reduced cyt c (E_{m7} ~+270mV of horse heart cyt c [173] and Em_7 ~+260mV of yeast iso-1 cyt c [174]).

2.20 Determination of oxygen affinity

The apparent K_m of C*c*O for oxygen was measured using the myoglobin method [175]. Oxygen consumption rates at low oxygen concentrations were monitored by following the conversion of oxymyoglobin (MbO_2) to ferrous myoglobin. In order to prepare oxygenated ferrous myoglobin, a 15 mM stock of ferric myoglobin (as prepared) in 10 mM KPi, 50 mM KCl pH 6.6 was reduced with 200 mM sodium ascorbate (solid). The sample was allowed to equilibrate for 20 mins at 4 ^{o}C. The sample was then passed through a Sephadex G-25 column (15 x 1 cm) equilibrated with aerobic 10 mM KPi, 50 mM KCl pH 6.6 to remove sodium ascorbate. Myoglobin eluted in the ferrous oxygenated state. The total concentration of myoglobin was determined from a visible absorption spectrum of a dithionite reduced sample, at 555 nm, **ε** 12.92 $mM^{-1}.cm^{-1}$ [176]. Samples were typically ~1 mM and consisted of 85 % MbO_2 and 15 % ferric myoglobin. The oxygen affinity assay was carried out using a dual wavelength visible spectrophotometer (Model UV 3000, Shimadzu). This enables the absorption measurement to be taken at two specified wavelengths (a sample wavelength vs. a reference wavelength) simultaneously in the same cuvette. Absorbance measurements were made at 582-564 nm, a wavelength pair at which the difference between the MbO_2 state and ferrous state was the largest, in a stoppered cuvette with stirring at 25 ^{o}C. The cuvette was filled with 10 mM KPi pH 6.6, 50 mM KCl, 0.05 % (w/v) DDM, 2 mM sodium ascorbate, 40 µM TMPD, 30 µM total myoglobin and mitos to give 1-3 nM C*c*O. After the baseline had stabilised the reaction was initiated with 50 µM horse heart cyt *c*. Figure 2-23 shows how the data of absorbance change vs. time (inset A) was converted to the velocity (µM O_2/s/µM C*c*O) vs time (inset D). Initially the data were converted to fraction of MbO_2 present (Fraction) vs time (inset B). The concentration of free oxygen was calculated using the following equation;

$$[O_2 \text{ free}] = \frac{K_d * \text{Fraction}}{1 - \text{Fraction}}$$

K_d = 1.34 µM, oxygen dissociation constant of horse heart myoglobin [177]. Fraction refers to fraction of MbO_2.

The total [O_2] (Figure 2-23C) was calculated using;

$$\text{Total } [O_2] = \text{Fraction} * [MbO_2] + [O_2 \text{ free}]$$

Finally the oxygen consumption rate (µM O_2/s/µM C*c*O) was calculated using;

$$V = \frac{(O_2 \text{ total}_1) - (O_2 \text{ total}_2)}{(t_1 - t_2) * [CcO]}$$

$t_1 - t_2$ refers to a time interval, 5 seconds was used here.

From these values a plot of oxygen consumption rate versus free oxygen concentration was drawn (Figure 2-23D). The K_m value was determined by a non-linear fit of the Michaelis-Menten equation using OriginPro8.6.

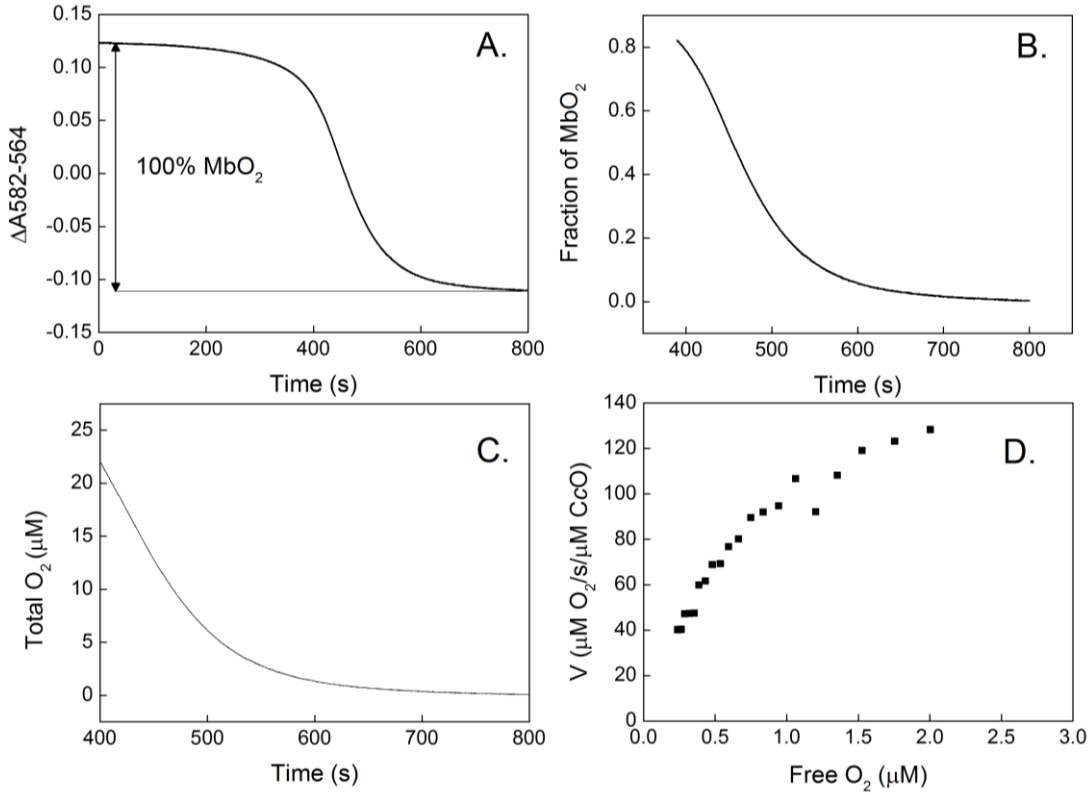

Figure 2-23. The deoxygenation kinetics of oxymyoglobin to ferrous myoglobin were used to measure oxygen consumption rates of CcO so that the oxygen affinity of CcO could be determined.
A. The recorded data. B. Data converted to fraction of MbO_2 vs. time. C. The total O_2 concentration was calculated as described in the main text. D. Determined by calculating the rate of oxygen consumption in (C) in 5 second time intervals and division by the CcO concentration used.

2.21 Membrane reconstitution of bovine CcO

Reconstitution of the C*c*O into vesicles to form COVs was performed by combining the cholate dialysis methods of Casey, *et al.*, Wrigglesworth, *et al.* and Hosler, *et al.* [178-180]. A round bottomed glass tube was rinsed with water, ethanol and then chloroform. The tube was used to dissolve 40 mg of lecithin (Type IV-S) in 300 µL chloroform. The chloroform was evaporated with nitrogen to leave a thin layer of lipid. The layer was washed with 2 mL of acetone, dried with nitrogen, and held under vacuum for 15-20 mins. It was then re-suspended using a homogeniser into 1 mL of 2 % (w/v) potassium cholate, 75 mM HEPES, pH 7.4 to give 40 mg/mL final lipid concentration. The phospholipid suspension was degassed and sonicated at 1 min/mL, 4 ^{o}C using a sonicator probe (5 µm amplitude setting, 3 mm tip diameter) for intervals of 15 s on and 20 s off, which gave a clear solution. The sample was centrifuged at 12,000 x *g* for 15 mins, 4 ^{o}C to remove titanium particles and any lipid aggregates. Bovine C*c*O was added to the lipid to give 0.19 nmole of C*c*O to 1 mg of lipid ratio (7.6 µM). This was then dialysed (10-14 kDa cut-off tubing) at 4 ^{o}C with rapid stirring to remove the detergent against: 2 x 1.5 h 500 mL of 75 mM HEPES pH 7.4, 14 mM KCl, 0.1 % (w/v) potassium cholate, 2 x 1.5 h without 0.1 % potassium cholate, and finally for 16 h against 500 mL of 0.5 mM HEPES pH 7.4, 44.6 mM KCl, 43.4 mM sucrose (Figure 2-24). This procedure formed COVs with a high intravesicular buffering capacity surrounded by a low buffering medium of the same osmotic strength. The COVs had an opalescent appearance and were stored at 4 ^{o}C.

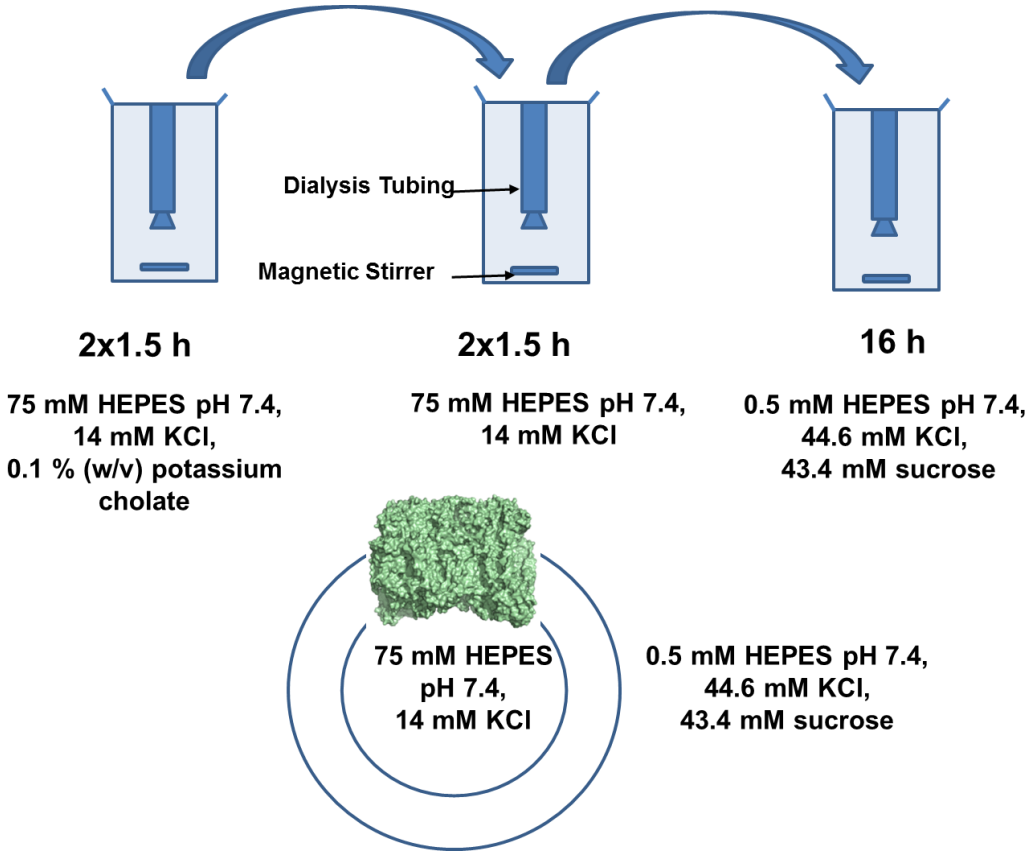

Figure 2-24. Dialysis protocol for the reconstitution of bovine CcO into phospholipid vesicles to produce CcO vesicles (COVs).

2.21.1 Optimisation of membrane reconstitution of yeast CcO

Purified yeast C*c*O was prepared using three principal methods described above. Since reconstitution of yeast C*c*O into liposomes using the method for bovine C*c*O described above proved unsuccessful, various alternative conditions for preparation of yeast C*c*O COVs were tested and are summarised in the Results.

2.21.2 Respiratory control ratio

The respiratory control ratio provides a facile means of estimating how well the C*c*O had incorporated into the membranes, and how intact the lipid vesicles were after reconstitution. The intactness could be compromised, for example, by residual detergent causing liposomes to become 'leaky' to protons, or by C*c*O not incorporating correctly in the membranes. In well-coupled COVs, C*c*O activity is slowed down by the PMF that is generated across the vesicle bilayer by enzymatic turnover. Removal of the PMF by uncoupling stimulates the rate and provides an indication of the COVs quality. The RCR is a ratio of the turnover number ($e.s^{-1}.CcO^{-1}$) in the presence of an uncoupler such as carbonyl cyanide m-chlorophenylhydrazone (CCCP), divided by the turnover

number without uncoupler. When added to COVs, CCCP equilibrates the proton concentration and charge gradient across the membrane, and so, increases the C*c*O turnover number which is no longer rate-limited by the PMF.

The RCR was measured using an O_2 electrode at 25 ^{o}C (see Figure 2-21). The reaction chamber contained 0.5 mM HEPES pH 7.4, 43.4 mM sucrose and 44.6 mM KCl, 50 µM horse heart cyt *c*, 2 mM sodium ascorbate and 40 µM TMPD. Once the baseline has stabilised, the assay was initiated with COVs to give 10 nM C*c*O. Once the rate had stabilised, 1 µM CCCP was added to uncouple the vesicles. Lastly, 0.05 % (w/v) DDM was added to solubilise the vesicles. Typically, the turnover number for bovine COVs was 30 $e.s^{-1}.Cc O^{-1}$ without uncoupler, and 90 $e.s^{-1}.Cc O^{-1}$ in the presence of uncoupler, which gave an RCR of 3. Following the addition of DDM it was ~160 e s^{-1} which shows that approximately half of the C*c*O was orientated with its cyt *c* binding site facing inwards.

2.21.3 Ferrocytochrome c preparation

Horse heart cyt c^{2+} for proton to electron stoichiometry studies was prepared by adding solid sodium ascorbate (to give a final concentration of 100 mM) to 15 mM cyt c^{3+} in 500 mM HEPES pH 7.4. After 15 mins incubation at 4 ^{o}C, the sodium ascorbate was separated from cyt c^{2+} with a Sephadex G-25 column (15 x 1 cm), equilibrated and eluted with 43.4 mM sucrose, 44.6 mM KCl. A pH electrode was used to ensure the pH was still pH 7.4. The cyt *c* concentration was measured by taking a visible absorbance spectrum after adding a small amount of sodium dithionite to fully reduce the sample, using ε of 27.7 cm^{-1} mM^{-1} at 550 nm for the reduced enzyme [181]. The percentage of cyt *c* in the reduced form was determined by comparing the size of the 550 nm absorption band (corresponding to the reduced form) before and after it was completely reduced with sodium dithionite. Typical samples had diluted to approximately 2 mM and were 98 % reduced. They were stored at -80 ^{o}C.

2.21.4 Proton/electron stoichiometry

The proton pumping measurements were performed with a dual wavelength UV/visible spectrophotometer. Measurements were carried out at 14 ^{o}C in 1.6 mL total volume, in a cuvette with rapid stirring. Proton pumping was measured by following the absorption changes of a pH indicator dye, phenol red, in response to the addition of cyt c^{2+}. In order to minimise absorption contribution from the redox change of cyt c^{2+} to cyt c^{3+}, the absorbance measurement was taken at $\Delta A_{556.5\text{-}504.0}$, which are isosbestic points of cyt *c* (Figure 2-25).

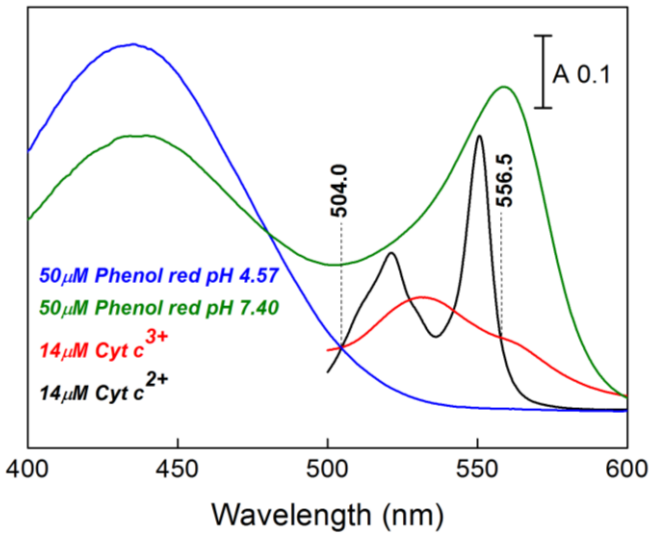

Figure 2-25. Comparison of the visible absorption spectra (400-600 nm) of phenol red at pH 7.4 and pH 4.6 and cyt c at pH 7.4.
Blue trace is of 50 µM phenol red in 44.6 mM KCl and 43.4 mM sucrose pH 4.6. Green trace is of 50 µM phenol red in 75 mM HEPES, 14 mM KCl pH 7.4. The spectrum of cyt c^{3+} (red) in 75 mM HEPES, 14 mM KCl, pH 7.4 was recorded against a buffer background. A small amount of solid sodium dithionite was added to record the reduced spectrum of cyt c^{2+}. Isosbestic points are indicated.

For a typical assay the cuvette was filled with 50 µM phenol red, 43.4 mM sucrose, 44.6 mM KCl, containing final concentrations of 0.5 µM COVs, 10 µg/mL carbonic anhydrase, 10 µM valinomycin and 1 nM CCCP. The latter two were added to relax any PMF which may have been present that would have a limiting effect on proton pumping. The pH of the solution was adjusted to pH 7.4 with 2 µL additions of 50 mM KOH. This was monitored by comparison of the $\Delta A_{556.5\text{-}504.0}$ size to a pre-recorded 50 µM phenol red in 75 mM HEPES pH 7.4 (Figure 2-25). Once the baseline had stabilised, the reaction was initiated with 1.35 µM cyt c^{2+}, after which a calibrating pulse of 2 µM HCl was added, and the pH was readjusted to its original value. The kinetic measurement was then repeated at $\Delta A_{549\text{-}566}$, wavelengths that enabled the initial oxidation rate of cyt c^{2+} to be measured without interference from pH induced changes of phenol red. The COVs were then uncoupled by the addition of 2.5 µM CCCP. After allowing the baseline to stabilise, and readjusting the pH to 7.4, the addition of 1.35 µM cyt c^{2+} followed by 2 µM HCl was repeated.

The proton to electron stoichiometry was estimated using two methods. For the first method, the measured extent of acidification of the external medium (protons pumped) was expressed as a ratio relative to the concentration of cyt c^{2+} added (electrons consumed). For the second method the measured rate constants of cyt c^{2+} oxidation and of proton re-entry into vesicles were combined with different assumed proton pumping stoichiometries to generate iteratively a best fit to the proton extrusion data.

2.22 Cyclic voltammetry

Cyclic voltammetry was used to test the electrochemistry of tyrosine, TMP, TBP and tyrosine-histidine model compounds at the electrode surface, with the view to induce a stable radical species. Cyclic voltammetry is an electrochemical technique used to provide information on electrode kinetics (electron transfer rate constants, k^o), electrochemical midpoint potentials (E_m) and can also be used to study effects of different solvents on redox processes. Figure 2-26 shows the experimental setup.

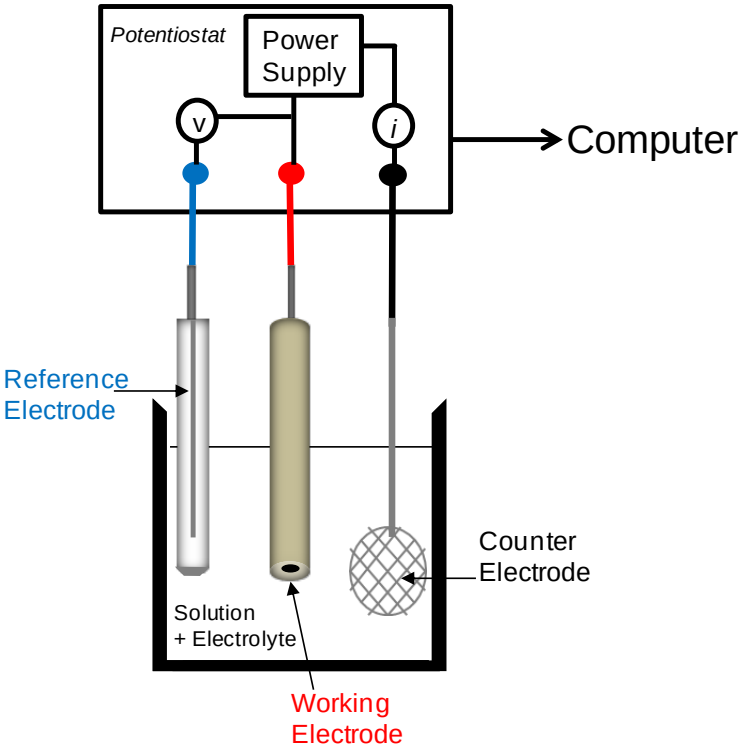

Figure 2-26. Electrochemical cell configuration for cyclic voltammetry.
Glassy carbon/platinum/gold/boron-doped-diamond were used as a working electrode. A platinum mesh counter and a Ag/AgCl/KCl reference electrode were used [182]. The working electrode is where the reaction will take place. The counter electrode completes the electrical circuit to allow current to flow at various potentials, whilst the potential at the working electrode is measured versus the reference electrode.

The current due to oxidation or reduction of a solution species, is measured as the potential of the working electrode (*versus* the reference electrode) is swept from one value, V_1, to another, V_2, before being swept in the reverse direction back to V_1, at a fixed scan rate [182]. The technique is carried out with a stationary solution and the resulting current depends on the rate of mass transport of substrate, via diffusion, to the working electrode surface and the k^o [182]. Figure 2-27 illustrates a typical cyclic voltammogram (CV) of a reversible 1-electron transfer reaction.

$$A_{(aq)} \rightleftharpoons B_{(aq)} + e^-_{(m)}$$

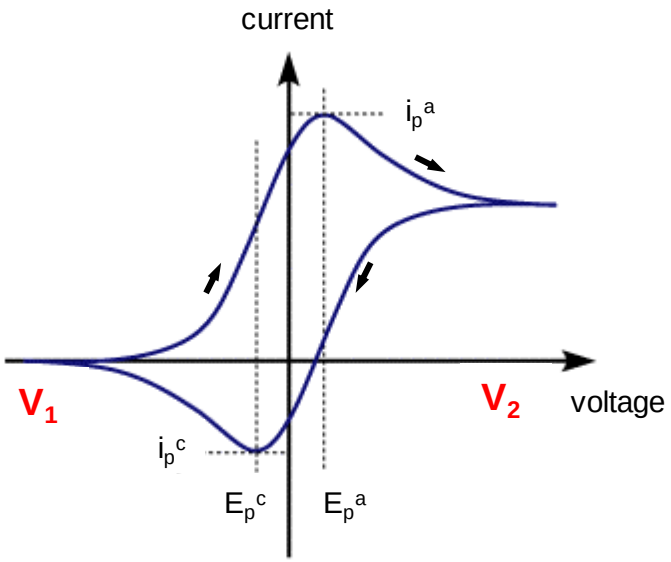

Figure 2-27. Cyclic voltammogram (CV) of a reversible 1-electron transfer reaction. *Anodic peak current (i_p^a), cathodic peak current (i_p^c), anodic peak potential (E_p^a), cathodic peak potential (E_p^c) are indicated.*

On the forward scan (V_1 to V_2), the increasing potential causes a current to increase as **A** is oxidised to give **B**, until the anodic peak current (i_p^a) is reached. At the peak, all of **A** at the electrode surface has been consumed and converted to **B**. Subsequently, the current falls, as the diffusion layer which **A** must travel through to reach the electrode surface from the bulk solution, becomes thicker. The measured current also becomes diffusion limited. Upon the reverse scan the product **B** is reduced to **A,** so the current flows in the opposite direction across the electrode, giving a cathodic peak current i_p^c [182].

The initial exponential increase in current with greater overpotentials can be rationalised with the Butler-Volmer equation, which describes how current varies exponentially with overpotential [182]. The rising current is influenced by the rate of electron transfer (k^o).

$$i = A\,F\,k^o \left([Red] \exp\left((1-\alpha)\,F\,(E-E_o) / RT \right) - [Ox] \exp\left(-\alpha\,F\,(E-E_o) / RT \right) \right)$$

i = current (amps), A = electrode surface area (m^2), k^o = standard rate constant, [Red] or [Ox] = reductant or oxidant concentration (M), α = transfer coefficient (normally 0.5), E= applied potential (V), E_o = standard potential (V), $E-E_o$ = overpotential, η (V), F = faradays constant 96485 C/mol, R = gas constant (8.314 J/K mol), T = temperature (K).

A reversible reaction is characterised as having a large k^o (fast electron transfer), and has a small activation energy. Oxidation and reduction peaks are observed at potentials just positive and negative of E_m. Overall the rising current is controlled by electrode kinetics (k^o) until the current falls where it is limited by the diffusion rate of **A**. The CV for a reversible 1-electron transfer reaction is defined by the following characteristics [183];

- *The peak separation is; $\Delta E = E^a_p - E^c_p$ = (59 mV /number of electrons transferred) at 25 ^oC.*
- *The peak positions are independent of scan rate (fast electrode kinetics).*
- *The peak current ratio is equal to 1; $I(i^a_p / i^c_p)I = 1$*
- *The midpoint potential is the midpoint of the oxidation and reduction peak potentials.*
- *The peak current is proportional to square root of scan rate, $i^a_p \alpha \sqrt{}$scan rate according to the following equation [182].*

$$i_p = (2.69x10^5)\, n^{3/2}\, A\, D^{1/2}\, C\, v^{1/2}$$

i_p = peak current (A), n = number of electrons transferred, A = electrode area (cm^2), D = diffusion coefficient (cm^2/s), C = concentration (mol/cm^3), v = scan rate (V/s)

For an irreversible electron transfer reaction, only a single peak is observed on the forward scan, as the product formed is no longer electroactive (see Figure 2-28, red). Another form of reaction is a quasi-reversible reaction where the peak current ratio is not equal to one (see Figure 2-28, green). Unlike the reversible reaction, where oxidation is only diffusion limited because the k^o is large, the irreversible and quasi-reversible reactions are limited by both diffusion and slow electron transfer (small k^o). Therefore, peaks are generally observed at greater overpotentials compared to reversible reactions. Greater overpotentials are required to overcome the large activation energy barrier. Furthermore, the peak separation varies with scan rate for quasi-reversible reactions, and it doesn't for a reversible reaction where the kinetics is fast. This is because the reaction equilibrium at the electrode surface cannot rapidly re-establish itself, to match the applied potentials during faster scan rates and so peaks begin to shift to greater overpotentials.

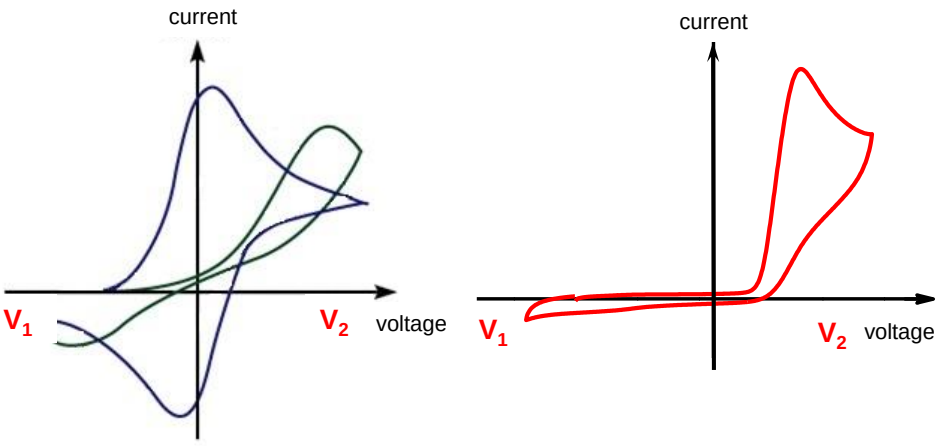

Figure 2-28. Example CVs of reversible (blue), quasi-reversible (green) and irreversible (red) electron transfer reactions.

2.22.1 Cyclic voltammetry measurements

A conventional three-electrode setup is illustrated in Figure 2-26. For a typical experiment, the working electrode was polished with 0.05 µm alumina paste and then in 0.3 µm alumina and rinsed thoroughly in dH_2O and dried. This removed adsorbed substances on the surface. Initially blank scans were recorded in a series of 3 consecutive scans, (typical scan, 0 V to +0.6 V to -0.2 V to 0 V) in a 5 mL solution. The blank buffer was replaced with one containing the dissolved compound, (~0.2 to 0.5 mM) from which 3 consecutive scans were recorded. The buffer conditions and the scan rates used are given in the Figure legends. A typical buffered solvent was 50 % (v/v) propan-2-ol 20 mM KPi, 500 mM KCl at pH 13.0 and scan rate was typically 0.1 V/s. All experiments were carried out at room temperature.

3 Separation and redox linkage of IR signatures of bovine cytochrome c oxidase

3.1 Introduction

<u>Author contributions:</u> all data and figures presented in this publication were measured and prepared by Raksha Dodia, the paper was written by Raksha Dodia with contributions from Amandine Maréchal and Peter R. Rich. Simona Bettini and Masayo Iwaki provided preliminary data upon which this project was extended. Additional spectra are also presented here.

Ligand-induced [102-105] and redox-induced [106,107,109,116] structural changes in C*c*O and related oxidases have been investigated using FTIR spectroscopy. Generally, this requires the averaging of many IR difference spectra that are accumulated by cycling between two defined states (provided they are reversible). Small IR signal changes of cofactors, functional amino acids and waters from the large overall background IR absorption, can be resolved in such averaged IR difference spectra [114].

Assignment of IR bands to specific ligands, cofactors, amino acids and water molecules, has been achieved with the combined use of: model compounds that provide reference spectra [184,185], or mutagenesis of specific residues [88,103], or introduction of isotopically labelled amino acids [186], or H/deuterium (D) exchange [104,187]. C*c*O contains four redox centres, Cu_A, haem *a*, haem a_3 and Cu_B. The association of observed structural changes to specific metal centre redox transitions has proved difficult since the metal centre redox titrations overlap and they have strong electrostatic interactions [115-117].

3.2 Aims

The aims of this project were to associate redox-induced IR changes observed in bovine C*c*O, with specific metal centre transitions by exploiting the mixed valence (MV) states of C*c*O ligated with either cyanide (CN) or carbon monoxide (CO). These states were produced by controlled electrochemistry, combined with ATR-FTIR spectroscopy, so that IR difference spectra associated with different redox transitions could be generated. In this manner, the redox-linked IR features, associated with haem a_3-CN, could be separated from those of Cu_A, haem *a*, and Cu_B [159,160], and those associated with haem *a* and Cu_A, could be separated from reduced haem a_3-CO and Cu_B [161]. The electrochemical potential scale shown in Figure 2-13 illustrates clearly the effect of the inhibitory ligands on the midpoint potential of the redox centres. The vibrational bands of the CN and CO ligands, are themselves sensitive to the redox states of the metal centres, and so were used to monitor the specific redox states being generated. In this chapter, bands appearing in the 1700-1000 cm^{-1} region of the IR spectrum are discussed. Changes in the protonated carboxylic acid (-COOH) region (1800-1700 cm^{-1}) are discussed in Chapter 4.

3.3 Results

3.3.1 Unligated CcO: FR – O difference spectra

Cu_A^{+}, a^{2+}, a_3^{2+}, Cu_B^{+} minus Cu_A^{2+}, a^{3+}, a_3^{3+}, Cu_B^{2+}

All experiments in this Results Chapter were carried out using purified bovine C*c*O as described in section 2.7 (Methods). Figure 3-1 shows the electrochemically-induced fully reduced (FR - Cu_A^{+}, haem a^{2+}, haem a_3^{2+}, Cu_B^{+}) *minus* oxidised (O - Cu_A^{2+}, haem a^{3+}, haem a_3^{3+}, Cu_B^{2+}) IR difference spectrum of unligated bovine C*c*O in the 1800-1000 cm^{-1} range. Positive signals arise from the FR state where all 4 redox centres are reduced (Cu_A^{+}, haem a^{2+}, haem a_3^{2+}, Cu_B^{+}), and negatives, from the fully oxidised state (Cu_A^{2+}, haem a^{3+}, haem a_3^{3+}, Cu_B^{2+}). The spectrum is dominated by amide I (primarily *v*(C=O), 1690-1610 cm^{-1} range) and amide II changes (primarily *v*(N-H) bond stretch; 1550-1500 cm^{-1} range) which arise from conformational changes in the protein backbone.

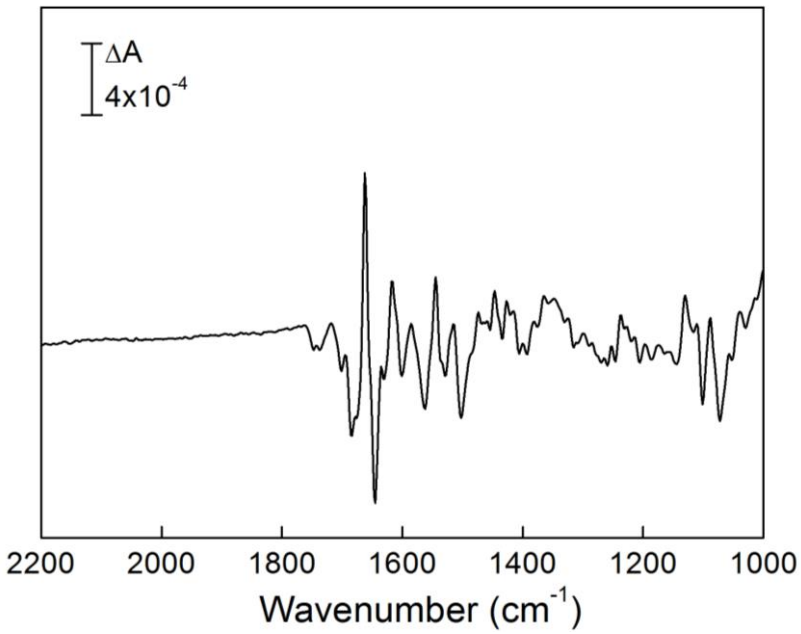

Figure 3-1. Electrochemically-induced FR minus O IR difference spectrum of unligated bovine CcO.
The buffer used was 0.1 M KPi, 0.1 M KCl pH 7 containing 50 µM benzyl viologen and 1 mM ferrocene methanol as redox mediators. The potentials applied for reduction and oxidation were -400 mV and +500 mV, respectively, with 30 mins equilibration in each direction. Each spectrum was generated from the average of 500 interferograms. The spectrum shown is an average of data from 20 redox cycles. This spectrum has been corrected for baseline changes caused by pH-induced phosphate changes, liquid water and water vapour variations. The spectrum has also been scaled x1.228 to the size of the ΔA_{II} in the absolute spectrum of Figure 3-5 so that its intensity is directly comparable to the other spectra shown in this chapter. All potentials are given versus the SHE.

3.3.2 CN-ligated CcO: MV-CN – O-CN difference spectra

(Cu_A^{+}, a^{2+}, a_3^{3+}-CN, Cu_B^{+} minus Cu_A^{2+}, a^{3+}, a_3^{3+}-CN, Cu_B^{2+})

The experiment was repeated in the presence of cyanide (CN) but the potentials applied were +500 mV and +80 mV, for oxidation and reduction, respectively. Figure 3-2 shows the MV-CN *minus* O-CN IR difference spectrum of CN-ligated bovine C*c*O. This spectrum shows the changes associated with the redox transition of all centres apart from haem a_3-CN, which remained oxidised at the reducing potential (+80 mV) of the experiment. CN stretching modes when bound to C*c*O in different redox states appear in the 2200-2000 cm^{-1} range. Their frequencies are characteristic of the redox state of C*c*O, and were used to monitor the redox transitions. CN bound to the fully O state has a *ν*(CN) at 2151 cm^{-1} [164]. This shifts to 2131 cm^{-1} in the MV state defined as Cu_A^{+}, a^{2+}, a_3^{3+}-CN, Cu_B^{+} [165] (see Table 3-1 in the discussion for assignment of CN bond stretches for each redox state). The appearance of a clear positive at 2131 cm^{-1} and a clear negative at 2151 cm^{-1} confirmed that this redox transition was taking place.

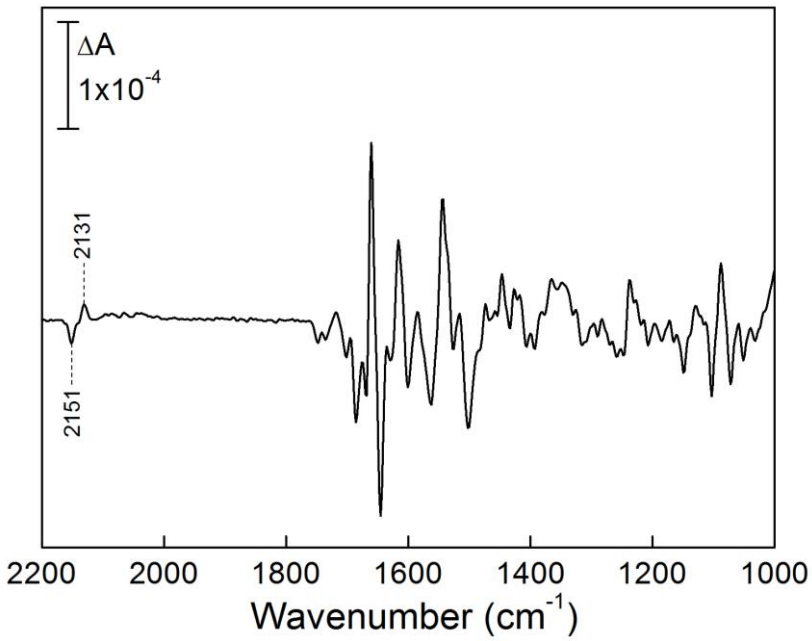

Figure 3-2. Electrochemically-induced MV-CN minus O-CN IR difference spectrum of bovine CcO.
The reaction conditions were the same as in Figure 3-1, with the addition of 10 mM KCN, 100 µM phenazine methosulphate and 50 µM 1,2-naphtoquinone sulphonate as redox mediators to the experiment buffer. The potentials applied were +500 mV and +80 mV for oxidation and reduction. The spectrum shown is an average of data from 49 redox cycles and was corrected for baseline changes caused by water vapour variations, and scaled x1.236 based on the ΔA_{II} in the absolute spectrum of Figure 3-5.

3.3.3 In situ visible spectra

Visible spectra were taken of the protein layer during the accumulation of redox cycles of the MV-CN *minus* O-CN IR difference spectra (Figure 3-2). These spectra were used to monitor sample quality and redox transitions, since they have been well characterised [188-191]. The MV-CN *minus* O-CN visible difference spectrum shows a positive at 606 nm of haem *a* redox transitions, this provided an additional control that ensured the enzyme was in the correct redox state (Figure 3-3).

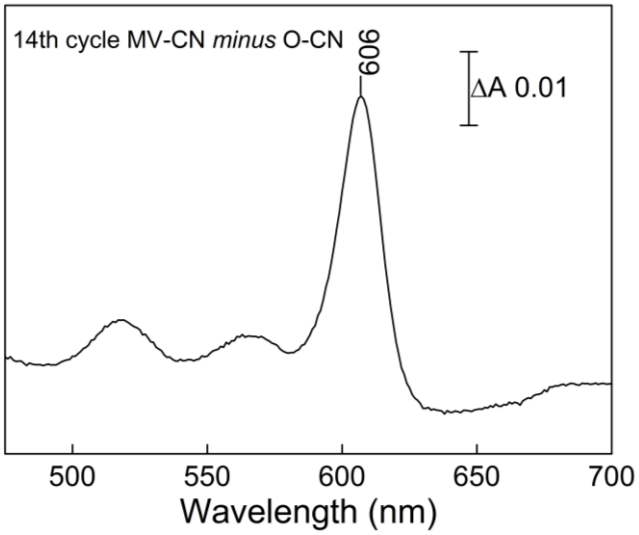

Figure 3-3. MV-CN minus O-CN visible difference spectrum of bovine CcO.
Visible difference spectra (475-700 nm) were measured of the protein layer simultaneously with accumulation of IR difference spectra for each experiment. This was achieved by the insertion of an fibre optic probe into the electrochemical device that was assembled above the layer. The spectrum has been scaled by the same factor as the IR difference spectrum (x1.236) so that it is comparable to the visible spectra in Figure 3-6.

3.3.4 CN-ligated CcO: FR-CN – O-CN difference spectra

(Cu_A^{+}, a^{2+}, a_3^{2+}-CN, Cu_B^{+} minus Cu_A^{2+}, a^{3+}, a_3^{3+}-CN, Cu_B^{2+})

The experiment with CN ligated C*c*O was repeated using -400 mV and +500 mV potentials for full reduction and full oxidation in order to generate a FR-CN *minus* O-CN IR difference spectrum, which should include redox transitions of all redox centres with CN bound to haem a_3. In this case the ν(CN) characteristic of the FR state is expected to give two bands at 2058 cm^{-1} and 2040 cm^{-1} [90] (Table 3-1). However, when measuring this FR-CN *minus* O-CN IR difference spectrum, there was a CN band at 2131 cm^{-1} after reduction (-400 mV), indicative of a small amount of the MV-CN state remaining (Figure 3-4-top blue trace). Even with longer equilibration times of 1 h it was not possible to fully reduce this MV-CN state to give FR-CN. Figure 3-4 shows how this contribution was instead iteratively subtracted by using the MV-CN *minus* O-CN IR difference spectrum shown in Figure 3-2.

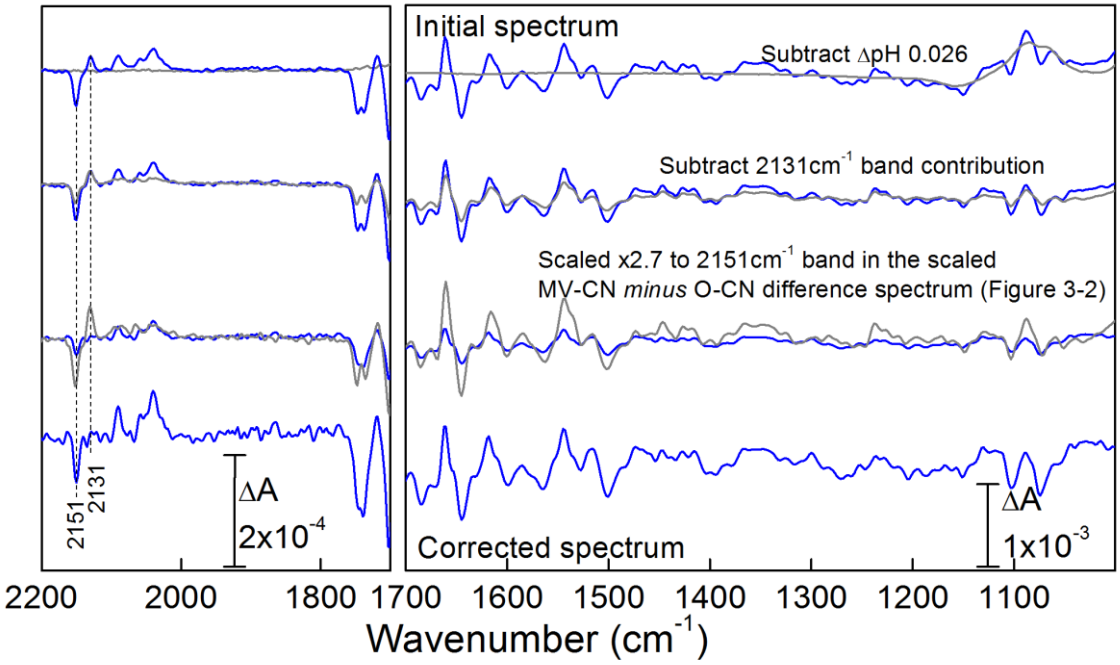

Figure 3-4. Correction of the electrochemically-induced FR-CN minus O-CN IR difference spectrum of bovine CcO.
Spectra shown in grey were used for subtraction or scaling. After correction of pH-induced phosphate changes, the MV contribution at 2131 cm^{-1} was subtracted using a fraction (x0.5) of MV-CN minus O-CN difference spectrum, then scaled x2.7 according to the size of the fully oxidised 2151 cm^{-1} band of the actual scaled MV-CN minus O-CN difference spectrum shown in Figure 3-2. Left: expansion of the cyanide and carboxylic acid region, 2200-1700 cm^{-1}.

Figure 3-5 shows the final corrected FR-CN *minus* O-CN IR difference spectrum after iterative subtraction of IR contributions from the MV-CN state. Two clear positives at 2058 cm^{-1} and 2040 cm^{-1} can be observed of the FR-CN state, and a clear negative at 2151 cm^{-1} of the O-CN, confirming the spectrum was of the full redox reaction. Note, a band at 2090 cm^{-1} also appeared upon reduction, but its identity is not fully understood (see discussion and Table 3-1) [90,164,192].

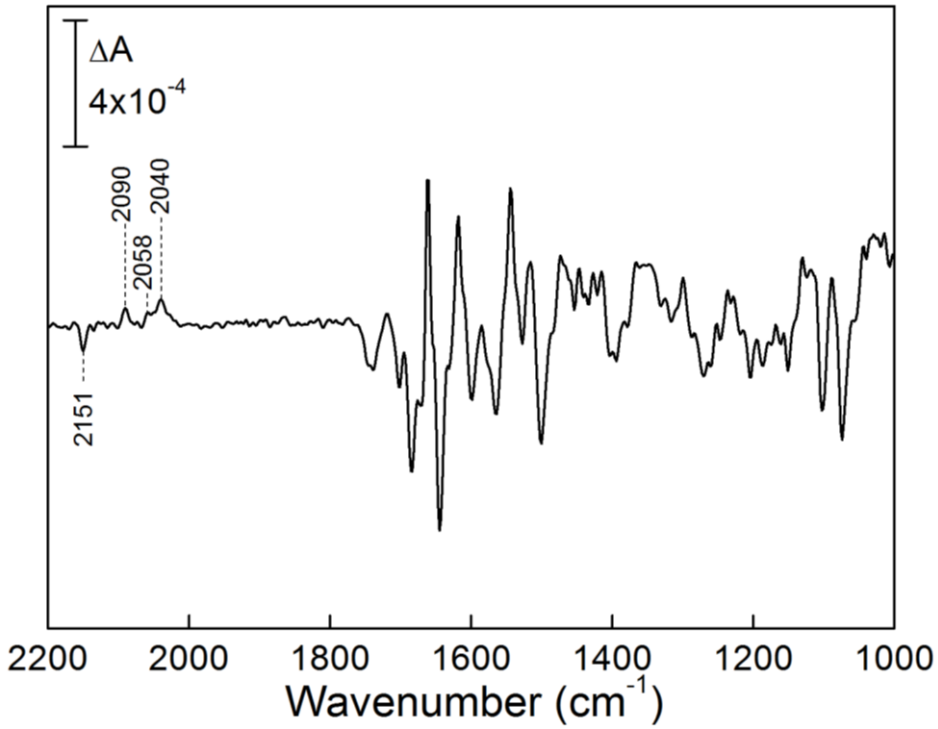

Figure 3-5. Electrochemically-induced FR-CN minus O-CN IR difference spectrum of bovine CcO.
The reaction conditions were the same as in Figure 3-1, with the addition of 10 mM KCN, 100 µM phenazine methosulphate and 50 µM 1,2-naphtoquinone sulphonate as redox mediators to the experiment buffer but the potentials applied were -400 mV and +500 mV. The spectrum shown is an average of data from 23 redox cycles. It has been corrected for baseline changes caused by pH-induced phosphate changes and water vapour variations. See Figure 3-4 for details on how this spectrum was corrected and then scaled. All spectra in this chapter have been scaled based on the ΔA_{II} intensity measured in the absolute absorbance spectrum of this experiment (a measure of total protein). This allowed intensity of all spectra to be directly comparable.

3.3.5 In situ visible spectra of unligated and CN-ligated CcO

In situ visible reduced *minus* oxidised difference spectra of CN-ligated (blue trace) and unligated C*c*O (black trace) are shown in Figure 3-6. The positive at 605 nm of unligated C*c*O is of reduced haems *a* and a_3, this positive is expected to shift to 600 nm in CN-ligated C*c*O of reduced haems *a* and a_3-CN [188-190]. However it was observed at 606 nm this can be explained by a smaller than expected contribution of haem a_3^{2+}-CN at its expected wavelength 590 nm [190] because full reduction was not achieved in this experiment as described above.

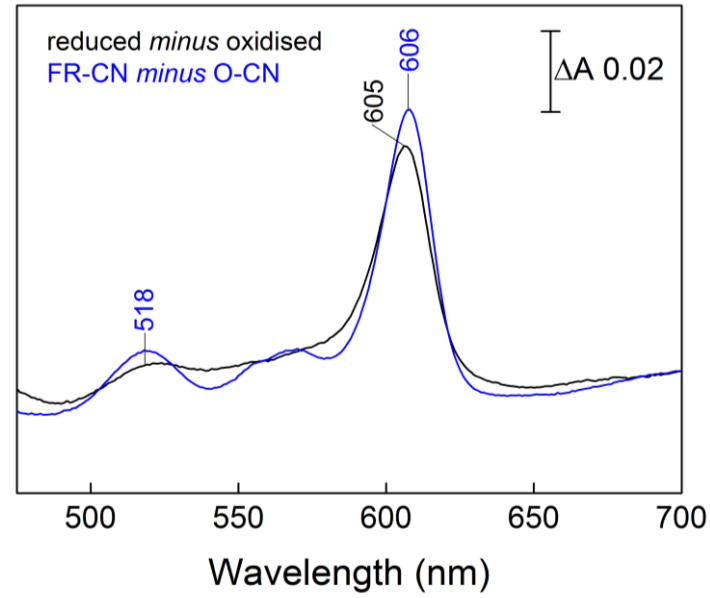

Figure 3-6. Reduced minus oxidised (black) and FR-CN minus O-CN (blue) visible difference spectra of bovine CcO.
Visible difference spectra (475-700 nm) were measured of the protein layer simultaneously with accumulation of IR difference spectra of Figure 3-1 and Figure 3-5. This was achieved by the insertion of an optic probe into the electrochemical device that was assembled above the layer. The black trace has been scaled by the same factor as the IR difference spectrum (x1.228) so it is comparable to the blue trace.

3.3.6 CN-ligated CcO: FR-CN – MV-CN difference spectra

(Cu_A^+, a^{2+}, a_3^{2+}-CN, Cu_B^+ minus Cu_A^+, a^{2+}, a_3^{3+}-CN, Cu_B^+)

Figure 3-7 shows the FR-CN *minus* MV-CN difference spectrum, calculated as the (FR-CN *minus* O-CN) *minus* (MV-CN *minus* O-CN) IR double difference spectrum of CN-ligated bovine C*c*O. This shows the changes associated specifically with the redox transition of only haem a_3-CN. This spectrum could not be generated experimentally because once FR-CN was formed; the transition to the MV-CN state could not be induced, at an intermediate potential of +80 mV, even when it was applied for 1 h. The negative at 2131 cm^{-1} and the pair of positives at 2058 cm^{-1} and 2040 cm^{-1} confirm that the spectrum is of the redox transition between the MV-CN and FR-CN states respectively.

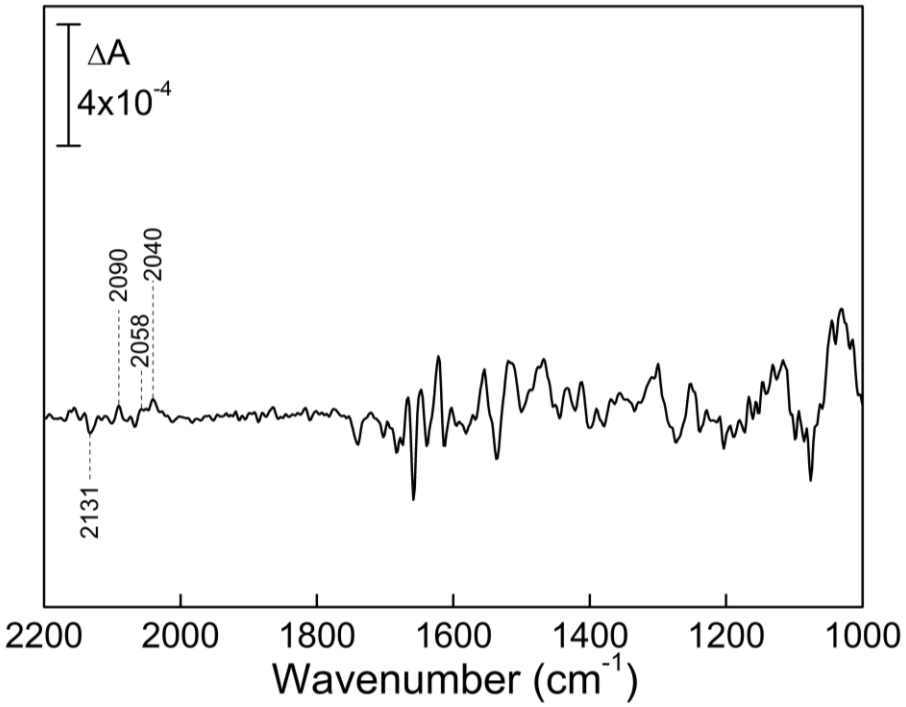

Figure 3-7. Calculated FR-CN minus MV-CN IR double difference spectrum of bovine CcO.
The spectrum was calculated by the direct subtraction of the (FR-CN minus O-CN) minus (MV-CN minus O-CN) from Figure 3-5 and Figure 3-2, respectively, which had been scaled according to the 2151 cm^{-1} band.

3.3.7 CN ligation to CcO: O-CN minus O spectra

(Cu_A^{2+}, a^{3+}, a_3^{3+}-CN, Cu_B^{2+} minus Cu_A^{2+}, a^{3+}, a_3^{3+}, Cu_B^{2+})

Figure 3-8 shows a perfusion-induced CN-ligated *versus* an unligated baseline spectrum of O state bovine C*c*O. The affinity of haem a_3 for CN in the FR state is low (K_d 0.7 mM at pH 7.4) [193] compared to the O state (K_d 0.092 mM at pH 7.4) [194]. Therefore, in order to confirm that the IR changes in the FR-CN *minus* MV-CN difference spectrum were not arising from the re-binding of CN to the MV-CN state and unbinding from the lower affinity FR state, a perfusion induced CN binding spectrum to the O state was recorded. The overall features of this CN binding spectrum are clearly different to, and absent from, those in the electrochemically-induced difference spectra of CN-ligated C*c*O. Furthermore, it was not possible to dissociate CN from the FR-CN state with 3 mM sodium dithionite perfusion. Hence, it can be concluded that cyanide remains bound to all redox states in the above experiments and the IR bands observed in the FR-CN *minus* MV-CN spectrum were not induced from binding changes.

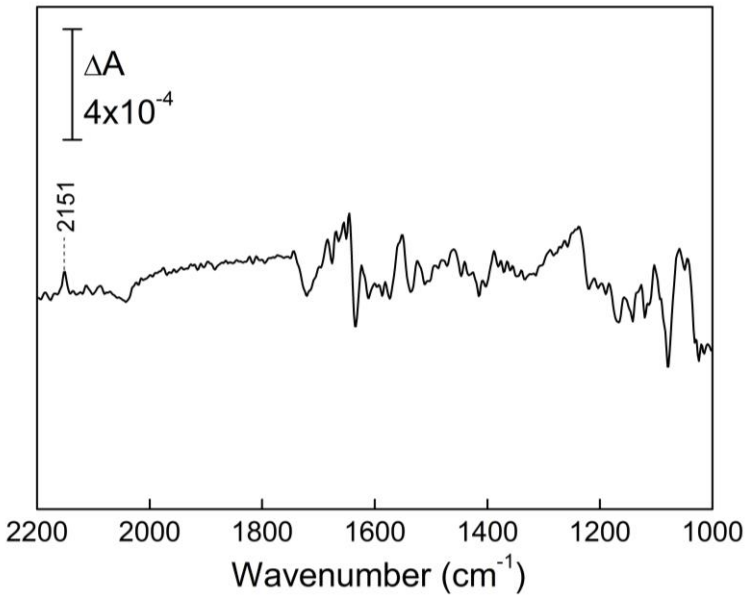

Figure 3-8. Perfusion-induced ligated O-CN minus unligated O spectrum of bovine CcO. *The buffer used was 0.1 M KPi, 0.1 M KCl pH 7. The protein layer was perfused with 3 mM dithionite, followed by 20 µM potassium ferricyanide to ensure all CcO was in the fast oxidised unligated form. An O state baseline (accumulation of 1000 interferograms) was taken before perfusion with 20 µM potassium ferricyanide and 2 mM KCN to record the O-CN spectrum vs. O baseline. The spectrum shown is an average of data (accumulation of 8000 interferograms) from 2 protein layers. This spectrum was normalised based on the size of 2151 cm^{-1} in Figure 3-2. This spectrum has been corrected for baseline changes caused by protein layer changes induced by layer expansion/contraction, 0.6 mM KPi pH 7.0, liquid water and water vapour variations.*

3.3.8 Visible spectrum of CN ligation

Binding and unbinding of CN in the electrochemical experiments was ruled out with the IR data presented above, and this was further confirmed by visible spectroscopy. Firstly, a visible difference spectrum of O-CN *minus* O was recorded that was consistent with [191] (Figure 3-9). This spectrum was measured using an electrochemical cell with an oxidative potential of +500 mV. A baseline was recorded of the unligated O-state and the buffer was replaced with one containing 10 mM KCN. More importantly, it is clear that the CN binding spectrum to haem a_3 in fully oxidised C*c*O can be clearly distinguished by the presence of two positives at 544 nm and 588 nm and negative at 645 nm that are characteristic of CN ligation [195]. These features are absent from the experimental redox spectra of CN-bound C*c*O and hence the binding and unbinding of CN to the oxidised high affinity state during the accumulation of IR redox spectra can be ruled out.

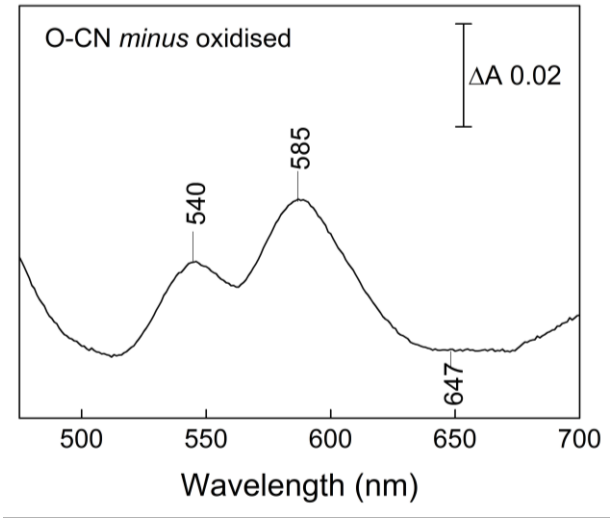

Figure 3-9. CN-ligated minus O visible difference spectrum of bovine CcO.
Visible difference spectra (475-700 nm) induced by binding of cyanide were measured with a fresh protein layer. This was achieved by assembly of an electrochemical device above the protein layer with an applied potential of +500 mV and addition of 10 mM KCN to induce binding. The spectrum has not been scaled and so cannot be compared quantitatively with other spectra in this report.

3.3.9 CO-ligated CcO: FR-CO – MV-CO spectra

(Cu_A^+, a^{2+}, a_3^{2+}-CO, Cu_B^+ minus Cu_A^{2+}, a^{3+}, a_3^{2+}-CO, Cu_B^+)

Figure 3-10 shows the FR-CO *minus* MV-CO IR spectrum of CO-ligated bovine C*c*O. This spectrum is associated with the redox transitions of only Cu_A and haem *a* while the CO-ligated BNC remained reduced. The symmetrical peak/trough at 1961/1967 cm^{-1}, results from the upshift of the ligated CO band by the FR-CO/MV-CO redox transition [102,104]. Note that *in situ* visible spectra could not be measured since the electrochemical device was one with a glassy carbon working electrode that did not permit insertion of a fibre optic probe. A platinum mesh working electrode was used for all other data presented in this chapter. The working electrode material used made no difference to the reaction monitored.

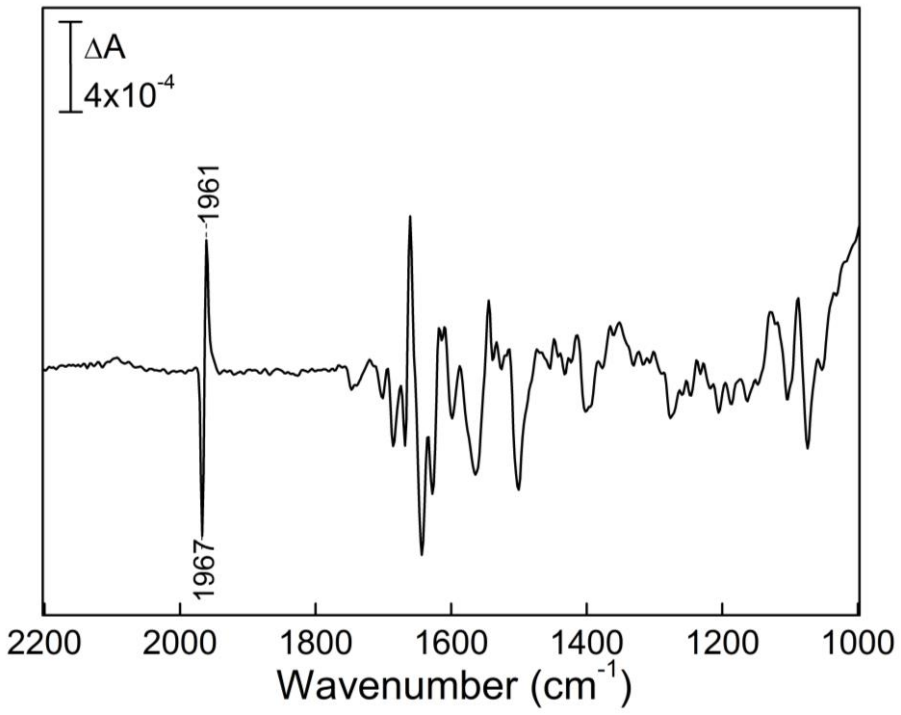

Figure 3-10. Electrochemically-induced FR-CO minus MV-CO IR spectrum of bovine CcO. *The experimental buffer was the same as in Figure 3-1. The equilibration time for reduction was 30 mins, and for oxidation was 4 mins. Each spectrum was generated from the average of 1000 interferograms and is an average of data from 16 redox cycles. The spectrum has been corrected for baseline changes caused by pH changes, liquid water and water vapour variations. The intensity of ΔA_{II} in the absolute spectrum (not shown) was normalised to the absolute spectrum of Figure 3-5.*

3.3.10 CN-ligated and CO-ligated CcO: calculated (MV-CN – O-CN) minus (FR-CO - MV-CO) double difference spectra

(Cu_B^+ minus Cu_B^{2+})

Figure 3-11 shows a Cu_B^+ *minus* Cu_B^{2+} difference spectrum of bovine C*c*O, this is derived by the subtraction of (FR-CO - MV-CO) IR difference spectrum which shows IR changes associated with transitions of two metal centres Cu_A and haem *a* from the MV-CN - O-CN IR difference spectrum which shows IR changes associated with transitions of the same metal centres as well as Cu_B. Hence this spectrum should show IR changes associated with redox transitions of only Cu_B. However, the spectrum is complicated as it is overlapped by positives associated with a_3^{3+}-CN and a_3^{2+}-CO from the MV states, and negatives associated with a_3^{3+}-CN from the O state and a_3^{2+}-CO from the FR-state. Therefore, it is possible that there will be IR bands associated with CN-ligated C*c*O in each direction and with CO-ligated C*c*O, and they may not give a perfect subtraction.

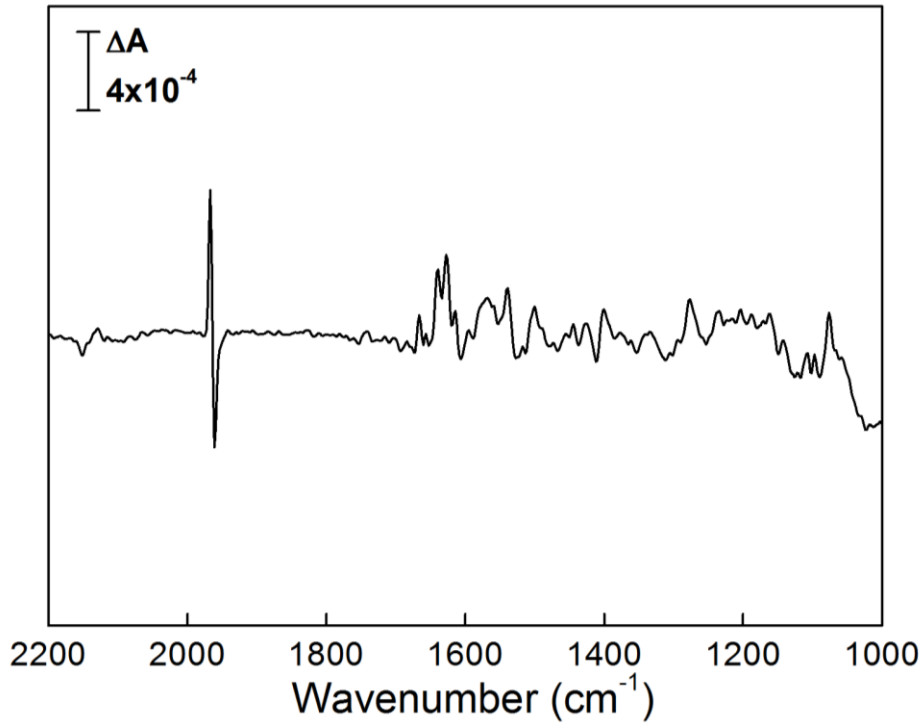

Figure 3-11. Calculated Cu_B^+ minus Cu_B^{2+} IR double difference spectrum of bovine CcO. *Spectrum was calculated by the following direct subtraction; (MV-CN – O-CN) minus (FR-CO - MV-CO) from Figure 3-2 and Figure 3-10, respectively which were scaled according to the ΔA_{II} intensity of their absolute IR spectra.*

3.3.11 Comparison of all redox difference spectra

Figure 3-12 shows a summary of all IR difference spectra recorded or calculated.

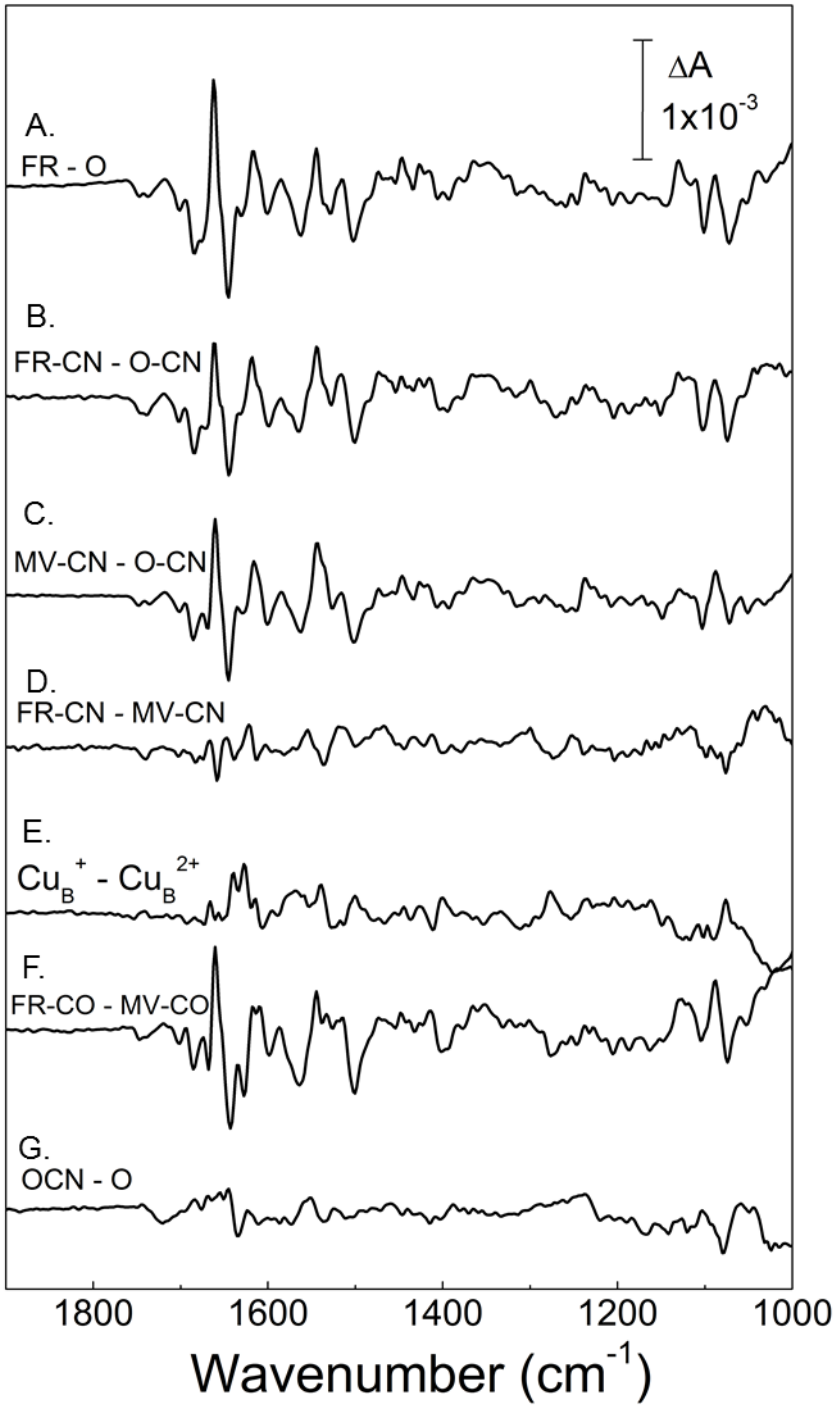

Figure 3-12. Summary of all IR difference spectra of bovine CcO presented in this chapter.
Trace A is from Figure 3-1, Trace B is from Figure 3-5; Trace C is from Figure 3-2; Trace D is from Figure 3-7; Trace E is from Figure 3-11; Trace F is from Figure 3-10; Trace G is from Figure 3-8.

3.3.12 Assigning IR changes in the 1700-1000 cm^{-1} range with specific metal centre redox transitions

Assignment of IR changes to specific metal centre transitions were made based on the IR difference spectra that were experimentally measured. These were the FR *minus* O difference spectrum of unligated C*c*O, the MV-CN *minus* O-CN difference spectrum and the FR-CO *minus* MV-CO difference spectrum, and are shown in Figure 3-13. The derived spectrum of FR-CN *minus* MV-CN was used to support assignment of IR changes linked to haem a_3 changes. The 1700-1000 cm^{-1} range of the IR difference spectra show various protein and haem spectral changes, associated with transitions of specific redox centres (Cu_A, *a*, a_3 and Cu_B).

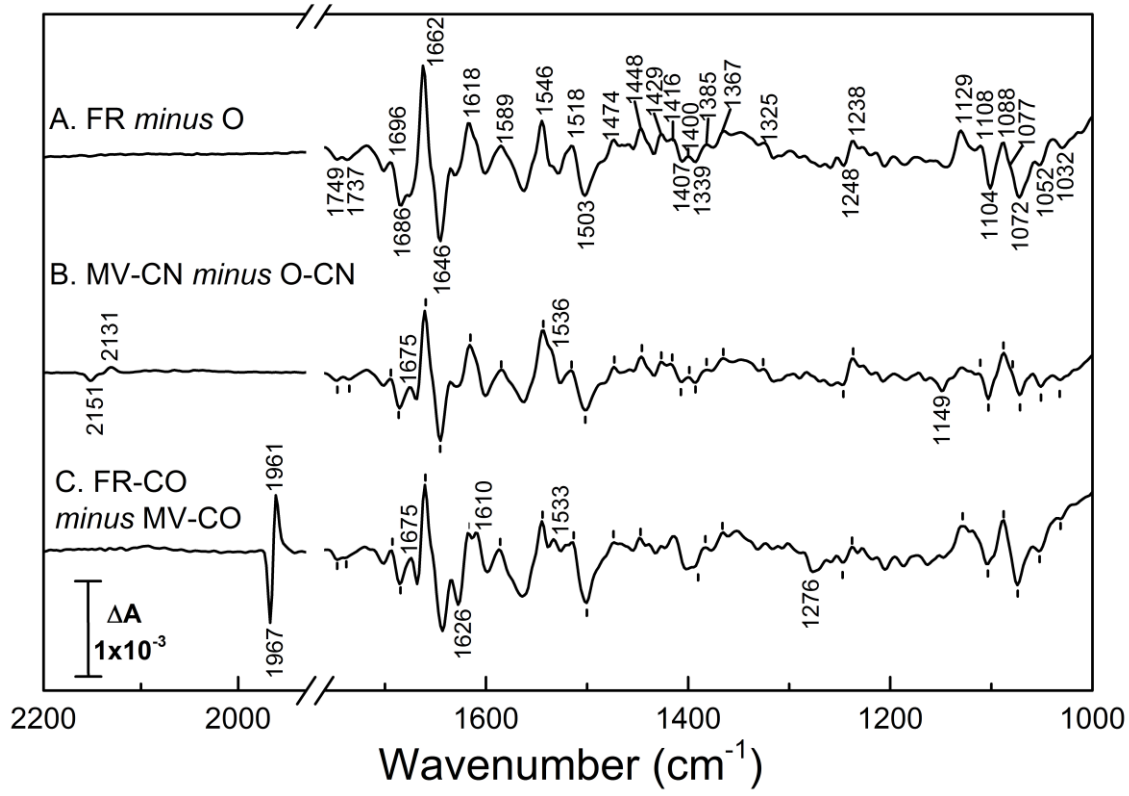

Figure 3-13. Electrochemically-induced ATR-FTIR difference spectra of bovine CcO.
A. FR minus O IR difference spectrum of unligated CcO; B. MV-CN minus O-CN IR difference spectrum; C. FR-CO minus MV-CO IR difference spectrum. Spectra are taken from Figure 3-1, Figure 3-2 and Figure 3-10 respectively. Band positions identical with those labelled in A are indicated with short vertical lines. Figure adapted from [158].

3.4 Discussion

3.4.1 FR minus O IR difference spectrum of unligated bovine CcO

The FR *minus* O IR difference spectrum of unligated C*c*O is consistent with published data (Figure 3-13A) [104,196,197]. It consists of the combined redox induced IR changes of C*c*O when all four centres are reduced and oxidised. The positive features are associated with the FR state in which all four redox centres are reduced (Cu_A^{+}, a^{2+}, Cu_B^{+}, a_3^{2+}), and negatives with the fully oxidized O state (Cu_A^{2+}, a^{3+}, Cu_B^{2+}, a_3^{3+}). The spectrum is dominated by amide I shifts (primarily C=O bond stretches) in the 1690–1600 cm^{-1} range, which arise from conformational and environmental changes in the polypeptide backbone, and changes in the 1550–1500 cm^{-1} range that arise from haem and amide II changes. A wide range of additional smaller changes in the 1800–1000 cm^{-1} range arise from individual amino acids and the redox cofactors themselves. Full separation of the redox transitions of the metal centres cannot be achieved electrochemically since they have strong electrostatic interactions and their redox potentials overlap. The strongest interaction is between the two haem groups. The midpoint potentials were originally designated as +220 mV haem *a* and +380 mV for haem a_3 [198]. However, the interaction is such that the reduction of haem a_3 will lower the midpoint potential of haem *a*, and when haem a_3 is oxidised the midpoint potential of haem *a* will be raised [199,200]. Additionally, the interaction of Cu_A and Cu_B with haem *a* was also shown to influence the haem *a* redox potential and *vice versa* in CN-ligated C*c*O [159]. Therefore the midpoint potentials of each metal centre cannot be defined by a single value in unligated C*c*O but fall into a range of +380 mV to +220 mV [159,160,201]. In this project, this was overcome by ligation of inhibitors cyanide (CN) and carbon monoxide (CO) to the BNC, as they allowed the midpoint potentials to be separated and so stable mixed valence states of C*c*O could be electrochemically generated.

3.4.2 Monitoring redox changes associated with CN-ligated bovine CcO

Bound CN lowers the E_{m7} of haem a_3 such that potentials as low as -400 mV to -500 mV are required to reduce it, whilst the E_{m7} of the other redox centres remain unaffected [159,160]. Therefore, with the use of intermediate potentials (+80 mV) it was possible to separate the redox transition of haem a_3-CN from all other redox centres and *vice versa*.

In situ visible difference spectra already provided an additional control of monitoring redox transitions as these spectra have been well characterised [188-191]. However spectra were only monitored in the 475-700 nm range. It was not possible to include the Soret region, where absorption contributions of haem *a* and a_3 are more pronounced, because of the configuration and frequency limits of the visible spectrometer at the time. Nevertheless the α band is well characterised, and based on this, the unligated redox spectrum (Figure 3-6, black trace) was consistent with literature and exhibited a positive at 605 nm with haem *a* reported to contribute ~70 % at ~605-603 nm to the total absorption and haem a_3 ~30 % at ~605-603 nm [188,189]. The position of the α band in the FR-CN *minus* O-CN visible difference spectrum was expected at ~600 nm, however it was observed at 607 nm, (Figure 3-6, blue trace) this can be explained by a smaller than expected contribution of haem a_3^{2+}-CN at 590 nm [188-190]. This is consistent with the IR difference spectrum where 100 % reduction of O-CN was not achieved and contained a proportion of MV-CN (see Figure 3-4). It is well known that the reduction of O-CN to FR-CN is difficult, with full conversion only being achieved by prolonged incubation in sodium dithionite [164,188]. It is possible that with the redox potential of haem *a* being greater than haem a_3-CN, it prevented haem a_3-CN reduction by blocking electron transfer, an effect that cannot be overcome by applying more negative potentials. Furthermore, once FR-CN was formed, the transition to the MV-CN state could not be induced at an intermediate potential of +80 mV (Figure 3-7). A possible explanation could be that haem a_3 oxidation is similarly blocked, this is because Cu_A and haem *a* are reduced and they must be oxidised first to allow for haem a_3 to be oxidised, and this would not be possible at +80 mV. The visible spectrum of MV-CN *minus* O-CN (Figure 3-3), was consistent with literature showing α and β band contributions associated with only haem *a* at 607 nm and 518 nm, respectively [188,189].

The vibrational bands of ligated CN (Figure 3-2, Figure 3-4 and Figure 3-7) are themselves sensitive to the redox states of the metal centres and, in addition to *in situ* visible difference spectra (Figure 3-3 and Figure 3-6), these bands provide additional markers to monitor which redox transitions are occurring in CN ligated C*c*O. Their assignments are shown in Table 3-1. The 2090 cm^{-1} band of FR-CN is not well understood [90,192]. Free HCN (pK_a 9.3 [202]) absorbs at 2093 cm^{-1}. CN photolysis studies in D_2O media [90] have been used to test whether a similar band arose from HCN; however the band remained at 2090 cm^{-1}, whereas free DCN absorbs at 1887 cm^{-1} [192]. An alternative assignment of the 2090 cm^{-1} band is of a population of C*c*O, where CN is bound to Cu_B^+, in the FR state, at high CN concentrations [90,164]. Hence, in the future lower concentrations could be tested.

Table 3-1. The assignment of the vibrational modes of CN ligated to bovine CcO.

CN v(cm^{-1})	***Oxidation State of CN-ligated CcO***	***Assignment***	***Reference***
2151	*O*	*Bridged a_3^{3+}-CN- - -Cu_B^{2+}*	[164]
2131	*MV*	*Bridged a_3^{3+}-CN- - -Cu_B^{+}*	[165]
		Broken bridge a_3^{3+}-CN Cu_B^{+}	[164]
2090	*FR*	*Free HCN or Cu_B^{+}-CN*	[164]
2058,2040	*FR*	*Mixed populations of a_3^{2+}-CN*	[90]

3.4.3 IR changes associated with CO-ligated bovine CcO

CO holds haem a_3 and Cu_B in their reduced states [161], enabling the separation of redox transitions of Cu_A and haem *a* from those of the BNC metals (Figure 3-13C). Once again the vibrational bands of the ligated CO are themselves sensitive to the redox transition of Cu_A and haem *a*, and so were used to monitor the redox transitions. In this case, the FR to MV transition was coupled with an upshift of the CO stretching mode, which gave a symmetrical peak/trough, 1961(FR state)/1967(MV) cm^{-1}, that was consistent with a previously reported spectrum of this transition [104]. The band shift was the result of electrostatic changes sensed by CO in its environment caused by the redox transitions of haem *a*.

3.4.4 Assigning IR changes in the 1700-1000 cm^{-1} range with specific metal centre redox transitions

The overall redox spectra of *Paraccocus denitrificans* and bovine C*c*Os are broadly similar [117,196]. Gorbikova, *et al.* [117] reported the linkage of IR bands to distinct metal centre transitions of bacterial *Paraccocus denitrificans* C*c*O. This was achieved by following IR changes as the potential was increased in +40 mV intervals starting from the FR state to the O state. The IR features were separated based on their redox titration curves. To aid comparison a table is reproduced here that shows the metal centre transitions to which they were assigned (Table 3-2). These IR features have been compared to the bovine C*c*O IR difference spectra presented here, namely FR-CN *minus* MV-CN, FR-CO *minus* MV-CO and Cu_B^{+} *minus* Cu_B^{2+}. The table shows that approximately half of the assignments disagree with those observed here and in most cases their IR bands are induced by a combination of metal centre transitions. Assignments highlighted in light grey were in agreement with the bovine C*c*O. Majority of the linkages in the 1400-1030 cm^{-1} were ascribed to Cu_B. However, here those IR features are linked with Cu_A and haem *a*, whilst it is clear from the calculated Cu_B^{+}

minus Cu_B^{2+} IR difference spectrum that IR contributions linked with this transition are few and small in intensity (Figure 3-11). This discrepancy is most likely due to the method adopted by [117] where E_m ranges of haem *a* and a_3 are overlapping in unligated C*c*O and this would complicate the interpretation of the resulting IR spectra.

Table 3-2. Comparison of IR bands assigned to specific redox centre transitions of Paraccocus denitrificans CcO [117], with bovine CcO data from Figure 3-10 (Cu_A and haem a redox transitions), Figure 3-7 (haem a_3) and Figure 3-11 (Cu_B).

Assignments highlighted in light grey are in agreement, those left clear do not agree, and those highlighted in dark grey show no band in the bovine CcO spectra recorded.

Literature Values of *Paraccocus denitrificans* C*c*O [117]			Bovine C*c*O
Band position (cm^{-1})	Redox state	Redox centre	Redox centre linkage
1746	ox	*a*	(Cu_A or *a*)
1737	red	*a*	(Cu_A or *a*)
1689	ox	Cu_A	(Cu_A or *a*)
1684	red	Cu_A	no band
1674	ox	a_3 complex band	a_3 (red)
1661	red	*a*	(Cu_A or *a*)
1655	ox	a_3	a_3
1651	red	Cu_A	(Cu_A or *a*) a_3
1641	ox	a_3	(Cu_A or *a*) (ox), a_3 (ox), Cu_B (red)
1630	red	a_3	Cu_B
1618	red	a_3	(Cu_A or *a*)
1603	red	Cu_A	(Cu_A or *a*) (ox), a_3 (red)
1592	ox	Cu_A	no band
1561	ox	a_3	(Cu_A or *a*)
1546	red	*a*	(Cu_A or *a*)
1537	ox	*a*	Cu_B (red), (Cu_A or *a*) (red)
1526	red	a_3	a_3 (ox), Cu_B (ox)
1510	red	Cu_A	(Cu_A or *a*), a_3
1489	red	Cu_B	a_3, Cu_B
1483	ox	Cu_B	(Cu_A or *a*), Cu_B
1473	red	a_3	(Cu_A or *a*), a_3
1468	ox	Cu_A	a_3 (red), Cu_B (ox)
1455	ox	Cu_B	(Cu_A or *a*), Cu_B (red)
1431	ox	Cu_A	(Cu_A or *a*)
1419	red	Cu_A	(Cu_A or *a*)
1407	red	Cu_A	(Cu_A or *a*), a_3
1389	ox	*a*	(Cu_A or *a*)
1354	red	a_3	(Cu_A or *a*), a_3, Cu_B
1332	ox	Cu_B	(Cu_A or *a*), Cu_B (red)
1321	red	Cu_B	(Cu_A or *a*)
1308	ox	Cu_B	(Cu_A or *a*), a_3 (red), Cu_B
1250	red	Cu_B	a_3, Cu_B (ox)
1151	red	*a*	(Cu_A or *a*) (ox)
1128	red	Cu_B	(Cu_A or *a*), Cu_B (ox)
1105	ox	Cu_B	(Cu_A or *a*)
1032	ox	Cu_B	(Cu_A or *a*)

A smaller set of more definitive assignments is presented in Table 3-3, based on the IR frequencies that are labelled in Figure 3-13. Here, assignments were based on those spectra that were generated experimentally, namely the MV-CN *minus* O-CN IR difference spectrum (showing transitions in Cu_A, haem *a*, and Cu_B) and the FR-CO *minus* MV-CO IR difference spectrum (showing transitions in Cu_A and haem *a*). The derived spectra showing changes in only haem a_3 (FR-CN *minus* MV-CN, Figure 3-7) was used to confirm haem a_3 linkages of IR bands. Therefore the summarised redox centre linkages could be made with confidence without complex separation of redox spectra based on redox titration curves.

Table 3-3. Redox linkages of principal bands of bovine CcO redox difference spectra
Band positions are taken from Figure 3-13. Redox centre linkage of bands refers to the metal centres whose redox change induces the vibrational band change. Adapted from [158].

Band positions (cm^{-1}) (+) reduced, (-) oxidised	Redox centre linkage
2151 (-) / 2131 (+)	Cu_A, *a*, Cu_B
1967(-) / 1961(+)	Cu_A, *a*
1749 (-)	Cu_A, *a*
1737 (-)	Cu_A, *a*
1696 (+) / 1686 (-)	Cu_A, *a*
~1670 (+ shoulder)	a_3
1662 (+) / 1646 (-)	Cu_A, *a*
1626 (-) / 1610 (+)	Cu_A, *a*
1618 (+)	Cu_A, *a*
1589 (+)	Cu_A, *a*
1546 (+),1518 (+) / 1503 (-)	Cu_A, *a*
1536 (+ shoulder)	Cu_A, *a,* Cu_B
1533 (+)	Cu_A, *a*
1490-1120	Mostly Cu_A, *a*
1276 (-)	Cu_A, *a*
1400 (+)	Possible Cu_B
1149 (-)	Cu_A, *a*
1108 (+)	Possible a_3
1104 (-)	Cu_A, *a*
1072 (-)	Cu_A, *a*
1052 (-), 1032 (-)	Cu_A, *a*

It is clear that most of the redox induced IR changes are linked with redox transitions in Cu_A and haem *a*. In particular, the amide I protein backbone related changes at 1696 (+) / 1686 (-) cm^{-1} and 1662 (+) / 1646 (-) cm^{-1} are linked with Cu_A and haem *a*. This suggests the amide I related structural changes surrounding the Cu_A and haem *a* region are more sensitive and flexible to re dox changes than the structure surrounding the BNC of the protein. This finding may provide a functional significance for the residues close to Cu_A and haem *a*. The nearby H channel could be a candidate of such changes, whose role is either to provide a hydrophilic pathway for translocated protons, or act as a dielectric channel (see Chapter 6).

3.5 Conclusions

In conclusion, controlled electrochemistry has been used to induce redox transitions in C*c*O. By combining controlled electrochemistry with CO- and CN-ligated C*c*O the redox transitions of metal centres were separated allowing stable MV states of C*c*O to be generated. The IR bands of CN and CO bound to C*c*O were characteristic of the redox state of C*c*O, and confirmed reactions were being monitored. Alongside IR bands of CO and CN, *in situ* visible spectroscopy provided an additional control of the reaction taking place. This enabled the definitive separation and redox-linkage of redox induced IR bands to specific metal centres. Although it was not possible to separate the redox transitions of Cu_A and haem *a*, it was clear that majority of the IR changes were induced by redox transitions in both of these centres. The intensities of those IR changes were larger than those fewer IR changes observed by transitions in haem a_3 and of Cu_B. The linkages reveal the environment surrounding Cu_A and haem *a* is more redox sensitive than the BNC. This indicates a more rigid structure of the BNC. This result may provide further insight into the location of residues involved in or necessary to the overall reaction mechanism of C*c*O. The protein backbone changes that have been linked with Cu_A and haem *a*, could be accounted for by the residues that make up the H channel.

3.6 Future work

This series of measurements were made at a fixed pH (7), and could be repeated for a range of pH values 6.5 to 9, as this would allow a further separation of bands based on their pH dependencies. This information will allow both the linkage of IR bands to specific metal centres and pH sensitivities. This will assist in the identification of functionally significant groups that are involved in the coupling of electron transfer with proton transfer, and to which metal centre redox transition they are linked. Furthermore, repeating experiments in D_2O will provide evidence as to the IR bands that are of proton exchangeable groups. H/D exchange will appear as band shifts in the IR difference spectrum. Finally, site-directed mutagenesis will provide the ultimate control to assess the identity of contributing amino acid residues, however this is experimentally challenging with bovine C*c*O. Therefore, yeast C*c*O is being used as a model system in which mutations can be introduced [118,203]. A comparison of wild type yeast C*c*O in itself will provide an interesting comparison to the results obtained here with bovine C*c*O.

4 Functional carboxylic acids in bovine cytochrome c oxidase studied by ATR-FTIR spectroscopy

4.1 Introduction

Previous FTIR spectroscopy studies have shown that full reduction of bovine C*c*O with four electrons is coupled with changes in at least two protonated carboxyl groups [104,196,197]. These have been assigned tentatively to a conserved glutamic acid (E242 in the bovine sequence) and aspartic acid (D51), both of which may play a key role in the reaction mechanism of mitochondrial C*c*O [38,115,196] (though D51 is absent from yeast mitochondrial and bacterial forms of C*c*O). However, the actual number of components contributing in the 1760-1710 cm^{-1} protonated carboxyl region of the bovine redox IR spectrum, and their linkage to specific redox centres are not well characterised and recently with the use of a newly developed time-resolved infrared system, this region has been shown to be more complex [204]. To investigate this further, inhibitory ligands of C*c*O, cyanide and carbon monoxide were used, as they allowed stable mixed valence states of C*c*O to be electrochemically generated (see Chapter 3) [160]. By consideration of literature data and with spectra reported here, a new model is proposed where the IR features in this region have been separated and linked with specific metal centre transitions (see below).

4.2 Aims

The aims of this project were to associate the carboxyl group changes observed in bovine C*c*O with specific redox groups by exploiting the mixed valence (MV) states of C*c*O ligated with CN or CO. These states were produced by controlled electrochemistry combined with ATR-FTIR spectroscopy to give IR difference spectra linked to specific redox centres. In this manner, the redox-linked IR features associated with haem a_3-CN could be separated from those of Cu_A, haem *a*, and Cu_B and those associated with haem *a* and Cu_A could be separated from reduced haem a_3-CO and Cu_B. Data are taken from Chapter 3 and are discussed in relation to the protonated carboxylic acid (-COOH) region (1800-1700 cm^{-1}).

4.3 Results

4.3.1 IR band changes in the protonated carboxylic group region

The 1800-1700 cm^{-1} range of all finalised IR difference spectra of bovine C*c*O is shown in Figure 4-1. Changes in this region can be attributed primarily to the IR band changes of protonated carboxylic groups, protonated propionates, or of the ester bond of phospholipids (see discussion) [184]. Note, the full IR spectra in the 1800-1000 cm^{-1} are presented and discussed in Chapter 3 and will not be discussed here.

4.3.1.1 Unligated CcO: FR – O difference spectra

(Cu_A^{+}, a^{2+}, a_3^{2+}, Cu_B^{+} *minus* Cu_A^{2+}, a^{3+}, a_3^{3+}, Cu_B^{2+})

Figure 4-1A shows the electrochemically-induced FR *minus* O IR difference spectrum of unligated bovine C*c*O. Positive signals are representative of the FR state where all 4 redox centres are reduced (Cu_A^{+}, haem a^{2+}, haem a_3^{2+}, Cu_B^{+}) and negatives are of the fully oxidised state (Cu_A^{2+}, haem a^{3+}, haem a_3^{3+}, Cu_B^{2+}). This difference spectrum shows two troughs at 1749 cm^{-1} and 1737 cm^{-1}.

4.3.1.2 CN-ligated CcO: FR-CN – O-CN difference spectra

(Cu_A^{+}, a^{2+}, a_3^{2+}-CN, Cu_B^{+} *minus* Cu_A^{2+}, a^{3+}, a_3^{3+}-CN, Cu_B^{2+})

Figure 4-1B shows the FR-CN *minus* O-CN IR difference spectrum of CN-ligated bovine C*c*O, which includes redox transitions of all redox centres with CN bound to haem a_3. Two troughs are present at 1749 cm^{-1} and 1740 cm^{-1}.

4.3.1.3 CN-ligated CcO: MV-CN – O-CN difference spectra

(Cu_A^{+}, a^{2+}, a_3^{3+}-CN, Cu_B^{+} minus Cu_A^{2+}, a^{3+}, a_3^{3+}-CN, Cu_B^{2+})

Figure 4-1C shows the MV-CN *minus* O-CN IR difference spectrum of CN-ligated bovine C*c*O. This spectrum shows the changes associated with the redox transition of all centres apart from haem a_3-CN, which remains oxidised at the reducing potential (+80 mV) of the experiment. Two troughs are present at 1749 cm^{-1} and 1737 cm^{-1}.

4.3.1.4 CN-ligated CcO: FR-CN – MV-CN difference spectra

(Cu_A^{+}, a^{2+}, a_3^{2+}-CN, Cu_B^{+} *minus* Cu_A^{+}, a^{2+}, a_3^{3+}-CN, Cu_B^{+})

Figure 4-1D shows the calculated (FR-CN *minus* O-CN) *minus* (MV-CN *minus* O-CN) IR double difference spectrum of CN-ligated bovine C*c*O. This results in a FR-CN

minus MV-CN difference spectrum and shows the changes associated with the redox transition of only haem a_3-CN. This spectrum could not be generated experimentally as the reoxidation of FR-CN to the MV-CN form could not be achieved. Here a single trough is present at 1740 cm^{-1}.

4.3.1.5 CO-ligated CcO: FR-CO – MV-CO spectra

(Cu_A^{+}, a^{2+}, a_3^{2+}-CO, Cu_B^{+} *minus* Cu_A^{2+}, a^{3+}, a_3^{2+}-CO, Cu_B^{+})

Figure 4-1E shows the FR-CO *minus* MV-CO IR spectrum of CO-ligated bovine C*c*O. This spectrum shows the redox transition of Cu_A and haem *a* while the CO-ligated BNC remained reduced. Two troughs are present at 1749 cm^{-1} and 1740 cm^{-1}.

4.3.1.6 CN-ligated and CO-ligated CcO: calculated (MV-CN – O-CN) minus (FR-CO - MV-CO) double difference spectra

(Cu_B^{+} *minus* Cu_B^{2+})

Figure 4-1F shows a Cu_B^{+} *minus* Cu_B^{2+} difference spectrum of bovine C*c*O. This was derived by subtraction of (FR-CO *minus* MV-CO) IR difference spectrum which shows IR changes associated with transitions of two metal centres, Cu_A and haem *a*, from the MV-CN *minus* O-CN difference spectrum which shows IR changes associated with transitions of the same metal centres as well as Cu_B. Hence, this spectrum should show IR changes associated with redox transitions of only Cu_B. This calculated spectrum has a single peak at 1740 cm^{-1}.

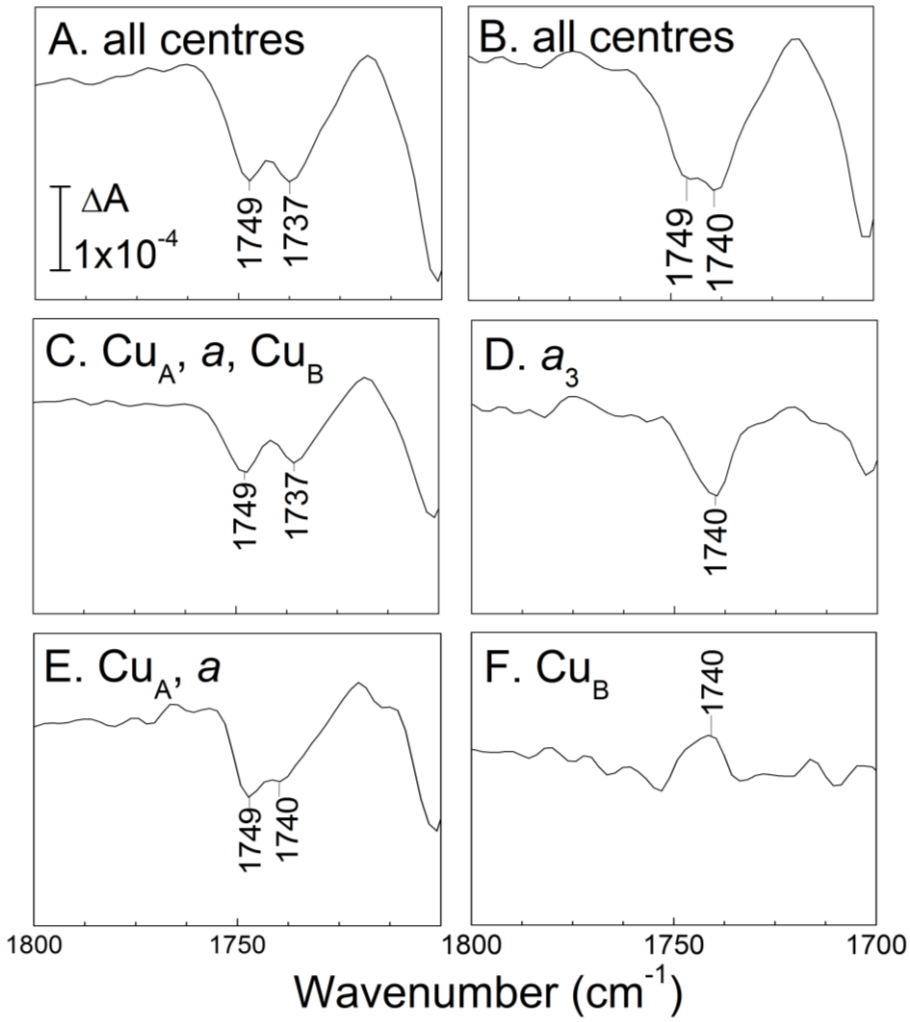

Figure 4-1. Electrochemically-induced and derived IR difference spectra of bovine CcO (1800-1700 cm^{-1}).

Each panel is labelled with the metal centre redox transition it represents. ***A.*** *FR minus O IR difference spectrum,* ***B.*** *FR-CN minus O-CN IR difference spectrum,* ***C.*** *MV-CN minus O-CN IR difference spectrum,* ***D.*** *derived FR-CN minus MV-CN IR double difference spectrum,* ***E.*** *FR-CO minus MV-CO IR spectrum and* ***F.*** *derived Cu_B^+ minus Cu_B^{2+} IR double difference spectrum. Spectra are taken from Chapter 3 and their detailed reaction conditions are given in Chapter 3. Buffer used was 0.1 M KPi, 0.1 M KCl pH 7.* ***Spectrum A*** *is an average of data from 20 redox cycles, redox mediators were 50 µM benzyl viologen and 1 mM ferrocene methanol, redox potentials were -400 mV and +500 mV with 30 mins equilibration time.* ***Spectrum B*** *is an average of 23 redox cycles, the reaction conditions were the same as in spectrum A, with the addition of 10 mM KCN, 100 µM phenazine methosulphate and 50µM 1,2-naphtoquinone sulphonate.* ***Spectrum C*** *is an average of 49 redox cycles, the reaction conditions were the same as in Spectrum B, but the potentials applied were +80 mV and +500 mV for reduction and oxidation.* ***Spectrum D*** *was derived by the following direct subtraction; (B. FR-CN minus O-CN) minus (C. MV-CN minus O-CN).* ***Spectrum E*** *is an average of 16 redox cycles, the experiment buffer was the same as in Spectrum A, the equilibration time for reduction was 30 mins and for oxidation was 4 mins.* ***Spectrum F*** *was derived by the following direct subtraction; (MV-CN - O-CN) minus (FR-CO - MV-CO). Where necessary each spectrum was corrected for baseline changes caused by pH-induced phosphate changes, liquid water and water vapour variations. All spectra were scaled based on the intensity of ΔA_{II} in the absolute spectrum of experiment* ***B*** *so that their intensities are directly comparable to all spectra shown in this chapter.*

4.3.2 CN ligation to CcO: O-CN minus O spectra

(Cu_A^{2+}, a^{3+}, a_3^{3+}-CN, Cu_B^{2+} *minus* Cu_A^{2+}, a^{3+}, a_3^{3+}, Cu_B^{2+})

Figure 4-2 shows a perfusion-induced CN-ligated spectrum *versus* an unligated baseline of O state bovine C*c*O. In order to confirm the IR change from the protonated carboxyl group in the FR-CN *minus* MV-CN difference spectrum was not arising from the re-binding of CN to the MV-CN state and unbinding from the lower affinity FR state a perfusion-induced CN binding spectrum to the O state was recorded. It is clear that the small positive observed upon CN binding is at 1744 cm^{-1} instead of 1740 cm^{-1} observed in the FR-CN *minus* MV-CN difference spectrum shown in grey. It is also of a smaller intensity. Furthermore the binding of CN to C*c*O was irreversible even with 3 mM sodium dithionite perfusion (45 mins). This confirms there was no CN re-binding to the O state taking place. The broad trough between 1740 cm^{-1} and 1700 cm^{-1} is caused by protein layer expansion/contraction that was difficult to subtract.

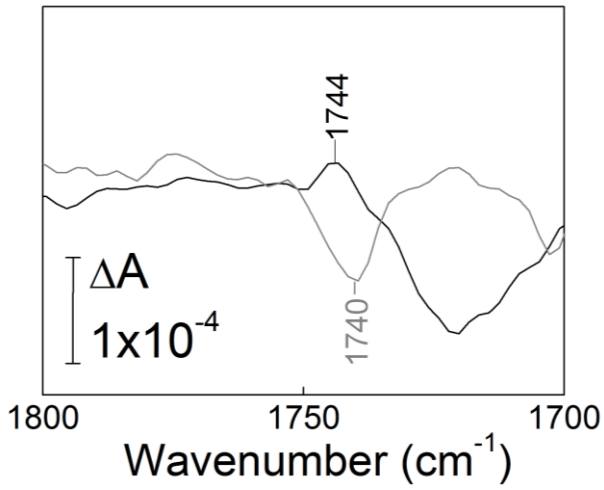

Figure 4-2. Perfusion-induced O-CN minus O IR spectrum of bovine CcO, 1800-1700 cm^{-1}. The derived FR-CN minus MV-CN IR double difference spectrum is overlaid for comparison.
CN binding to the O state induced a band at 1744 cm^{-1},and is therefore different to the band induced in the derived spectrum. The buffer used was 0.1 M KPi, 0.1 M KCl pH 7. The protein layer was perfused with 3 mM dithionite, followed by 20 µM potassium ferricyanide to ensure all CcO was in the fast oxidised unligated form, an O state baseline (accumulation of 1000 interferograms) was taken before perfusion with 20 µM potassium ferricyanide and 2 mM KCN to record the O-CN spectrum vs O baseline. The spectrum shown is an average of data (accumulation of 8000 interferograms) from 2 protein layers and is normalised based on the 2151 cm^{-1} band intensity CN ligated redox spectrum in Figure 4-1B. This spectrum has been corrected for baseline changes caused by protein layer changes induced by layer expansion/contraction, pH-induced phosphate changes, liquid water and water vapour variations.

4.4 Discussion

4.4.1 Carboxyl group changes associated with unligated bovine CcO

The 1800-1700 cm^{-1} region of the IR difference spectra is where the *v*(C=O) normal vibrational modes absorb [184]. They can arise from protonated carboxylic amino acids in the 1760–1710 cm^{-1} range [184]. However there can be overlap with *v*(C=O) modes of ester bonds of lipids that remain bound to purified C*c*O, or protonated haem propionate groups. However the v(C=O) modes of haem propionate are expected at lower frequencies and a band as low as 1676 cm^{-1} in *P. denitrificans* C*c*O, has been assigned to a protonated propionic acid group [109]. Moreover, the 1800-1700 cm^{-1} region of the FR *minus* O IR difference spectrum is sensitive to H/D exchange [104,205] therefore, it is unlikely that ester bonds of lipids (that should be insensitive to H/D exchange), contribute to this spectrum. Carboxylic groups are of functional significance in C*c*O, since they are implicated in the coupling of electron transfer with proton transfer by providing de/protonation sites through changes in their pK_a values. Any structural change in carboxylic groups that is coupled with redox transitions or ligation state could be of functional significance and warrants a method that can detect such changes. The 1800-1700 cm^{-1} region of the FR *minus* O IR difference spectrum is not overlapped by bands from other protein (amino acid) structural changes and so subtle changes in protonated carboxyl groups are easily detectable. Such band changes could arise from changes of **a)** orientation, **b)** environment such as extent of hydrogen bonding, and **c)** local dielectric strength. All 3 can affect the C=O bond dipole moment and could result in either, or a combination of, **1)** an extinction coefficient (signal intensity) change, **2)** a shift in band position, or **3)** an alteration in bandwidth (reviewed in Rich, *et al.* [206]). Alternatively a decrease in band intensity could arise from deprotonation since a deprotonated carboxylic group has two vibrational modes expected at 1580 cm^{-1} and 1398cm^{-1} (aspartate) and at 1556cm^{-1} and 1399cm^{-1} (glutamate) [184]. These are in a region masked by IR changes of additional protein related factors and so are not as easily accessible (see Chapter 3).

4.4.2 Identity of the redox induced 1749 cm^{-1} band

When redox transitions are induced in all metal centres in unligated bovine C*c*O, IR changes were induced in two components seen as troughs at 1749 cm^{-1} and 1737 cm^{-1} (Figure 4-1A). This is consistent with previous reports of the reduced *minus* oxidised IR difference spectra of bovine C*c*O [104,196,197]. There was no clear peak that could be associated with a band shift of the 1749 cm^{-1} trough in the FR state. However, it is clear

that a band at roughly the same frequency must be present in the FR state, because, in the CN or CO photolysis–induced unligated-FR *minus* ligated-FR difference spectra, the band shifts and becomes observable as a peak/trough at 1749 (unligated)/1741 (ligated) cm^{-1} with CO photolysis [104] and 1752/1740 cm^{-1} with CN photolysis [90]. Hence, the simplest explanation for the absence of a positive band in the FR *minus* O IR difference spectrum (Figure 4-1A), is that the O to FR transition simply causes an extinction coefficient decrease without any major frequency shift, hence the band appears only as a trough in the FR *minus* O IR difference spectrum [90]. The 1749 cm^{-1} band has been tentatively assigned to a functionally important and conserved glutamic acid (E242 in the bovine sequence) in subunit I. This assignment is based on mutagenesis studies of the same residue and H/D exchange experiments in bacterial C*c*Os [88,103,207]. E242 is a highly conserved residue that is essential for enzyme activity. It is equidistant from haems *a* and a_3, and is part of the pentameric ring structure H240-P-E-V-Y244 [34]. Its mutation in bacterial C*c*Os abolishes electron transfer [84,92]. Noteworthy, Okuno, *et al.* [104] have proposed that the haem a_3 propionate gives rise to this signal. However, protonated propionates generally have bands at lower frequencies. The alternative explanation for the absence of a peak is that the residue deprotonates on reduction. However, this can be ruled out as the pK_a of E242 has been shown to be > 8.5 in FR bovine C*c*O [90,208] and during the P_R to F transition of the reaction cycle it is shown to be ~8 [209]. Based on this it is likely that in the fully oxidised state it also has a high pK_a.

4.4.3 Identity of the redox induced 1737 cm^{-1} band

The second component that appears as a trough at 1737 cm^{-1} is not present in bacterial C*c*O [210] and has only been observed in bovine C*c*O. X-ray crystallographic data of the O and FR states of bovine C*c*O showed aspartic acid (D51) in subunit I to undergo a redox-linked conformational change; on reduction it moved from being buried inside the structure to being accessible to the IMS, an event that should be coupled to a decrease in its pK_a [38]. Moreover this residue is not conserved in bacterial C*c*Os. Based on this, the band was tentatively assigned to the deprotonation of D51 when C*c*O is reduced, hence causing a loss of its 1737 cm^{-1} band and resulting in the trough in the FR *minus* O IR difference spectrum [196].

Overall, the FR *minus* O difference spectrum of unligated C*c*O showed two overall troughs and in the minimal and simplest interpretation, based on the data discussed above, the region can be modelled with three Gaussian shaped bands where the 1749

cm^{-1} trough is the sum of a small positive and a large negative as described above (Figure 4-3).

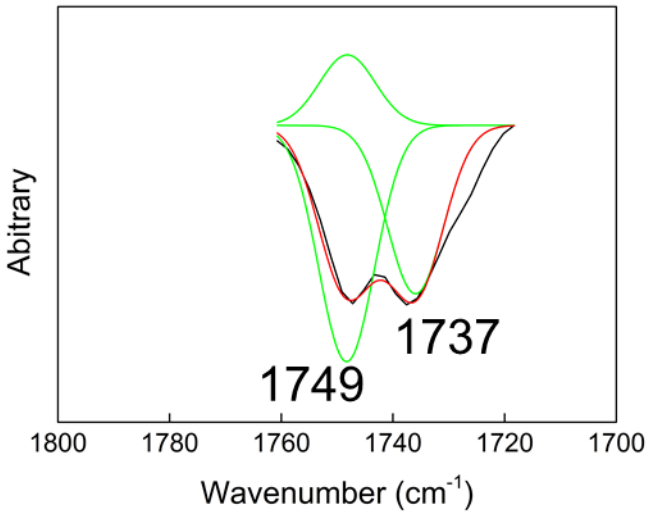

Figure 4-3. The simplest 3 component model of the FR minus O IR difference spectrum. *The measured data (black) is taken from Figure 4-1A. IR bands were simulated using Gaussian bands at 1749 cm^{-1} and 1737 cm^{-1} shown in green with a fixed band width at half maximum of 11.75 cm^{-1}. The red trace shows the sum of the three Gaussian components (green).*

4.4.4 Carboxyl group IR changes associated with CN-ligated bovine CcO

CN ligated bovine C*c*O allowed a stable mixed valence state of Cu_A^+, a^{2+}, a_3^{3+}-CN, Cu_B^+ to be electrochemically generated [160,211]. The feature in the FR-CN *minus* O-CN IR difference spectrum was distorted but displayed two overall troughs at 1749 cm^{-1} and 1740 cm^{-1} and was not completely identical to the symmetrical feature in the unligated C*c*O spectrum, indicating a possible effect of CN. As described in the results, two overall negatives at 1749 cm^{-1} and 1737 cm^{-1} were induced by the combined redox transitions of Cu_A, haem *a* and Cu_B whilst haem a_3-CN remained oxidised (Figure 4-1B). And a single trough at a new position of 1740 cm^{-1} was induced by the redox transition of haem a_3-CN alone, whilst the other redox centres remained reduced (Figure 4-1D). This band may have been induced by CN binding to the O state and unbinding upon reduction, as the affinity of haem a_3 for CN in the FR state is very low (K_d 0.7 mM at pH 7.4) [193] compared to the O state (K_d 0.092 mM at pH 7.4) [194]. However, this was disproven as the perfusion-induced O-CN *minus* O spectrum (Figure 4-2) showed no 1740 cm^{-1} band but a new smaller intensity band at 1744 cm^{-1}.

4.4.5 Carboxyl group IR changes associated with CO ligated bovine CcO

The FR-CO *minus* MV-CO IR spectrum (Figure 4-1E) shows protein associated changes coupled to the redox transition of only Cu_A and haem *a*, whilst the BNC is held reduced [161]. This overall feature was again distorted but still displayed two troughs, at 1749 cm^{-1} and 1740 cm^{-1}, indicating an influence of bound CO. The band changes must be coupled to redox transitions of Cu_A and haem *a*. However the position of the second trough remains speculative as the 1740 cm^{-1} band is coupled to the redox transition of haem a_3 based on the FR-CN *minus* MV-CN difference spectrum (Figure 4-1D). Furthermore there must be a 1737 cm^{-1} trough present as it is present in the O-CN state. A plausible explanation for this comes from the peak/trough (1749/1741 cm^{-1}, FR/FR-CO) from CO photolysis studies on FR bovine C*c*O [90,104], which indicates the FR-CO state also induces a 1741 cm^{-1} band which would produce a positive in the FR-CO *minus* MV-CO spectrum. Hence the overall feature in the FR-CO *minus* MV-CO IR spectrum must consist of three components, two negatives at 1749 cm^{-1} and 1737 cm^{-1} and a smaller positive at 1741 cm^{-1}, which distorts the overall feature observed.

It is noteworthy that the 1740 cm^{-1} band also appeared as a positive in the derived Cu_B^+ *minus* Cu_B^{2+} difference spectrum (Figure 4-1E) that indicates there must be an underlying positive at 1740 cm^{-1} that must also be larger in intensity in the MV-CN *minus* O-CN spectrum than in the FR-CO *minus* MV-CO spectrum. Another experiment that requires consideration is the MV/MV-CO photolysis [104,208]. However its interpretation is complicated as the unbinding of CO causes 'reversed electron transfer' from haem a_3 to *a*. Hence the feature observed in the unligated *minus* MV-CO would have positives of oxidised haem a_3 and reduced haem *a*, and negatives of reduced haem a_3-CO and oxidised haem *a* whilst the Cu centres are reduced. This spectrum has been reported to contain an overall trough [104,208], and at pH 7 it is reported to be at 1735 cm^{-1}. This band may be the same as the 1737 cm^{-1} band reported here and the simplest explanation would be that it is linked with Cu_A/haem *a* redox transition and this is a deprotonation effect as described above. Although it is not clear why a positive is not observed at 1740 cm^{-1} when haem a_3 is oxidised but this may be an additional effect of CO unbinding that is linked with haem a_3 oxidation in this transition. A possible explanation for the absence of the 1749 cm^{-1} band is given below.

4.4.6 A proposed model of contributing carboxyl bands and their metal centre linkages

From the results presented and the data from previous studies on CO photolysis and CN photolysis on reduced C*c*O [90,104], up to three components can be identified at 1749 cm^{-1}, 1740 cm^{-1} and 1737 cm^{-1} in various redox difference spectra (Figure 4-1). The two components at 1749 cm^{-1} and 1737 cm^{-1} are linked with the oxidation of Cu_A and haem *a*, a finding that is consistent with prior literature linkages of these bands [104,115,117]. The small positive at 1749 cm^{-1} has also been linked with the reduction of Cu_A and haem *a* (see below).

The 1740 cm^{-1} component is present in the FR-CN *minus* MV-CN difference spectrum (Figure 4-1D) and has been linked with the oxidation of haem a_3-CN, however this seems to be electrochemically induced upon reduction of Cu_A and haem *a* in the CO ligated C*c*O, where the BNC is held reduced, and in the reduction of Cu_B^{2+} which further complicates the assignment. This band can be interpreted with two models; **(1)** the 1740 cm^{-1} positive that is linked with Cu_A and haem *a* reduction in the FR-CO *minus* MV-CO spectrum is in fact the small 1749 cm^{-1} positive in the unligated spectrum that has shifted position in the ligated-CO/CN C*c*O and the 1740 cm^{-1} that is linked with Cu_B reduction and haem a_3 oxidation is a third new component. **(2)** The second model is the 1740 cm^{-1} band is still a third component, but is linked with all four metal centres, and is additional to the 1749 cm^{-1} positive in the unligated spectrum that always cancels out in the overall difference spectrum. Based on the data presented here, it is clear that the feature in the CN ligated FR-CN *minus* O-CN full redox spectrum, and in the CO ligated FR-CO *minus* MV-CO spectrum, is distorted compared to the unligated spectrum. This suggests that the first model is the most accurate so far, and the position of the 1749 cm^{-1} positive is shifted in the reduced state when C*c*O is ligated to CN or CO but not in the unligated state. Based on this, the positive at 1749 cm^{-1} in unligated C*c*O that shifts to 1740 cm^{-1} in ligated C*c*O, has been associated with redox transitions in Cu_A and haem *a* since it is present as a positive in the FR-CO *minus* MV-CO difference spectrum that shows redox transitions in these centres. Figure 4-4 displays this model and summarises the metal centre linkages of each component.

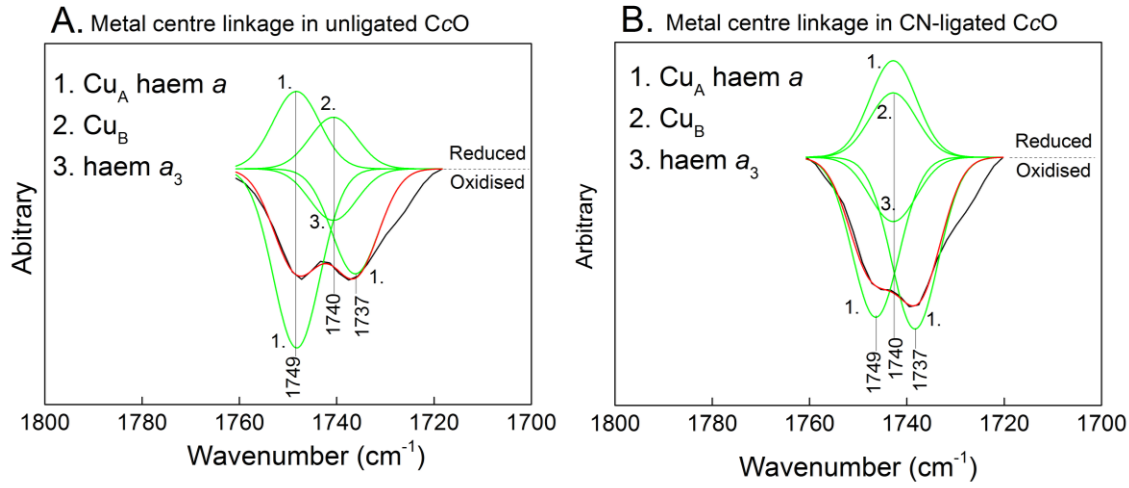

Figure 4-4. A 5 component model and redox centre linkage of carboxyl IR bands.
*Metal centre linkage in **A.** unligated CcO and **B.** ligated CcO. Data (black trace) is taken from Figure 4-1A and B The data in **B** has been baseline corrected. IR bands were simulated using Gaussian bands (green) with a fixed band width at half maximum of 11.28 cm^{-1}. The red trace shows the sum of the Gaussian components.*

Note this model makes the following assumptions; that bands labelled 2 and 3 are the same intensity, although in Figure 4-1F and Figure 4-1D they are not identical in size. Their intensities are dictated by the size of the trough in Figure 4-1D. The intensity of the positive at 1749 cm^{-1} has been given an arbitrary value. The relative intensity of the negative at 1749 cm^{-1} is decreased in the ligated form of C*c*O in this case with CN. CO and CN ligands induce the same set of differences in the carboxyl region of bovine C*c*O.

This model along with its assumption would explain the missing 1749 cm^{-1} band in the MV/MV-CO photolysis spectrum described above, that must cancel out. The positive in this spectrum would appear at 1749 cm^{-1} since C*c*O is unligated and haem *a* is reduced. The negative in this spectrum would appear at 1749 cm^{-1} since haem *a* is oxidised, and according to the assumption here, its intensity would be smaller since C*c*O is ligated to CO. Its size would be such that the IR bands cancel out.

The amino acid assignment of the third component and whether it appears from changes in extinction coefficients or protonation changes is not clear and will require further investigation. Nevertheless this model provides insight into possible directions of future experiments (see Future work).

4.4.7 Possible candidates for the third component

Carboxyl group amino acid candidates that could give rise to the third component are shown in Figure 4-5, E242 and D51 are also shown. These residues were identified as being functionally important by Rich, P. R. and Maréchal, A. (2008) [206]. They include carboxylic acids (D369, D364 and E198) close to the Mg^{2+} site, since that is where the proton trap site is located, that receives translocated protons from the D channel via E242 (if that is operative as a translocating pathway in mitochondrial C*c*Os - see main introduction). These residues are also close to the BNC whose redox transitions have been assigned to give rise to this third component. D91 in subunit I is at the entrance of the D channel and in crystal structures a nearby histidine residue (H503) is shown to undergo a redox linked conformational change that is proposed to result in D91 deprotonation upon reduction [35]. Other amino acids include D442 and E40. These are proposed to be involved in binding Na^{+}/Ca^{2+} cations at the interface of subunits I and II, they are also close to the top of the H channel [38,212]. Alternatively, it could be a more remote residue on another subunit, such as E90 and D246, in subunit III since these residues are located in the central region of C*c*O where the dielectric strength is low, and so, they are likely to be protonated [206]. They could give rise to this signal via long range structural changes. E62 in subunit II is at the entrance of the K channel. The K channel is involved in delivering 2 out of 4 substrate protons to the BNC [83,84], and/or providing a dielectric well to stabilise transient intermediates [86]. Site-directed mutagenesis of this residue in *Rba. sphaeroides* C*c*O causes loss of turnover activity and blocks the K channel, and so is therefore suggested to be the predominant entry point for protons in the K channel [213].

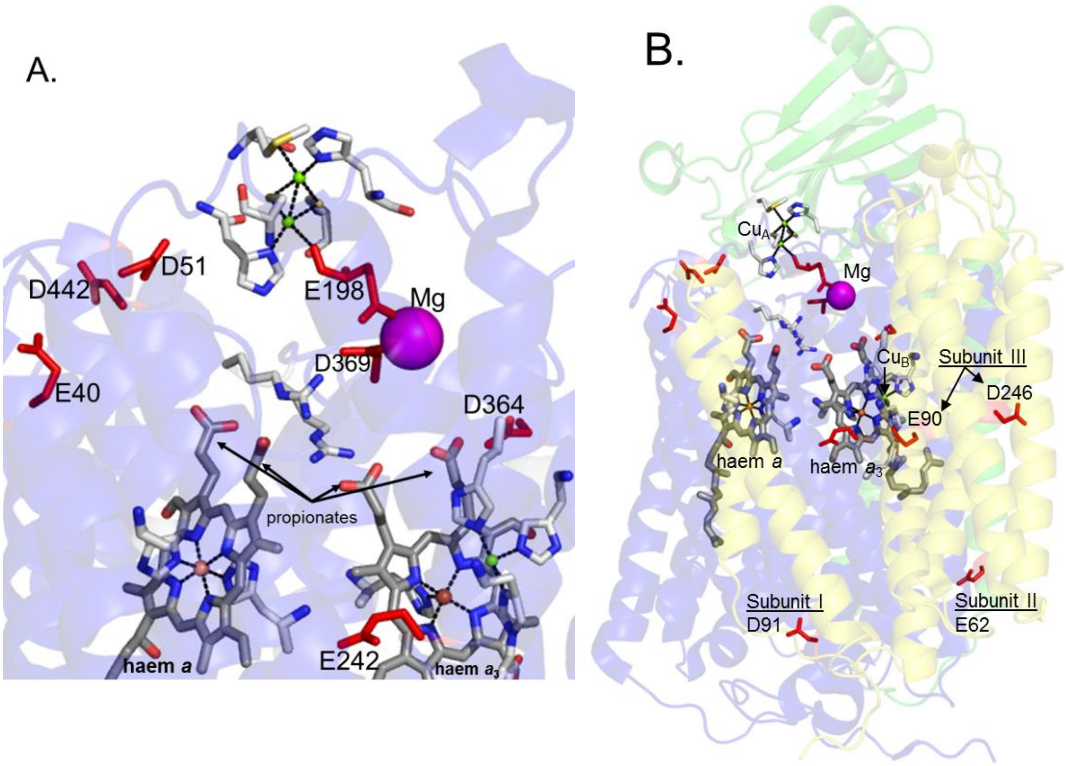

Figure 4-5. Structure of bovine CcO showing possible carboxyl group candidates (red) for the third 1740 cm^{-1} IR component (PDB:1V54), haem propionates are also highlighted. *A. An expansion of carboxyl groups in subunit I close to the metal centres and Mg site (purple sphere). B. Remote carboxyl groups in subunits I (blue), II (green) and III (yellow).*

4.5 Conclusions

In conclusion, both CN and CO ligands of C*c*O were efficient in separating the redox transitions of the redox centres by allowing stable MV states of C*c*O to be generated with controlled electrochemistry. In doing so, it was possible to couple the protonated carboxyl bands in the IR difference spectra with specific redox transitions in bovine C*c*O. Up to three components were identified at 1749 cm^{-1}, 1740 cm^{-1} and 1737 cm^{-1}. The 1749 cm^{-1} and 1737 cm^{-1} components have been coupled to the redox transition of Cu_A and haem *a*. The 1749 cm^{-1} component in the unligated-FR is proposed to shift to 1740 cm^{-1} when CO or CN are ligated. The third 1740 cm^{-1} component has a more complicated coupling mechanism, it has been linked with the redox transitions of the Cu_B and haem a_3 in such a way that its contribution cancels out in the FR *minus* O IR difference spectrum. Its assignment to a specific residue requires further investigation and several candidates are shown in Figure 4-5. A change in extinction coefficient of E242 and the protonation change in D51 have been tentatively assigned to the 1749 cm^{-1} and 1737 cm^{-1} troughs, respectively.

4.6 Future work

Different strategies will be needed to fully understand the role and contribution of protonated carboxyl groups in C*c*O reaction mechanism. The model proposed is based on a number of assumptions, and extension will require repeating these series of measurements with CN and CO in D_2O. H/D exchange is expected to shift and possibly separate the IR bands, hence providing further insight into the number of contributing components. If the IR bands are sensitive to H/D exchange it will provide confirmation that they do not arise from ester bonds of lipids. Definitive assignment of the third IR component to a protonated carboxylic group will require site-directed mutagenesis.

Yeast C*c*O is highly homologous to bovine C*c*O [26,41] and can be used to produce mutants in order to help with the assignment of the signals observed [118]. To date, mutants of different candidate carboxyl groups and surrounding residues have been produced based on a homology model of yeast C*c*O [41]. This will allow the definitive assignment of signals observed to specific carboxyl groups within the structure of a mitochondrial form of C*c*O. For example, a yeast C*c*O mutant, E243D, has confirmed the assignment of the equivalent 1749 cm^{-1} band to the conserved glutamic acid (Amandine Maréchal, personal communication). Also noteworthy is that the second 1737 cm^{-1} component in bovine C*c*O is absent from yeast C*c*O as is the D51 residue (replaced by S52) to which it has been assigned.

The spectra reported have been recorded of electrochemically poised C*c*O. Therefore they do not provide kinetic information on the appearance or disappearance of IR bands. Time resolved infrared spectroscopy has recently been developed as a technique that can monitor spectral changes, at the nano to micro second timescale, with high signal to noise [204]. This technique has been used to follow the kinetics of spectral changes in the carboxyl group region during the CO photolysis of CO bound C*c*O, and has in fact detected four bands [204]. The use of time resolved methods will provide yet another approach to separate IR bands in the carboxyl region (as well as other parts of the spectrum), according to their kinetics. This will provide further insight into the number of contributing components in regions of the IR spectrum where bands are overlapping and the order of appearance/disappearance of IR bands.

5 Electrochemical and infrared properties of radicals related to the tyrosine-histidine cofactor involved in the catalytic P_M intermediate of bovine cytochrome c oxidase

5.1 Introduction

The reaction cycle of C*c*O is summarised in the main introduction. Starting from the fully reduced (FR) state, C*c*O steps through five intermediates; A, P (ferryl plus associated radical), F (ferryl), O (oxidised), E, and back to FR (reduced). The conserved covalently linked Tyr-His structure is thought to provide an electron and a proton during the R→P catalytic step, in which the dioxygen bond is broken [38,48,49,214]. As a result, it is thought to form a phenoxyl radical that becomes re-reduced to form the F intermediate in the next step. In order to definitively confirm this role, a method to detect the tyrosine radical species is required, that should also be correlated with the specific P intermediate of the reaction cycle. EPR [215-217], UV/visible [218], and resonance Raman [219] have been used to characterise phenoxyl radicals. Extensive EPR spectroscopic studies of C*c*O have in fact detected one or two tyrosine radical species [52-54,71]. However, there has not always been a direct correlation of its presence with specific intermediates of the reaction cycle (see Introduction). IR spectroscopy can also offer a means to detect a protein associated radical. However, to date there is very little information on IR reference spectra of phenoxyl radicals. For those that are available, the radical has been induced by photolysis. This is an irreversible approach and can result in large baseline distortions of the IR spectrum and other products of the photochemistry [220-223].

5.2 Aims

Electrochemistry can provide a cleaner approach to induce radical species at an electrode surface. Infrared spectra of radicals induced this way [224] can provide reliable reference spectra that can be used to aid assignment of radicals in proteins. The aim of this project was to use cyclic voltammetry to characterise the electrochemical properties of Tyr-His model compounds that were constructed to mimic the conserved structure in C*c*O. Their structures were based on the phenol compounds; 2,6-di-*tert*-butylmethoxyphenol (TMP) and 2,4,6-tri-*tert*-butylphenol (TBP) that can form stable radicals [224,225]. To characterise them further, the pK_a values of the optimal Tyr-His structure were determined and the IR absolute spectra in the fully protonated, neutral and fully deprotonated state were assigned by comparison to known model compounds and by Gaussian-predicted IR bands. Finally, the optimal electrochemical conditions to induce a stable radical species were combined with ATR-FTIR spectroscopy, to generate reduced *minus* oxidised (radical) IR difference spectra. These spectra, together with published spectra, were used to tentatively assign, tyrosine radical and Tyr-His associated IR bands, in the P_M (oxyferryl associated radical) *minus* oxidised IR difference spectrum of bovine C*c*O.

5.3 Results

5.3.1 Structures of all compounds

The structures of tyrosine, TMP, TBP, Tyr-His(trimethyl) Tyr-His(dimethyl) and Tyr-His(dimethylbutyl) are summarised in Figure 5-1. The structure of cross-linked Y244-H240 in the distal pocket environment of haem a_3 of bovine C*c*O is also shown for comparison.

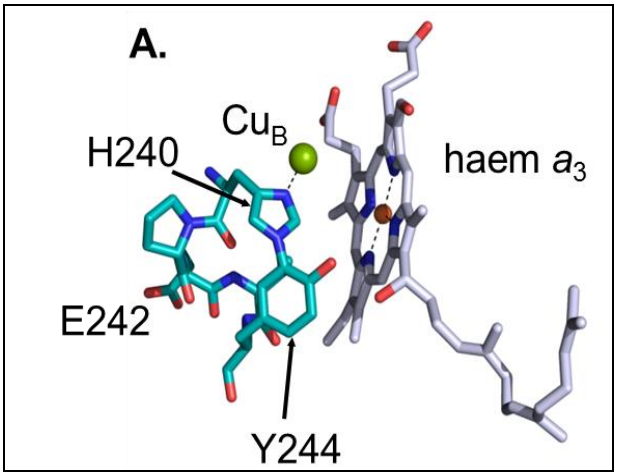

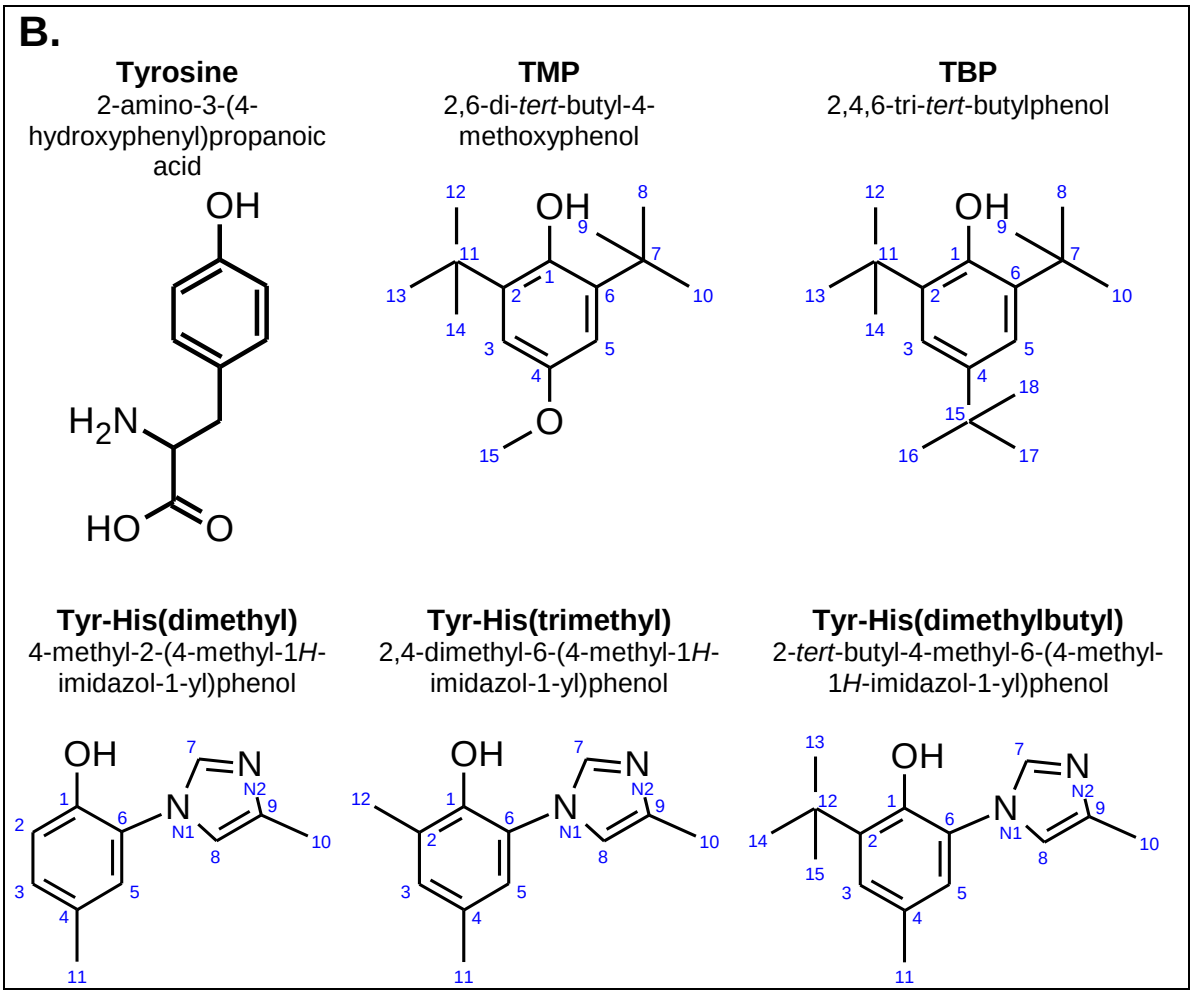

Figure 5-1. A. Close up of Tyr240-His244 cross linked structure in bovine CcO. B. Structures of Tyr and Tyr-His model compounds.

A. haem a_3 and Cu_B are also shown. B. The full names of each structure at neutral pH and their abbreviations are given.

B.

5.3.2 Effect of working electrode on cyclic voltammetry

Initially, cyclic voltammetric (CV) behaviour of each compound was tested with different working electrode materials since the surface groups on each are different and may improve the electrochemical response of the compound. Figure 5-2 shows the CV of 3 successive scans of tyrosine at glassy carbon (GC), boron-doped diamond (BDD), platinum (Pt) or gold (Au) working electrodes. The Au electrode was itself electrochemically active within the required potential window and so was not useful for detecting tyrosine. BDD and Pt each gave irreversible oxidation peaks, which were broader than those recorded using GC due to slower electron transfer. Overall GC was the optimum working electrode since it gave the most reproducible, and defined tyrosine oxidation peaks, over successive scans. In addition, electrochemical changes of TBP, TMP, Tyr-His(trimethyl), Tyr-His(dimethyl), and Tyr-His(dimethylbutyl) could only be detected with GC. Therefore, the CVs presented in this chapter have all been measured using GC as the working electrode.

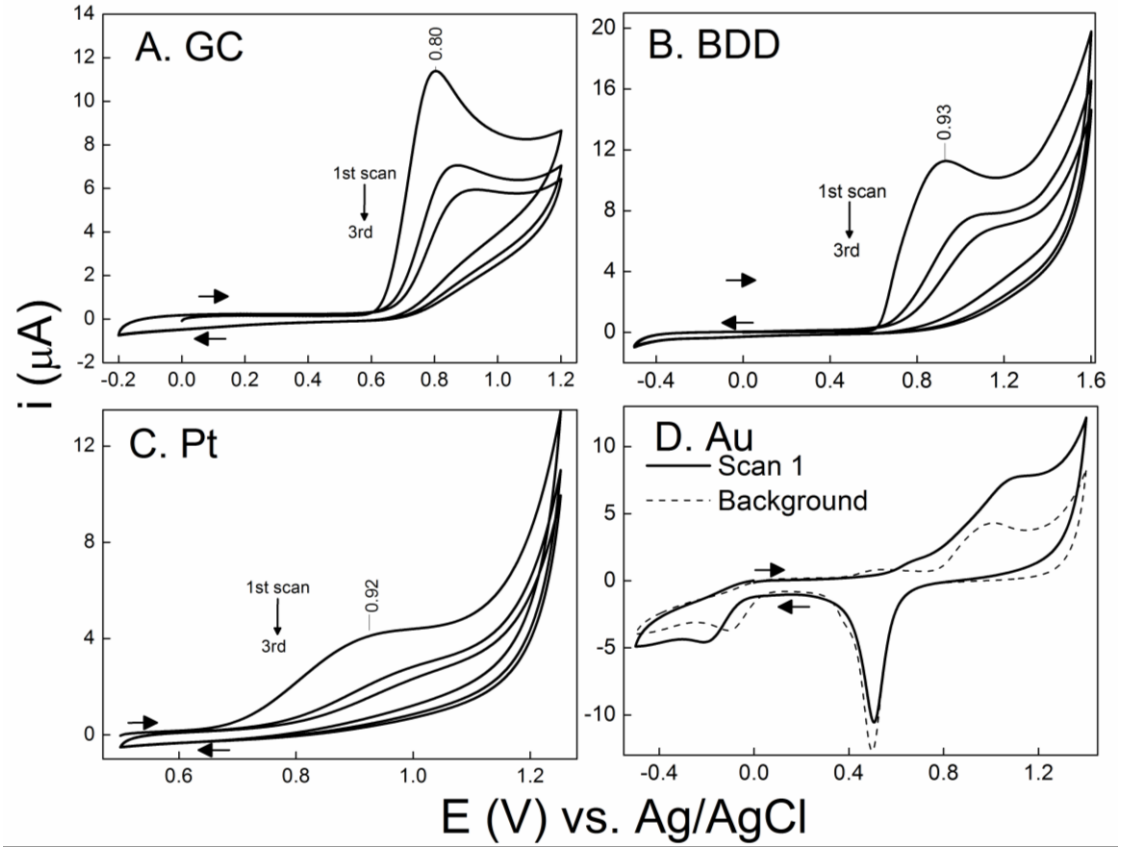

Figure 5-2. Three consecutive CVs of tyrosine using a (A) GC, (B) BDD, (C) Pt and (D) Au (only first scan is shown) working electrode.
The three consecutive scans were recorded in one measurement and are indicated as $1^{st} \rightarrow 3^{rd}$ in panels A., B., and C. Dashed line in D. is a CV of the blank solvent. All CVs are of 0.5 mM tyrosine in 0.1 M KPi pH 7 and were measured at 0.1 V/s scan rate.

5.3.3 CVs with all compounds

The CVs of tyrosine, TMP, TBP, Tyr-His(trimethyl), Tyr-His(dimethyl), and TyrHis(dimethylbutyl), in optimum solvent conditions are summarised in Figure 5-3. The CVs of tyrosine showed irreversible electrochemistry at pH 11 and pH 6. The CVs of TMP and TBP were reversible and reproducible on successive scans at pH 11. They each had peak current ratios of ~1 and peak separation of ~59 mV, consistent with the theoretical properties of a reversible reaction [183] that is described in the Methods. The oxidation peak potentials (E_p^{ox}) of TMP and TBP shifted to more positive potentials at pH 6, the TMP reaction became irreversible and the TBP reaction exhibited a broader oxidation peak. Since alkaline conditions favoured reaction reversibility, CVs of the model compounds of Tyr-His were measured at pH 13. Tyr-His(trimethyl) had partially reversible electrochemistry; the reduction peak current was smaller than the oxidation peak current. Both Tyr-His(dimethyl) and Tyr-His(dimethylbutyl) displayed irreversible oxidation and the peak current decreased substantially on successive scans. This was most likely due to adsorption of the compound onto the electrode surface that meant less electro-active surface area was available. This interpretation has been used to explain the same behaviour of decreasing current on successive scans observed for tyrosine [226]. Upon oxidation, Tyr-His(dimethylbutyl) produced two oxidation peaks, and the second irreversible oxidation peak increased in size with successive scans.

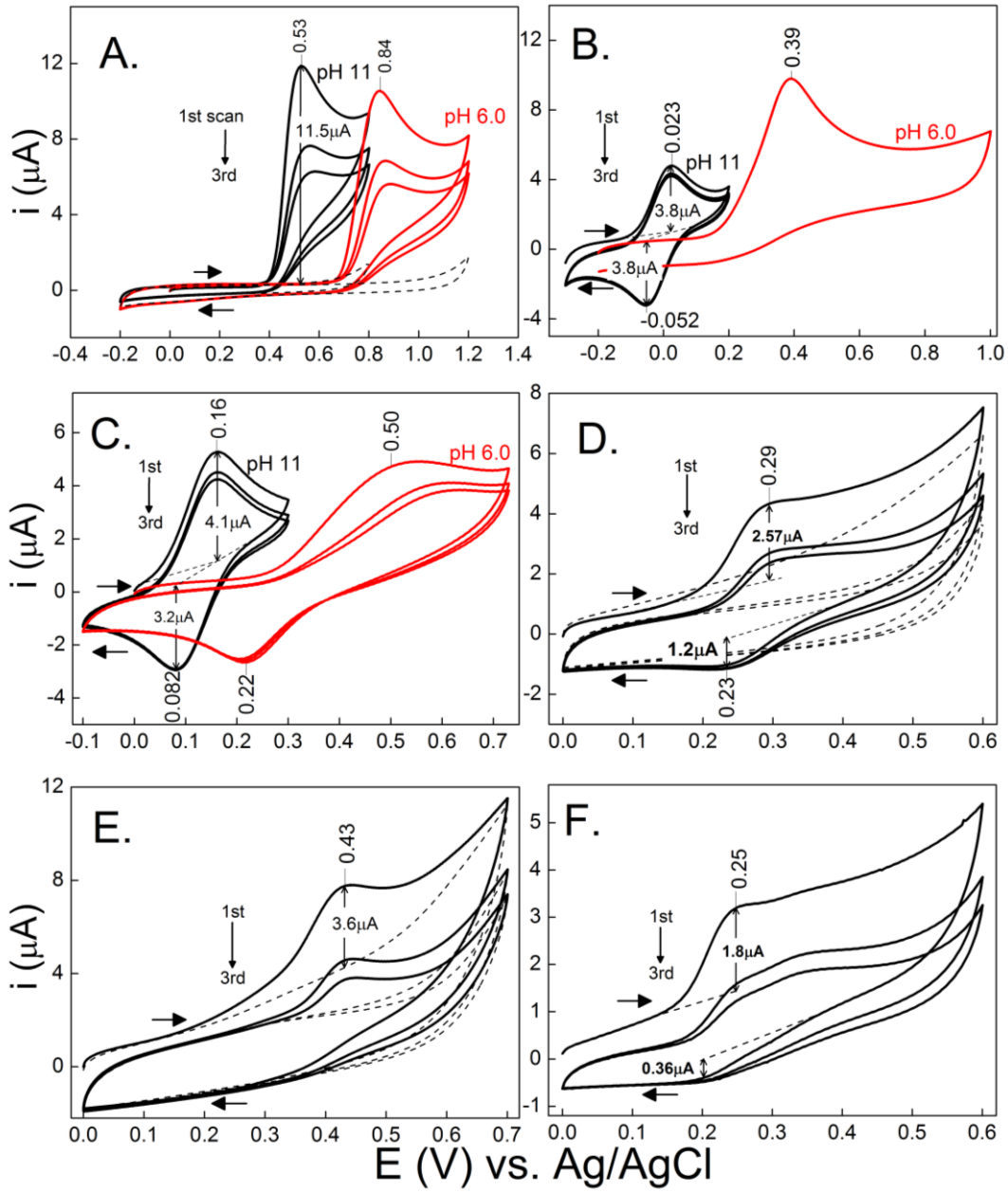

Figure 5-3. CVs of (A) tyrosine, (B) TMP, (C) TBP, (D) Tyr-His(trimethyl), (E) Tyr-His(dimethyl) and (F) TyrHis(dimethylbutyl).
Three consecutive scans were recorded for each measurement the order of scans is labelled as $1^{st} \rightarrow 3^{rd}$ in each panel. The dashed lines are scans of the blank solvent (A, D and E). For those scans where a blank was not measured the baseline was estimated by extrapolation of the measured scan. A. 0.5 mM tyrosine was measured in 0.1 M KPi pH 6 (red) and pH 11 (black). B. 0.5 mM TBP and C. 0.5 mM TMP were measured in 57 % (v/v) ethanol 0.1 M KPi pH 6 (red) and pH 11 (black). 0.2 mM Tyr-His model compounds were measured in 50 % (v/v) propan-2-ol 20 mM KPi, 500 mM KCl at pH 13. All scans were measured using GC at 0.1 V/s.

5.3.4 Effect of pH

CV of tyrosine was repeated for a range of pH values to explore the effects of the protonation state on its electrochemistry. A plot of E_p^{ox} *versus* pH is shown in Figure 5-4. The E_p^{ox} values decreased with increasing pH until pH >11. The slope of the linear portion of the graph was -55 ±0.4 mV/pH within the pH range of 5 to 11, and is consistent with the theoretical -59 mV/pH slope, characteristic of an oxidation event that is coupled to a deprotonation event [227,228]. However, for all pHs tested using tyrosine, the reaction remained irreversible. In the case of TMP, TBP and TyrHis(trimethyl), the nature of the reaction changed as well as the peak position where it became irreversible or quasi reversible (TBP) at pH 6. This suggests that the 1 or 2 electron oxidation of the protonated form, leads to further chemical reaction of the oxidised product in such a way that the reaction is no longer reversible [225].

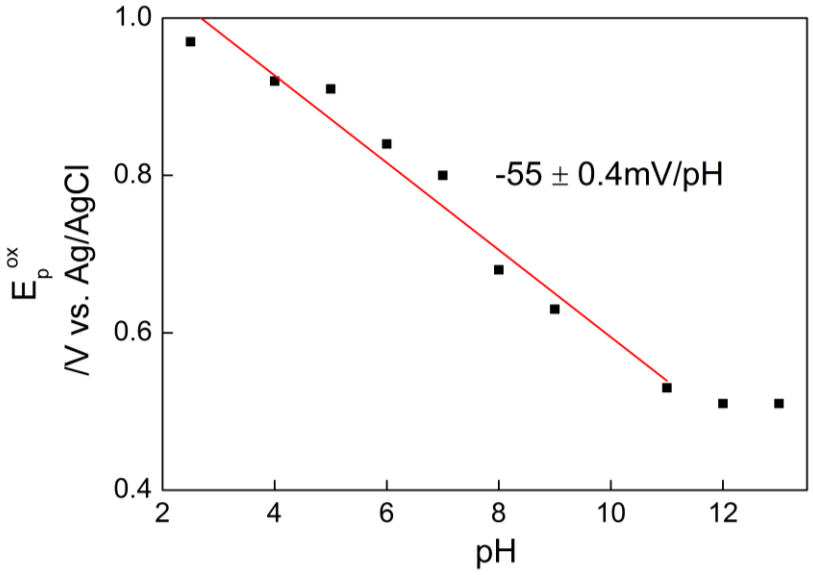

Figure 5-4. A E_p^{ox} versus pH plot of tyrosine.
CVs were of 0.5 mM tyrosine prepared in 0.1 M KPi at a range of pH values using GC working electrode at 0.1 V/s scan rate. The error is from the linear fit performed on OriginPro8.6. Each data point is from a single measurement.

5.3.5 Characterising the reaction; 1- or 2-electron oxidation

The oxidation of TBP at alkaline pH has previously been characterised as a one electron transfer [224]. To confirm this, the CV of TBP was compared to that of ferrocene methanol. The following equation describes the relationship between peak current and number of electrons transferred [183].

$$i_p = (2.69 \times 10^5)\, n^{3/2}\, A\, D^{1/2}\, C\, v^{1/2}$$

i_p = peak current (A), n = number of electrons transferred, A = electrode area (cm^2), D = diffusion coefficient (cm^2/s), C = concentration (mol/cm^3), and v = scan rate (V/s).

Ferrocene methanol is a redox mediator that also undergoes reversible 1-electron oxidation. Hence, if also a 1-electron oxidation, the peak current of TBP should be approximately equal to that of ferrocene methanol (measured in the same conditions). This was the case, confirming prior reports [224] (Figure 5-5B). According to the above equation a 2-electron oxidation should give a current 2.8 times larger than ferrocene methanol [183]. However, in order to compare values based on peak currents, an assumption must be made that the diffusion coefficients are equivalent. Since TBP and ferrocene methanol undergo 1-electron oxidation and they shared the same peak current values under the same conditions, their diffusion coefficients must therefore be similar. Therefore, peak currents of all compounds were compared to that of ferrocene methanol assuming that they have the same diffusion coefficients, and this allowed their reactions to be characterised as a 1-electron transfer, as expected for stable phenoxyl radical formation, or a 2-electron transfer (Figure 5-5).

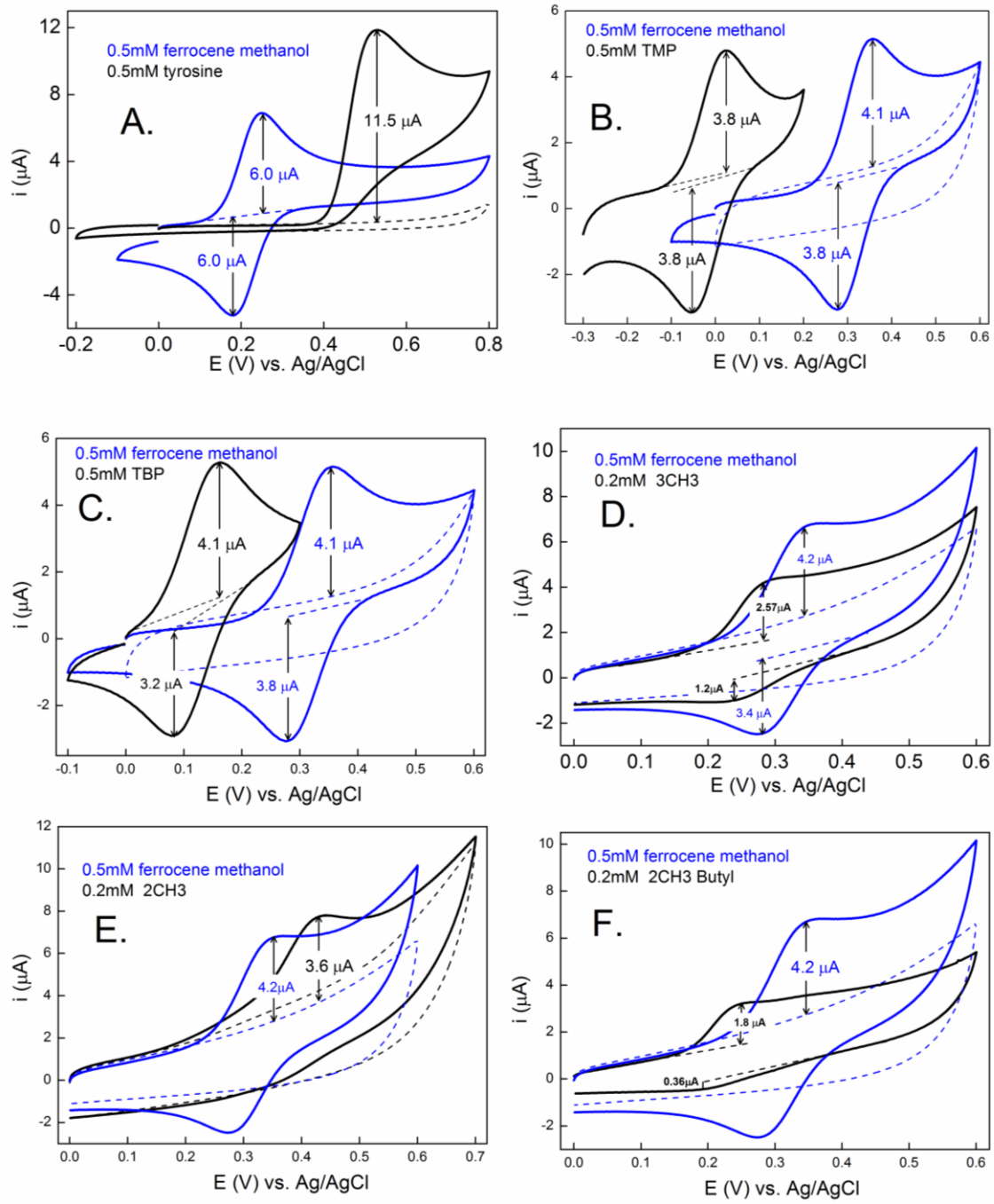

Figure 5-5. Comparison of CVs to 0.5 mM ferrocene methanol.
CVs of A. 0.5 mM tyrosine, B. 0.5 mM TMP, C. 0.5 mM TBP, D. 0.2 mM Tyr-His(trimethyl), E. 0.2 mM Tyr-His(dimethyl), and F. 0.2 mM TyrHis(dimethylbutyl) at 0.1 V/s using GC are shown in black. The black dashed scan is a measurement in the absence of the compound (blank scan). The buffer conditions were the same for each compound as mentioned in Figure 5-3. Ferrocene methanol scans are shown in blue and were recorded in the same buffer conditions as each compound. The blue dashed scans are of the blank solvent but were measured in the same potential range as ferrocene methanol. Peak currents were estimated based on their size from an experimentally measured baseline (black dashed scan) or through the extrapolation of the scan in the forward or reverse directions (black dashed line).

The peak current of tyrosine was 1.9 times larger than that of ferrocene methanol. This suggests that a combination of 1- and 2-electron oxidation events was occurring. The peak currents of TMP and TBP were equivalent, which indicated a 1-electron transfer of TMP oxidation and reduction, as previously confirmed using EPR spectroscopy [224]. The oxidation peak current of Tyr-His(trimethyl) (after normalising the concentration measured), was 1.5 fold greater than that of ferrocene methanol, a combination of 1- and 2-electron oxidation events was occurring. However the reduction peak current was smaller than the oxidation peak current suggesting that out of the oxidised product, the 1-electron oxidised radical population was stable enough for reduction. The oxidation peak current of Tyr-His(dimethyl) was 2.9 times greater than that of ferrocene methanol, indicating all of Tyr-His(dimethyl) underwent an irreversible 2-electron oxidation. The oxidation peak current of Tyr-His(dimethylbutyl) was equal to that of ferrocene methanol, suggesting this compound undergoes a 1-electron oxidation. However the estimated reduction peak current was 5 fold smaller than the oxidation peak current. This suggests the radical formed was unstable and so was unavailable for reduction on the reverse scan.

5.3.6 Effect of scan rate

CVs of tyrosine (1 V/s and 10 V/s), Tyr-His(trimethyl), Tyr-His(dimethyl), and Tyr-His(dimethylbutyl) were measured at fast scan rates (2 V/s) (Figure 5-6). These indicated whether the irreversible reaction was due to a further chemical reaction of the radical species (adsorption and/or polymerisation), that could be prevented by more rapid reduction of the initial radical product. CVs of tyrosine showed irreversible oxidation, even when the scan rate was increased to 10 V/s, suggesting that any secondary reaction after oxidation was very fast. CV of Tyr-His(dimethyl) also showed irreversible oxidation at 2 V/s (and at 4 V/s, data not shown). CV of Tyr-His(trimethyl) at 2 V/s had reversible electrochemistry where the ratio of the peak currents was almost 1 (0.93). Similarly, the CV of Tyr-His(dimethylbutyl) showed reversible electrochemistry where the difference in the size of the oxidation and reduction peak currents, decreased from 5 fold at 0.1 V/s, to 1.3 fold at 2 V/s. This suggests that almost all of the radical products of Tyr-His(trimethyl) and Tyr-His(dimethylbutyl) could be reduced at 2 V/s scan rates. Furthermore, the faster scan rates resulted in a positive shift in E_p^{ox} of all compounds. This is a property of irreversible and quasi-reversible reactions (see Methods) where the oxidation reaction at the electrode surface cannot occur fast enough to match the applied potential. The reactions with tyrosine and Tyr-His(dimethyl) were irreversible because the oxidation kinetics were slower than the chemical side reaction of the oxidised product. The reactions with Tyr-His(trimethyl)

and Tyr-His(dimethylbutyl) were reversible because the oxidation kinetics were still slow, but the radical product was sufficiently stable to be available for reduction.

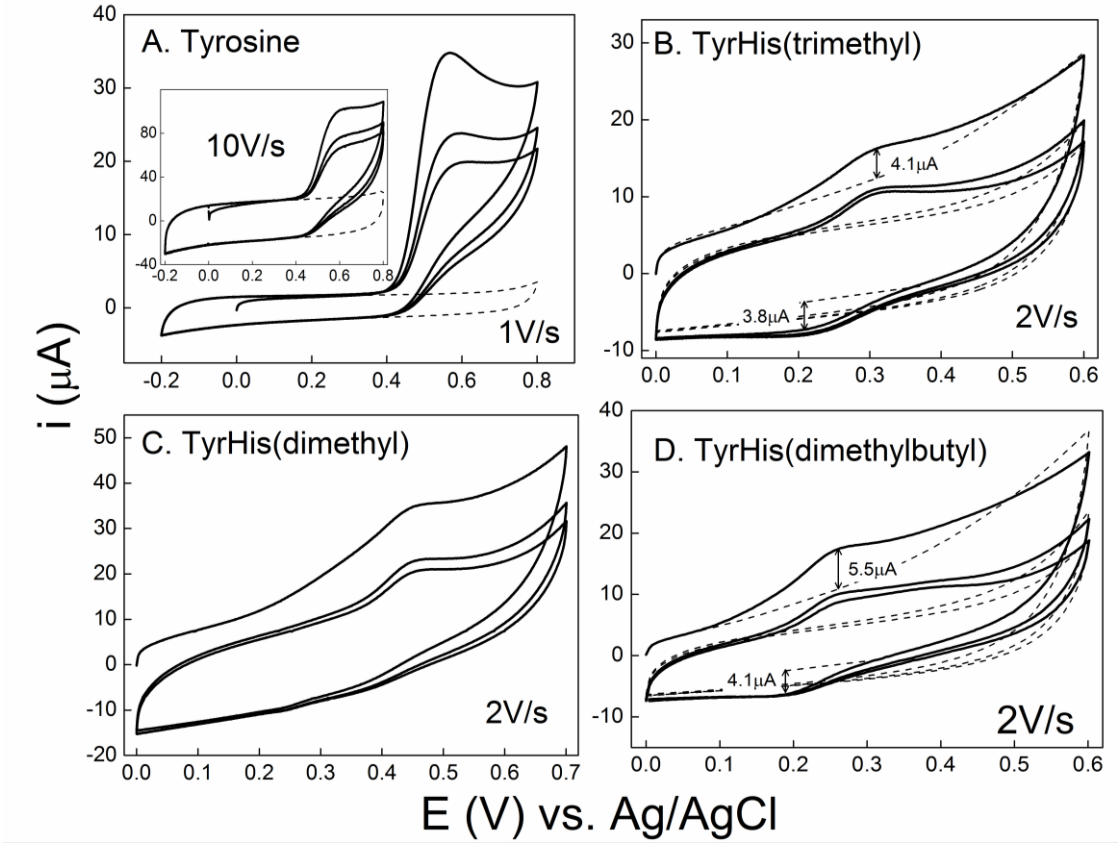

Figure 5-6. Effect of increased scan rate.
CVs are of A. 0.5 mM tyrosine at 1 V/s and 10 V/s, B. 0.2 mM TyrHis(trimethyl) at 2 V/s, C. 0.2 mM TyrHis(dimethyl) at 2 V/s, and D. 0.2 mM TyrHis(dimethylbutyl) at 2 V/s. Three consecutive scans were measured for each compound. The dashed lines are scans of the blank solvent (A, B and D).

The stability of Tyr-His(trimethyl) and Tyr-His(dimethylbutyl) radicals were measured in different solvent conditions. To decrease the rates of the side-reactions, the effects of solvent viscosity were tested with glycerol:buffer solutions (Figure 5-7). At 0.1 V/s, this resulted in better defined oxidation and reduction peaks, with shallow baseline slopes. However, the ratio of the peak currents remained the same as those measured in Figure 5-3.

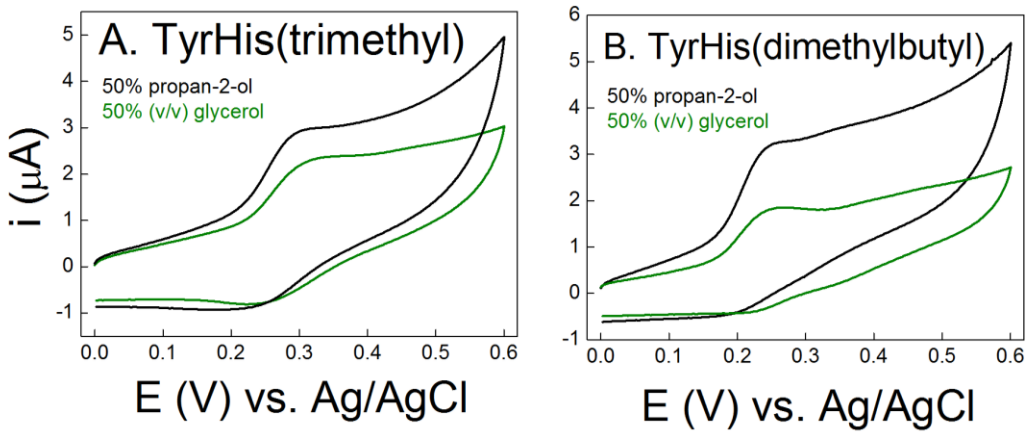

Figure 5-7. Effect of glycerol compared to propan-2-ol.
CVs of A. 0.2 mM TyrHis(trimethyl) and B. 0.2 mM TyrHis(dimethylbutyl) measured in 50 % (v/v) propan-2-ol (black) or 50 % (v/v) glycerol (green) in 20 mM KPi, 500 mM KCl at pH 13 using GC electrode and 0.1 V/s scan rate.

5.3.7 Summary of optimal electrochemical conditions

The midpoint potentials, oxidation/reduction peak potentials, and peak current ratios are summarised in Table 5-1. Since TMP, TBP and Tyr-His(trimethyl) displayed reversible electrochemistry with a stable enough 1-electron oxidation, these compounds were taken forward for combined electrochemistry-IR spectroscopic analysis.

Table 5-1. Summary of electrochemical properties of all compounds.
Table shows the optimal solvent conditions for each compound and, for those compounds that exhibited reaction reversibility, the midpoint potentials, peak current ratios and the electrons transferred. Midpoint potentials were determined from scans shown in Figure 5-3 using GC at 0.1 V/s scan rate.

Compound	***Solvent***	***E_m vs. Ag/AgCl***	***$I(i^a_p / i^c_p)I$***	***1 or 2 e- oxidation***	***Reversible reaction***
Tyrosine	*0.1 M KPi pH 11*	-	-	Combination	No
TMP	*57 % (v/v) ethanol 0.1 M KPi pH 11*	-0.015	1	1	Yes
TBP	*As above*	+0.12	1.3	1	Yes
Tyr-His(trimethyl)	*50 % (v/v) propan-2-ol 20 mM KPi, 500 mM KCl pH 13*	+0.27	2.14	Combination	Yes
Tyr-His(dimethyl)	*As above*	-	-	2	No
Tyr-His (dimethylbutyl)	*As above*	~0.23	5	1	Mild

5.3.8 UV/Visible spectroscopic characterisation

TyrHis(trimethyl) was characterised using UV/visible spectroscopy. Three characteristic absorbance spectra were observed in acid, alkaline and neutral solvent (Figure 5-8), consistent with the structure having two protonatable groups, one on the phenol group and another on the imidazole group.

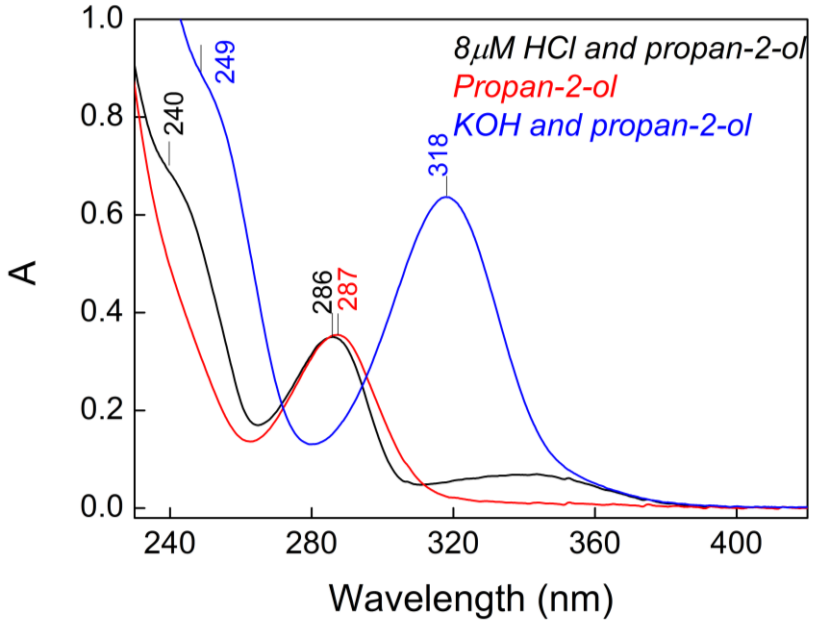

Figure 5-8. UV/visible absorbance spectra of TyrHis(trimethyl) in the fully protonated (red), intermediate (propan-2-ol), and fully deprotonated states (blue) (230-430nm).
100 μM TyrHis(trimethyl) was dissolved in propan-2-ol to give the intermediate spectrum (black) HCl was added to give the protonated spectrum (red) or KOH was added to give the deprotonated spectrum (blue).

The pK_a values of the two protonatable sites were determined by pH titration of the UV-visible spectra (Figure 5-9A). Plots were made of 'peak 1' position vs. pH and of 'peak 2' absorbance intensity vs. pH (Figure 5-9A and B). The Henderson-Hasselbalch equation was used to estimate pK_a values that were found to be 6.8 ±0.4 and 9.2 ±0.2. Errors were determined by fitting the data with pK_a values with boundaries that accommodated the most scattered data points (Figure 5-9B and C, grey lines).

$$pH = pK_a + \log_{10}(\text{deprotonated/protonated})$$

$$(10^{(x- pKa)}/ 1+10^{(x- pKa)}) \text{ x range}) + \text{offset} = y$$

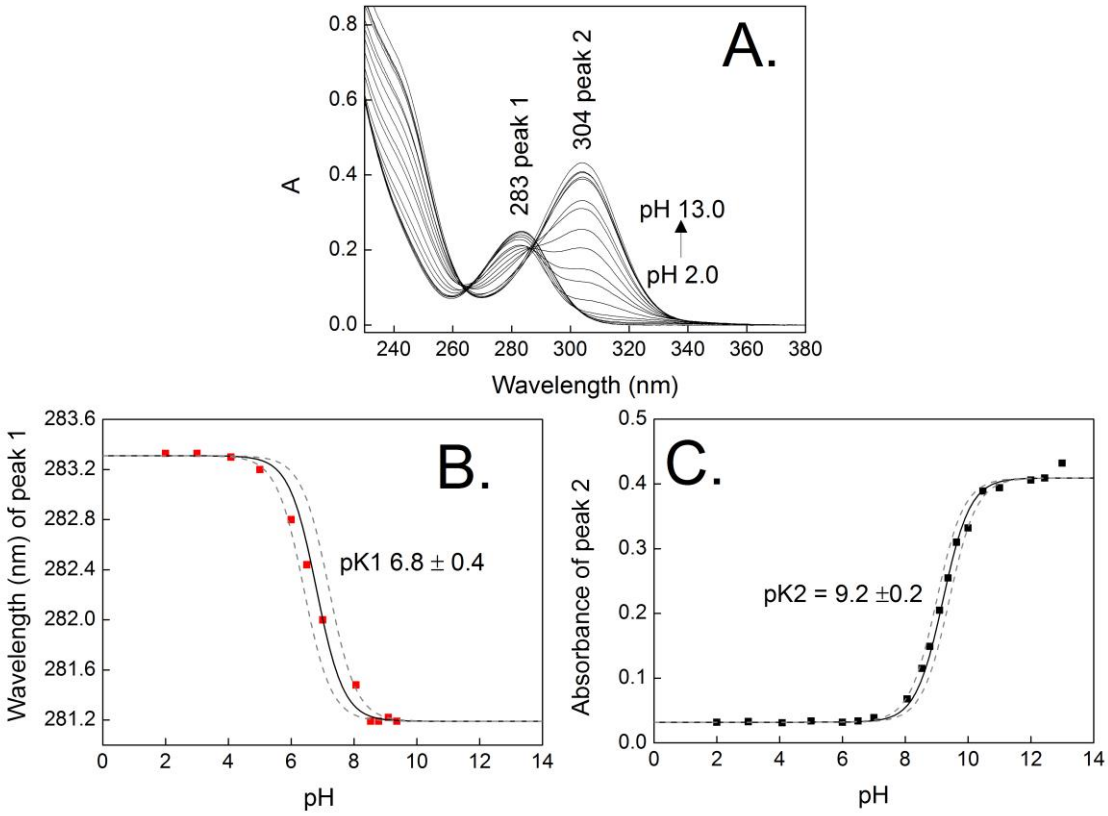

Figure 5-9. A. UV/visible absorbance spectra showing a pH titration of TyrHis(trimethyl) (230-380 nm). Henderson-Hasselbalch fit on (B) peak 1 position vs. pH and on (C) peak 2 absorbance intensity vs. pH.
Errors were determined by fits that covered the furthest point from the best fit (grey). Peak 1 positions were determined after subtraction of the peak 2 component from the spectrum. 50 µM TyrHis(trimethyl) was prepared in 20 mM KPi 500 mM KCl at pH values from pH 2 to 13.

The pK_a of 6.8 ±0.4 was assigned to the imidazole group and the pK_a of 9.2 ±0.2 to the phenol group. These transitions are summarised in Figure 5-10.

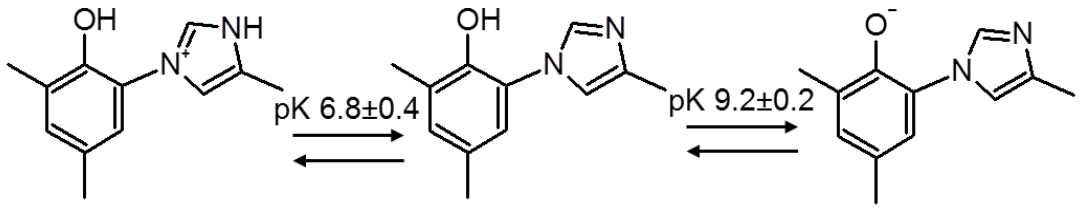

Fully Protonated
3-(2-hydroxy-3,5-dimethylphenyl)
-5-methyl-1*H*-imidazol-3-ium

Imidazole deprotonated
2,4-dimethyl-6-(4-methyl-
1*H*-imidazol-1-yl)phenol

Fully deprotonated
2,4-dimethyl-6-(4-methyl-
1*H*-imidazol-1-yl)phenolate

Figure 5-10. Structures of the fully protonated, neutral and fully deprotonated TyrHis(trimethyl).
The pK_a of each transition is labelled; the chemical names are also given.

5.3.9 IR absorbance spectra of TBP and TMP

The IR absorbance spectra (1800-1100 cm^{-1}) of protonated and deprotonated TMP and protonated TBP are shown in Figure 5-11. The pH sensitive IR bands of TMP are highlighted where the methoxy group IR band at 1598 cm^{-1} shifted to a higher frequency, 1650 cm^{-1} in alkaline conditions. The absorbance spectra are consistent with those recorded by Webster, 2003 [224].

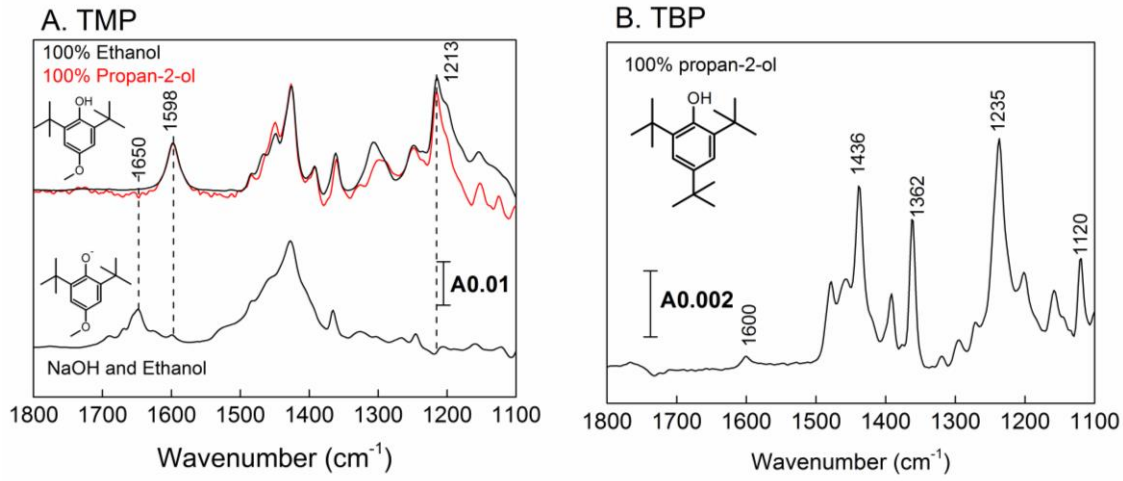

Figure 5-11. IR absorbance spectra (1800-1100 cm^{-1}) of (A) TMP and (B) TBP.
0.2 M TMP was recorded in ethanol (black) and in propan-2-ol (red) to give the protonated state and in 90 % (v/v) ethanol 0.1 M NaOH to give the deprotonated state. 0.05 M TBP was recorded in propan-2-ol (black).

5.3.10 IR absorbance spectra of TyrHis(trimethyl) compared to Gaussian predicted spectra

In comparison to individually recorded phenol and imidazole IR spectra, the IR spectrum of TyrHis(trimethyl) may be altered due the structural influence of the covalent cross-link between the phenol and imidazole group. Hence, predicted IR absolute spectra of each protonation state were calculated using Gaussian03 [167]. Initially, the geometry was optimised to give the energy minimised structure of each protonation state (Figure 5-12), and then the IR normal vibrational modes were computed (Figure 5-13). The majority of the measured peaks were consistent with the calculated spectra and so could be assigned to specific normal modes. The calculated spectrum of fully deprotonated TyrHis(trimethyl) was the least similar to the measured spectrum. This structure has a negative charge that most likely interacts with water molecules in the solvent. Therefore, a water molecule was added to the Gaussian-predicted structure close to the O^- group of phenol (Figure 5-12C). The resulting

hydrogen bond interaction caused some peak shifts. The most dramatic shift was that of the combination band of the C-O^- stretch, phenol and imidazole ring structural changes from 1525 cm^{-1} (without water) to 1500 cm^{-1} (with water). The latter frequency was consistent with the measured spectrum. The normal vibrational modes calculated with Gaussian were used to make tentative assignments of the measured IR bands (Table 5-2).

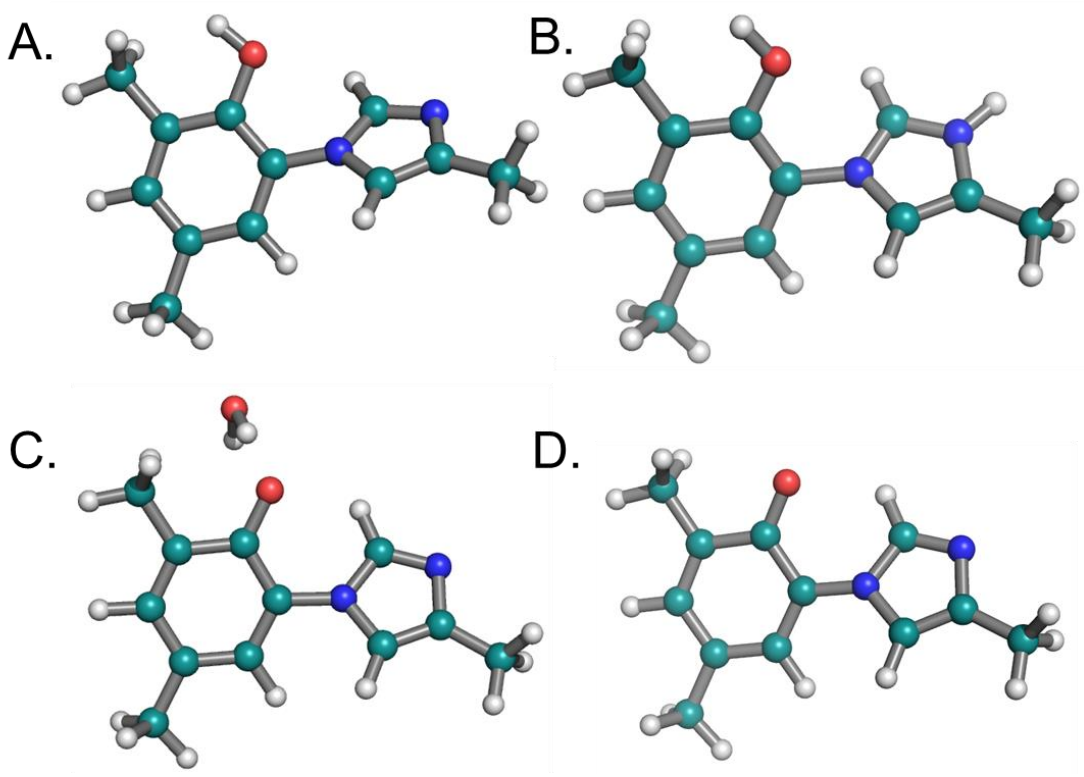

Figure 5-12. Optimised geometry of TyrHis(trimethyl).
A. Fully protonated, B. neutral, C. fully deprotonated with water, D. neutral radical. Gaussian was used to optimise their structures, their calculated IR absorbance spectra are shown in Figure 5-13. The calculated radical IR absorbance spectrum is shown in Figure 5-15.

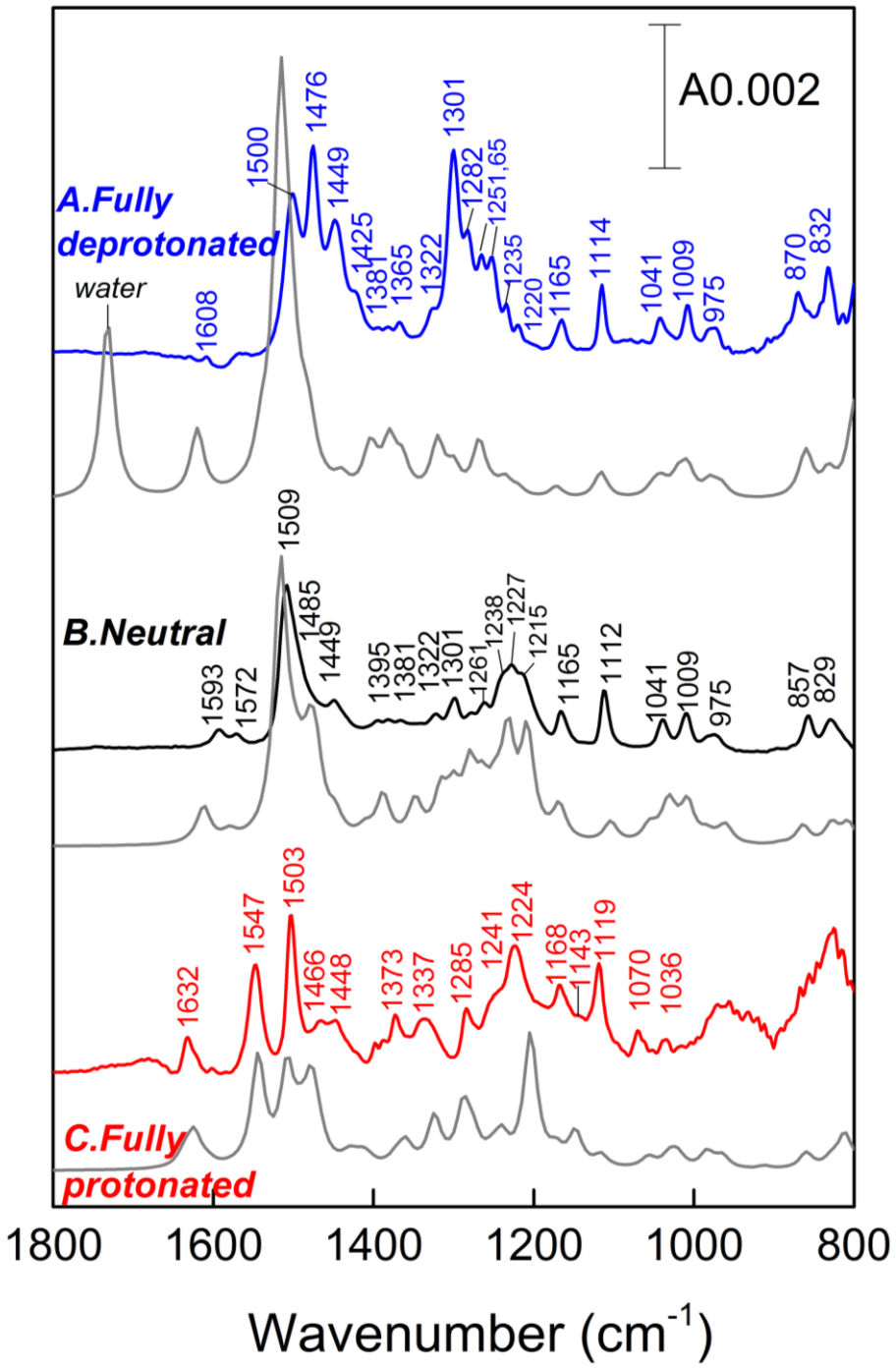

Figure 5-13. Comparison of measured IR absorbance spectra of TyrHis(trimethyl) to Gaussian calculated spectra (1800-800 cm^{-1}).
A. fully deprotonated (phenol and imidazole deprotonated, -1 net charge), the peak at 1730 cm^{-1} is of a water vibrational mode. B. neutral (imidazole deprotonated, 0 net charge), C. fully protonated (imidazole protonated, +1 net charge). Samples of measured spectra were prepared in 20 mM KPi 500 mM KCl pH 13 to give the deprotonated spectrum and in 100 % propan-2-ol and dried onto the IR prism with nitrogen gas for the neutral spectrum and in 500 mM KPi 500 mM KCl pH 2 for the fully protonated spectrum. Gaussian calculated spectra were determined using the B3LYP 6-31g(d) method and an IR frequency scaling factor of 0.9614. IR band assignments are summarised in Table 5-2.

Table 5-2. Tentative assignment of the IR modes of TyrHis(trimethyl) in the fully protonated, neutral and deprotonated states.
Band positions are taken from Figure 5-13, assignments were made based on Gaussian normal mode predictions using the B3LYP 6-31g(d) method.

Tentative assignment	***Fully protonated***		***Neutral***		***Fully deprotonated***	
	Freq (cm^{-1})	***+Associated modes***	***Freq (cm^{-1})***	***+Associated modes***	***Freq (cm^{-1})***	***+Associated modes***
water bend					1732	
Phenol defined normal modes and associated his ring mode	*v*8a 1632 *v*19b1448 *v*14 1373 *v*3 1337	+δ(N^2-H) +δ(N^2-H),3δ(CH_3) +δ(N^2-H),*v*(N^2C^9),*v*($C^{10}H_3$) +*v*(C^6-N^1)	*v*8b 1593 *v*19a 1509 *v*15 1449 *v*14 1322 *v*3 1367 *v*19b 1261	(w/o his) +δ($C^{12}H_3$),*v*(C^6N^1) +3δ(CH_3) - (w/o his ring) +3δ(CH_3)	*v*8a 1608 *v*7a 1500 *v*15 1449 *v*18a 1381 *v*9a 1365 *v*9b 1322 *v*3 1283 *v*7b 1265/51 *v*15 1235 *v*18a 1165	- - - +3δ(CH_3) +3δ(CH_3) - +δ($C^{11,12}H_3$) +3δ(CH_3) +(w/o his ring) +*v*(C^6N^1)
His ring mode	1143	+*v*(N^2C^7)+δ(C^7H)+δ(N^2H)	1572 1485 1041 1009	+δ($C^{10}H_3$),*v*(C^8C^9) +3δ(CH_3),*v*(N^2C^7) +3δ(CH_3) +δ(C^8H),δ($C^{10}H_3$)	1476 1041 1009	+*v*(CO),*v*(N^2C^7),3δCH_3 +(ring exp),3δ(CH_3) +δ(C^8H),δ($C^{10}H_3$)
Tyr ring mode	1503	+*v*(C-OH),δ($C^{12}H_3$)	975	+3δ(CH_3)	975	+3δ(CH_3)
Other Tyr+His ring modes+ δ(CH)+ δ(COH)	1285 1168 1119	+*v*(N^2-C9),δ(N^2H),δ(C-O-H),δ(C^5H) +*v*(C^6N^1),δ(N^2H) +3δ(CH_3)	1301 1238 1227 1165 1112	+*v*(C-OH),δ(C-O-H),*v*(N^2-C^9),δ($C^{10}H_3$) +δ(C-O-H),δ(CH) +δ(C-O-H),δ(CH) +*v*(C^6N^1) +3δ(CH_3)	1114	+δ(CH_3),without δ(COH)
V(C^6N^1)	1547 1337 1168	+δ(N^2H),his mode +*v*3,his ring mode +tyr,his ring,δ(C-O-H),δ(C-H),δ(N^2H)	1381 1165	+3δ(CH_3),tyr,his modes +tyr,hismodes,δ(CH),δ(COH)	1301 1165	+his ring mode,δ($C^{10}H_3$) +*v*18a,his ring mode
3δ(CH_3)	1466 1070		1395 1009	- δ($C^{10}H_3$) only	1425	-
δ(C-O-H)+ all δ(C-H)	1241 1224 1036	+*v*(C-OH),δ(N^2H) - Only δ($C^{10}H_3$),δ($C^{7,8}$H)	1215 857 829	+*v*(C^9C^{10}) Only δ(C^3H) Only δ(C^5H)	1219 870 832	Only δ($C^{7,8}$-H) Only δ(C^3H) Only δ(C^5H)

5.3.11 Reduced minus oxidised (radical) IR difference spectra

Figure 5-14 shows the reduced *minus* radical (oxidised) difference spectra of TMP, TBP and TyrHis(trimethyl). In general the positives are of the deprotonated compound and negatives are of the oxidised phenoxyl radical. Spectra shown of TMP and TBP are an average of 5 and 3 successive redox cycles of the same sample. Although the CVs of TyrHis(trimethyl) showed reversible electrochemistry, the sample prepared for IR spectroscopy, showed irreversible electrochemistry. This was possibly due to the instability of the radical at high concentration that was used for IR spectroscopy (10 mM) compared to CV (0.2 mM). This might explain why the yield of the induced radical was much less (smaller negative IR features) (Figure 5-14, black). The experiment was also repeated in 50 % (v/v) glycerol, 20 mM KPi, 500 mM KCl, pH 13, since the CVs showed reversible electrochemistry in this solvent. However, the compound had irreversible electrochemistry in the IR spectroscopy setup (data not shown). Figure 5-14 highlights IR bands that are shared across all 3 structures and those that will be discussed.

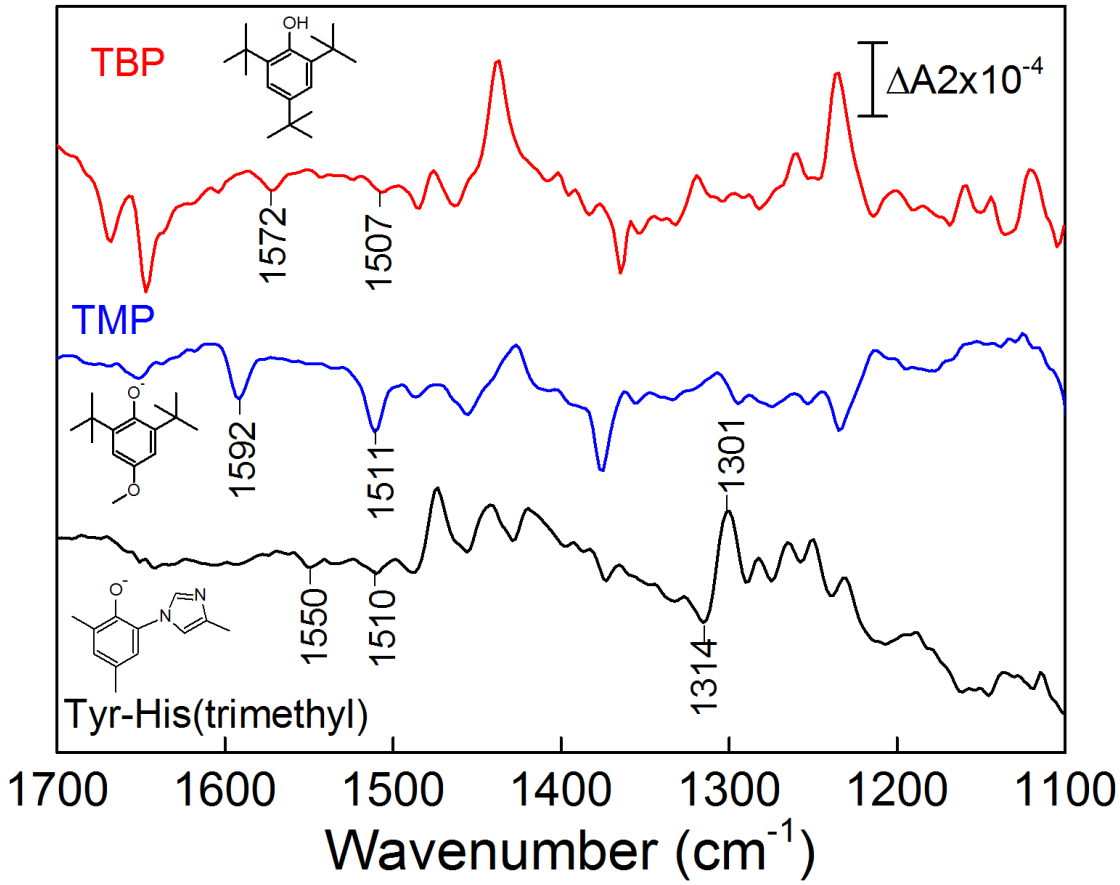

Figure 5-14. Reduced minus oxidised IR spectrum of TBP (red), TMP (blue) and TyrHis(trimethyl) (black).
Samples were prepared in 50 % (v/v) propan-2-ol, 20 mM KPi 500 mM KCl, pH 13. TBP (red); -0.1/+0.4 V reduction/oxidation, spectrum is an average of 3 redox cycles. TMP (blue); -0.20/+0.15 V reduction/oxidation, average of 5 redox cycles, equilibration times were 5mins in each direction. TyrHis(trimethyl) (black) electrochemistry was irreversible, spectrum is an average of 10 oxidations at +0.5 V vs. a reduced baseline at -0.5 V of 10 freshly prepared samples. Equilibration times were 10 mins. Each spectrum was corrected for propan-2-ol, water and water vapour changes. All spectra were normalised to give a 10 mM concentration.

5.3.12 Detailed assignment of reduced minus oxidised (radical) spectrum of Tyr-His(trimethyl)

Gaussian calculated IR spectra of the deprotonated TyrHis(trimethyl) and radical state of TyrHis(trimethyl) were used to calculate a reduced *minus* oxidised (radical) IR difference spectrum (Figure 5-15). However, the difference spectrum shared little resemblance to the measured spectrum. This was most likely due to shifts in the peak positions of each calculated absolute spectrum that would impact the IR features drastically in the difference spectrum. Hence this spectrum was not used for assignment.

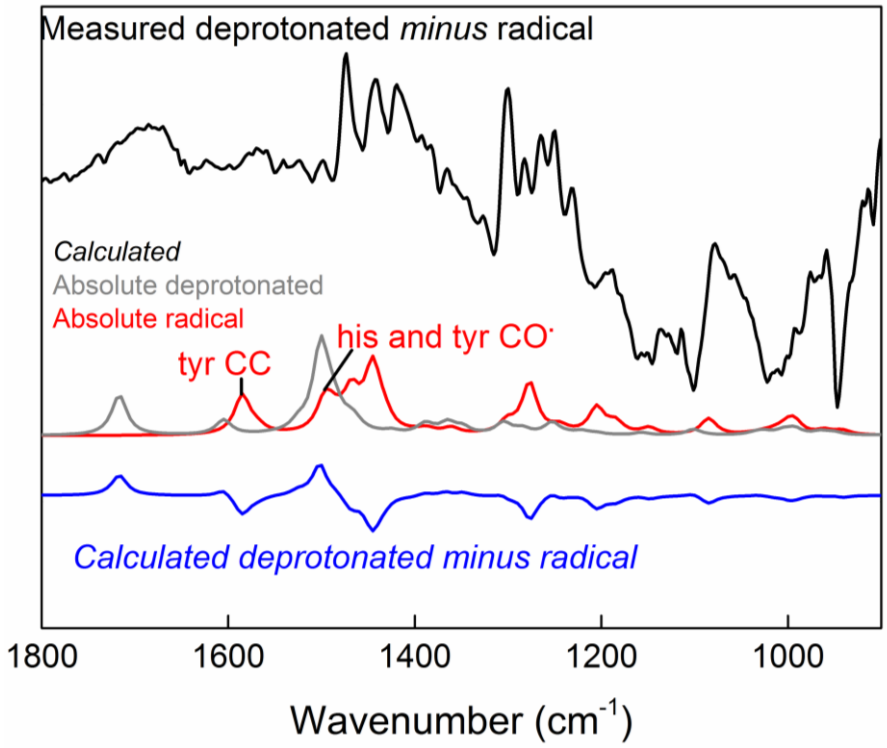

Figure 5-15. Comparison of Gaussian calculated and experimentally recorded reduced minus oxidised (radical) IR difference spectrum of TyrHis(trimethyl).
Calculated absolute IR spectra of the deprotonated (grey) and radical (red) are overlaid, their difference is shown in blue.

Therefore assignments were based on literature assignments of ground and radical states of phenol and imidazole structures [221] and a Tyr-His model compound (1-o-phenol(acetyl)histidine methyl ester) [222], as well as with the Gaussian predicted ground state assignments reported here in Table 5-2. Tentative assignments of the IR bands labelled in Figure 5-16 are summarised in Table 5-3, the majority of which agree with the literature reports.

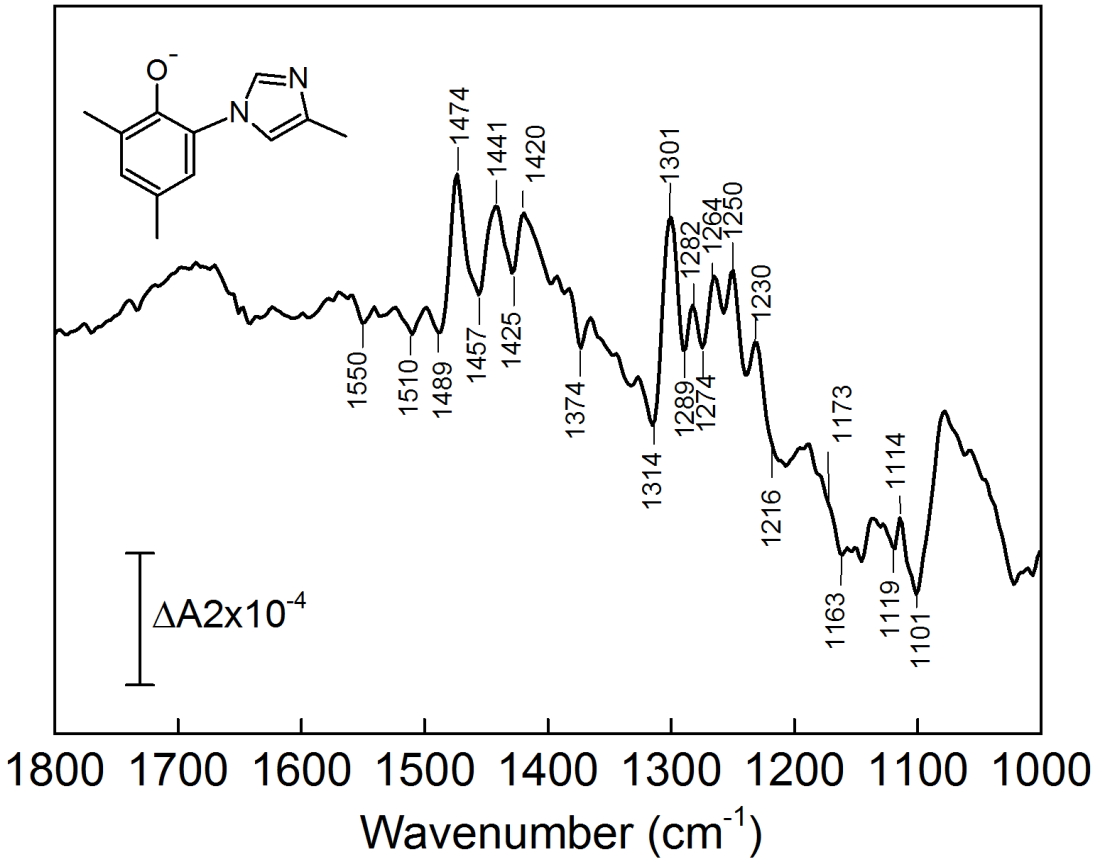

Figure 5-16. Reduced minus oxidised (radical) IR spectrum of TyrHis(trimethyl). *Spectrum is redrawn from Figure 5-14.*

Table 5-3. Tentative assignment of the reduced minus oxidised IR difference spectrum of Tyr-His(trimethyl).
Assignments are made by comparison to literature values [221,222,224] and Gaussian predicted assignments.

Tentative assignments	***Band positions (cm^{-1}) (+) reduced, (-) oxidised(radical)***
v8b(C-C) (2) v8a(C-C) (3)	1550(-)
v7a(C-O·)	1510(-)
v19b (2) or his ring mode+3δCH_3	1489(-)
His ring stretch (1) or coupled Tyr+His ring stretches	1474(+)/1457(-)
v14 +δCH_3 (2) or v3+his ring+δ($C^{11,12}H_3$)	1282(+)/1289(-)
v7b +his ring+3δ(CH_3)	1250(+)
v9a (2) or v18a+his ring and v(C^6-N^1)	1173(+)/1163(-)
δCH_3 (2)	1441(+) 1420(+)/1425(-) 1374(-)
His ring stretch (1)	1301(+)/1314(-)
His ring stretch (2) or v7a'C-O str (1) or v7b +his ring +3δCH_3	1264(+)/1274(-)
His ring stretch NCN stretching (2) or v15 of tyr	1230(+)/1216(-)
His ring stretch (2) or Tyr+His ring modes+ δ(CH)+ δ(COH)	1114(+)/1119(-)

(1) Cappuccio, et al., (2) Berthomieu, et al., (3) Webster,

5.3.13 Perfusion-induced reduced minus oxidised visible and IR difference spectra of bovine CcO

The experimentally generated P intermediate of C*c*O is referred to as P_M [64,65]. Before the P_M (associated radical) catalytic intermediate of bovine C*c*O was induced, the oxidation state of C*c*O had to be in the fast CO-reactive oxidised state. In order to achieve this, the layer was fully reduced and then reoxidised [229]. Reduced *minus* oxidised visible spectra showed a positive at 605 nm, characteristic of reduced C*c*O [188]; this confirmed that the reaction was complete during reduction and reoxidation (Figure 5-17, black trace). A baseline of oxidised C*c*O was then recorded. The P_M state was generated by perfusion of aerobic 20 mM KCl 100 mM CHES pH 9.0 that had been bubbled for 2 mins with CO gas. After 5 mins, the visible spectra showed the reaction was complete due to a positive at 607 nm that is characteristic of the P_M state (Figure 5-17, red trace) [51,64]. The extinction coefficient for $\Delta A_{607-630}$ of the P_M state *minus* oxidised visible spectrum (10.4 $mM^{-1}.cm^{-1}$), is ~2.5 fold smaller than for $\Delta A_{605-621}$ of the reduced *minus* oxidised spectrum (25.7 $mM^{-1}.cm^{-1}$). Thus based on their relative intensities, it was possible to estimate the yield of P_M state formed. It was estimated to be an average of 75 %.

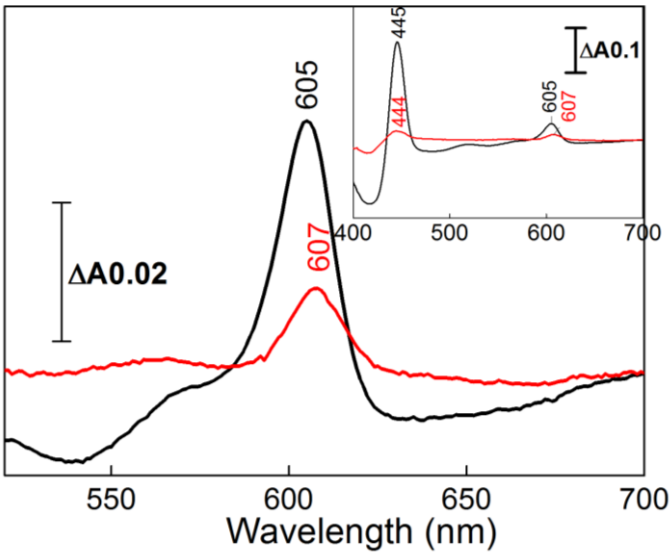

Figure 5-17. Reduced minus oxidised (black) and P_M minus oxidised (red) visible difference spectra of bovine CcO (520-700 nm).
Inset shows the full measurable range of 400-700 nm. Spectra were taken simultaneously with IR spectra. The protein layer was reduced by perfusion of degassed 100 mM CHES 20 mM KCl pH 9.0 with 4 mM sodium dithionite, a baseline was taken, oxidation was induced with aerobic buffer without dithionite, to give the oxidised minus reduced difference spectrum that has been inverted in the figure (black). A baseline was taken of the oxidised state and the P_M state was induced by perfusion with the same buffer that had been bubbled with CO gas to give the P_M minus oxidised difference spectrum (red).

The reduced *minus* oxidised IR difference spectrum is shown in Figure 5-18 using the regular silicon ATR-IR prism to record in the 2000-1000 cm^{-1} range, and again using a diamond ATR-IR prism to record at a lower frequency range of 1800-700 cm^{-1}. The spectrum is consistent with the electrochemically-induced reduced *minus* oxidised IR difference spectrum shown in Chapter 3 and literature [104,196,197]. In general the spectrum is dominated by redox-induced amide I shifts (primarily C=O bond stretches) in the 1690–1600 cm^{-1} range, which arise from primarily conformational and environmental changes in the polypeptide backbone, and changes in the 1550–1500 cm^{-1} range that arise from primarily haem and amide II changes. A wide range of additional smaller changes in the 1800–1000 cm^{-1} range arise from individual amino acids and the redox cofactors themselves.

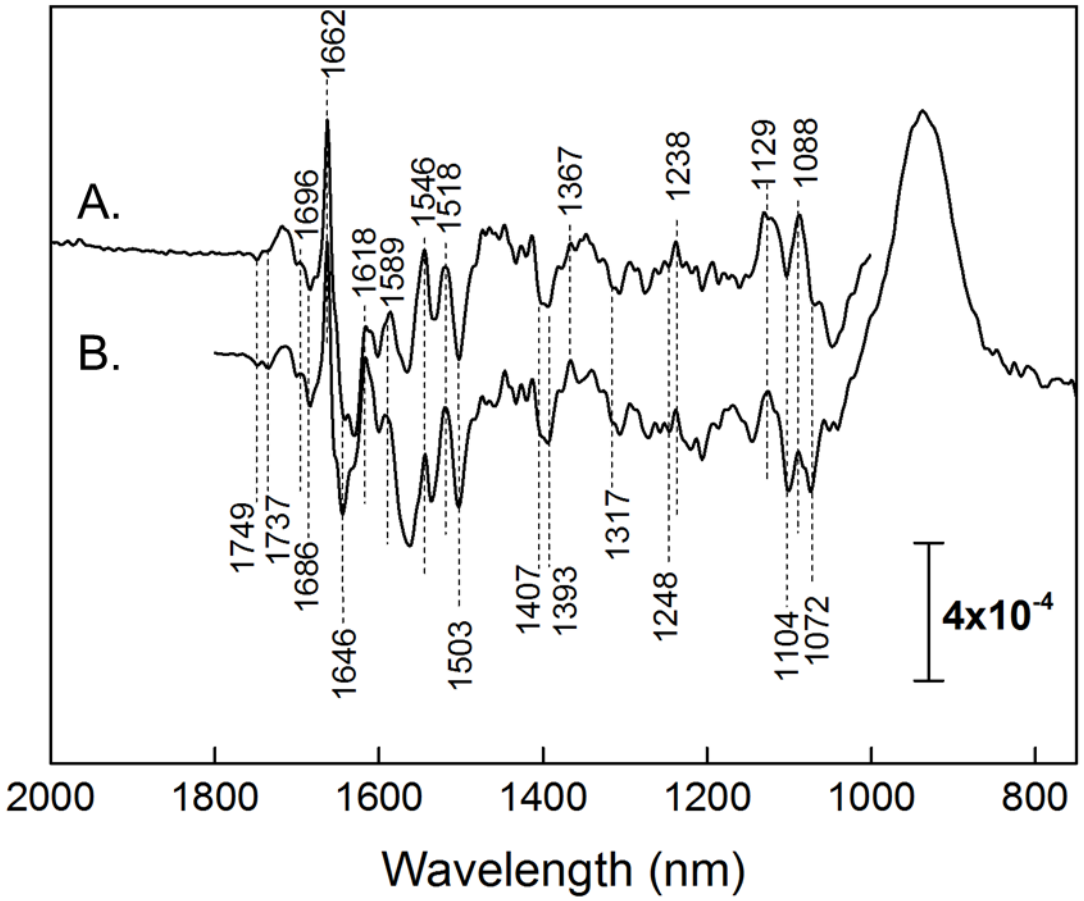

Figure 5-18. Perfusion-induced reduced minus oxidised IR difference spectra of bovine CcO measured using a silicon ATR IR prism (Trace A) and also with using a diamond ATR-IR prism (Trace B).
Transitions between fully reduced and oxidised states were induced by alternating perfusion of degassed 100 mM CHES 20 mM KCl pH 9 with 4 mM sodium dithionite for reduction and aerobic buffer without sodium dithionite for oxidation. A silicon ATR IR prism was used to record in the 2000-1000 cm^{-1} range, spectrum is an average of 4 redox cycles. Diamond ATR IR prism was used to record in the 1800-750 cm^{-1} range, spectrum is an average of 18 redox cycles. Spectra were normalised based on ΔA_{II} of the absolute spectrum before averaging and corrected for pH change, protein layer expansion/contraction, and dithionite contributions by iterative subtraction of reference spectra.

5.3.14 Perfusion-induced P_M minus oxidised IR difference spectra of bovine CcO

The P_M *minus* oxidised IR difference spectrum is shown in Figure 5-19. The positive IR bands are of the CO/O_2 perfusion-induced P_M state (Cu_A^{2+}, a^{3+}, Cu_B^{2+}, a_3^{4+}=O^{2-}) and the negative features are of the oxidised state (Cu_A^{2+}, a^{3+}, Cu_B^{2+}, a_3^{3+}). The spectrum is dominated by protein and haem structural changes that arise from the ferric to ferryl transition. This includes a ligation state change of haem a_3, and changes associated with the Tyr-His radical. IR features that could be assigned to an associated tyrosine radical species, will be discussed below.

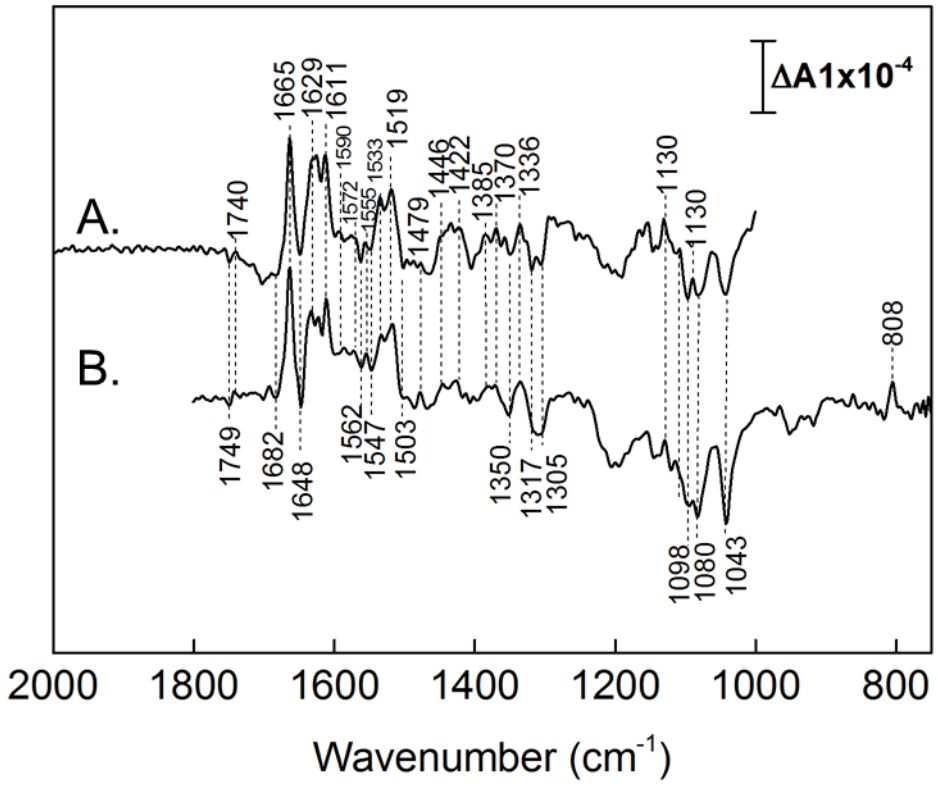

Figure 5-19. Perfusion-induced P_M minus oxidised IR difference spectrum of bovine CcO measured using a silicon ATR IR prism (Trace A) and also with using a diamond ATR-IR prism (Trace B).
The transition from fully oxidised to P_M state was perfusion-induced by switching from aerobic 100 mM CHES pH 9, 20 mM KCl (fully oxidised) to the same buffer that had been bubbled with CO gas (P_M state). Spectra in both IR ranges (Trace A. silicon ATR IR prism; 2000-1000 cm^{-1} Trace B. diamond ATR IR prism; 1800-750 cm^{-1}) are an average of 4 oxidations of 4 separate protein layers. Spectra were normalised based on ΔA_{II} of the absolute spectrum before averaging.

5.3.15 Isotope $^{18}O_2$ to assign 808 cm^{-1} to $Fe^{4+}=O^{2-}$ stretch

Resonance Raman spectroscopy has detected a band at 803 cm^{-1} that has been assigned to the $Fe^{4+}=O^{2-}$ stretch in the P_M state of bovine C*c*O. This band downshifted by 40 cm^{-1} when formed with the ^{18}O-isotope [57-59]. Therefore the IR spectrum in the low frequency region was measured, as it is where the metal-ligand vibrational modes absorb. IR band observed at 808 cm^{-1} in the $^{16}O_2$ P_M *minus* oxidised IR difference spectrum disappeared in the spectrum measured in the presence of $^{18}O_2$-isotope (Figure 5-20). Hence, the 808 cm^{-1} band has been tentatively assigned to the $Fe^{4+}=O^{2-}$ stretch of the P_M intermediate.

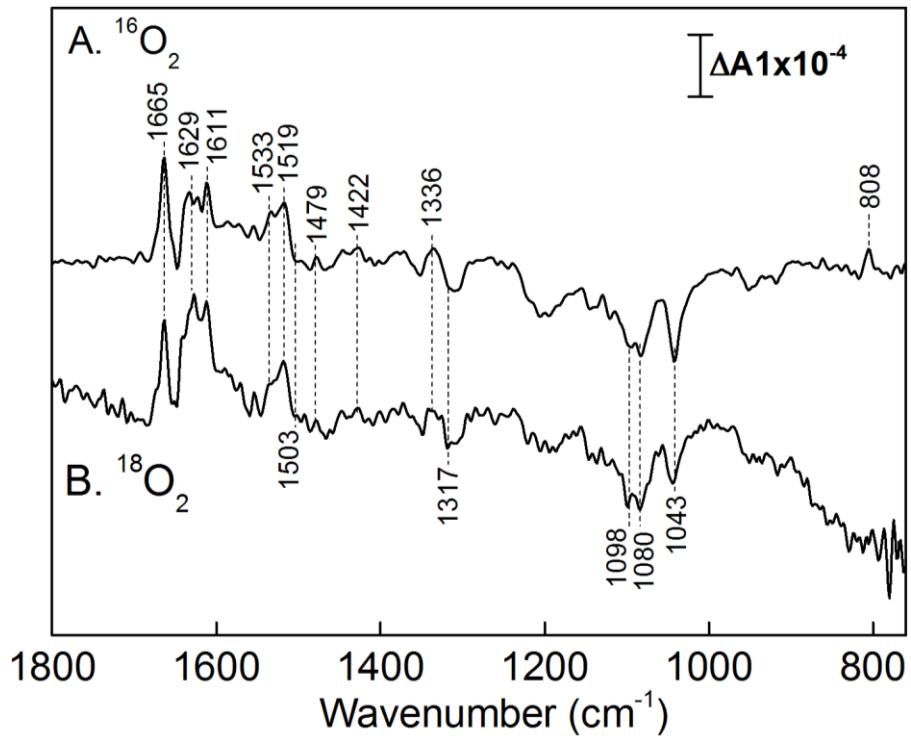

Figure 5-20. Effect of isotope $^{18}O_2$ on the perfusion-induced P_M minus oxidised IR difference spectrum of bovine CcO.
Trace A (1800-750 cm^{-1}) is taken from Figure 5-19. Trace B was measured in the same conditions as Trace A using a diamond ATR prism, however the oxidation buffer was degassed with argon to remove $^{16}O_2$ and was bubbled with $^{18}O_2$. To induce the P_M state, the $^{18}O_2$-containing buffer was bubbled with CO gas. Trace B is from a single experiment (4000 interferograms vs 1000 interferograms background), the spectrum has been normalised to Trace A based on their absolute ΔA_{II} intensity.

5.4 Discussion

Radical forms of amino acids are thought to play key roles in the catalytic mechanisms of many types of proteins, including C*c*O (reviewed in Berthomieu, *et al.* [230]). The experimentally generated P and F intermediates of C*c*O are designated P_M [64,65] and F [52,67,68]. Isotope labelling and site-directed mutagenesis of tyrosine [108,186], and H/D exchange [186,197,231] has so far enabled tentative assignments of IR changes, associated with the experimentally induced O to P_M transition in bacterial oxidases [186]. Definitive assignmnent of IR bands associated with a tyrosine radical species, in a protein spectrum, requires reference spectra of model compounds. Model compounds of a cross-linked Tyr-His structure, as well as phenol and imidazole structures in their ground state, have provided reference spectra to aid assignment [108,232-234]. Photolysis induced radicals of tyrosine, imidazole and Tyr-His model compounds have provided reference spectra of their radical state [220-223]. However this technique is irreversible and causes large IR baseline distortions. Electrochemistry can provide an alternative approach to reversibly induce radicals (provided they are stable) at an electrode surface, without the addition of chemical agents or UV irradiation [224,225]. When combined with IR spectroscopy, it can allow vibrational structural changes to be followed in both directions (reduction and oxidation), and aid in the identification of redox sensitive IR bands [112-114]. Such spectra can complement the array of UV photolysis induced radical IR reference spectra available in the literature [223,230].

In this project, Tyr-His model compounds were constructed to mimic the conserved structural feature in C*c*O. The structures were adapted with the aim to give reversible electrochemistry, based on the redox active phenol structures; 2,6-di-*tert*-butylmethoxyphenol (TMP) and 2,4,6-tri-*tert*-butylphenol (TBP) [224,225]. To date this has not been achieved (2-imidazol-1-yl-4-methylphenol ([233]- supporting information), or has been achieved in a phenol-benzimidazole construct [235,236], or in cobalt-ligated complexes of phenol-imidazole constructs [237], although the cross link was in the incorrect position (C^6-C^7, numbering is based on structures reported here). The aim of this project was to use cyclic voltammetry to find the best conditions to form stable phenoxyl radicals. The pK_a values of the analogue showing the most reversible electrochemistry were determined by spectrophotometric titration. The optimised electrochemical conditions were combined with ATR-FTIR spectroscopy to record reduced *minus* oxidised (radical) IR difference spectra of the construct. This was compared to the difference spectra of TMP and TBP, which have so far been reported as absolute spectra [224]. Finally, these spectra of the model compounds were used to

make tentative assignments of IR radical bands in the catalytic P_M (oxyferryl associated radical) intermediate of bovine C*c*O.

5.4.1 Cyclic voltammetry

The structures of each compound are shown in Figure 5-1, and their electrochemical properties are summarised in Table 5-1. The irreversible 2 electron oxidation of tyrosine and the decrease in magnitude of the current upon successive scans, is consistent with published data (see Figure 5-4 and Figure 5-5A) [226,228,238]. This has been reported to be due to tyrosine radical polymerisation and adsorption to the electrode surface [226], or a 2 electron oxidation coupled to 2 deprotonations [228,238]. Various phenol structures were investigated as model compounds of tyrosine. Phenol, o- /m- /p- cresol [239], bisphenol A [240], and 4-chlorophenol [241] all give irreversible oxidation peaks. In all of these structures the hydroxyl group is exposed. The reaction of a phenol model compound, TBP at alkaline pH, has previously been characterised as a 1-electron oxidation by coulometry experiments [225,242]. This was later confirmed by EPR spectroscopy of electrochemically oxidised samples of TMP and TBP [224]. In each structure, the hydroxyl group is protected by butyl groups at the *ortho* positions and this stabilises the radical that is formed after oxidation [218]. The cyclic voltammograms of these compounds were reproduced in this report (Figure 5-3B and C) [225]. Consistent with literature, TMP and TBP, exhibited reversible 1-electron electrochemistry at alkaline pH (Figure 5-5B and C and Table 5-1).

The structures of Tyr-His compounds were inspired by TMP and TBP, where C^2 (position-2) and/or C^4 of the phenol group and C^4 of the imidazole, were protected by bulky methyl/butyl groups. CVs of Tyr-His(trimethyl) gave the best 1-electron reversible electrochemistry, where all sites were protected by methyl groups (Figure 5-3D and Figure 5-5D). TyrHis(dimethyl) showed irreversible electrochemistry. In this structure the C-2 site was not protected and most likely underwent further side reactions (Figure 5-3E and Figure 5-5E). Tyr-His(dimethylbutyl) had all sites protected and C^2 was instead protected by a bulkier butyl group, however this did not further improve the stability of the phenoxyl radical and in fact resulted in less reaction reversibility (Figure 5-3F and Figure 5-5F).

5.4.2 Visible spectroscopy

Visible spectroscopy allowed the protonation states and the associated pK_a values of TyrHis(trimethyl) to be determined (Figure 5-9). The pK_a of the imidazole group was

6.8 ±0.4 and the pK_a of phenol was 9.2 ±0.2 (Figure 5-10). The pK_a of the phenol was low in comparison to that of free tyrosine (10.1) [222] and was even lower than that of TBP (12.19) and TMP (12.15) [243]. This suggests the covalent cross link, rather than the bulky groups, is causing the lowering of the pK_a. This finding agrees with a similar Tyr-His cross-linked model compound (1-o-phenol(acetyl)histidine methyl ester) that also has a low pK_a of phenol at 8.34 (imidazole pK_a 5.56) [222] and another (2-imidazol-1-yl-4-methylphenol) with a phenolic pK_a of 8.6 (imidazole pK_a 5.54) [233]. The function of the cross link favours the electron density of the phenolate anion to become delocalised across two rings. In doing so, it becomes thermodynamically more favourable for deprotonation. Furthermore, this cross link is advantageous for C*c*O, as it would lower the pK_a of the tyrosine side chain that may favour its proposed role as a proton and electron donor in C*c*O, at physiological pHs [38,214].

5.4.3 Assignment of IR absorbance spectra of TyrHis(trimethyl)

The overall band pattern of measured IR absorbance spectra of the fully protonated (imidazole protonated, +1 net charge), neutral (imidazole deprotonated) and fully deprotonated (phenol and imidazole deprotonated, -1 net charge) TyrHis(trimethyl) compared well with the computed spectra. Tentative assignments are summarised in Table 5-2.

5.4.3.1 Phenol vibrational modes

Most modes arose from a combination of imidazole and phenol ring vibrational modes. However, it was possible to assign some specific bands, that were in similar positions to previously reported IR assignments [221], to primarily phenol vibrational modes [170]. These include the *v*8a(CC) mode to 1608 cm^{-1} in the fully deprotonated structure, that shifts to *v*8b(CC) 1593 cm^{-1} and *v*8a(CC) 1632 cm^{-1} in the neutral and fully protonated structures, respectively. *v*7a(CO) at 1500 cm^{-1}, *v*9a(δCH) at 1365 cm^{-1}, *v*9b(δCH) at 1322 cm^{-1}, *v*15 at 1275 cm^{-1} and *v*18a(CH) at 1165 cm^{-1}, in the deprotonated structure were also in positions similar to literature assignments of phenol [221]. Additional modes equivalent to *v*15 at 1449 cm^{-1} and *v*18a at 1381 cm^{-1} were also observed, and so were *v*7b(ring mode) at 1265/51 cm^{-1} and *v*3(CC + δCH) at 1283 cm^{-1}. These were not observed in the literature spectra of phenols and may arise from the influence of imidazole ring stretches.

The neutral and fully protonated structures shared the same phenol vibrational modes whose positions shifted ±50 cm^{-1} when imidazole N^2 was protonated. These include *v*8b(CC) 1593 cm^{-1} to 1632 cm^{-1}, *v*14(*v*CC + δCH) 1322 cm^{-1} to 1373 cm^{-1} and *v*3(CC + δCH) 1367 cm^{-1} to 1337 cm^{-1}. Modes of *v*14(vCC + δCH), *v*19a(CC) at 1509

cm^{-1} and *v*19b(CC) at 1448 cm^{-1} are consistent with literature assignments [221]. Modes of *v*15 at 1449 cm^{-1}, *v*3 at 1367 cm^{-1} and *v*19b(CC) at 1261 cm^{-1} were observed as additional modes in the neutral and deprotonated structure.

5.4.3.2 Imidazole ring modes

The band at 1143 cm^{-1} in the fully protonated state, was attributed to a combination of an N^2C^7 ring stretch, C^7-H and N^2-H bends of protonated imidazole [221]. 1041 cm^{-1}, 1009 cm^{-1} band positions of imidazole vibrational modes stayed the same in the neutral and deprotonated structures, where 1041 cm^{-1} is consistent with literature [221]. The large band at 1301 cm^{-1} of the deprotonated structure is a well characterised marker of deprotonated imidazole [221,222].

5.4.3.3 Combined phenol-imidazole ring modes, C^6-N^1 crosslink modes and others

Other bands in the 1300-1100 cm^{-1} region in particular, were attributed to a combination of Tyr and His ring modes in the neutral and fully protonated structure that could not be assigned to defined phenol vibrational modes and were probably influenced by the imidazole ring modes. There were some IR bands that were associated with the crosslink C^6-N^1 stretch as well as ring modes. The 1165 cm^{-1} of the C^6-N^1 stretch was common in all protonation states and could be used as a marker. The large bands at 1547 cm^{-1} (associated with N^2-H bend, ring mode of His and the cross-link stretch) and at 1337 cm^{-1} (assigned to *v*3, ring mode of His and the cross-link stretch) are also observed in the protonated imidazole spectra [221]. Bands at 1301 cm^{-1}, 1238 cm^{-1} and 1227 cm^{-1} were assigned to C-H and C-O-H bending modes in the neutral structure. Other bands in the 1400-1300 cm^{-1} region were attributed to δCH_3 modes [221] and others in the 1240-800 cm^{-1} region to C-O-H and C-H bends. The bands observed at 975 cm^{-1} in the neutral and deprotonated structures were assigned to a combination of phenol ring and $\delta(C^{11}H_3)$ and $\delta(C^{12}H_3)$ modes.

5.4.4 Reduced minus radical difference spectra of model compounds

The reduced *minus* radical IR difference spectra of TBP, TMP and TyrHis(trimethyl) are summarised in Figure 5-14. The redox-induced IR bands of TBP and TMP (1700-1100 cm^{-1}) agreed with the absolute absorbance spectral changes previously reported when monitored from the ground state to the oxidised state [224]. Based on literature assignments, the troughs at 1572 cm^{-1} (TBP) and 1592 cm^{-1} (TMP) have been assigned to the *v*8a(C-C) ring mode and troughs at 1507 cm^{-1} (TBP) and 1511 cm^{-1}

(TMP) have been assigned to *v*7a(C-O$^{\cdot}$) mode of a phenoxyl radical [224]. Tentative assignments of redox-induced IR bands of TyrHis(trimethyl) are summarised in Table 5-3. Most importantly, Tyr-His(trimethyl) also displayed two troughs of equivalent intensity and band width in the 1600-1500 cm^{-1} region at 1550 cm^{-1} and 1510 cm^{-1} and by comparison to TBP and TMP they have also been assigned to *v*8a(C_oC_m) and *v*7a(C-O$^{\cdot}$) modes of a phenoxyl radical, respectively.

TyrHis(trimethyl) displayed a third IR band upon oxidation that could also provide a marker of the cross-linked Tyr-His radical. This was a peak/trough at 1301(+)/1314(-) cm^{-1} and was assigned to a redox linked structural change of the histidine ring when it is cross-linked to the phenol group. Photolysis-induced IR difference spectrum of a similar model compound of Tyr-His, 1-*o*-phenol(acetyl)histidine methyl ester has been measured [222]. Although there are large baseline distortions, this spectrum also displayed an equivalent peak at 1303 cm^{-1} (ground state) with a less defined peak at 1322 cm^{-1} (photolysed radical state). These spectra along with literature spectra can aid assignment of a radical species residing on the cross-linked Tyr-His structure in the P_M (associated radical) *minus* oxidised IR difference spectra of C*c*O.

5.4.5 Assignment of P_M minus oxidised IR difference spectrum of bovine CcO

The reduced *minus* oxidised IR difference spectrum is discussed in Chapter 3 and will not be discussed here. The P_M *minus* oxidised IR spectra of *P. denitrificans* C*c*O is similar to bovine C*c*O (Figure 5-19) [197]. H/Deuterium exchange has allowed assignment of IR bands to protonatable groups. Studies with *P. denitrificans* C*c*O have enabled detailed assignment of P_M *minus* oxidised IR difference spectra through isotope labelling (universally ^{15}N-labelled C*c*O, $^{13}C_6{}^{15}N_3$-histidine labelled C*c*O, $^{13}C_9{}^{15}$N-tyrosine-labeled, ring-$^{13}C_6$-tyrosine-labeled, ring-d_4-tyrosine-labeled C*c*O) [186,187]. The P_M *minus* oxidised spectrum of bovine C*c*O is consistent with previously reported spectra (Figure 5-19) [166,197], and has better defined peaks. Based on the assignment of *P. denitrificans* C*c*O, tentative assignments of the P_M *minus* oxidised spectrum of bovine C*c*O are summarised in Table 5-4.

Table 5-4. Tentative assignment of P_M minus oxidised IR difference spectrum of bovine CcO, bands attributed to a tyr-his radical are highlighted.
Assignments are based on TMP, TBP and TyrHis(trimethyl) reported here and literature assignments from [166,186,187,197,222,231].

TMP/TBP/TyrHis(trimethyl) Reduced minus radical *Frequency (cm^{-1})*	***P_M (radical) (+)minus oxidised(-)*** *Frequency (cm^{-1})*	***Tentative Assignment***
	1749(-)/1740(+)	*Glu (Glu242) (vC=O)*
	1682(-)/1665(+)	*amide I +haem a_3 formyl*
	1648(-)	
	1629(+)	*Tyr amide I*
	1611(+)	*His amide I*
1592(-)(TMP) 1572(-) (TBP) 1550(-) (TyrHis)	1572(+) or 1555(+)	*His-Tyr, possibly neutral phenolic radical ring v8a(C-C) ring stretch*
	1547(-)	*possibly haem a_3 (formerly assigned to C-N bond in His-Tyr)*
	1533(+)	*ferryl haem a_3*
1511(-) (TMP) 1507(-) (TBP) 1510(-) (TyrHis)	1519(+)	*His-Tyr, possibly neutral phenolic radical ring v7a(C-O·)*
	1503(-)	*His-Tyr*
	1479(+)	*ferryl haem a_3*
	1350(-)	*haem a_3*
1314(-) (TyrHis)	1336(+)	*His-Tyr, neutral phenolic radical His ring stretch*
1301(+) (TyrHis)	1317(-)	*His-Tyr*
	1130(+)	*His-Tyr*
	1098(-)	*His-Tyr*
	1109(+)/1080(-)	*His, possibly proximal ligand of haem a_3*
	808(+)	*Fe^{4+}=O^{2-}*

5.4.6 Bands assigned to Tyr-His in the P_M State

5.4.6.1 $CO^{\cdot}$ stretch of a tyrosine radical

The positive at 1519(+) cm^{-1} is observed in bovine, *P. denitrificans* and *Rba. sphaeroides* (1517 cm^{-1}) C*c*O and has been assigned to the *v*7a(C-O·) of a neutral tyrosine radical, and is in a similar range to the IR bands observed in the model compounds. Additional evidence that supports this assignment is that it is unaffected by H/D exchange, and tyrosine labelling causes a downshift of this band to 1479-1483 cm^{-1} in *P. denitrificans* C*c*O [186]. Secondly, this band is absent in the F intermediate of bovine and *P. denitrificans*, a state identical to P_M but where the radical is absent (Cu_A^{2+}, a^{3+}, Fe^{4+}=O^{2-}, Cu_B^{2+}) [197].

5.4.6.2 C-C stretch of a tyrosine radical

The *v*7a(C-O·) mode of a tyrosine radical should be accompanied by a *v*8a(C-C) mode of the phenol ring as observed for TMP, TBP and TyrHis(trimethyl). However, a peak of equal intensity was not obvious from the P_M *minus* oxidised difference spectrum (Figure 5-19). The positive at 1533 cm^{-1}, also observed in *P. denitrificans* C*c*O and *Rba. sphaeroides* C*c*O, would be a candidate however this peak is present in their F intermediates where a radical should not occur, and has been assigned to a haem a_3 vibrational mode [186,231]. There is also a positive at 1590 cm^{-1} that is consistent with previous bovine IR spectra and has been observed in *Rba. sphaeroides* C*c*O [231]. This positive in *P. denitrificans* C*c*O is unaffected by tyrosine labelling or universal ^{15}N labelling and can be ruled out. Furthermore, it is still present in the F intermediate of bovine C*c*O. An alternative candidate is a positive at 1572 cm^{-1} that has been suggested to arise from *v*8a(C-C), since this peak is lost in the F intermediate and is insensitive to H/D exchange in *P. denitrificans* C*c*O. Its behaviour in response to tyrosine labelling, was not conclusive since the signal was small [186]. The spectrum reported here has better signal-to-noise in this region, and as well as the 1572 cm^{-1} band, an additional peak at 1555 cm^{-1} could be assigned to this mode (Figure 5-19). Although the signal-to-noise is low in the literature spectra in this region for bovine C*c*O, it is possible that this positive is also lost in the F intermediate of bovine C*c*O [197]. Overall 1572 cm^{-1} and 1555 cm^{-1} bands are in the same frequency range as those measured with TBP, TMP and TyrHis(trimethyl), and both are possible candidates for a C-C ring stretch of the phenol ring (Figure 5-14).

5.4.6.3 A third IR marker of the Tyr-His radical in CcO

TyrHis(trimethyl) displayed a third IR band upon oxidation that could also provide a marker of the Tyr-His radical in C*c*O. This was a peak/trough at 1301(+) ground state / 1314(-) radical cm^{-1} and this has been assigned to an imidazole ring stretch unique to the cross-linked structure in response to radical formation (Figure 5-16; Table 5-3). The P_M *minus* oxidised difference spectrum also exhibited a trough/peak at 1317(-) oxidised/1336(+) P_M cm^{-1} that has been assigned to the same imidazole ring stretch. This is consistent with previous assignment of the trough associated with the oxidised state at 1317 cm^{-1} that was downshifted in labelled-tyrosine and labelled-histidine C*c*O [186]. Although the peak associated with the P_M state at 1336 cm^{-1} was not discussed it was also downshifted in labelled-tyrosine and labelled-histidine C*c*O and altered/shifted in the F state [186]. Hence, this feature may provide a third IR marker of the tyrosine radical.

5.4.7 Other IR features associated with cross-linked Tyr-His

Similarly, by comparison to *P. denitrificans* C*c*O [186], the negative at 1503 cm^{-1} (1506 cm^{-1} *P. denitrificans* C*c*O*)* has been associated with the cross-linked Tyr-His structure since it is downshifted in tyrosine-labelled C*c*O and lost in the F intermediate. The peak and trough at 1130(+) cm^{-1} and 1098(-) cm^{-1} were assigned to a histidine ring stretch of the cross-linked structure and 1109(+)/1080(-) cm^{-1} to proximal histidine of haem a_3. This is because the equivalent 1130 cm^{-1} and 1098 cm^{-1} IR bands of *P. denitrificans* C*c*O were altered in response to tyrosine-labelling as well as histidine-labelling, whereas all four IR features were sensitive to H/D exchange, global ^{15}N- and histidine-labelling, consistent with a histidine origin.

5.4.8 $Fe^{4+}=O^{2-}$ stretch

The P_M *minus* oxidised IR difference spectrum of bovine C*c*O, recorded using a diamond ATR prism, allowed detection of IR bands in the lower frequency range (1800-750 cm^{-1}) (Figure 5-19), where the metal-ligand vibrational modes absorb. The spectrum was consistent with spectra of bovine C*c*O measured using a silicon ATR prism in the 2000-1000 cm^{-1} range. Resonance Raman spectroscopy has shown a band at 803 cm^{-1} that has been assigned to the $Fe^{4+}=O^{2-}$ stretch in the P_M state of bovine C*c*O. This band downshifted by 40 cm^{-1} when formed with the ^{18}O-isotope [57-59]. The IR band observed at 808 cm^{-1} was also sensitive to ^{18}O, where it disappeared and is assumed to have similarly downshifted into a region, where it cannot presently be resolved. Hence, it is tentatively assigned to the same $Fe^{4+}=O^{2-}$ bond of the P_M intermediate (Figure 5-20). This assignment is further supported by its absence in the reduced *minus* oxidised IR difference spectrum.

5.4.9 Protonation state of tyrosine in oxidised CcO

pK_a of tyrosine in the ground state is ~10, which is lowered to pK_a 8-9 in the cross-linked structure which must favour proton donation in C*c*O [222,233]. In the radical state the pK_a is -2 and so it must be deprotonated [217]. The protonation state of ground state tyrosine in fully oxidised C*c*O is still not resolved. The measured IR absorbance spectrum of protonated TyrHis(trimethyl), displays a large band at 1547 cm^{-1} of protonated TyrHis(trimethyl) (Figure 5-13C) (also observed in a related protonated Tyr-His compound (2-imidazole-1-yl-4-methylphenol) [108]. This could be attributed to the negative at 1547(-) cm^{-1} of oxidised C*c*O. Hence it would suggest tyrosine is protonated in oxidised C*c*O, and becomes deprotonated during the transition to P_M. However the 1547 cm^{-1} is insensitive to H/D exchange or to tyrosine- and histidine- labelling. Instead it was sensitive to global ^{15}N labelling and therefore 1547(-)

cm^{-1} was assigned to a haem a_3 vibrational mode [186,187,197]. The measured IR absorbance spectrum of deprotonated TyrHis(trimethyl) displays a large band at 1301 cm^{-1} (Figure 5-13A) that is not present in the protonated spectrum (Figure 5-13C). Therefore the equivalent 1317(-) cm^{-1} observed in oxidised C*c*O may be of deprotonated tyrosine that forms the deprotonated tyrosine radical in the P_M state. Hence, overall, the data reported here suggest tyrosine in the P_M *minus* oxidised IR difference spectrum is deprotonated in the oxidised state. This is further supported by Gorbikova, *et al.* [214,244] that have used D channel mutants of *P. denitrificans* C*c*O and have shown the equivalent 1317 cm^{-1} (~1308 cm^{-1}) band (also attributed to a deprotonated tyrosine) is present in the P_R, F, and O states, and not in the FR state or P_M state. Thus it was proposed that tyrosine was protonated in the FR state, a radical in the P_M state and deprotonated in the subsequent P_R, F, and O states of the natural cycle. It was suggested that tyrosine would be reprotonated in the O→E catalytic step [214].

5.5 Conclusion

In conclusion, a Tyr-His model compound has been synthesised to mimic the conserved structural feature in C*c*O. This structure was adapted based on the structures of TMP and TBP to give a stable electrochemically induced radical species. CV was used to characterise its electrochemical properties and the pK_a values (6.8 ±0.4 of imidazole) and (9.2 ±0.2 of phenol) of TyrHis(trimethyl) were determined by titration of their UV-visible spectra. IR absolute spectra of fully protonated, neutral and fully deprotonated Tyr-His(trimethyl) have been tentatively assigned by comparison to IR bands predicted by calculation using Gaussian. Finally, the optimised electrochemical conditions to induce a radical on TMP, TBP and TyrHis(trimethyl) were combined with ATR-FTIR spectroscopy to record reduced *minus* oxidised (radical) IR difference spectra. Based on literature assignments, the bands at 1592 cm^{-1} (TMP) and 1572 cm^{-1} (TBP), have been assigned to *v*8a(C-C) and the bands at 1511 cm^{-1} (TMP) and 1507 cm^{-1} (TBP) to *v*7a(C-$O^{\cdot}$) of a phenoxyl radical. By comparison to TMP and TBP, the bands at 1550 cm^{-1} and 1510 cm^{-1} of TyrHis(trimethyl), were also assigned to *v*8a(C-C) and *v*7a(C-$O^{\cdot}$) of a phenoxyl radical, respectively. The peak/trough at 1301(+)/1314(-) cm^{-1} was only observed for TyrHis(trimethyl) and has been assigned to an imidazole ring stretch. Subsequently, the P_M *minus* oxidised IR spectrum of bovine C*c*O was recorded, and the presence of the P_M state was confirmed by *in situ* recording of visible spectra, that are well characterised for the P_M state. In doing so tentative assignments of possible tyrosine radical bands, in the P_M intermediate, have been made by comparison to the model compounds (TMP, TBP and TyrHis(trimethyl). An IR band at 1572 cm^{-1} or 1555 cm^{-1} has been assigned to *v*8a(C-C), and at 1519 cm^{-1} to *v*7a(C-$O^{\cdot}$) of a phenoxyl radical of tyrosine in the P_M state. 1336 cm^{-1} has been assigned to a histidine ring stretch of the cross-linked Tyr His radical in the P_M state. The P_M *minus* oxidised IR difference spectrum is also presented in the low frequency range for the first time, and a band at 808 cm^{-1} has been shown to be ^{18}O–sensitive, and has therefore been assigned to $Fe^{4+}=O^{2-}$ stretch in the P_M state.

5.6 Future work

Assignment of the reduced *minus* radical IR spectrum of TyrHis(trimethyl) was achieved by comparison to TMP and TBP. Definitive assignment of these bands, will require repeating the experiment with an isotopically labelled structure of TyrHis(trimethyl), for example ^{13}C, where the two bands will be expected to shift.

It was clear that the reaction of TyrHis(trimethyl) was irreversible when the measurement was carried out in the IR spectroscopy setup, and is possibly because of the higher concentrations (10 mM) used of this compound, compared to the dilute conditions of the cyclic voltammetry measurements (0.2 mM). In order to overcome the irreversibility, the structure could be optimised further. It is possible that if a butyl group is placed at both ^{2}C and ^{4}C sites of the phenol ring the presence of the bulkier group may sterically stabilise/protect the radical, and possibly improve the reaction reversibility.

The electrochemistry-ATR-FTIR setup shown in the methods relied on diffusion of the species to and from the electrode surface and the ATR-prism. This factor may be another reason for the irreversible reaction observed for TyrHis(trimethyl). This is because the radical induced may have been short-lived resulting in a low yield. In contrast, in cyclic voltammetry the radical is always measured at the electrode surface. To overcome the limitation of time required for diffusion, an alternative ATR setup could be used with a boron doped diamond (BDD) ATR prism [245]. Here, a thin layer of boron doped diamond conducting material is deposited onto a silicon ATR prism. The BDD is optically transparent in the frequency range expected for a phenol radical, and so the IR beam would travel through the electrode material, and produce an evanescent wave that penetrates into the electrolyte on the top surface. In this way, the compound can be oxidised and reduced at the same site as the IR measurement. More importantly, it will allow IR spectra of the compound to be taken at the same time as the electrochemical reaction. However, preliminary cyclic voltammetry measurements with BDD did not detect any oxidation or reduction peaks for this compound. This could be due to the solvent conditions or the surface groups of the electrode material. In order to use this setup, different solvent conditions could be tested, for example acetonitrile containing tetraethylammonium hydroxide to deprotonate the compound and tetrabutylammonium hexafluorophosphate as supporting electrolyte. These conditions have been used for TBP and TMP with a platinum electrode [224] but they may also be compatible with a BDD electrode.

6 Possible functions of the H channel in yeast cytochrome c oxidase

6.1 Introduction

Subunit I of channel C*c*O houses the BNC for oxygen reduction and the three possible proton pathways (H, D and K channels) (Figure 6-1, green residues). The pathways are composed of a hydrogen bonded network of hydrophilic amino acids and water molecules. There is good evidence from mutagenesis studies in bacterial C*c*Os that the D channel, which is well conserved in mitochondrial and bacterial C*c*Os, provides the route for all translocated protons (reviewed by Rich, P. R. and Maréchal, A. 2013 [78]). However, the pathway for translocated protons in mitochondrial C*c*Os remains more controversial. This is because X ray crystallographic data of bovine C*c*O have revealed a third pathway of hydrophilic residues termed the H channel [38-40]. In contrast to the more limited structure in bacterial C*c*Os, it provides a more extensive hydrophilic pathway throughout the entire bovine C*c*O structure, from the matrix side to the IMS. In particular, mutagenesis of this extensive hydrophilic H channel in a human/bovine hybrid C*c*O, has given support to the proposal that this channel provides the route for translocated protons, at least in mammalian C*c*Os (reviewed by Yoshikawa, *et al.* [87]). With this observation, a model based on redox-linked X ray structural changes has been proposed for mammalian C*c*Os [38], where the H channel provides the route for proton translocation rather than the D channel [87]. This H is also evident in a predicted structural model of yeast (*Saccharomyces cerevisiae*) mitochondrial C*c*O [41]. This is shown in Figure 6-1(-white residues) and its possible role as a proton channel or, alternatively, as a dielectric channel [78] is now being addressed by mutagenesis studies [118].

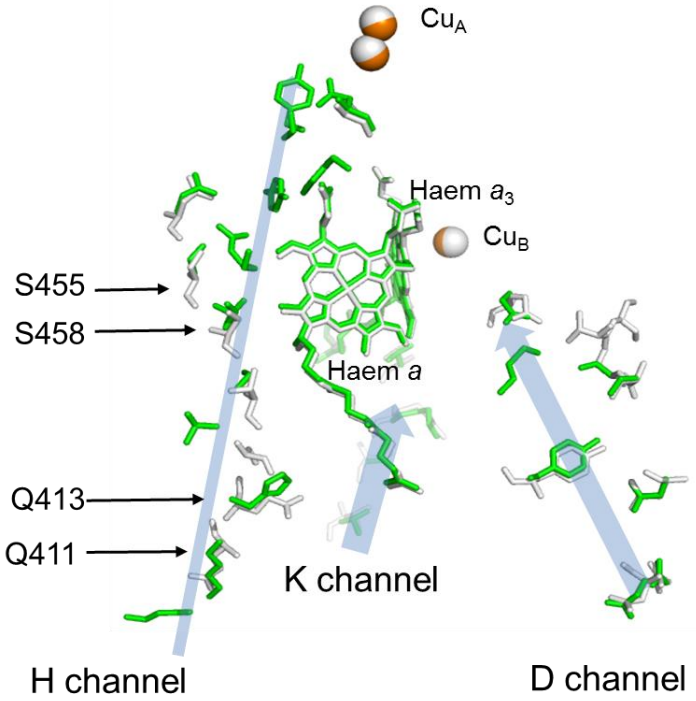

Figure 6-1. The D, K and H Channels of bovine CcO and of the homology model of yeast CcO are overlaid.
The pathways of bovine CcO (PDB:2Y69) are shown in green and yeast CcO are shown in white. Homology model of yeast CcO is taken and adapted from [41]. The labelled residues are of yeast CcO and indicate mutated positions that have been studied in this chapter.

6.2 Aims

Our collaborator and yeast geneticist Dr Brigitte Meunier (Gif, France) can successfully introduce mutations into the mitochondrially-encoded subunits of yeast C*c*O, including subunit I [118]. Therefore, through mutagenesis yeast C*c*O can now be used as a model system, to analyse various proposed mechanisms of mitochondrial C*c*Os [41,118]. The aim of this project was to develop a protocol to reconstitute yeast WT C*c*O into liposomes, so that its proton translocation activity could be quantitatively assayed, in single point H channel mutants and also in the extreme 4H mutant (Q411L/Q413L/S458A/S455A). This allowed the possible role of the H channel as a proton translocating pathway in yeast mitochondrial C*c*O to be investigated. In order to facilitate this, a protocol was required to reconstitute yeast C*c*O into phospholipid vesicles. To develop the protocol, it was optimised with bovine C*c*O since its coupling efficiency has already been extensively studied in reconstituted vesicles (COVs) [178-180,246].

6.3 Results

6.3.1 Optimisation of assay conditions; WT yeast mitos

Yeast mitochondrial membranes (mitos) were prepared as described in section 2.4. Turnover numbers of wild type (WT) yeast mitochondrial membranes (mitos) were measured to find the optimal conditions for enzyme activity of yeast C*c*O (Figure 6-2). The protein content in the mitos preparations for these strains was not determined and so the rates and V_{max} values could not be expressed as $e.s^{-1}.mg^{-1}$ protein and have therefore been expressed in terms of the number of electrons transferred from cyt *c* per second per C*c*O ($e.s^{-1}.Cc O^{-1}$). C*c*O content was determined by measurement of reduced *minus* oxidised visible difference spectra as described in section 2.6. Figure 6-2A shows that the optimal pH for enzyme activity was pH 6.6. At this pH the optimal DDM concentration was 0.05 % (w/v), where the turnover number increased ~1.5-2 fold at concentrations greater than 0.025 % (w/v) (Figure 6-2B). 50 mM KCl was the optimal ionic strength (Figure 6-2C). The error bars in Figure 6-2A, B and C. indication repeats using the same mitos sample. Under these optimal assay conditions, the V_{max} and apparent K_m values for horse heart cyt *c* (substrate) were determined. Values derived from a non-linear fit to a Michaelis-Menten plot were 1894 ±27 $e.s^{-1}.Cc O^{-1}$ and 15.3 ±0.6 µM cyt *c,* respectively (Figure 6-2D). The errors associated with V_{max} and apparent K_m are standard errors of the mean given by the curve fitting tool on OriginPro8.6.

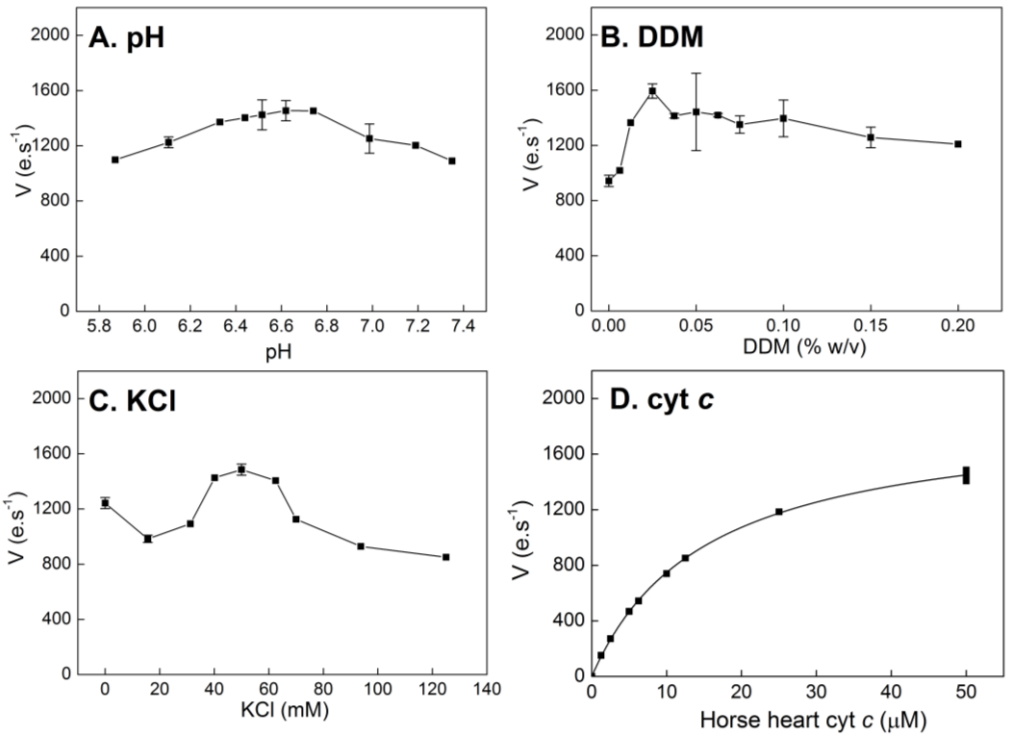

Figure 6-2. Optimisation of WT yeast CcO activity in mitos preparations.
A. Effect of pH. B. effect of detergent (DDM), C. effect of ionic strength [KCl], D. Michaelis-menten plot showing effect of cyt c. Turnover numbers were measured using an oxygen electrode assay at 25 ^{o}C. A. The reaction vessel contained, 40 µM TMPD, 50 µM horse heart cyt c, mitos containing 1-3 nM CcO, 0.05 % (w/v) DDM, 50 mM KCl and 10 mM KPi at various pHs. The reaction was initiated with 2 mM sodium ascorbate. B. At the optimum pH 6.60, the DDM concentration was varied, C. at optimum pH 6.6 and 0.05 % DDM, the [KCl] was varied, D. at optimum pH 6.6, 0.05 % DDM and 50 mM KCl, the cyt c concentration was varied. Non-linear regression analysis was performed using the Michaelis-Menten equation to determine the V_{max} and apparent K_m. Error bars represent repeats from 2 to 3 assays.

6.3.2 Comparison of activity profiles of WT and H channel mutants

The bc_1 content across strains remained fairly constant at 0.76-1.18 nmoles bc_1.mg^{-1} and so the amount of C*c*O present in the mitos preparations was expressed as a ratio of C*c*O to bc_1. C*c*O and bc_1 contents were determined from reduced *minus* oxidised visible difference spectra using Δε of 26 $mM^{-1}.cm^{-1}$ at $\Delta A_{605-621}$ for C*c*O and Δε of 28 $mM^{-1}.cm^{-1}$ at $\Delta A_{562-578}$ for bc_1. The ratio of C*c*O:bc_1 (0.25:1) was the same for Q411L and S458A mutants as WT. However it was ~5 times less for the 4H mutant (~0.05:1). The activity profiles of these mutants were compared to WT mitos in Figure 6-3. Initially, turnover numbers of C*c*O in WT, Q411L, 4H mutant and S458A mitos were measured at various pHs (Figure 6-3A). Overall the H channel mutants had a greater activity than WT C*c*O mitos. The most optimal pH of WT, Q411L, S485A and 4H mutant mitos was pH 6.6, and was taken forward to test the other factors (ionic strength and cyt *c* concentration). At pH 6.6, 50 mM KCl was the optimal concentration for WT, Q411L and S458A. The 4H mutant was more active at 40 mM KCl or less (Figure 6-3B). The activity profile at KCl concentrations below 40 mM remained constant for all H channel mutants, whereas it decreased substantially at 20 mM KCl for WT mitos. Michaelis-Menten plots were determined using horse heart cyt *c* at pH 6.6 and 50 mM KCl (or 40 mM KCl for the 4H mutant) (Figure 6-3C). Table 6-1 summarises the V_{max} and apparent K_m values. All H channel mutants had a greater V_{max} than WT. The apparent K_m value of Q411L (24.6 ±2.9 μM) and S458A (19.8 ±4.1 μM) was greater than WT (15.3 ±0.6 μM). Interestingly the 4H mutant (7.9 ±0.4 μM) had a 2 fold smaller K_m than WT.

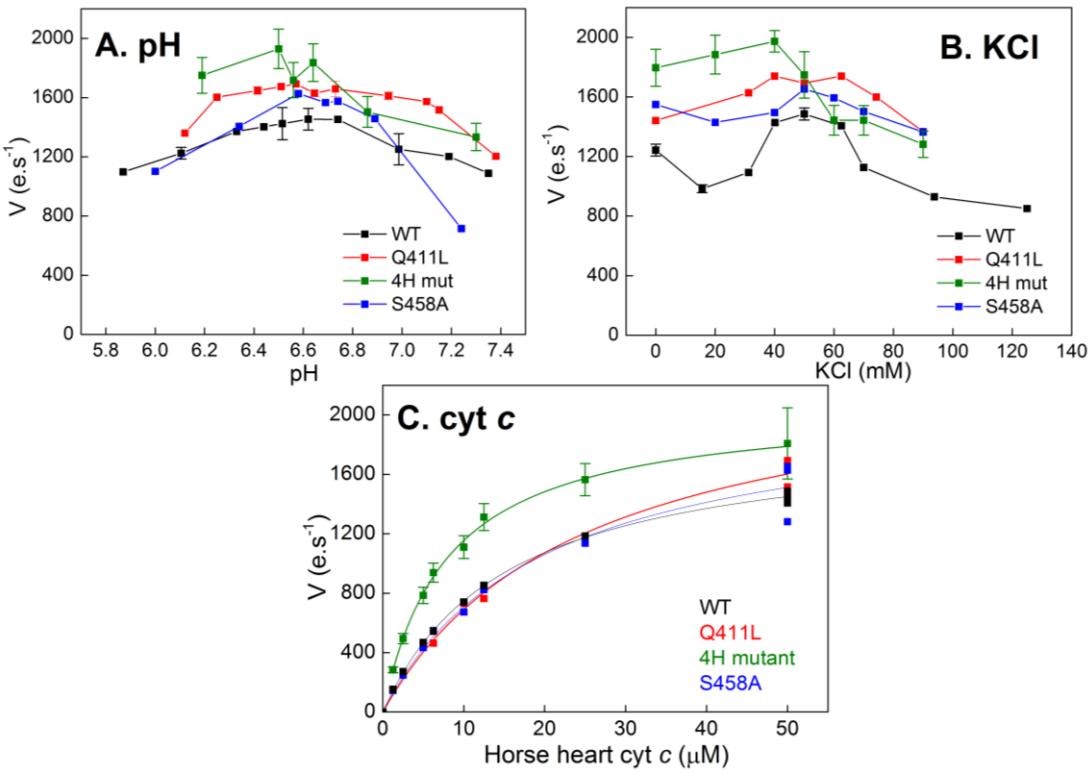

Figure 6-3. Comparison of activity profiles of WT and H channel mutants.
A. Effect of pH, B. effect of ionic strength [KCl], C. Michaelis-Menten plot showing effect of cyt c. Turnover numbers were measured using an oxygen electrode assay at 25 ^{o}C. A. The reaction vessel contained, 40 µM TMPD, 50 µM horse heart cyt c, mitos containing 1-3 nM CcO, 0.05 % (w/v) DDM, 50 mM KCl and 10 mM KPi at various pHs. The reaction was initiated with 2 mM sodium ascorbate, B. at the optimum pH 6.6, the [KCl] was varied, C. at optimum pH 6.6 and 50 mM KCl (40 mM KCl for 4H mutant), the cyt c concentration was varied. Non-linear regression analysis was performed using the Michaelis-Menten equation to determine the V_{max} and apparent K_m. Error bars represent repeats from 2 to 3 assays using the same mitos preparation.

Table 6-1. Summary table of V_{max} and apparent K_m of WT, Q411L, 4H mutant, and S458A yeast mitos.
Optimal reaction buffer was 10 mM KPi pH 6.6, 50 mM KCl 0.05 % (w/v) DDM, (for the 4H mutant 40 mM KCl was used). Non-linear regression analysis was performed using the Michaelis-Menten equation to determine the V_{max} and apparent K_m. Standard errors and R-squared values are given.

Mitos	V_{max} ($e.s^{-1}.CcO^{-1}$)	K_m (µM)	R-squared
WT	1894 ±27	15.3 ±0.6	0.99883
Q411L	2391 ±122	24.6 ±2.9	0.99257
4H mutant	2073 ±55	7.9 ±0.4	0.99815
S458A	2112 ±178	19.8 ±4.1	0.97253

6.3.3 H^+/e^- stoichiometry assay in coupled bovine COVs

In order to determine the H^+/e^- stoichiometry of bovine C*c*O the purified enzyme was reconstituted into vesicles following the exact protocol described in Section 2.21 of the Methods. The respiratory control ratio RCR provided a facile means of estimating how well the C*c*O had incorporated into the membranes, and how intact the lipid vesicles were after reconstitution. The intactness could be compromised, for example, by residual detergent causing liposomes to become 'leaky' to protons, or by C*c*O not incorporating correctly in the membranes. In well-coupled COVs, C*c*O activity is slowed down by the PMF that is generated across the vesicle bilayer by enzymatic turnover. Removal of the PMF by uncoupling stimulates the rate and provides an indication of the COVs quality. The RCR is a ratio of the turnover number ($e.s^{-1}.Cc O^{-1}$) in the presence CCCP, divided by the turnover number without uncoupler. When added to COVs, CCCP equilibrates the proton concentration and charge gradient across the membrane, and so, increases the C*c*O turnover number which is no longer rate-limited by the PMF. The turnover numbers were determined using the oxygen electrode assay as described in Section 2.21.2 of the Methods.

The Bovine C*c*O reconstituted into phospholipid vesicles, showed respiratory control ratio (RCR) values that ranged from 2 to 10, dependent on the purified enzyme preparation used. The addition of 0.05 % (w/v) DDM solubilised the vesicle membranes, and caused approximate 2 fold stimulation in turnover number, suggesting that 50 % of C*c*O was incorporated with the cyt *c* binding site facing outwards, and 50 % facing inwards.

The H^+/e^- stoichiometry assay of bovine COVs was performed using a dual wavelength spectrophotometer. Figure 6-4 shows the proton translocation activity of bovine COVs when 1.35 µM horse heart cyt c^{2+} was added to 0.5 µM C*c*O in COVs, which was sufficient to induce, on average, one full catalytic turnover of each C*c*O with its cyt *c* binding site facing outwards. This cyt *c* addition resulted in an immediate acidification of the medium as a result of proton pumping, and was measured as a decrease in absorbance of the pH indicator dye, phenol red. This phase was followed by an alkalinisation phase, this was due to the re-entry and equilibration of protons into the interior of the vesicles where alkalisation had occurred from proton pumping, and from the net consumption of four protons per O_2 reduced to water. The H^+ inflow had a typical rate constant of 0.043 s^{-1}. The proton to electron stoichiometry was determined by comparison of the total extent of acidification in the initial phase, to the absorbance change caused by a calibrating acid pulse. The H^+/e^- stoichiometry was 0.91 ±0.07.

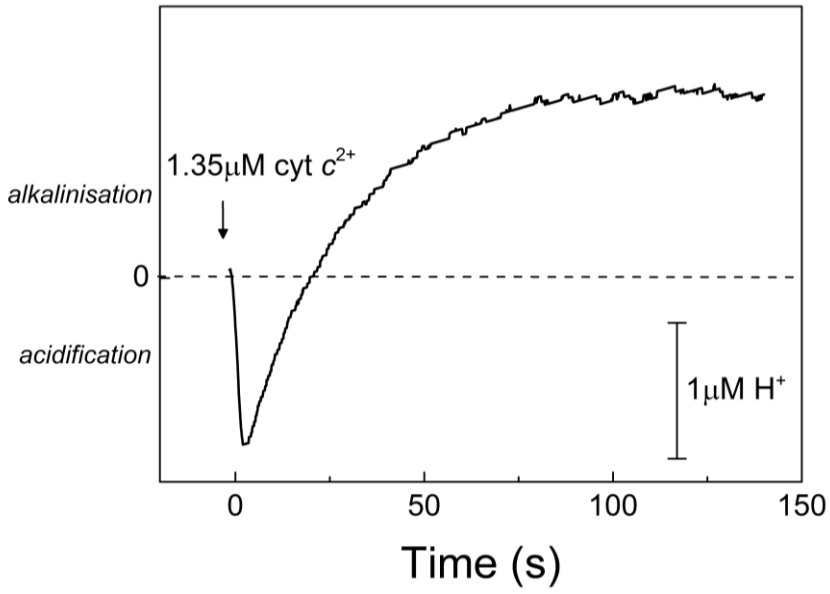

Figure 6-4. External H^+ concentration changes in response to the proton pumping activity of bovine COVs induced by 1.35 μM cyt c^{2+}.
160 μL of COVs were added to give a final concentration of 0.5 μM CcO to 1440 μL of 50 μM phenol red (pH indicator dye), 44.6 mM KCl, 43.4 mM sucrose, followed by 10 μg/mL carbonic anhydrase (1.6 μL), 10 μM valinomycin (10.7 μL) and 1 nM CCCP (1.6 μL). pH was adjusted to pH 7.4 as mentioned in the methods, the reaction was initiated with 1.35 μM horse heart cyt c^{2+} (1.5 μL) as indicated. Absorbance changes of phenol red were measured at $\Delta A_{556.5-504.0}$ and converted to $[H^+]$ changes using a calibrating 1 μM acid pulse. The reaction was carried out at 14 ^oC.

6.3.4 Proton to electron stoichiometry assay in uncoupled bovine COVs

CCCP is a proton ionophore that collapses any protonmotive force by rapidly equilibrating the H^+ concentration inside and outside the vesicles. Figure 6-5 shows the immediate proton consumption for water formation in response to a pulse of 1.35 µM cyt c^{2+} to bovine COVs, that were uncoupled with 2.5 µM CCCP. The size of the alkalinisation was equivalent to 1 ±0.1 H^+ per electron.

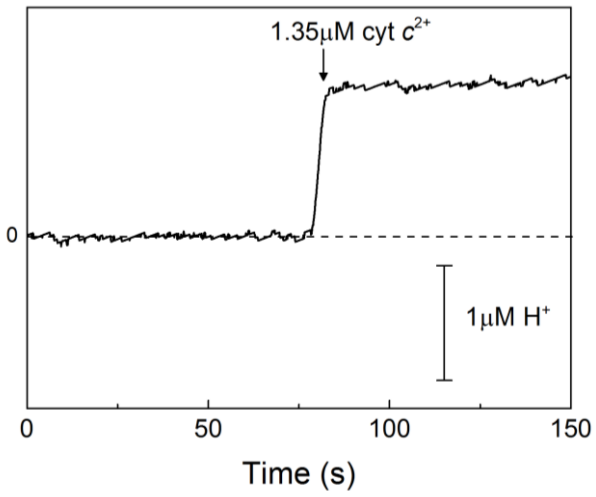

Figure 6-5. External H^+ concentration changes in response to the addition of cyt c^{2+} to uncoupled bovine COVs.
Bovine COVs were uncoupled by the addition of 2.5 µM CCCP (4 µL) in the same cuvette as Figure 6-4. The baseline was allowed to stabilise and the pH was adjusted to pH 7.4. 1.35 µM horse heart cyt c^{2+} (1.5 µL) was added at the time indicated. The size of a calibrating 1.35 µM acid pulse after addition of 2.5 µM CCCP is also shown. Absorbance changes of phenol red were measured at $\Delta A_{556.5-504.0}$ and converted to $[H^+]$ changes using a calibrating 1 µM acid pulse. Reaction was carried out at 14 ^oC.

6.3.5 Reconstitution of purified yeast CcO into phospholipid vesicles

It has not yet been possible to generate yeast WT COVs that were as tightly coupled as the bovine COVs when using the same protocol; the highest RCR value measured was very low (~1.2). The addition of 0.05 % (w/v) DDM to uncoupled COVs had no effect on the turnover activity, and in some cases it caused the activity to decrease. Nevertheless, the H^+/e^- stoichiometry assay was carried out. However, the traces following a cyt c^{2+} pulse, gave the same result as that of uncoupled COVs (immediate alkalinisation), with a 1 H^+ consumed per electron stoichiometry (data not shown).

Hence, changes were made to the protocol that was used for bovine C*c*O reconstitution that is described in Section 2.21 to generate coupled yeast WT COVs. These conditions and the resulting RCR values are summarised in Table 6-2. Purified yeast C*c*O was prepared in 50 mM KPi, 250 mM NaCl, 0.01 % (w/v) DDM pH 8.0. The lipid composition was altered from all lecithin to 1:4 (w/w) ratio of cardiolipin to lecithin because cardiolipin is a mitochondrial inner membrane lipid. The pH of the entire reconstitution procedure was lowered from pH 7.4 to pH 6.9, which was near the optimum turnover activity. The enzyme to lipid ratio was halved to give 0.095 nmole C*c*O/mg of lipid. The divalent cation, Mg^{2+}, was added to the enzyme/lipid preparation before dialysis, and to all the dialysis buffers at 10 mM $MgCl_2$ [247]. Octyl glucoside (>99.5 %, Melford Laboratories Ltd, UK) detergent was tested instead of potassium cholate for promoting the association of C*c*O with the liposomes. Since the RCR of bovine C*c*O was variable across 5 different enzyme preparations, the effect of using different enzyme preparations was also tested. Hence, further WT yeast C*c*O preparations that had been purified in the presence of lipids, or in the presence of digitonin, instead of DDM were also tested, as was a 4H mutant C*c*O preparation (see below). The condition that gave the highest RCR was with digitonin-purified WT C*c*O with 3.9 pmole C*c*O/mg lecithin and extended dialysis times, and with all other conditions for reconstitution the same as for bovine C*c*O reconstitution. Larger volume preparations were also necessary for better coupling. An RCR of ~1.4 was achieved with WT C*c*O, but proton pumping experiments still showed the behaviour of uncoupled COVs.

Table 6-2. Summary of conditions for membrane reconstitution of yeast CcO (WT and 4Hmutant).
RCR repeats represent COVs that were prepared more than once. Abbreviations are; OG, octyl glucoside, w/o, without, PC, phosphatidylcholine, PI phosphatidylinositol, PE, phosphatidylethanolamine.

Dialysis protocol	Condition tested	Details	RCR
Fast dialysis protocol. The protocol that was used for bovine C*c*O; 2x1.5 h 250 mL 75 mM HEPES pH 7.4, 14 mM KCl, 0.1 % cholate, 2x1.5 h same buffer w/o cholate overnight, 500 mL 0.5 mM HEPES pH 7.4, 44.6 mM KCl, 43.4 mM sucrose overnight.	**Effect of cardiolipin**	40 mg/mL lecithin, 2 % (w/v) K^+ cholate	1.21, 1.15, 1, 1
		1:4 cardiolipin:lecithin (20 % w/w cardiolipin)	No coupling
	Effect of pH, 20% w/w cardiolipin	pH 7.4	No coupling
		pH 6.9	No coupling
	Effect of C*c*O:lipid ratio, pH 7.4, 20 %(w/w) cardiolipin	0.19 nmole C*c*O/mg of lipid	No coupling
		0.095 nmole C*c*O/mg of lipid	No coupling
	Effect of Mg^{2+}, pH 7.4, 20 % (w/w) cardiolipin	10 mM $MgCl_2$	1.21, 1.15
		w/o $MgCl_2$	No coupling
	Effect of OG, pH 7.4, 20 % (w/w) cardiolipin	10 mM $MgCl_2$ 2 % OG	1.04
		10 mM $MgCl_2$, 2 % K^+ cholate	1.21, 1.15
		w/o 10 mM $MgCl_2$, 2 % OG	1.16
	Effect of 4H mutant preparation, pH 7.4, 20 % (w/w) cardiolipin, 10 mM $MgCl_2$	4H mutant, 2 % K^+ cholate	1.51, 1.40, 1.81
Prolonged dialysis protocol Dialysis was 3 h 500 mL 75 mM HEPES pH 7.4, 14 mM KCl, 0.1 % cholate, 1x500 mL same buffer w/o cholate overnight, 1x6 h 500 mL same buffer all day, 1x 1 L 0.5 mM HEPES pH 7.4, 44.6 mM KCl, 43.4 mM sucrose overnight	**Effect of different yeast C*c*O preparations,** pH 7.4	Yeast WT C*c*O purified in the absence of lipids	All the above
		Yeast WT C*c*O presence of lipids (1:1:1) PC, PE, PI. COVs were prepared with 20 % w/w cardiolipin, 10 mM $MgCl_2$ 2 % K^+ cholate. (USED FAST DIALYSIS)	1.21, 1.18
		WT C*c*O purified by FPLC in the absence of lipids, used fraction collected after passing through Ni Column. COVs prepared with 40 mg/mL lecithin, w/o $MgCl_2$, 2 % K^+ cholate	1.26
		Purified using FPLC absence of lipids, fraction collected after passing through Ni column and gel filtration. COVs prepared with 40 mg/mL lecithin, w/o $MgCl_2$, 2 % K^+ cholate	1.18, 1.30, 1.33
		Using 1 % digitonin solubilised WT mitos. COVs were prepared with 40 mg/mL lecithin, w/o $MgCl_2$, 2 % K^+ cholate	1.40
		Purified in the presence of 0.01 % (w/v) digitonin instead of 0.05 % (w/v) DDM using fraction collected after Ni column. COVs were prepared with 40 mg/mL lecithin, w/o $MgCl_2$, 2 % K^+ cholate	1.44

An observation worth noting was that the profiles of a calibrating acid pulse before and after CCCP addition were different. This is shown in Figure 6-6 for a blank COVs preparation (as a control), and for yeast COVs that exhibited an RCR of 1.4, and that were prepared using C*c*O that was purified in the presence of digitonin. An acid pulse in a low background concentration of CCCP, resulted in an acidification followed by an alkalinisation phase, this was due to the equilibration of protons into the interior of the vesicles until the pH had stabilised. In the presence of high [CCCP], the vesicles were uncoupled and the acid pulse equilibrated rapidly inside and outside the vesicles to the same final extent. By comparison to the blank COVs this evidence suggests that intact liposomes were indeed present, and that the method used to form liposomes worked well. Therefore the low RCR values obtained of yeast C*c*O and the subsequent absence of proton pumping, suggests that C*c*O did not fully incorporate into the liposomes.

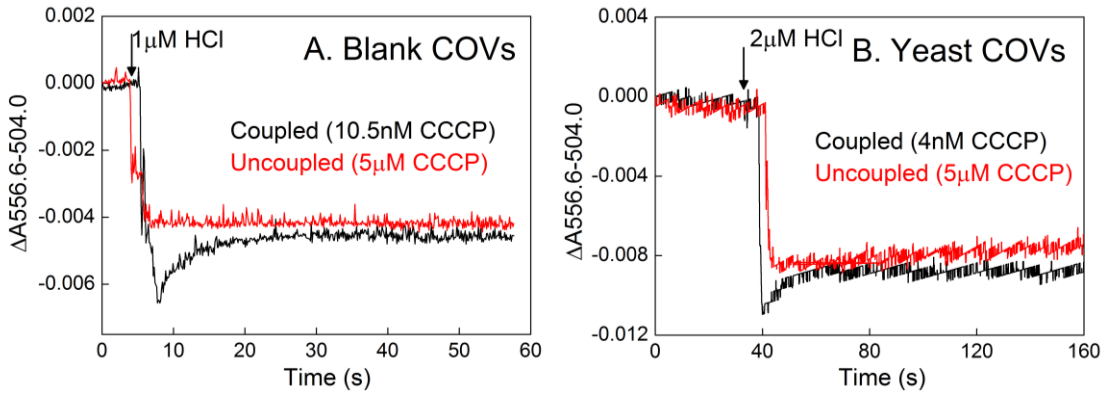

Figure 6-6. Comparison of HCl pulses in coupled and uncoupled vesicles prepared in the (A) absence of CcO and (B) presence of yeast CcO.
A. 464 µL blank COVs in 2 mL of 50 µM phenol red, 44.6 mM KCl, 43.4 mM sucrose, 10 µg/mL carbonic anhydrase, 10 µM valinomycin and 10.5 nM CCCP. pH was adjusted to pH 7.4 and temperature was set to 25 ^{o}C. A pulse of 1 µM HCl was added (black trace). Once baseline had stabilised the blank COVs were uncoupled with 5 µM CCCP and the acid pulse was repeated (red trace). B. 150 µL of WT yeast COVs (RCR of 1.4) in 1.6 mL of the same buffer but with 4 nM background CCCP. A pulse of 2 µM HCl was added (black trace). The yeast COVs were uncoupled with 5 µM CCCP and the acid pulse was repeated (red). Absorbance changes of phenol red were measured at $\Delta A_{556.5\text{-}504.0}$.

6.3.6 H^+/e^- stoichiometry assay in coupled 4H mutant COVs

Mitos of the 4H mutant were solubilised with DDM and 4H mutant C*c*O was purified in the presence of DDM using the standard purification conditions [118]. 4H mutant COVs were then prepared in the same way as bovine COVs but with the following changes; a 1:4 (w/w) ratio of cardiolipin to lecithin and the presence of 10 mM $MgCl_2$ in the COVs preparation and in the dialysis buffer at pH 7.4. Since the purification yield was low for the 4H mutant, the ratio of enzyme to lipid was also lowered to 6.6 pmole C*c*O/mg. The COVs produced under these conditions, gave a slightly higher RCR value (1.8-1.2) than the WT C*c*O COVs (1.2). When 0.05 % (w/v) DDM was added to uncoupled 4H mutant COVs, there was no further stimulation in turnover number, suggesting that this mutant C*c*O was incorporated with 100 % of its binding site facing outwards.

Figure 6-7 shows the proton translocation activity when 2 µM horse heart cyt c^{2+} was added to 0.08 µM C*c*O in COVs. This would induce an average of ~6 turnovers of C*c*O from a single pulse of cyt *c*, instead of 1 turnover that was induced with the bovine COVs. The number of turnovers had to be high to give large enough pH changes and, therefore, a greater signal:noise for the proton measurement. This is because the [C*c*O] was low in the 4H mutant COVs (0.08 µM) compared to bovine COVs (0.5 µM). Cyt *c* addition resulted in an acidification phase (proton pumping), which was smaller than the size of the subsequent alkalisation. However, the low RCR in the case of the 4H mutant COVs suggests that the vesicles are poorly coupled since some pumping was observed. As a result, the rate of influx of protons into the interior of the vesicles is so rapid that it overlaps with the proton extrusion, and decreases its extent. Hence, the coupling ratio based purely on maximum extent of H^+ extrusion (0.2 ±0.1 H^+/e^-) will be an underestimate of the true value.

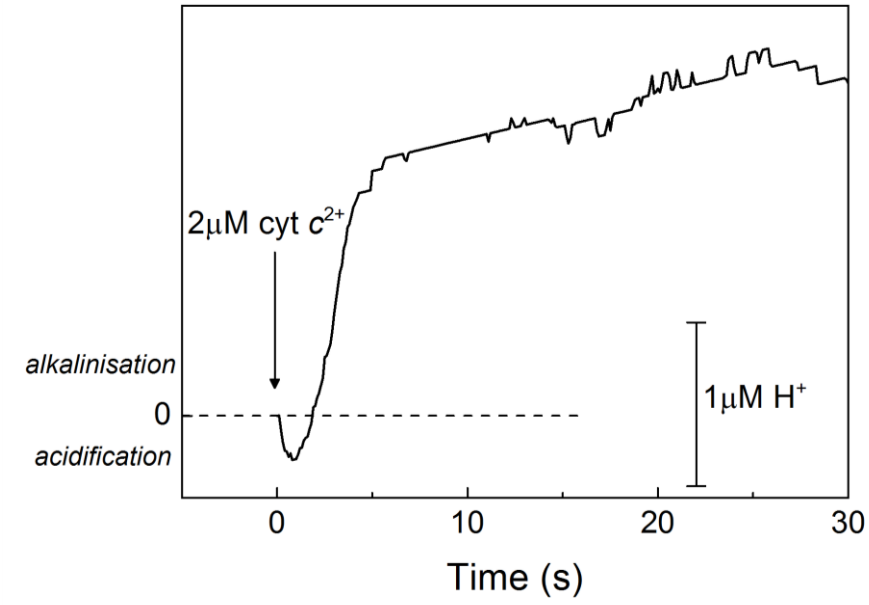

Figure 6-7. External H^+ concentration changes in response to the proton pumping activity and proton re-entry of 4H Mutant COVs induced by 2 μM cyt c^{2+}.
500 μL of COVs were added to give a final concentration of 0.08 μM to 1063 μL of 50 μM phenol red, 44.6 mM KCl, 43.4 mM sucrose, followed by 10 μg/mL carbonic anhydrase (1.6 μL), 28.6 μM valinomycin (30.5 μL) and 2.7 nM CCCP (4.57 μL). pH was adjusted to pH 7.4 as mentioned in the methods, the reaction was initiated with 2 μM horse heart cyt c^{2+} (1.56 μL) as indicated. Absorbance changes of phenol red were measured at $\Delta A_{556.5-504.0}$ and converted to $[H^+]$ changes using a calibrating 1 μM acid pulse. The reaction was carried out at 14 ^oC.

6.3.7 Proton to electron stoichiometry assay in uncoupled 4H mutant COVs

The 4H mutant COVs were uncoupled with 2.5 µM CCCP. Figure 6-8 shows the immediate proton consumption by 4H mutant for water formation that was initiated by a pulse of 2 µM cyt c^{2+}. The extent of the alkalinisation was equivalent to 1 ±0.1 H^+ consumed per electron.

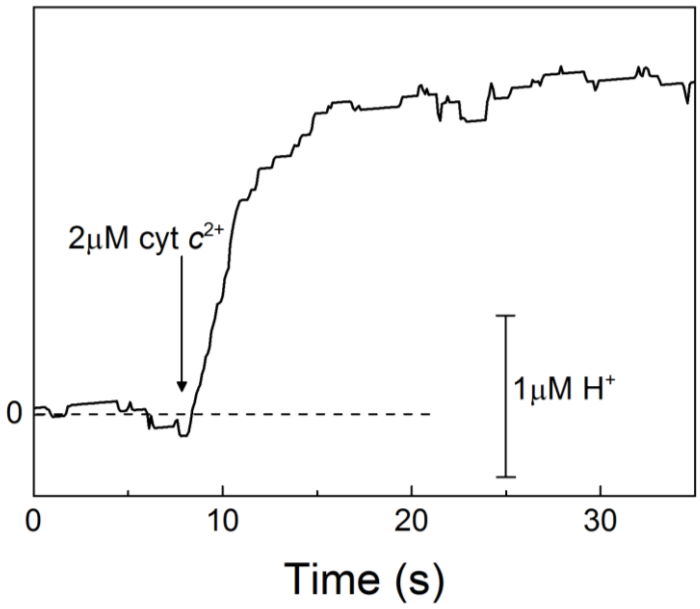

Figure 6-8. External H^+ concentration changes in response to the addition of cyt c^{2+} to uncoupled 4H mutant COVs.
4H mutant COVs were uncoupled by the addition of 2.5 µM CCCP (4 µL) in the same cuvette as Figure 6-7. The baseline was allowed to stabilise and the pH was adjusted to pH 7.4. 2 µM cyt c^{2+} (1.56 µL) was added at the time indicated. Absorbance changes of phenol red were measured at $\Delta A_{556.5-504.0}$ and converted to $[H^+]$ changes using a calibrating 1 µM acid pulse that was made after the addition of 2.5 µM CCCP. Reaction was carried out at 14 ^oC.

6.3.8 Iterative fit to estimate H^+/e^- stoichiometry

Since the proton influx rate was too rapid to allow H^+/e^- to be measured from the total extent of acidification, an alternative approach to calculate the H^+/e^- stoichiometry was used. The measured rate constants of cyt c^{2+} oxidation (see Figure 6-9), and of proton re-entry into vesicles, can be combined with different assumed proton pumping stoichiometries, to generate iteratively a best fit to the proton extrusion data. See Appendix 1.2 for how this fit was calculated. Cyt c^{2+} oxidation was measured by selecting two wavelengths ($\Delta A_{549.0\text{-}566.0}$) for absorbance changes of cyt *c* that did not have interference from phenol red absorbance changes. Figure 6-9 shows a typical profile of cyt *c* oxidation by 4H mutant COVs, which had a rate constant of 1.2 sec^{-1}.

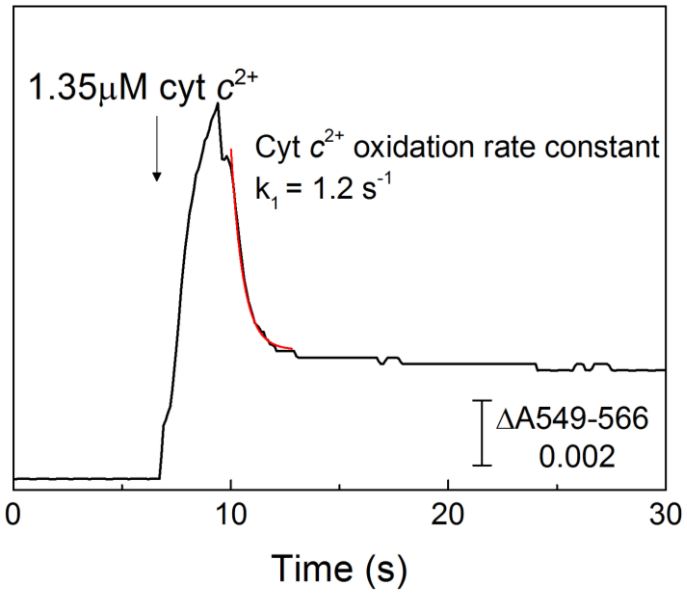

Figure 6-9. Absorbance change ($\Delta A_{549.0\text{-}566.0}$) of cyt c^{2+} oxidation in response to the addition of 1.35 µM cyt c^{2+} to coupled 4H mutant COVs.
1.35 µM cyt c^{2+} was added to the cuvette in the same experiment shown in Figure 6-7 before the COVs were uncoupled with CCCP. A single exponential curve (red) was fitted to estimate the initial oxidation rate of cyt c.

Figure 6-10 and Figure 6-11 show the best fits to the measured proton pumping data of bovine COVs and 4H mutant COVs. H^+/e^- stoichiometries were estimated as 1.0 ±0.1 for bovine COVs and 1 ±0.07 H^+/e^- for 4H mutant COVs. Errors represent a fit that is ±10 % of the measured value of the total extent of acidification.

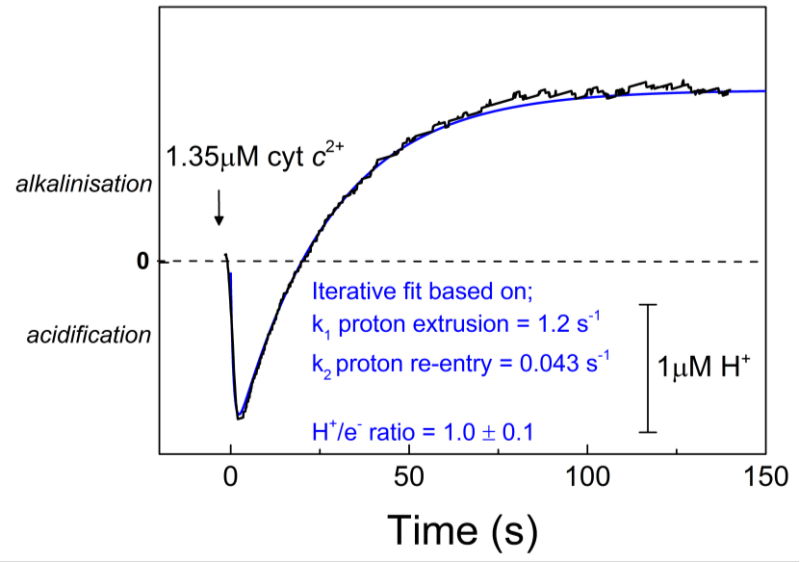

Figure 6-10. Iterative best fit to the measured proton pumping activity and re-uptake of bovine COVs induced by horse heart cyt c^{2+}.
Data was taken from Figure 6-4.

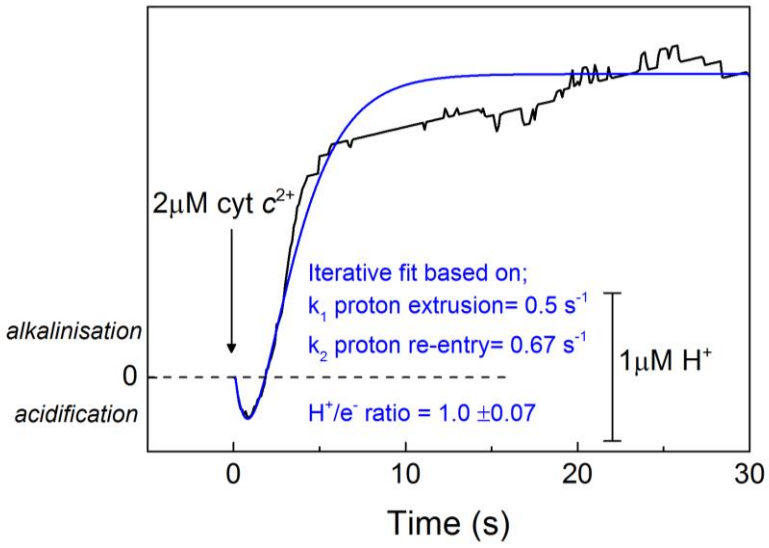

Figure 6-11. Iterative best fit to the measured proton pumping activity and re-uptake of 4H mutant COVs induced by horse heart cyt c^{2+}.
Data was taken from Figure 6-7.

6.4 Discussion

The aim of this project was to establish whether the H channel functions as a route for translocated protons in yeast mitochondrial C*c*O. In order to assess this, a protocol to reconstitute yeast C*c*O into liposomes was necessary. As a control, it was firstly optimised using bovine C*c*O for which the dialysis protocol is well established [178-180]. The stoichiometries were compared with those of a yeast C*c*O H channel mutant, the 4H mutant (with 4 mutations, S455A/S458A/Q413L/Q411L, along its H channel).

6.4.1 Bovine CcO membrane reconstitution and H^+/e^- stoichiometry

The dialysis protocol successfully produced bovine COVs with RCR values of 6 -10 that were stable for approximately 1 week, at 4 ^oC, after which the RCR dropped to approx. 2.7, which was still enough to make a stoichiometry measurement. The percentage of C*c*O orientated with their cyt *c* binding sites facing outward was 50 %, which was lower than that expected when using the cholate dialysis protocol (75-100 %) [248-250]. The orientation of C*c*O would anyway not affect measurements as the added cyt *c* can only bind and be oxidised by the 'right side out' C*c*Os, which have an accessible cyt *c* site. The stoichiometry of proton extrusion by bovine COVs was measured to be 1.0 ±0.1 H^+/e^- (Figure 6-10), which is consistent with literature values [178,249,251,252], and uncoupled COVs gave a ratio of 1 ±0.1 H^+ consumed per electron (Figure 6-5). These values confirm that, for every electron received at the BNC, one proton is translocated and another proton is consumed, consistent with the overall value for reduction of oxygen to water from the reaction;-

$$4\ cyt\ c^{2+}\ (IMS) + O_2 + 8\ H^+\ (matrix) \rightarrow 4\ cyt\ c^{3+}(IMS) + 2\ H_2O + 4\ H^+\ (IMS)$$

6.4.2 Yeast CcO membrane reconstitution

To date when membrane reconstitution of yeast C*c*O has been reported, neither RCR values nor their H^+/e^- stoichiometries have been provided [253]. The RCR value is an accurate measure of the quality of the COVs in terms of incorporation of C*c*O, and tightness to protons. The RCR value of WT yeast COVs was never greater than 1.4, which indicated poorly coupled COVs or poor C*c*O incorporation. A list of all conditions tested to optimise the reconstitution procedure of the yeast COVs, is given in Table 6-2. It is possible that the 0.05 % (w/v) DDM used for the yeast C*c*O preparation was not completely removed with dialysis, and prevented the assembly of intact vesicles, because this detergent has a low critical micelle concentration (CMC) of 0.009 % (w/v). Therefore at 0.05 % (w/v) DDM, it would form large detergent micelles (76 kDa [254])

that would exceed the cut-off limit of the dialysis tubing (10-14 kDa). However, high RCR values (4-10) of COVs have been obtained using a cholate dialysis protocol with *Rba. sphaeroides* C*c*O, that was also prepared in DDM [180]. The DDM-containing yeast C*c*O preparations, required dialysis times which were extended for each buffer (see Table 6-2) compared to bovine C*c*O, to allow time for the micelles to dissociate and be removed, but this still did not improve the RCR significantly. Membrane reconstitution of bovine C*c*O has also been achieved by the incremental addition of Bio-Beads (SM-2, Bio-Rad) to a suspension of lipid/detergent/protein, achieving RCRs of 15-20 [246]. Detergent removal relies on the adsorption of detergent and is reported to be more efficient for the removal of DDM, compared to dialysis [255]. However, yeast COVs produced this way still had a poor RCR value (1.2). The RCR was found to be variable across 5 different preparations of bovine C*c*O. Hence, further WT yeast C*c*O preparations were also tested, including the 4H mutant C*c*O preparation that exhibited a slightly better RCR of 1.2-1.8 (see below).

The most significant difference between the 4H mutant and the WT strains was the decreased C*c*O expression level in the 4H mutant, such that the ratio of C*c*O to bc_1 content in the 4H mutant mitos (~0.05:1) was almost 5 times less compared to WT yeast mitos (0.25:1). The V_{max} values in Table 6-1 are given as electrons transferred from cyt c^{2+} per second per C*c*O ($e.s^{-1}.Cc O^{-1}$) and therefore do not reflect the lower expression level of the 4H mutant and instead allow the activity to be compared independent of expression level. It is known that yeast C*c*O can be associated with the bc_1 complex as a supercomplex [256,257]. It is possible that a greater proportion of C*c*O is incorporated into such supercomplexes in the 4H mutant because of the much lower C*c*O:bc_1 ratio. Some evidence that this may be the case comes from the behaviour during nickel-affinity and the DEAE column chromatography, where the bc_1 complex co-eluted in the same fractions as the oxidase. This bc_1:C*c*O supercomplex may facilitate the reconstitution of yeast C*c*O into COVs. To test this notion further, supercomplexes of WT C*c*O:bc_1 were purified by mitochondrial solubilisation in digitonin, and subsequent nickel affinity purification. The reconstitution behaviour was tested of the resulting solubilised material, and the nickel affinity fractions containing C*c*O:bc_1 (Table 6-2). Digitonin was used since it has been reported to result in preservation of the complex III-IV supercomplexes after solubilisation [128,256]. However, although the RCR of the resulting WT COVs increased from 1.2 to 1.4, they still did not show any pumping activity. They did, however, have the typical behaviour of coupled COVs when their response towards an acid pulse was measured (Figure 6-6). By comparison to blank COVs in the coupled state, an acid pulse resulted in an acidification burst followed by a slow alkalinisation, which can only occur in the

presence of intact vesicles that provide an interior volume for equilibration of protons. Moreover, once the COVs were uncoupled, the protons equilibrated rapidly with the interior of the vesicle, and so the slow alkalinisation phase was not observed. This suggests that intact liposomes were indeed present, but the WT yeast C*c*O did not get incorporated during the reconstitution procedure, resulting in a low RCR value. This is most likely linked with the nature of the purified preparation, which was most likely not homogeneous and contained aggregates of dimers with dimers, and/or C*c*O was occupied in detergent micelles that prevented its incorporation into liposomes.

6.4.3 4H mutant; H^+/e^- stoichiometry

When the stoichiometry assay was performed with the 4H mutant COVs, the extruded pH profile displayed a small acidification phase followed by a large alkalisation phase (Figure 6-11). However, the coupling stoichiometry could not be estimated accurately, based solely on the extent of acidification relative to a calibrating acid pulse. This is because the rapid proton re-entry rate into the vesicles due to poor coupling competed with the rate of acidification. Hence, an alternative approach was used in which the profile was calculated iteratively, to give a best fit to data and provide an estimate of the H^+/e^- stoichiometry. This fit took into account **(1)** the measured rate constant of the influx of protons, **(2)** the rate constant of alkalinisation phase, after the initial acidification caused by the calibrating acid pulse (Figure 6-6) and **(3)** the measured rate constant of cyt *c* oxidation, which for a 1 H^+/e^- stoichiometry, will be equivalent to the rate constant of proton extrusion. The coupling stoichiometry (given by the ratio of rate constant of cyt *c* oxidation, to the rate constant of proton extrusion) was varied until the best fit of the extent and kinetics of the extruded protons was reached. This approach was tested with bovine COVs, where the estimated stoichiometry of 1.0 ±0.1 was consistent (Figure 6-10) with the total extents approach (Figure 6-4). For the 4H mutant, the best fit to the data was obtained with a coupling stoichiometry of 1 ±0.07 H^+/e^-.

6.4.4 Interpretation of findings

The results show that the yeast 4H mutant with four hydrophilic to hydrophobic replacements, along the H channel, still retained proton translocating activity. Thus it can be concluded that the H channel is not critical for proton translocation in yeast C*c*O. This provides the first preliminary evidence against the proposal [38-40,87] that the H channel provides the route for translocated protons in a mitochondrial form of C*c*O. Instead it is likely that the D channel provides this route in yeast C*c*O as has been shown by mutagenesis in bacterial C*c*Os [84,91,92].

An alternative proposal is that the H channel functions as a dielectric channel [78], which could facilitate rapid electron transfer into/out of haem *a* (the nearest metal centre), by modulating the dielectric strength around an otherwise deeply buried site of the enzyme. The H channel is a candidate for this role since the hydrophilic residues connect the region around haem *a* to the aqueous phases (IMS/matrix), where surface changes and re-orientation of dipoles along the H channel, can influence the properties of haem *a*, which could include minimisation of net charge changes and the energy barrier for electron transfer. Although not a complete pathway in bacterial C*c*Os, it is also evident, and may have the same role. An interesting observation that may support such a function is the altered kinetic properties of the 4H mutant compared to WT (Figure 6-3), that had a 2-fold smaller apparent K_m value compared to the WT (Table 6-1 and Figure 6-3C) that could point towards an activity modulating role of the H channel. It is well known that the electrostatic binding/unbinding of cyt *c* to its site on subunit II is influenced by ionic strength [42,43,258]. In WT yeast C*c*O, this leads to a marked decrease in turnover activity between 10-40 mM KCl concentrations (Figure 6-3B). However no decrease in turnover activity was observed in this concentration range for all the H channel mutants, and in fact, the activity stayed the same. This finding suggests that the H channel may either have an allosteric effect on the cyt *c* binding site, or that the dielectric properties of the H channel have been changed by the mutations, in such a way that it results in an alteration of the activity profile with KCl concentration.

6.5 Conclusions

The activity profiles of the WT and mutant mitos allowed us to identify the optimal activity conditions. The reconstitution protocol produced well-coupled bovine COVs that had a measured H^+/e^- stoichiometry of 1.0 ±0.1, consistent with literature values [178,249,251,252]. Various factors were tested to improve the reconstitution behaviour of WT yeast C*c*O, but to date, the COVs produced were too poorly coupled or did not incorporate C*c*O to allow measurement of their H^+/e^- stoichiometries. COVs with a measurable, but low, RCR were produced with the 4H mutant C*c*O. This gave the first H^+/e^- stoichiometry data that show definitively, that the proton translocating activity of 1 ±0.07 H^+/e is retained in this mutant. The H channel has alternatively been proposed to act as a dielectric channel [78], and the altered kinetics of the H channel mutants could possibly be explained by a modulation of the H channel dielectric properties.

6.6 Future work

The quality of the reconstituted COVs may be affected by as yet unknown factors associated with the purified preparations of the enzyme. Factors related to the composition/nature of the purified enzyme preparations will be tested, to see whether any affect the reconstitution behaviour (e.g. dimer versus monomer state, alternative detergents). Initially the standard method of purification of yeast C*c*O involved two chromatography steps; nickel affinity, and DEAE column chromatography, the resulting fractions containing C*c*O as determined by visible spectroscopy were pooled together, concentrated, and stored at -80 ^{o}C [118]. C*c*O preparations of WT and 4H mutant C*c*O purified this way were used for membrane reconstitution. Since then efforts were made to improve the purification procedure that employed the use of automated FPLC, and replacing DEAE column chromatography with gel filtration. Gel filtration was an important control in determining the homogeneity of the preparation. It showed that WT C*c*O was present as a mixture of trimer/dimers/monomers and included a large excluded front of lipid/C*c*O/detergent aggregates. Fractions were collected of the mostly dimeric state and their membrane reconstitution was tested (Table 6-2), however the RCR was not significantly improved. However, this method of purification, and the use of sodium dodecyl sulphate-polyacrylamide gel electrophoresis (SDS PAGE) will provide useful controls to test various factors, with the aim of producing a homogeneous preparation with a single elution peak from gel filtration. Factors that could be tested include for example, changing the detergent from DDM (12 carbon alkyl chain length) to, n-decyl-β-D-maltopyranoside (DM) (10 carbons) or n-octyl-β-D-maltopyranoside (OM) (8 carbons) or n-octyl-β-D-glucopyranoside. Glycerol/ethylene glycol could be added to the running buffers to avoid aggregation. EDTA could be added to chelate any traces of metal (Ni ions) that could have eluted from the Ni column. Yeast mitochondrial lipids could be added to the running buffers, and to the columns to stabilise C*c*O. The pH, ionic strength and the buffer used could also be optimised. So far the most optimal conditions have been 50 mM HEPES, 500 mM NaCl, 0.05 % DDM at pH 7.4.

7 Comparisons of subunit 5A and 5B isozymes of yeast cytochrome c oxidase

Author contributions: This chapter has been published in the Biochemical Journal [259]. This publication was written by Raksha Dodia with contributions from all authors. Brigitte Meunier constructed and characterised all mutant strains and Raksha Dodia carried out all biochemical and kinetic experiments. Chris Kay carried out the fitting of the kinetic data. In this chapter all figures have been redrawn and the fitting to kinetic data has been done by Raksha Dodia.

7.1 Introduction

There are eight nuclear-encoded supernumerary subunits of yeast C*c*O that each share homologs with eight of the ten supernumerary subunits of human/bovine C*c*O (see Introduction) [26,41,121]. Subunit IV of mammalian C*c*O is the largest supernumerary subunit (~17 kDa), and along with four other subunits, it has two isoforms (IV-1 and IV-2) whose expression is dependent on tissue type or stage of development [27,125,260]. Subunit IV is of particular interest since it is proposed to be a key regulatory subunit that provides binding sites for ATP (allosteric inhibitor) or ADP (allosteric activator) [122,123], and/or phosphorylation sites [139]. Moreover, the turnover activity of IV-2 isozyme from lung has been reported to be faster than IV-1 isozyme from liver [137], and was shown to be insensitive to allosteric inhibitory effects of ATP [27,141].

Subunit 5 of yeast C*c*O is homologous to mammalian subunit IV [26], and also has two isoforms (5A and 5B) [26,145]. The predicted structure of yeast isoform 5A has been overlaid with bovine isoform IV-1 along with subunit I to highlight its relative structural location (Figure 7-1). *COX5A* expression is induced under aerobic conditions, while *COX5B* is expressed only at very low oxygen tensions (<0.5 μM O_2) (see Introduction) [148]. Subunit 5 is essential for C*c*O assembly and, therefore, under normal oxygen levels a *COX5A*-deleted strain contains no or very low levels of assembled C*c*O. It has been reported that *COX5B* gene expression (in a *COX5A*-deleted strain) under normal oxygen levels, can be de-repressed by mutation of *ROX1* that encodes a hypoxic transcription repressor of *COX5B,* resulting in an assembled 5B isozyme [147]. However, in this mutant strain the expression level of C*c*O was 2-3 fold lower compared to the WT strain (*COX5A*-expressing strain). Subsequent comparative studies reported that the 5B isozyme had a turnover number that was up to 3 times faster than that of the 5A isozyme [28,151,261]. This was attributed to an allosteric effect of 5A/5B isoforms upon the protein environment around haems *a* and a_3 [28,151]. Infrared analysis of the carbon monoxide (CO) IR band of ligated C*c*O, revealed two interchangeable conformers described as CI and CII of 5A isozyme, and only one (CII)

conformer of 5B isozyme, where CII was assigned to the conformer capable of faster turnover activity [151].

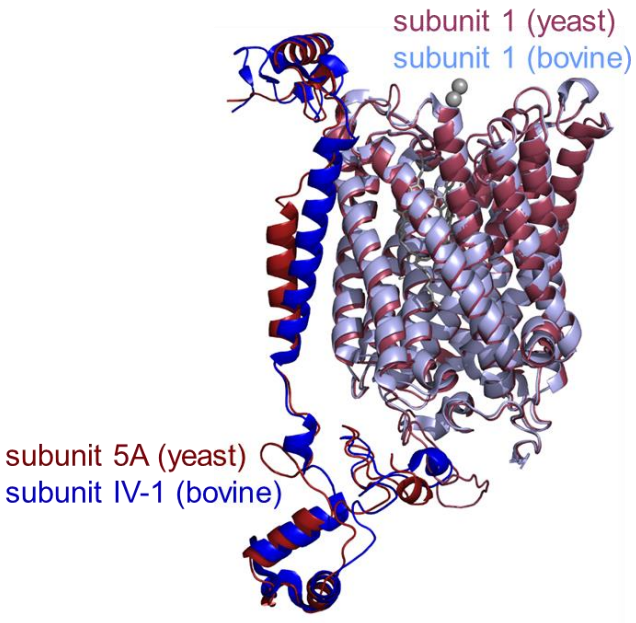

Figure 7-1. Subunit 5 of yeast CcO (red) homology model overlaid on the homologous subunit IV (blue) of bovine CcO.
Although the yeast 5A isoform [41] is overlaid with the bovine IV-1 isoform (PDB:1V54), the pairing of specific isoforms (5A with IV-1/IV-2 and 5B with IV-2/IV-1) is not possible based on their modest ~20 % sequence identities [26,41].

7.2 Aims

The aim of this project was to firstly confirm the previous observations of increased core catalytic activity of the 5B isozyme described in the literature [147], and secondly, to investigate the origin of this effect. In order to do so, mutant strains were constructed by Brigitte Meunier following a BBSRC funded 3 week visit to her laboratory. The mutant strains expressed wholly subunit 5B, by replacing the *COX5A* open reading frame with *COX5B*, so that it was under the control of the *COX5A* promoter. This gene replacement was achieved at the *COX5A* nuclear locus or on a centromeric plasmid. Such mutants expressed the 5B isozyme to wild type (5A isozyme) levels under aerobic growth conditions, and without the complication of secondary effects caused by mutation of *ROX1*-encoded transcription factor. This allowed comparison of the catalytic properties of the 5A and 5B isozymes that have been expressed in identical conditions.

7.3 Results

7.3.1 Outline of strains constructed

A summary of the wild type and mutant strains constructed and analyzed in this chapter is given in Table 2-1. Since *COX5B* gene is only expressed under hypoxic conditions, the *COX5B* gene at its genomic locus was not deleted in these mutants, since it would anyway not be expressed under normoxic conditions. This was confirmed since the *COX5A*-deleted strain was not able to grow on respiratory medium (1 % yeast extract, 2 % peptone, 2 % glycerol, 2 % agar), under the aerobic conditions of this study. As shown in Table 2-1, 5B isozyme expression was achieved by replacing *COX5A* by *COX5B* downstream of the *COX5A* promoter. This replacement was made on the genomic locus and on a centromeric plasmid to give two strains termed COX5B and pCOX5B, respectively. This allowed aerobic expression of *COX5B* so that the assembled 5B isozyme could be compared to 5A isozyme. These strains were respiratory growth competent. Similarly a mutant strain (ΔCOX5ApCOX5A) was constructed as a control that expressed *COX5A* from a centromeric plasmid, instead of the genomic locus. To investigate the effect of *ROX1* that encodes a transcription repressor of *COX5B*, three more mutants were constructed. Firstly, a mutant similar to the one described in the literature [147] was constructed, where *ROX1* and *COX5A* were deleted, allowing expression of *COX5B* from its own promoter, and was termed ΔROX1ΔCOX5A. This mutant grew on respiratory medium more slowly than the wild type (COX5A). In the last two mutants, *COX5A*-promoter that controlled expression of either *COX5A* or *COX5B* from a centromeric plasmid, was combined with deletion of *ROX1* to give ΔROX1ΔCOX5ApCOX5A and ΔROX1ΔCOX5ApCOX5B, respectively. Both strains were respiratory growth competent.

Table 7-1. Saccharomyces cerevisiae strains constructed and analysed.
All strains were constructed by Brigitte Meunier. Respiratory growth phenotype was assessed on respiratory YPG medium by Brigitte Meunier (1 % yeast extract, 2 % peptone, 2 % glycerol, 2 % agar). Table is adapted from [259].

Genotype	Description	Respiratory growth	Strain
COX5A	Expression of *COX5A* under normal aerobic growth conditions.	Yes	WTCOX5A
cox5a::URA3	Deletion of *COX5A*	Respiratory growth deficient	ΔCOX5A
cox5a::URA3, pCOX5A	*COX5A* cloned on a centromeric plasmid under the control of its own promoter. Deletion of genomic *COX5A*.	Yes	ΔCOX5ApCOX5A
cox5a::COX5B	Replacement of *COX5A* by *COX5B* downstream of the *COX5A* promoter on the nuclear genome. Expression of *COX5B* under normal aerobic growth conditions.	Yes	COX5B
cox5a::URA3, pcox5a::COX5B	*COX5B* cloned downstream of *COX5A* promoter on a centromeric plasmid. Deletion of genomic *COX5A*.	Yes	pCOX5B
rox1::kanMX4, cox5a::URA3	Up-regulation of *COX5B* through deletion of its transcription repressor *ROX1* in *COX5A*-deleted background.	Weak respiratory growth	ΔROX1ΔCOX5A
rox1::kanMX4, cox5a::URA3, pCOX5A	*COX5A* with its own promoter on a centromeric plasmid. Deletion of *ROX1*, the transcription repressor of *COX5B*.	Yes	ΔROX1ΔCOX5A pCOX5A
rox1::kanMX4, cox5a::URA3, pcox5a::COX5B	*COX5B* cloned downstream of the *COX5A* promoter on a centromeric plasmid. Deletion of *ROX1*, in *COX5A*-deleted background.	Yes	ΔROX1ΔCOX5A pCOX5B

7.3.2 Cell growth curves in YPGal media

All strains were grown and harvested in YPGal (1 % (w/v) yeast extract, 2 % (w/v) peptone, 2 % (w/v) galactose) media. Figure 7-2 shows growth curves of each strain. All strains had doubling times similar to that of wild type (2.7-3.0 h), and were harvested when they reached late log phase; 14-16 h incubation at 28 ^{o}C, logOD = 0.9 to 1. Although the doubling times were similar, it was noted that the yield of cells after incubation was 2 times less for ΔROX1ΔCOX5A (~6 g wet mass of cells per 1 L of culture) than for all other strains, that yielded 11 g. This difference in biomass was most likely due to the respiration/fermentation ratio being different at early log phase, versus late log phase, when yeast cells are grown in galactose medium. For example, the biomass was measured at late log phase and doubling times were measured during early log phase where the strains might use more fermentation than respiration. Therefore no difference in doubling times could be observed between strains.

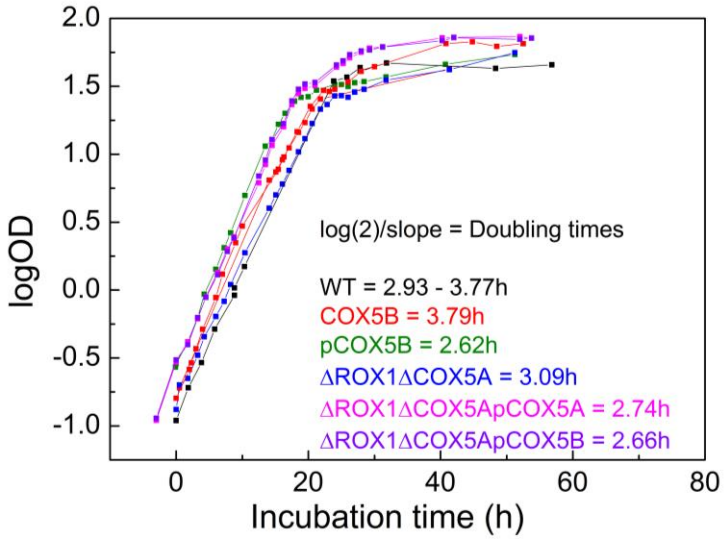

Figure 7-2. Growth curves in YPGal media.
Cell growth was monitored by taking optical density measurements at various time points of 2 L cultures, incubated at 28 ^{o}C with shaking (200 rpm). The cell doubling times are shown for each strain.

7.3.3 Expression levels of 5A/5B isozymes

After harvesting the cells, reduced *minus* oxidised visible absorbance difference spectra, were recorded to confirm that C*c*O was present. In COX5B, pCOX5B, ΔROX1ΔCOX5ApCOX5A and ΔROX1ΔCOX5ApCOX5B C*c*O was approximately 2 nmoles per gram wet weight cells, consistent with the WTCOX5A strain. The C*c*O level in ΔROX1ΔCOX5A cells was significantly less than 1 nmole.g^{-1}, though difficult to quantitate accurately in whole cell spectra. The concentration was derived from visible redox spectra and was used to estimate the turnover number of C*c*O in whole cell measurements. Concentration determination was repeated using mitos preparations of each strain that provided reliable redox spectra. Mitos from WTCOX5A, COX5B, pCOX5B, ΔROX1ΔCOX5ApCOX5A and ΔROX1ΔCOX5ApCOX5B had roughly equivalent levels of C*c*O (0.23-0.31 nmoles per mg mitochondrial protein; nmoles C*c*O.mg^{-1}) whereas mitos from ΔROX1ΔCOX5A contained 5-6 times less C*c*O (0.05 ± 0.01 nmoles.mg^{-1}). The level of bc_1 complex remained fairly constant at 0.76-1.2 nmoles bc_1.mg^{-1} (as measured from the visible band at 562-575 nm using an Δε of 28 mM^{-1}.cm^{-1}) in mitos preparations of all strains and so provided an internal control. Hence, C*c*O levels are given as a ratio of C*c*O:bc_1 to compare the relative level of C*c*O present in each strain as shown in Figure 7-3B. Consistently the C*c*O:bc_1 ratios illustrate clearly that the ratio was ~0.25:1 for all strains and it was ~6 fold less for ΔROX1ΔCOX5A (~0.04:1).

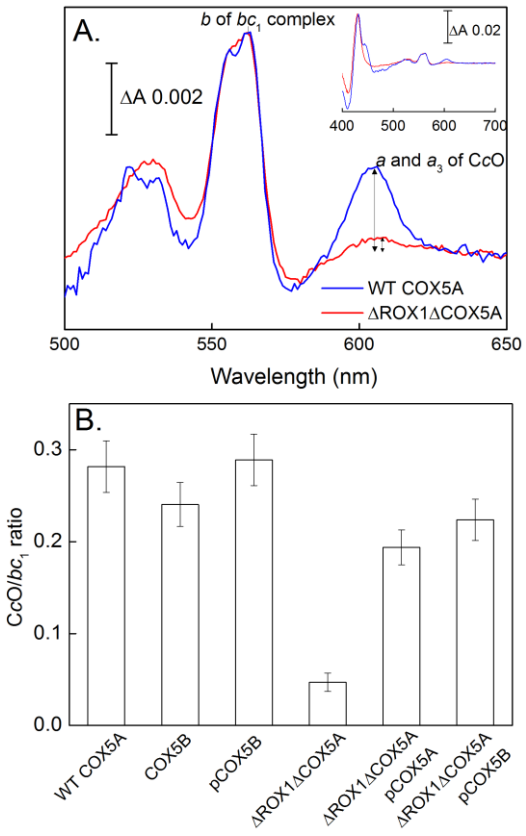

Figure 7-3. A. Dithionite reduced minus oxidised visible difference spectra of WTCOX5A (blue) and ΔROX1ΔCOX5A (red) mitos preparations. B. CcO:bc_1 ratio in mitos preparations of all strains.
Mitos were diluted in 50 mM potassium phosphate, 2 mM EDTA(K^+) pH 7.4. Spectra illustrate a ~6 fold decreased CcO:bc_1 ratio in ΔROX1ΔCOX5A. Inset shows the 400-700 nm range. Extinction coefficients used to determine the amount of bc_1 complex and CcO content were 28 $mM^{-1}.cm^{-1}$ at 562-578 nm and 26 $mM^{-1}.cm^{-1}$ at 605-621 nm, respectively. Figure (A) is adapted from [259]. Figure B shows the CcO:bc_1 ratio in mitos preparations, errors are +/- 10 % of the measured values of absorbance of bc_1 and CcO.

7.3.4 Turnover numbers in whole cells

Figure 7-4 shows a comparison of the steady-state turnover numbers of C*c*O in whole cells under uncoupled conditions. It is clear that its turnover number in the ΔROX1ΔCOX5A strain (870 $e.s^{-1}.CcO^{-1}$) was 3 fold greater than that in WTCOX5A, COX5B, pCOX5B, ΔROX1ΔCOX5ApCOX5A and ΔROX1ΔCOX5ApCOX5B that all shared similar values (300-400 $e.s^{-1}.CcO^{-1}$). This meant that when the 5B isozyme is expressed under the control of the *COX5A* promoter, it has the same activity as the 5A isozyme (COX5A strain), and this activity stays the same when it is expressed from the nuclear genome (COX5B) or a centromeric plasmid (pCOX5B and ΔROX1ΔCOX5ApCOX5B). However, when the 5B isozyme is expressed under the control of its own promoter after deletion of *ROX1* in the ΔROX1ΔCOX5A strain,

elevated activity is observed, the elevated activity of this mutant is consistent with prior literature reports [28].

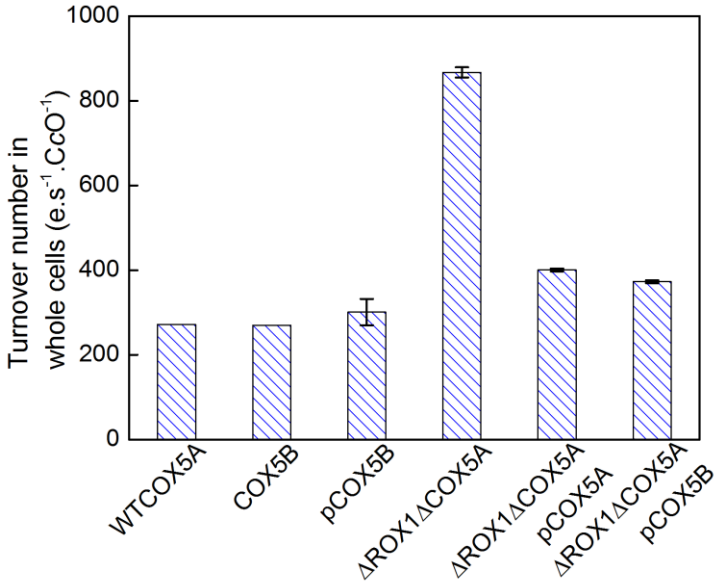

Figure 7-4. Turnover numbers of yeast CcO strains in whole cells.
Turnover numbers ($e.s^{-1}.CcO^{-1}$) were measured using an oxygen electrode with 12.5 mg/mL cells containing 10-25 nM CcO in 440 mM sucrose, 50 mM potassium phosphate pH 7.2, 10 mM lactate, 1.8 µM CCCP and 1 µM valinomycin at 25 ^{o}C. Error bars indicate standard deviations of 2 to 4 repeats. Figure is adapted from [259].

7.3.5 Turnover numbers in mitos preparations

The uncoupled turnover numbers of C*c*O in whole cells will most likely be limited by additional factors, and the concentration of C*c*O in whole cells may not have been entirely accurate. Hence, turnover numbers in isolated mitos (mitochondrial membrane fragments) were also compared, for which the concentration of C*c*O was accurately determined (Figure 7-5). The assay conditions were optimised for oxidation of horse heart cyt *c* by WTCOX5A mitos and the optimisation results are presented in Chapter 6. Furthermore the comparisons were repeated under the same assay conditions using yeast iso-1 cyt *c* and iso-2 cyt *c* (see Discussion). For all strains, the turnover numbers were faster with horse heart cyt *c* than with yeast iso-2 cyt *c*, which was faster than with iso-1 cyt *c* (Figure 7-5). Similarly to whole cell turnover values, the only mutant to show elevated turnover activity was the ΔROX1ΔCOX5A mutant strain that had ~1.5-2 fold greater activity, compared to all other mutants, irrespective of the cyt *c* substrate used.

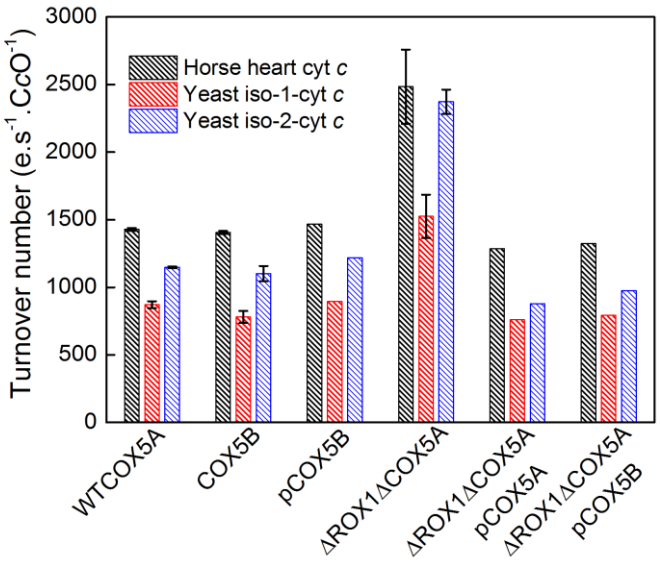

Figure 7-5. Turnover numbers of yeast CcO strains in mitos preparations using horse heart cyt c (black), yeast iso-1 cyt c (red) and yeast iso-2 cyt c (blue) as substrate.
Turnover numbers ($e.s^{-1}.CcO^{-1}$) were measured using mitos containing 2-10 nM CcO in 10 mM KPi, 50 mM KCl, pH 6.6, 0.05 % (w/v) DDM, 40 µM TMPD, 2 mM sodium ascorbate at 25 ^{o}C and 1 mL final volumes. Once the baseline had stabilised 50 µM cyt c was added to initiate the reaction. Error bars indicate standard deviations of 2 to 4 repeats using the same mitos preparations. Figure is adapted from [259].

7.3.6 Determination of apparent K_m for oxygen

To further probe possible differences between 5A and 5B isozyme, their oxygen affinities were determined using the oxymyoglobin method [175] by monitoring the rate of oxygen dissociation from oxymyoglobin, at $\Delta A_{582\text{-}564,}$ using a Shimadzu dual-wavelength spectrophotometer. The data were fitted with a Michaelis-Menten equation (Equation 1):

$$\textbf{(1)}\quad v = \frac{V_{max}.[S]}{K_m + [S]}$$

v = velocity, V_{max} = maximum velocity achieved at saturating substrate concentration, [S] = substrate concentration, K_m = Michaelis constant, substrate concentration at which the velocity is half of V_{max}.

The Michaelis-Menten plots for WTCOX5A, COX5B and ΔROX1ΔCOX5A mitos are shown in Figure 7-6, and the apparent K_m and V_{max} values are summarised in Table 7-2. No significant differences in apparent K_m were observed, but again the V_{max} of ΔROX1ΔCOX5A was at least 1.5-2 fold greater compared to that of WTCOX5A and COX5B.

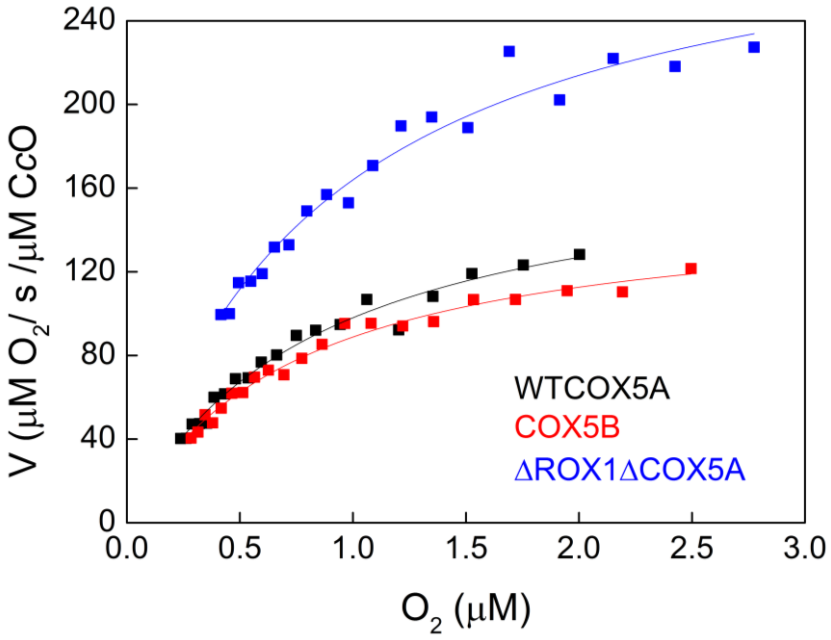

Figure 7-6. Michaelis-Menten plots derived by following the deoxygenation of horse heart oxymyoglobin by mitos preparations of yeast WTCOX5A (black), COX5B (red) and ΔROX1ΔCOX5A (blue).
The reaction buffer contained 30 μM total horse heart myoglobin whilst all other conditions were the same as in Figure 7-5 using 50 μM horse heart cyt c as substrate. V_{max} and apparent K_m values were determined using non-linear fitting of the Michaelis-Menten equation and are summarised in Table 7-2. Figure is adapted from [259].

Table 7-2. Comparison of oxygen affinities and V_{max} of WTCOX5A, COX5B and ΔROX1ΔCOX5A mitos
Non-linear fitting of the Michaelis-Menten equation to data in Figure 7-6 was performed on OriginPro 8.6 this was used to determine the apparent K_m and V_{max} values. Standard errors of the derived parameters and R-squared values are also shown. Table is adapted from [259].

Substrate	Strain (mitos)	V_{max} (μM O_2/s/μM C*c*O)	K_m (μM)	R-squared
Oxygen	WT	179 ± 7.6	0.84 ± 0.07	0.97667
	COX5B	154 ± 4.2	0.74 ± 0.05	0.98244
	ΔROX1ΔCOX5A	307.8 ± 11.4	0.88 ± 0.08	0.96577

7.3.7 V_{max} and apparent K_m for cytochrome c

For a full comparison of the kinetics of WTCOX5A, COX5B and ΔROX1ΔCOX5A mitos, V_{max} and apparent K_m values were determined for horse heart and yeast iso-1 and iso-2 cyts *c* as substrate. However, Eadie-Hofstee transformation of the data displayed monophasic kinetics for horse heart cyt *c*, but biphasic kinetics for yeast iso-1 and iso-2 cyt *c.* Therefore, the data obtained for horse heart cyt *c* was fit with a single Michaelis-Menten equation (Equation 1). The data obtained for yeast iso-1 and iso-2 cyt *c* was fit with the sum of two Michaelis-Menten terms using nonlinear regression analysis with OriginPro8.6 (Equation 2). The fits gave R-squared values greater than 0.95 and are shown in Figure 7-7.

$$\textbf{(2)}\quad v = \frac{V_{max1}.[S]}{K_{m1} + [S]} + \frac{V_{max2}.[S]}{K_{m2} + [S]}$$

The fit obtained with this analysis was confirmed by linear transformation to an Eadie-Hofstee plot, and by overlaying it on the Eadie-Hofstee transformed data, this illustrated more clearly the fit to all data points (Figure 7-8). The derived V_{max}, apparent K_m, and R-squared values are summarised in Table 7-3. WTCOX5A and COX5B displayed similar V_{max} and apparent K_m values irrespective of the cyt *c* source, whereas the ΔROX1ΔCOX5A strain again had a 1.5-2 fold greater V_{max}, but with a similar apparent K_m.

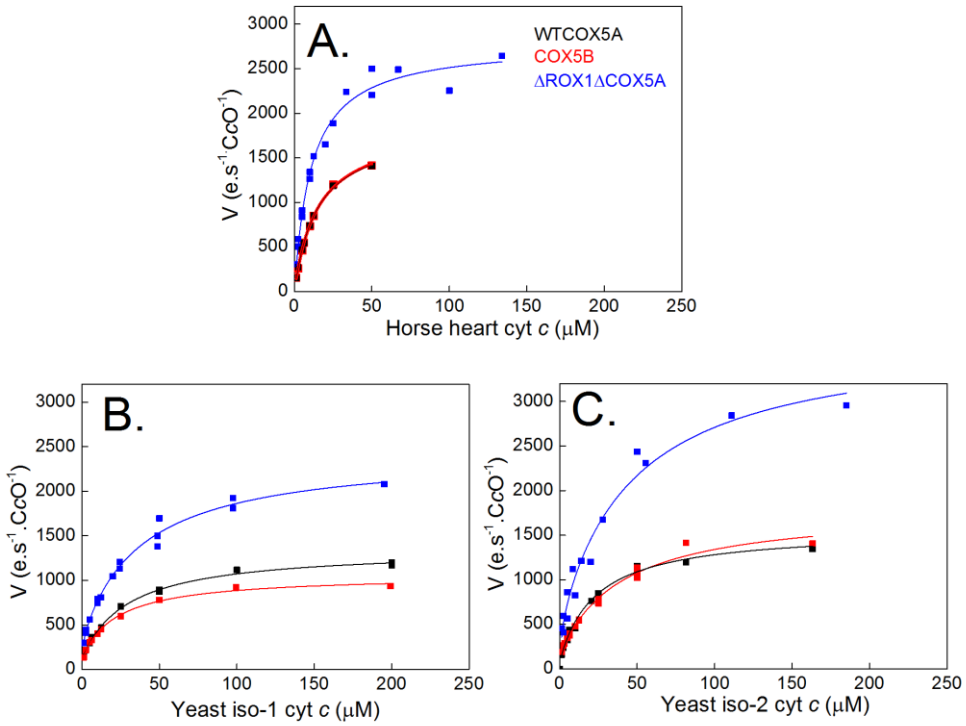

Figure 7-7. Michaelis-Menten plots of WTCOX5A (black), COX5B (red) and ΔROX1ΔCOX5A (blue) mitos using horse heart cyt c (A), yeast iso-1 cyt c (B) and yeast iso-2 cyt c (C)

Assay conditions were the same as in Figure 7-5 but the rate was measured at multiple cyt c concentrations (1.25-400 μM). V_{max} and apparent K_m values (Table 7-3) were determined using non-linear fitting of the Michaelis-Menten equation for data displaying single phase kinetics (A) and two Michaelis-Menten terms for those with biphasic kinetics (B and C). Figure is adapted from [259].

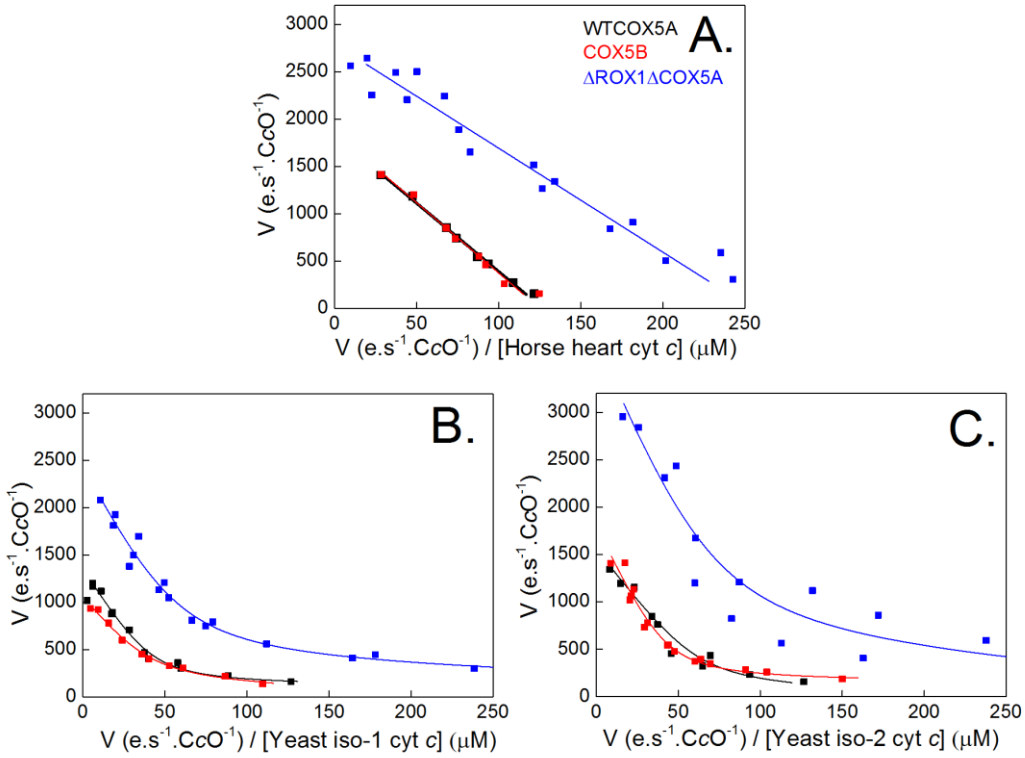

Figure 7-8. Eadie-Hofstee plots of WTCOX5A (black), COX5B (red) and ΔROX1ΔCOX5A (blue) mitos using horse heart cyt c (A), yeast iso-1 cyt c (B) and yeast iso-2 cyt c (C). *The data is overlaid with the Eadie-Hofstee transformation of the non-linear fit from Figure 7-7. Assay conditions are described in Figure 7-7. This figure is adapted from [259].*

Table 7-3. Summary of V_{max} and apparent K_m of WTCOX5A, COX5B and ΔROX1ΔCOX5A mitos for horse heart cyt c, yeast iso-1 cyt c and iso-2 cyt c.

Non-linear fitting of the Michaelis-Menten equation was performed for data showing single phase kinetics (Figure 7-8A), and the sum of two Michaelis-Menten terms was used for data that displayed biphasic kinetics (Figure 7-8B and C). Fitting was performed with OriginPro 8.6 and was used to determine the V_{max} and apparent K_m values. Standard errors of the derived parameters and R-squared values are also shown. Table is adapted from [259].

Substrate	**Strain (mitos)**	**Low affinity phase**		**High affinity phase**		
		V_{max} ($e.s^{-1}.CcO^{-1}$)	**K_m (μM)**	**V_{max} ($e.s^{-1}.CcO^{-1}$)**	**K_m (μM)**	**R-squared**
Horse heart cyt *c*	WT	1831 ± 25	14.4 ± 0.4	-	-	0.99924
	COX5B	1858 ± 38	14.9 ± 0.7	-	-	0.99843
	ΔROX1ΔCOX5A	2788 ± 82	11.0 ± 1.1	-	-	0.97906
Yeast Iso-1 cyt *c*	WT	1233 ± 43	29.7 ± 4.6	122.2 ± 52.8	0.09 ± 0.68	0.99645
	COX5B	910 ± 70	23.7 ± 6.1	151.8 ± 86.7	0.65 ± 1.1	0.99581
	ΔROX1ΔCOX5A	2099 ± 111	37.8 ± 9.2	341.9 ± 139.2	0.49 ± 0.91	0.98827
Yeast Iso-2 cyt *c*	WT	1452 ± 59	24.1 ± 3.0	110 *	0.53 ± 0.91	0.99088
	COX5B	1655 ± 92	39.4 ± 9.6	151.8 ± 78.9	0.03 ± 0.90	0.98449
	ΔROX1ΔCOX5A	3230 ± 289	47.5±10.5	526 *	1.2 ± 0.90	0.97083

**fits were based on fixing one variable (V_{max} of high affinity phase) to a value optimised based on the R-squared.*

7.4 Discussion

7.4.1 Prior reports on 5A and 5B isozymes

The gene that encodes the transcription repressor of *COX5B* under aerobic conditions, was identified by growing a *COX5A*-deleted strain on respiratory medium under aerobic conditions. Since subunit 5A or 5B is required for C*c*O assembly, only strains that had a mutation that could recover the phenotype could grow. Such strains were selected and found to have mutations in *ROX1* (also called *REO1*), a negative regulator of *COX5B* expression [147].

Subsequent comparisons of the 5A and 5B isozymes provided the intriguing observation that the 5B isozyme, was 2-3 fold more catalytically active than the 5A isozyme, in both whole cells and mitochondrial preparations. In this project, a mutant was constructed that was similar to that described in the literature. The only difference was that the *ROX1* gene was knocked-out, allowing *COX5B* gene expression from its nuclear locus, whereas in the literature the *ROX1* gene was mutated and the selected strain had two copies of *COX5B* [147]. Even with these small differences the results presented here with the equivalent ΔROX1ΔCOX5A mutant, confirm faster catalytic activity for 5B isozyme compared to WTCOX5A (Table 7-3 and Figure 7-5). In addition to this mutant, 5B isozyme expression, has been achieved in another *COX5A*-deleted strain that had wild type *ROX1* and where *COX5B* was cloned on a high copy plasmid [144]. Similarly 5B isozyme expressed this way was also reported to exhibit faster (2 fold) catalytic activity [261].

It is noteworthy that for those strains reported to date, in which elevated 5B isozyme turnover is observed, the expression level of C*c*O was substantially less than wild type levels. For example in the literature mutant that had mutated *rox1*, *Δcox5A* and two copies of *COX5B* the expression level of 5B isozyme was 34 % of the control [28]. In the mutant strain with normal *ROX1* expression, *Δcox5A,* and a higher copy number plasmid of *COX5B*, the expression level of 5B isozyme was still under 50 % of the control [261]. Lastly in the equivalent mutant strain reported in this chapter, ΔROX1ΔCOX5A, the expression level was ~14 % of wild type control (Figure 7-3).

7.4.2 COX5B expression under the control of the COX5A promoter

The observed elevated activity of the 5B isozyme may be influenced by additional effects, such as *ROX1* mutations and/or decreased C*c*O expression levels. In order to investigate the origin of this effect, *COX5A*-deleted mutant strains were constructed

that expressed *COX5B* downstream of the *COX5A* promoter. This type of genetic replacement at the *COX5A* genomic locus has been reported previously [262]. However, this was a chimeric construct, where the first 12 amino acids were encoded by *COX5A* and the remaining amino acids were encoded by *COX5B*, and so it was not a complete replacement of genes. Likewise, at the *COX5B* genomic locus, the first 12 amino acids were encoded by *COX5B* and the remaining were encoded by *COX5A*. Unfortunately turnover numbers of 5A and 5B isozymes were not compared in these mutants, but they were used to show that the *COX5B* promoter was weak compared to the *COX5A* promoter, shown by the transcript abundance being greater for *COX5A* than *COX5B* [262]. This would explain the diminished levels of assembled 5B isozyme in the mutants that express *COX5B* downstream of its own weak promoter [28,144]. Very recently, Hess, *et al.* [263] also produced yeast strains with this same gene replacement, however, K_m/V_{max} parameters were not determined but ATP/ADP and phosphorylation effects were investigated (see below).

In this project the *COX5B* replaced the entire *COX5A* gene downstream of the *COX5A* promoter. Here, the gene replacement was carried out at the nuclear locus of *COX5A* (COX5B strain), or on a centromeric plasmid in a *COX5A*-deleted strain (pCOX5B). In addition the effect of Rox1 was investigated by comparison of *COX5A*-deleted strains, with or without *ROX1* deletion, that contained a centromeric plasmid expressing either 5A isoforms (WTCOX5A and ΔROX1ΔCOX5ApCOX5A) or 5B isoforms (pCOX5B and ΔROX1ΔCOX5ApCOX5B), under the control of the *COX5A* promoter. This enabled expression of 5A or 5B isoforms at wild type levels with aerobic growth conditions and with the same status (present or deleted) of *ROX1*. When compared in these constructs, the 5A and 5B isozymes failed to show any difference in maximal turnover numbers, in either cells or membrane preparations (discussed below).

7.4.3 Comparison of oxygen affinities

The oxygen affinity of WTCOX5A is reported here for the first time in yeast C*c*O as 0.84 ±0.07 μM (Figure 7-6 and Table 7-2). This value was also measured in the COX5B and ΔROX1ΔCOX5A strains (Figure 7-6 and Table 7-2). This is because differences may be apparent at only low oxygen levels since 5A and 5B isoform expression, *in vivo*, is regulated by oxygen concentration. However, their apparent K_m values were the same as wild type, 0.74 ±0.05 μM for COX5B and 0.88 ±0.08 μM for ΔROX1ΔCOX5A. These values are in a similar range to those previously reported for bovine C*c*O (1 μM [264] and 0.95 μM [265]). This shows that COX5B, which expressed

COX5B downstream of the *COX5A* promoter, cannot be distinguished from WTCOX5A, based on their affinities for oxygen. The V_{max} values were the same between WTCOX5A and COX5B and 1.5 fold greater for the ΔROX1ΔCOX5A mutant.

7.4.4 Comparisons of V_{max} and apparent K_m values for cyt c

The V_{max} and apparent K_m values for cyt *c* were determined (Table 7-3). Using cyt *c* from horse heart, no differences between WTCOX5A and COX5B were found but again the V_{max} of ΔROX1ΔCOX5A was ~1.5-2 fold greater. The values determined for WTCOX5A with horse heart cyt *c* were in a range consistent with Geier, *et al.* (V_{max} 1773 $e.s^{-1}.CcO^{-1}$, 15.3 μM; [37]).

Saccharomyces cerevisiae cyt *c* has two isoforms, whose expression is also differentially regulated by oxygen concentration under the control of the *ROX1* transcription repressor [148,149]. Yeast iso-1 cyt *c* is expressed aerobically and yeast iso-2 cyt *c* is expressed under hypoxic conditions. They share 84 % amino acid sequence identity [266]. Hence, these physiologically relevant isoforms of yeast cyt *c*, were used as substrate to determine the V_{max} and apparent K_m of WTCOX5A, COX5B and ΔROX1ΔCOX5A mitos preparations (Table 7-2). However, there were no significant differences in V_{max} between WTCOX5A and COX5B, but once again, the mutant equivalent to the literature had values that were 1.5-2 fold greater (Figure 7-5 and Table 7-3). The V_{max} and apparent K_m values for yeast iso-1 and iso-2 cyt *c*, have been reported previously with 5A or 5B isozyme mitos where V_{max} values were below 40 s^{-1} and K_m values below 10 μM [151]. These values are considerably lower than those reported here for each strain. This difference could be due to the assay conditions used and possibly the method used to prepare mitos, or they could be due to the higher and more physiologically relevant (0.5 mM [267]) cyt *c* concentration range used in this study (300 μM to 1.25 μM) compared to the 20 μM to 0.05 μM range of Allen, *et al.* [151]. It was evident that the apparent K_m values for cyt *c* regardless of its source were similar for WTCOX5A, COX5B and ΔROX1ΔCOX5A strains, this is consistent with [37,151]. This shows that the 5A and 5B isoforms do not affect cyt *c* binding on subunit II.

Allen, *et al.* [151] reported a greater difference in activity when the non-physiological isoform pairs were put together (C*c*O isozyme 5A/iso-2 cyt *c* and C*c*O isozyme 5B/iso-1 cyt *c*). Hence it was reported that when the physiological isoform pairs are put together aerobic (C*c*O isozyme 5A/iso-1 cyt *c*) and hypoxic (C*c*O isozyme 5B/iso-2 cyt *c*), they act synergistically to dampen the difference in rates in 5A versus 5B, from 4 fold to 1.6 fold. However, no preferences for specific cyt *c* isoforms were

evident in the 5A and 5B isozymes reported here. If anything, the opposite effect was observed where the activity difference was enhanced when comparing physiological pairs; WTCOX5A/iso-1 cyt *c* and ΔROX1ΔCOX5A/iso-2 cyt *c* pairs (Figure 7-5). It is also obvious that the V_{max} values, regardless of the strain analysed, were in the order: horse heart > iso-2 > iso-1 cyt *c* (Figure 7-5 and Table 7-3). These differences could be accounted for by the assay conditions that had been optimised in pH and ionic strength for horse heart cyt *c*.

7.4.5 Biphasic kinetics

C*c*O displayed biphasic kinetics with yeast cyt *c*, as also observed by Allen, *et al.* [151] (Figure 7-8B and C). However, C*c*O displayed single phase kinetics with horse heart cyt *c* and this is consistent with Geier, *et al.* [37] (Figure 7-8A), this difference in kinetics between yeast versus horse heart cyt *c*, was apparent when the cyt *c* concentration range (1.25 µM to ~300 µM) and assay conditions were the same.

To date there are no crystal structures of a cyt *c* bound to C*c*O, the ionic strength dependence of the cyt *c* reaction with C*c*O, provided a clue that their interaction was electrostatic [268]. However studies with chemically modified cyt *c* [43,269,270] and site-directed mutagenesis of bacterial forms of C*c*O [271,272], have identified a set of positively charged lysines on cyt *c* and negatively charged glutamates and aspartates on C*c*O (subunit II) that are involved in the electrostatic interaction. Similarly a patch of negatively charged residues is predicted on the bovine C*c*O crystal structure [34]. A conserved tryptophan (trp-121 *P. denitrificans* C*c*O) on subunit II is shown through mutagenesis to provide the entry site for electrons into C*c*O [273]. Biphasic kinetics have been observed using bovine C*c*O with different cyts *c* [274,275]. It was noted from studies on bovine C*c*O that the appearance of two phases was dependent on the use of low cyt *c* concentrations (0.02-5 µM), at low ionic strength (<25 mM phosphate), and at pH values below ~7.5 that are conditions in which the electrostatic interactions between cyt *c* and C*c*O would be the most pronounced [274]. There are various models in the literature used to explain the biphasic behaviour. One such model is that there are two catalytic sites on C*c*O that can bind cyt *c* with different affinities resulting in biphasic kinetics [274]. Although the location of a second electron entry site is not clear. A second model is that the binding region on C*c*O can accommodate two cyts *c*. At low ionic strength the first cyt *c* binds with high affinity due to the large long range electrostatic interactions, the second binds with lower affinity since part of the charge on C*c*O is neutralised, and as a result of the repulsion between the cyts *c*, the dissociation rate of both cyts *c* is increased. The dissociation rate constant of ferricyt *c*

was proposed to be the rate limiting step. At high ionic strength, the ions would mask out the electrostatic influence of one cyt *c* with another and with the binding region, hence, each cyt *c* would bind independently and with low affinity resulting in monophasic kinetics [276]. A third model, is that the second site is on another location on C*c*O (or on an associated acidic phospholipid) [258]. This acts as a regulatory non-catalytic binding site for cyt *c* that allosterically changes the conformation of the catalytic binding site [258]. The transition of high affinity to low affinity phase, was suggested to arise from an increase in the dissociation rate constant of ferricyt *c* (the rate limiting step) when the regulatory site was bound by a second cyt *c*. Recently, another model was proposed, that in addition to the effects of the second regulatory site, oxidised cyt *c* acts as a competitive inhibitor of C*c*O, competing for the same catalytic site as ferrocyt *c* but with weaker affinity, and at high ionic strength, the affinity becomes less [277]. However, the assays reported here maintained cyt *c* in the reduced state by the presence of ascorbate and TMPD.

Here the assay conditions were optimised to give fast turnover activities of C*c*O with horse heart cyt *c*, resulting in a single low affinity-high velocity phase*;* it is possible that these (ionic strength) conditions are not optimal for yeast iso-1 and iso-2 cyt *c* and could explain why biphasic kinetics were observed with yeast cyt *c* and not with horse heart cyt *c*. Moreover, it is clear that the apparent K_m values for the high affinity phase, could not be determined with high accuracy because at such low cyt *c* concentrations, the rates were slow and approaching the detection limit of the oxygen electrode assay (Table 2-1). Nevertheless, it is clear from the Eadie-Hofstee plots, that two phases exist (Figure 7-8). However, only the much more accurate high velocity-low affinity phase data were used to make meaningful comparisons of COX5A, COX5B and ΔROX1ΔCOX5A isozymes. Furthermore this phase may predominate under physiological conditions based on the fact that cyt *c* concentrations in the intermembrane space is at 0.5 mM [267], and because this same phase is observed with horse heart, yeast iso-1 and iso-2 cyt *c* (Table 3).

7.4.6 Two possible interpretations of findings

In summary, the findings in this chapter show definitively that when 5A or 5B isozymes are expressed from the same *COX5A* promoter, (from the nuclear locus or a centromeric plasmid) to the same level, under aerobic conditions and with or without *ROX1* deletion, they exhibit the same V_{max} and apparent K_m for cyt *c* and affinity for oxygen. However, it is also clear that the 5B isozyme, when expressed from its own promoter (ΔROX1ΔCOX5A strain), does have greater catalytic activity as reported

previously [28,151]. Hence, the elevated activity of the 5B isozyme expressed this way must be caused by a secondary effect. Two possible explanations are discussed here.

7.4.6.1 An effect of ROX1

In addition to *COX5B* and *CYC7* (encoding iso-2 cyt *c*) genes, Rox1 is a transcription repressor of at least 25 more different target genes in yeast [278,279]. It is possible that loss of the Rox1 transcription repressor of *COX5B*, could cause increased 5B isozyme activity through separate effects that might lead to post-translational modification of subunit 5B, for example phosphorylation. The isoforms share a high amino acid sequence identity of 66 % [145]. Recent *in silico* analysis, however, has identified T65 and S43 residues in the matrix facing domain of subunit 5A, as phosphorylation sites that are replaced with N65 and N43 in subunit 5B [263]. These sites however were suggested to be targets of a different regulatory pathway in the mitochondria, involving CO_2/adenylyl cyclase/cyclic AMP/protein kinase A, in which the phosphorylation decreased the activity of 5A isozyme. Moreover a change in the ATP/ADP ratio has been reported to alter C*c*O activity in yeast, in which ATP binding caused an inhibitory effect on 5A isozyme activity [280] and not 5B isozyme acitivity [263]. Furthermore, phosphorylation of T65 and S43 site on subunit 5A prevents the allosteric inhibitory effect of ATP [263]. However this level of regulation on C*c*O activity, cannot explain the observed elevated activity difference of the 5B isozyme in ΔROX1ΔCOX5A compared to COX5B, since they both contain subunit 5B. It is still possible that the Rox1 mediated signalling could phosphorylate subunit 5B. Sequence comparisons show that there are five threonines, that could be potential phosphorylation sites on the hydrophilic matrix domain of 5B that are not present on 5A, these are; Thr4Asn, Thr18Val, Thr30Ala, Thr32Met, Thr63Gln and are highlighted in Figure 7-9.

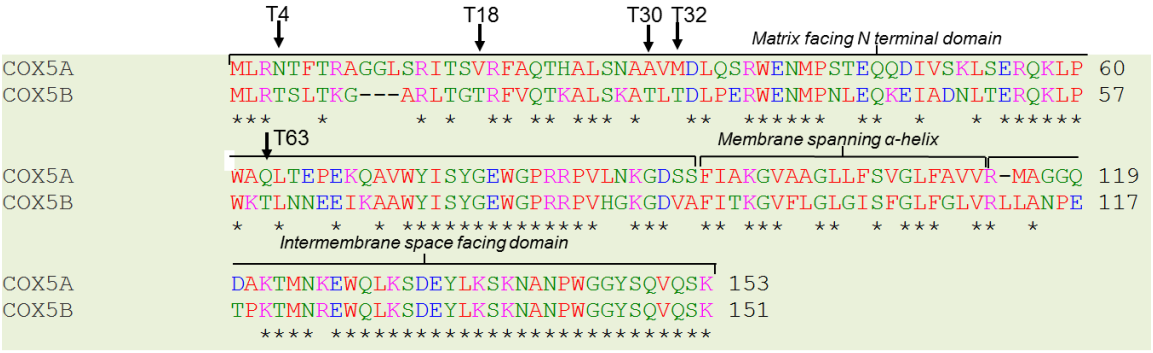

Figure 7-9. Amino acid sequence alignment of subunits 5A and 5B showing possible phosphorylation sites on 5B.
Sequences are of YNL052W_W303 for 5A subunit and YNL052W_W303 for 5B subunit and are taken from Saccharomyces genome database. Asterisk indicates identical residues, sequences are divided to show the approximate regions that correspond to the matrix domain, membrane spanning α-helix and IMS domain. Red, small hydrophobic residues; blue, acidic residues; magenta, basic residues apart from histidine; green, hydroxyl, sulfhydryl, amine, and glycine residues.

However, the following experimental evidence argues against these factors being the secondary effect of *ROX1* deletion that results in an increased activity. First of all, elevated activity was observed when 5B isozyme was expressed from a high copy number plasmid, both in the presence of *ROX1* [261] and in a *rox1*-mutated strain [151]. In addition, data here show that the 5B isozyme had the same activity (and expression level) as the 5A isozyme, when expressed both with (in the COX5B strain) and without (in the ΔROX1ΔCOX5ApCOX5B strain) a functioning Rox1 (Figure 7-5).

7.4.7 Low expression levels

Increased catalytic activity of the 5B isozyme has been observed only under conditions in which its expression level was significantly lower than in WT strains [28,261]. The level of 5B isozyme in ΔROX1ΔCOX5A strain, was also lowered by a factor of ~6 (Figure 7-3) because the *COX5B* promoter is a weak promoter [262]. However, the bc_1 complex expression levels remained relatively constant. This therefore resulted in the ΔROX1ΔCOX5A strain having a much smaller C*c*O:bc_1 ratio. In yeast mitochondria, C*c*O/bc_1 supercomplexes have been shown to form [131,135,281]. It is possible that, when the C*c*O:bc_1 ratio is low, the proportion of C*c*O that assembles into such supercomplexes is greater. Such an interaction may induce allosteric effects that elevate the catalytic activity of C*c*O. Interestingly, the III_2IV_2 supercomplex structure of yeast C*c*O shows that subunit 5 is close to the interface with

the bc_1 complex [135] (Figure 7-10). The extent of supercomplex formation, and the allosteric effect that it induces, could be different with the 5A and 5B isoforms.

Figure 7-10. (A) Cryo-EM three-dimensional map and the III_2IV_2 supercomplex in S. cerevisiae and (B) the fitted X-ray crystal structures of S. cerevisiae complex III dimer and bovine CcO monomors.
Subunit IV of bovine CcO (pink), homologous to subunit 5 in yeast CcO, is in close interaction with bc_1 complex. Figure is adapted from figure 4A and 5A in ref [135].

Digitonin is a mild detergent that was used to isolate such supercomplexes for cryo-electron microscopy [135]. In order to assess whether such supercomplex did indeed elevate the activity of WT (5A isozyme) C*c*O, C*c*O:bc_1 supercomplexes were isolated using the same detergent. Initially mitochondrial fragments were solubilised in digitonin, and the supercomplex was purified by nickel affinity column chromatography against the his-tag on C*c*O. The protocol is described in Section 2.6.3. C*c*O co-eluted with bc_1 complex and their presence was confirmed by visible redox spectra (see Figure 2-8). The activity of this supercomplex was compared to C*c*O that was purified in the same way, but in the presence of DDM, in which visible redox spectra of the eluted fraction showed the presence of predominantly C*c*O (data not shown) but spectrum was similar to that shown in Figure 2-5. The turnover activity of the supercomplex (500 $e.s^{-1}.CcO^{-1}$, measured in 10 mM KPi, 50 mM KCl, 0.05 % (w/v) DDM pH 6.6) was found to be 3-4 fold faster than the isolated C*c*O (170 $e.s^{-1}.CcO^{-1}$, same conditions). However, this elevated activity could also arise from the stabilising effects of the detergents used (digitonin vs. DDM) and the possible differences in the extent of delipidation by each detergent during the washing of the nickel column before elution and must be interpreted with caution.

The allosteric effect from this interaction could be mediated via the H channel that runs parallel to the membrane spanning α-helix of subunit 5, and this could support the proposal of the role of the H channel as a dielectric channel [78] (Figure 7-11).

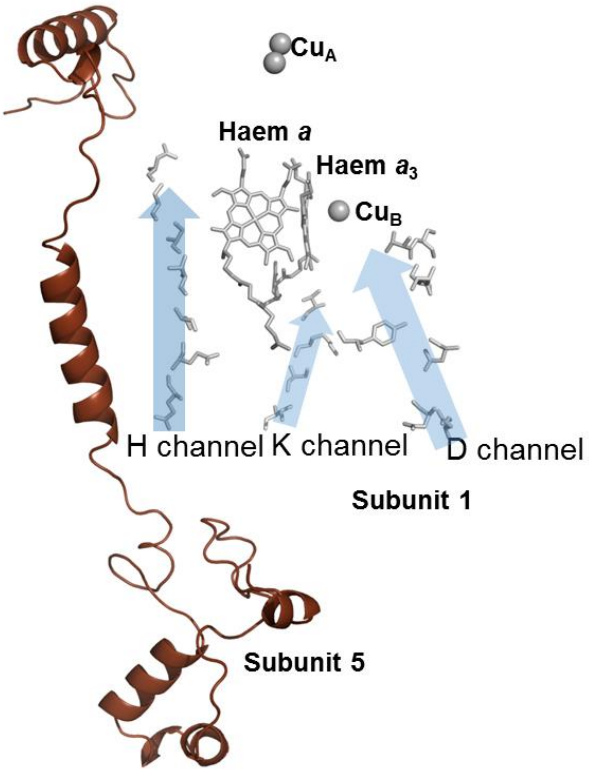

Figure 7-11. The close proximity of the α-helix of subunit 5 (red) and the H channel in subunit I (grey) of yeast CcO.
The residues that make up the H channel reside in helices 11 and 12 of subunit I. These helices are the most closest to subunit 5 (Figure 7-1).

7.5 Conclusions

The aim of this project was to compare 5A and 5B isozymes of yeast C*c*O under controlled conditions. Mutant strains were constructed in which the *COX5A* gene was replaced with *COX5B* downstream of the *COX5A* promoter, at the nuclear locus of *COX5A*. In addition the effect of Rox1 was investigated by comparison of *COX5A*-deleted strains with or without *ROX1* deletion; these contained either a centromeric plasmid expressing 5A isoforms (ΔCOX5ApCOX5A and ΔROX1ΔCOX5ApCOX5A) or 5B isoforms (pCOX5B and ΔROX1ΔCOX5ApCOX5B) under the control of the *COX5A* promoter. When expressed under the control of the *COX5A* promoter, the strains grew with doubling times (2.7-3.0 h) and with final wet mass of cells (11 g) that were the same as wild type, in YPGal media. *COX5B* was expressed under aerobic conditions, with expression levels the same as wild type (5A isozyme). When compared under these controlled conditions, the 5A and 5B isozymes displayed no significant differences in their maximum turnover activities, in either cells or membrane preparations, or in their V_{max} and apparent K_m values for cyt *c*, or affinities for oxygen. As a further control, a mutant equivalent to that previously reported was constructed in which *COX5A* mutation, was combined with *ROX1* deletion enabling aerobic expression of *COX5B* from its own promoter. This confirmed prior reports that the 5B isozyme expression level, was decreased (~6 fold) and that it exhibited 1.5-2 fold greater catalytic turnover activities and V_{max} values for cyt *c*, compared to the 5A isozyme. It is concluded that the elevated activity of the 5B isozyme, in the *rox1* mutant, is not caused simply by exchange of isoforms and must arise from an additional effect that is still to be resolved. It is possible that it is linked with the low C*c*O:bc_1 complex ratio observed in ΔROX1ΔCOX5A. This could result in a greater proportion of C*c*O present as a supercomplex of C*c*O/bc_1, in which C*c*O could be capable of faster catalytic activity. This could be mediated by an allosteric effect of subunit 5, which is at the interface with complex III. This interaction could modulate the H channel dielectric properties and in turn the catalytic activity of C*c*O. The extent of supercomplex formation, and the allosteric effect that it induces, could be different with the 5A and 5B isoforms, providing a novel possible functional basis for the existence of the isozymes.

7.6 Future work

In order to test whether the increased catalytic activity is the result of low expression levels of C*c*O, or a combination of low expression levels of C*c*O assembled with the 5B isoform, the activity of ΔROX1ΔCOX5A could be compared to another control mutant strain. This strain should be a *COX5A*-deleted strain where *COX5B* is replaced by *COX5A* downstream of the *COX5B* promoter on the nuclear genome, with the deletion of *ROX1* to enable aerobic expression. This would result in low levels of assembled 5A isozyme, and provide experimental evidence that will resolve this hypothesis.

In order to assess for the presence of a C*c*O:bc_1 supercomplex, a blue native polyacrylamide gel electrophoresis of ΔROX1ΔCOX5A in one lane could be compared to WTCOX5A and COX5B strains. According to this supercomplex hypothesis, WTCOX5A and COX5B strains would show separate bands corresponding to molecular weights of bc_1 and C*c*O, whereas ΔROX1ΔCOX5A should display a large MW band corresponding to the supercomplex [131,135,281].

The assay conditions were optimised for horse heart cyt *c* oxidation by WTCOX5A mitos, and these conditions were used for all comparisons between mitos preparations. It is possible that a kinetic difference between 5A and 5B isozymes may be resolved at different ionic strength or pH conditions. However, it is unlikely since the subunits share high sequence identity and matching average hydropathy plots [145].

Post-translational modifications such as phosphorylation can be measured using mass spectrometry. Mass spectrometry is being carried out on WT, COX5B, pCOX5B and ΔROX1ΔCOX5A mitos by our collaborator Dr. Susanne Arnold (Radboud University Nijmegen Medical Centre, Netherlands). Mass spectra will be compared to determine if there are any differences in post-translational modifications (presence of phosphate groups) between 5A and 5B isozymes, and more importantly between WTCOX5A and ΔROX1ΔCOX5A.

8 Final conclusions

In this work the structure and function of mitochondrial C*c*O has been investigated by focusing on several key areas. These include redox-linked IR structural changes, the role of the conserved cross-linked Tyr-His feature, the function of the H channel in yeast C*c*O and the role of supernumerary subunits, 5A/5B, of yeast C*c*O.

CN and CO ligands of C*c*O allowed stable MV states of bovine C*c*O to be induced electrochemically; they enabled the definitive separation and linkage of redox-induced IR bands to specific metal centres in the 1800-1000 cm^{-1} range. The findings show that the majority of the IR changes are induced by transitions in Cu_A and haem *a*. Meanwhile fewer IR bands of smaller intensity have been linked with redox transitions of haem a_3 and Cu_B. The linkages indicate that the environment surrounding Cu_A and haem *a* is more redox sensitive than the BNC, suggesting a more rigid structure of the BNC. This result may provide further insight into the location of residues involved in or necessary to the overall reaction mechanism of C*c*O. The protein backbone changes linked with Cu_A and haem *a* could be accounted for by the residues that make up the H channel since this H channel is closest to Cu_A and haem *a*. The 1760-1710 cm^{-1} region of the FR *minus* O IR difference spectrum of C*c*O is where the *v*(C=O) modes of protonated carboxylic amino acids appear amongst other components such as ester bonds of lipids and protonated propionates [184]. Carboxylic groups in C*c*O are implicated in the coupling of electron transfer with proton transfer by providing de/protonation sites. This region of the IR difference spectrum appears as two overall troughs at 1749 cm^{-1} and 1737 cm^{-1} attributed to E242 and D51 of bovine C*c*O respectively and, in the simplest case, it can be simulated with at least three Gaussian shaped bands [90,104,115]. In this study this region of the IR spectrum has been separated and linked to specific metal centre transitions and has revealed an additional component at 1740 cm^{-1}. The two components at 1749 cm^{-1} and 1737 cm^{-1} have been linked with the oxidation of Cu_A and haem *a*, a finding that is consistent with prior literature [104,115,117]. The third 1740 cm^{-1} component seems to be linked with haem a_3 oxidation and Cu_B reduction. By consideration of literature data [90,104,115] and the findings reported here, a model with five Gaussian components has been proposed to account for the data. This model makes a few assumptions such as the relative intensities of the IR components; nevertheless it provides insight into how the project can be extended in the future. The assignment of the 1740 cm^{-1} component to a specific residue will require further investigation and several candidates have been

proposed such as D369, D364, E198, D442, E40 (subunit I) and E62 (subunit II) and E90 and D246 (subunit III).

Cyclic voltammetric characterisation of various Tyr-His model compounds has identified an optimal structure (TyrHis(trimethyl)) that can partially stabilise an electrochemically induced tyrosine radical. Its pK_as are 6.8 ±0.4 for imidazole and 9.2 ±0.2 for the phenol group. IR absolute spectra of this structure in the fully protonated, neutral and fully deprotonated states have been tentatively assigned by comparison to IR bands predicted by calculation using Gaussian. The optimised electrochemical conditions were combined with ATR-FTIR spectroscopy to record reduced *minus* oxidised (radical) IR difference spectra. By comparison to IR difference spectra of TMP and TBP (phenol model compounds) the bands at 1550 cm^{-1} and 1510 cm^{-1} of TyrHis(trimethyl) have been assigned to *v*8a(C-C) and *v*7a(C-$O^{\bullet}$) of a phenoxyl radical, respectively. The peak/trough at 1301(+)/1314(-) cm^{-1} has been assigned to an imidazole ring stretch. TyrHis(trimethyl), along with TMP and TBP, have provided IR reference spectra to aid assignment of IR radical bands in the P_M catalytic intermediate of bovine C*c*O. By also considering literature assignments, an IR band at 1572 cm^{-1} [186] or at 1555 cm^{-1} has been tentatively assigned to *v*8a(C-C) and at 1519 cm^{-1} [166,186,197] to the *v*7a(C-$O^{\bullet}$) of a phenoxyl radical in the P_M state. 1336 cm^{-1} has been assigned to a histidine ring stretch of the cross-linked structure in the P_M state. The P_M *minus* oxidised IR difference spectrum is also presented in the low frequency range for the first time, and a band at 808 cm^{-1} has been shown to be $^{18}O_2$ –sensitive, and has therefore, been assigned to $Fe^{4+}=O^{2-}$ stretch of the P_M state. Hence in addition to simultaneously recorded visible spectra, this band can provide a further control to monitor the extent of P_M formation. These findings add further weight to the proposal that a tyrosine radical is formed on the Tyr-His cross-linked structure in the P_M state, consistent with its proposed role as a proton/electron donor in the overall catalytic cycle [38,48,49,244].

Yeast is a model system to study mitochondrial forms of C*c*O because mutations can be introduced into the nuclear and mitochondrially encoded subunits [118]. In this study the function of the H channel was assessed as a possible proton translocation pathway since it is believed to provide this role in mammalian C*c*Os [87]. Its role was tested by measurement of the H^+/e^- stoichiometry of an extreme 4H mutant (Q411L/Q413L/S458A/S455A) after membrane reconstitution into vesicles. The findings show that the 4H mutant retains full proton translocating activity of 1 ±0.07 H^+/e^- and so is not a critical pathway for proton translocation in yeast C*c*O. The H channel has alternatively been proposed to act as a dielectric channel [78] and the

altered kinetics that were observed for the H channel mutants could possibly be explained by a modulation of the H channel dielectric properties.

Supernumerary subunits 5A and 5B of yeast C*c*O are differentially regulated by oxygen concentration where *COX5B* expression is induced at low oxygen levels <1 µM [148]. Previously aerobic expression of the 5B isozyme has been achieved in a *COX5A*-deleted strain by mutation of *rox1*, a transcription repressor of *COX5B* [147]. The expression level of assembled 5B isozyme was 30-50 % of wild type and it exhibited a ~2-3 fold faster turnover activity [28,151,261]. To further assess the role of the isoforms, a mutant ΔROX1ΔCOX5A, equivalent to that reported in the literature, confirmed the low levels of 5B isozyme expression and its 1.5-2 fold faster activity. In addition, new strains have been constructed that allow aerobic expression of *COX5B* by placing *COX5B* in a *COX5A*-deleted strain downstream of the *COX5A* promoter at the *COX5A* nuclear locus or on a centromeric plasmid. This allowed wild type levels of 5B isozyme to be assembled and, when compared to 5A isozyme, there was no difference in the V_{max} or apparent K_m values for cyt *c* or affinities for oxygen. The effect of Rox1 was investigated by comparison of isozymes from *COX5A*- or *COX5B*-expressing strains with or without *ROX1* deletion and where expression of *COX5A/5B* was always under the control of the *COX5A* promoter. However, there was no difference in their kinetic properties. It is concluded that the elevated activity of the 5B isozyme in the *rox1* mutant, where *COX5B* expression is controlled by its own promoter, is not caused simply by exchange of isoforms and must arise from an additional effect that is still to be resolved. It is possible that it is linked with the low C*c*O:bc_1 complex ratio in ΔROX1ΔCOX5A. This could result in a greater proportion of C*c*O present as a supercomplex of C*c*O/bc_1, in which C*c*O could be capable of faster catalytic activity. This could be mediated by an allosteric effect of subunit 5, which is at the interface with complex III [135]. This interaction could modulate the H channel dielectric properties and, in turn, the catalytic activity of C*c*O. The extent of supercomplex formation, and the allosteric effect that it induces, could be different with the 5A and 5B isoforms, providing a novel possible functional basis for the existence of the isozymes.

9 Reference list

1 Nelson, N. L., Lehninger, A. L., and Cox, M. M. (2008) Lehninger Principles of Biochemistry pp. 1-1158, W. H. Freeman and Company, New York

2 Carroll, J., Fearnley, I. M., Skehel, J. M., Shannon, R. J., Hirst, J. and Walker, J. E. (2006) Bovine complex I is a complex of 45 different subunits. J. Biol. Chem. **281**, 32724-32727

3 Baradaran, R., Berrisford, J. M., Minhas, G. S. and Sazanov, L. A. (2013) Crystal structure of the entire respiratory complex I. Nature. **494**, 443-448 doi:10.1038/nature11871

4 de Vries, S. and Grivell, L. A. (1988) Purification and characterization of a rotenone-insensitive NADH:Q6 oxidoreductase from mitochondria of *Saccharomyces cerevisiae*. Eur. J. Biochem. **176**, 377-384

5 de Vries, S., Van Witzenburg, R., Grivell, L. A. and Marres, C. A. M. (1992) Primary structure and import pathway of the rotenone-insensitive NADH-ubiquinone oxidoreductase of mitochondria from *Saccharomyces cerevisiae*. Eur. J. Biochem. **203**, 587-592

6 Luttik, M. A. H., Overkamp, K. M., Kötter, P., de Vries, S., van Dijken, J. P. and Pronk, J. T. (1998) The *saccharomyces cerevisiae NDE1* and *NDE2* genes encode separate mitochondrial NADH dehydrogenases catalysing the oxidation of cytosolic NADH. J. Biol. Chem. **273**, 24529-24534

7 Iwata, M., Lee, Y., Yamashita, T., Yagi, T., Iwata, S., Cameron, A. D. and Maher, M. J. (2012) The structure of the yeast NADH dehydrogenase (Ndi1) reveals overlapping binding sites for water- and lipid-soluble substrates. Proc. Natl. Acad. Sci. USA. **109**, 15247-15252 doi:10.1073/pnas.1210059109

8 Sun, F., Huo, X., Zhai, Y., Wang, A., Xu, J., Su, D., Bartlam, M. and Rao, Z. (2005) Crystal structure of mitochondrial respiratory membrane protein complex II. Cell. **121**, 1043-1057 doi:10.1016/j.cell.2005.05.025

9 Yu, L., Xu, J.-X., Haley, P. E. and Yu, C.-A. (1987) Properties of bovine heart mitochondrial cytochrome b_{560}. J. Biol. Chem. **262**, 1137-1143

10 Yankovskaya, V., Horsefield, R., Törnroth, S., Luna-Chavez, C., Myoshi, H., Léger, C., Byrne, B., Ceccini, G. and Iwata, S. (2003) Architecture of succinate dehydrogenase and reactive oxygen species generation. Science. **299**, 700-704

11 Hägerhäll, C. (1997) Succinate: quinone oxidoreductases. Variations on a conserved theme. Biochim. Biophys. Acta. **1320**, 107-141

12 Rich, P. R. (1984) Electron and proton transfers through quinones and cytochrome *bc* complexes. Biochim. Biophys. Acta. **768**, 53-79

13 Oyedotun, K. S., Sit, C. S. and Lemire, B. D. (2007) The *Saccharomyces cerevisiae* succinate dehydrogenase does not require heme for ubiquinone

reduction. Biochim. Biophys. Acta. **1767**, 1436-1445 doi:10.1016/j.bbabio.2007.09.008

14 Anderson, R. F., Hille, R., Shinde, S. S. and Cecchini, G. (2005) Electron transfer within complex II. Succinate:ubiquinone oxidoreductase of *Escherichia coli*. J. Biol. Chem. **280**, 33331-33337

15 Iwata, S., Lee, J. W., Okada, K., Lee, J. K., Iwata, M., Rasmussen, B., Link, T. A., Ramaswamy, S. and Jap, B. K. (1998) Complete structure of the 11-subunit bovine mitochondrial bc_1 complex. Science. **281**, 64-71

16 Esser, L., Elberry, M., Zhou, F., Yu, C. A., Yu, L. and Xia, D. (2008) Inhibitor-complexed structures of the cytochrome bc_1 from the photosynthetic bacterium *Rhodobacter sphaeroides*. J. Biol. Chem. **283**, 2846-2857

17 Mitchell, P. (1976) Possible molecular mechanisms of the protonmotive function of cytochrome systems. J. Theor. Biol. **62**, 327-367

18 Rich, P. R. and Maréchal, A. (2010) The mitochondrial respiratory chain. Essays Biochem. **47**, 1-23 doi:10.1042/bse0470001

19 Rich, P. R. and Maréchal, A. (2012) Electron transfer chains: structures, mechanisms and energy coupling. In Comprehensive Biophysics (Ferguson, S. J., ed.). pp. 72-93, Elsevier Academic Press Inc, San Diego

20 Mitchell, P. (1961) Coupling of phosphorylation to electron and proton transfer by a chemi-osmotic type of mechanism. Nature. **191**, 144-148

21 Stock, D., Leslie, A. G. W. and Walker, J. E. (1999) Molecular architecture of the rotary motor in ATP synthase. Science. **286**, 1700-1705

22 Watt, I. N., Montgomery, M. G., Runswick, M. J., Leslie, A. G. W. and Walker, J. E. (2010) Bioenergetic cost of making an adenosine triphosphate molecule in animal mitochondria. Proc. Natl. Acad. Sci. USA. **107**, 16823-16827

23 Meier, T., Polzer, P., Diederichs, K., Welte, W. and Dimrith, P. (2005) Structure of the rotor ring of F-type Na^+-ATPase from *Ilyobacter tartaricus*. Science. **308**, 659-662

24 Vollmar, M., Schlieper, D., Winn, M., Buchner, C. and Groth, G. (2009) Structure of the c_{14} rotor ring of the proton translocating chloroplast ATP synthase. J. Biol. Chem. **284**, 18228-18235

25 Goodsell, D. Molecule of the month. (2005). http:// www.rcsb.org/pdb/101/motm.do?momID=72, RCSB Protein Data Bank.

26 Capaldi, R. A., González-Halphen, D. and Takamiya, S. (1986) Sequence homologies and structural similarities between the polypeptides of yeast and beef heart cytochrome *c* oxidase. FEBS Lett. **207**, 11-17

27 Arnold, S. (2012) The power of life-cytochrome *c* oxidase takes center stage in metabolic control, cell signalling and survival. Mitochondrion. **12**, 46-56 doi:10.1016/j.mito.2011.05.003

28 Waterland, R. A., Basu, A., Chance, B. and Poyton, R. O. (1991) The isoforms of yeast cytochrome *c* oxidase subunit V alter the *in vivo* kinetic properties of the holoenzyme. J. Biol. Chem. **266**, 4180-4186

29 Wikström, M. K. F. (1977) Proton pump coupled to cytochrome *c* oxidase in mitochondria. Nature. **266**, 271-273 doi:10.1038/266271a0

30 Harrenga, A. and Michel, H. (1999) The cytochrome *c* oxidase from *Paracoccus denitrificans* does not change the metal centre ligation upon reduction. J. Biol. Chem. **274**, 33296-33299

31 Svensson-Ek, M., Abramson, J., Larsson, G., Törnroth, S., Brzezinski, P. and Iwata, S. (2002) The X-ray crystal structures of wild-type and EQ(I-286) mutant cytochrome *c* oxidases from *Rhodobacter sphaeroides*. J. Mol. Biol. **321**, 329-339 doi:10.1016/S0022-2836(02)00619-8

32 Hunsicker-Wang, L. M., Pacoma, R. L., Chen, Y., Fee, J. A. and Stout, C. D. (2005) A novel cryoprotection scheme for enhancing the diffraction of crystals of recombinant cytochrome ba_3 oxidase from *Thermus thermophilus*. Acta Crystallogr. D Biol. Crystallogr. **61**, 340-343

33 Abramson, J., Riistama, S., Larrson, G., Jasaitis, A., Svensson-Ek, M., Laakkonen, L., Puustinen, A., Iwata, S. and Wikström, M. (2000) The structure of the ubiquinol oxidase from *Escherichia coli* and its ubiquinone binding site. Nat. Struct. Biol. **7**, 910-917

34 Tsukihara, T., Aoyama, H., Yamashita, E., Tomizaki, T., Yamaguchi, H., Shinzawa-Itoh, K., Nakashima, R., Yaono, R. and Yoshikawa, S. (1996) The whole structure of the 13-subunit oxidized cytochrome *c* oxidase at 2.8 Å. Science. **272**, 1136-1144 doi:10.1126/science.272.5265.1136

35 Muramoto, K., Hirata, K., Shinzawa-Itoh, K., Yoko-o, S., Yamashita, E., Aoyama, H., Tsukihara, T. and Yoshikawa, S. (2007) A histidine residue acting as a controlling site for dioxygen reduction and proton pumping by cytochrome *c* oxidase. Proc. Natl. Acad. Sci. USA. **104**, 7881-7886

36 Pereira, M. M., Santana, M. and Teixeira, M. (2001) A novel scenario for the evolution of haem-copper oxygen reductases. Biochim. Biophys. Acta. **1505**, 185-208

37 Geier, B. M., Schägger, H., Ortwein, C., Link, T. A., Hagen, W. R., Brandt, U. and von Jagow, G. (1995) Kinetic properties and ligand binding of the eleven subunit cytochrome *c* oxidase from *Saccharomyces cerevisiae* isolated with a novel large scale purification method. Eur. J. Biochem. **227**, 296-302

38 Yoshikawa, S., Shinzawa-Itoh, K., Nakashima, R., Yaono, R., Yamashita, E., Inoue, N., Yao, M., Fei, M. J., Libeu, C. P., Mizushima, T., Yamaguchi, H., Tomizaki, T. and Tsukihara, T. (1998) Redox-coupled crystal structural changes in bovine heart cytochrome *c* oxidase. Science. **280**, 1723-1729 doi:10.1126/science.280.5370.1723

39 Tsukihara, T., Shimokata, K., Katayama, Y., Shimada, H., Muramoto, K., Aoyama, H., Mochizuki, M., Shinozawa-Itoh, K., Yamashita, E., Yao, M., Ishimura, Y. and Yoshikawa, S. (2003) The low-spin heme of cytochrome *c* oxidase as the driving element of the proton-pumping process. Proc. Natl. Acad. Sci. USA. **100**, 15304-15309 doi:10.1073/pnas.2635097100

40 Muramoto, K., Ohta, K., Shinzawa-Itoh, K., Kanda, K., Taniguchi, M., Nabekura, H., Yamashita, E., Tsukihara, T. and Yoshikawa, S. (2010) Bovine cytochrome *c* oxidase structures enable O_2 reduction with minimization of reactive oxygens and provide a proton-pumping gate. Proc. Nat. Acad. Sci. USA. **107**, 7740-7745

41 Maréchal, A., Meunier, B., Lee, D., Orengo, C. and Rich, P. R. (2012) Yeast cytochrome *c* oxidase: a model system to study mitochondrial forms of the haem-copper oxidase superfamily. Biochim. Biophys. Acta. **1817**, 620-628 doi:10.1016/j.bbabio.2011.08.011

42 Smith, H. T., Ahmed, A. J. and Millett, F. (1981) Electrostatic interaction of cytochrome *c* with cytochrome c_1 and cytochrome oxidase. J. Biol. Chem. **256**, 4984-4990

43 Ferguson-Miller, S., Brautigan, D. L. and Margoliash, E. (1978) Definition of cytochrome *c* binding domains by chemical modification. III. Kinetics of reaction of carboxydinitrophenyl cytochromes *c* with cytochrome *c* oxidase. J. Biol. Chem. **253**, 149-159

44 Bratton, M. R., Pressler, M. A. and Hosler, J. P. (1999) Suicide inactivation of cytochrome *c* oxidase: catalytic turnover in the absence of subunit III alters the active site. Biochemistry. **38**, 16236-16245 doi:10.1021/bi9914107

45 Riistama, S., Puustinen, A., Garcia-Horsman, A., Iwata, S., Michel, H. and Wkström, M. (1996) Channelling of dioxygen into the respiratory enzyme. Biochim. Biophys. Acta. **1275**, 1-4

46 Luna, V. M., Chen, Y., Fee, J. A. and Stout, C. D. (2008) Crystallographic studies of Xe and Kr binding within the large internal cavity of cytochrome ba_3 from *Thermus thermophilus*: structural analysis and role of oxygen transport channels in the heme-Cu oxidases. Biochemistry. **47**, 4657-4665 doi:10.1021/bi800045y

47 Luna, V. M., Fee, J. A., Deniz, A. A. and Stout, C. D. (2012) Mobility of Xe atoms within the oxygen diffusion channel of cytochrome ba_3 oxidase. Biochemistry. **51**, 4669-4676 doi:10.1021/bi3003988

48 Babcock, G. T. (1999) How oxygen is activated and reduced in respiration. Proc. Natl. Acad. Sci. USA. **96**, 12971-12973

49 Ostermeier, C., Harrenga, A., Ermler, U. and Michel, H. (1997) Structure at 2.7 Å resolution of the *Paracoccus denitrificans* two-subunit cytochrome *c* oxidase complexed with an antibody F_v fragment. Proc. Natl. Acad. Sci. USA. **94**, 10547-10553

50 Wikström, M. (1981) Energy-dependent reversal of the cytochrome oxidase reaction. Proc. Natl. Acad. Sci. USA. **78**, 4051-4054

51 Wikström, M. and Morgan, J. E. (1992) The dioxygen cycle. Spectral, kinetic, and thermodynamic characteristics of ferryl and peroxy intermediates observed by reversal of the cytochrome oxidase reaction. J. Biol. Chem. **267**, 10266-10273

52 Fabian, M. and Palmer, G. (1995) The interaction of cytochrome oxidase with hydrogen peroxide: the relationship of compounds P and F. Biochemistry. **34**, 13802-13810

53 Yu, M. A., Egawa, T., Shinzawa-Itoh, K., Yoshikawa, S., Guallar, V., Yeh, S.-R., Rousseau, D. L. and Gerfen, G. J. (2012) Two tyrosyl radicals stabilize high oxidation states in cytochrome *c* oxidase for efficient energy conservation and proton translocation. J. Amer. Chem. Soc. **134**, 4753-4761 doi:10.1021/ja210535w

54 Rich, P. R., Rigby, S. E. J. and Heathcote, P. (2002) Radicals associated with the catalytic intermediates of bovine cytochrome *c* oxidase. Biochim. Biophys. Acta. **1554**, 137-146

55 Wikström, M. (2012) Active site intermediates in the reduction of O_2 by cytochrome oxidase, and their derivatives. Biochim. Biophys. Acta. **1817**, 468-475 doi:10.1016/j.bbabio.2011.10.010

56 Babcock, G. T., Varotsis, C. and Zhang, Y. (1992) O_2 activation in cytochrome oxidase and in other heme proteins. Biochim. Biophys. Acta. **1101**, 192-194

57 Proshlyakov, D. A., Ogura, T., Shinzawa-Itoh, K., Yoshikawa, S. and Kitagawa, T. (1996) Microcirculating system for simultaneous determination of Raman and absorption spectra of enzymatic reaction intermediates and its application to the reaction of cytochrome *c* oxidase with hydrogen peroxide. Biochemistry. **35**, 76-82

58 Proshlyakov, D. A., Ogura, T., Shinzawa-Itoh, K., Yoshikawa, S. and Kitagawa, T. (1996) Resonance Raman/absorption characterization of the oxo intermediates of cytochrome *c* oxidase generated in its reaction with hydrogen peroxide: pH and H_2O_2 concentration dependence. Biochemistry. **35**, 8580-8586

59 Proshlyakov, D. A., Ogura, T., Shinzawa-Itoh, K., Yoshikawa, S., Appelman, E. H. and Kitagawa, T. (1994) Selective resonance Raman observation of the "607 nm" form generated in the reaction of oxidized cytochrome *c* oxidase with hydrogen peroxide. J. Biol. Chem. **269**, 29385-29388

60 Fabian, M., Wong, W. W., Gennis, R. B. and Palmer, G. (1999) Mass spectrometric determination of dioxygen bond splitting in the "peroxy" intermediate of cytochrome *c* oxidase. Proc. Natl. Acad. Sci. USA. **96**, 13114-13117

61 Blumberg, W. E., Peisach, J., Wittenberg, B. A. and Wittenberg, J. B. (1968) The electronic structure of protoheme proteins. I. An electron paramagnetic resonance and optical study of horseradish peroxidase and its derivatives. J. Biol. Chem. **243**, 1854-1862

62 Hewson, W. D. and Hager, L. P. (1979) Oxidation of horseradish peroxidase compound II to compound I. J. Biol. Chem. **254**, 3182-3186

63 Yonetani, T. and Ray, G. S. (1965) Studies of cytochrome *c* peroxidase. I. Purification and some properties. J. Biol. Chem. **240**, 4503-4508

64 Nicholls, P. and Chanady, G. A. (1981) Interactions of cytochrome aa_3 with oxygen and carbon monoxide. The role of the 607 nm complexes. Biochim. Biophys. Acta. **634**, 256-265

65 Chance, B., Saronio, C. and Leigh, J. S. (1975) Functional intermediates in the reaction of membrane-bound cytochrome oxidase with oxygen. J. Biol. Chem. **250**, 9226-9237

66 Morgan, J. E., Verkhovsky, M. I., Palmer, G. and Wikström, M. (2001) The role of the P_R intermediate of cytochrome *c* oxidase with O_2. Biochemistry. **40**, 6882-6892

67 Wrigglesworth, J. M. (1984) Formation and reduction of a 'peroxy' intermediate of cytochrome *c* oxidase by hydrogen peroxide. Biochem. J. **217**, 715-719

68 Weng, L. and Baker, G. M. (1991) Reaction of hydrogen peroxide with the rapid form of resting cytochrome oxidase. Biochemistry. **30**, 5727-5733

69 Fabian, M. and Palmer, G. (1999) Redox state of peroxy and ferryl intermediates in cytochrome *c* oxidase catalysis. Biochemistry. **38**, 6270-6275

70 Jünemann, S., Heathcote, P. and Rich, P. R. (2000) The reactions of hydrogen peroxide with bovine cytochrome *c* oxidase. Biochim. Biophys. Acta. **1456**, 56-66

71 MacMillan, F., Kannt, A., Behr, J., Prisner, T. and Michel, H. (1999) Direct evidence for a tyrosine radical in the reaction of cytochrome *c* oxidase with hydrogen peroxide. Biochemistry. **38**, 9179-9184

72 Svistunenko, D. A., Wilson, M. T. and Cooper, C. E. (2004) Tryptophan or tyrosine? On the nature of the amino acid radical formed following hydrogen peroxide treatment of cytochrome *c* oxidase. Biochim. Biophys. Acta. **1655**, 372-380 doi:10.1016/j.bbabio.2003.06.006

73 Budiman, K., Kannt, A., Lyubenova, S., Richter, O.-M. H., Ludwig, B., Michel, H. and MacMillan, F. (2004) Tyrosine 167: The origin of the radical species observed in the reaction of cytochrome *c* oxidase with hydrogen peroxide in *Paracoccus denitrificans*. Biochemistry. **43**, 11709-11716

74 Rigby, S. E. J., Jünemann, S., Rich, P. R. and Heathcote, P. (2000) The reaction of hydrogen peroxide with bovine cytochrome *c* oxidase produces a tryptophan cation radical and a porphyrin cation radical. Biochemistry. **39**, 5921-5928

75 Proshlyakov, D. A., Pressler, M. A. and Babcock, G. T. (1998) Dioxygen activation and bond cleavage by mixed-valence cytochrome *c* oxidase. Proc. Natl. Acad. Sci. USA. **95**, 8020-8025

76 Proshlyakov, D. A., Pressler, M. A., DeMaso, C., Leykam, J. F., DeWitt, D. L. and Babcock, G. T. (2000) Oxygen activation and reduction in respiration: Involvement of redox-active tyrosine 244. Science. **290**, 1588-1591

77 Uchida, T., Mogi, T. and Kitagawa, T. (2000) Resonance Raman studies of oxo intermediates in the reaction of pulsed cytochrome *bo* with hydrogen peroxide. Biochemistry. **39**, 6669-6678

78 Rich, P. R. and Maréchal, A. (2013) Functions of the hydrophilic channels in protonmotive cytochrome *c* oxidase. J. R. Soc. Interface. **10**, 1-14 doi:10.1098/rsif.2013.0183

79 Wikström, M., Verkhovsky, M. I. and Hummer, G. (2003) Water-gated mechanism of proton translocation by cytochrome *c* oxidase. Biochim. Biophys. Acta. **1604**, 61-65 doi:10.1016/S0005-2728(03)00041-0

80 Gennis, R. B. (1998) Multiple proton-conducting pathways in cytochrome oxidase and a proposed role for the active-site tyrosine. Biochim. Biophys. Acta. **1365**, 241-248 doi:10.1016/S0005-2728(98)00075-9

81 Wikström, M., Jasaitis, A., Backgren, C., Puustinen, A. and Verkhovsky, M. I. (2000) The role of the D- and K-pathways of proton transfer in the function of the haem-copper oxidases. Biochim. Biophys. Acta. **1459**, 514-520 doi:10.1016/S0005-2728(00)00191-2

82 Oliveberg, M., Hallén, S. and Nilsson, T. (1991) Uptake and release of protons during the reaction between cytochrome *c* oxidase and molecular oxygen: A flow-flash investigation. Biochemistry. **30**, 436-440

83 Ädelroth, P., Gennis, R. B. and Brzezinski, P. (1998) Role of the pathway through K(I-362) in proton transfer in cytochrome *c* oxidase from *R. sphaeroides*. Biochemistry. **36**, 2470-2476

84 Ädelroth, P., Svensson-Ek, M., Mitchell, D. M., Gennis, R. B. and Brzezinski, P. (1997) Glutamate 286 in cytochrome aa_3 from *Rhodobacter sphaeroides* in involved in proton uptake during the reaction of the fully-reduced enzyme with dioxygen. Biochemistry. **36**, 13824-13829 doi:10.1021/bi9629079

85 Mitchell, R. and Rich, P. R. (1994) Proton uptake by cytochrome *c* oxidase on reduction and on ligand binding. Biochim. Biophys. Acta. **1186**, 19-26 doi:10.1016/0005-2728(94)90130-9

86 Jünemann, S., Meunier, B., Gennis, R. B. and Rich, P. R. (1997) Effects of mutation of the conserved lysine-362 in cytochrome *c* oxidase from *Rhodobacter sphaeroides*. Biochemistry. **36**, 14456-14464 doi:10.1021/bi971458p

87 Yoshikawa, S., Muramoto, K., Shinozawa-Itoh, K., Aoyama, H., Tsukihara, T., Shimokata, K., Katayama, Y. and Shimada, H. (2006) Proton pumping mechanism of bovine heart cytochrome *c* oxidase. Biochim. Biophys. Acta. **1757**, 1110-1116

88 Hellwig, P., Behr, J., Ostermeier, C., Richter, O.-M. H., Pfitzner, U., Odenwald, A., Ludwig, B., Michel, H. and Mäntele, W. (1998) Involvement of glutamic acid 278 in the redox reaction of the cytochrome *c* oxidase from *Paracoccus denitrificans* investigated by FTIR spectroscopy. Biochemistry. **37**, 7390-7399 doi:10.1021/bi9725576

89 Rich, P. R., Breton, J., Jünemann, S. and Heathcote, P. (2000) Protonation reactions in relation to the coupling mechanism of bovine cytochrome *c* oxidase. Biochim. Biophys. Acta. **1459**, 475-480

90 Rich, P. R. and Breton, J. (2001) FTIR studies of the CO and cyanide adducts of fully reduced bovine cytochrome *c* oxidase. Biochemistry. **40**, 6441-6449 doi:10.1021/bi0027332

91 Jünemann, S., Meunier, B., Fisher, N. and Rich, P. R. (1999) Effects of mutation of the conserved glutamic acid-286 in subunit I of cytochrome *c*

oxidase from *Rhodobacter sphaeroides*. Biochemistry. **38**, 5248-5255 doi:10.1021/bi9830112

92 Verkhovskaya, M. L., García-Horsman, A., Puustinen, A., Rigaud, J.-L., Morgan, J. E., Verkhovsky, M. I. and Wikström, M. (1997) Glutamic acid 286 in subunit I of cytochrome bo_3 is involved in proton translocation. Proc. Natl. Acad. Sci. USA. **94**, 10128-10131

93 Pawate, A. S., Morgan, J., Namslauer, A., Mills, D., Brzezinski, P., Ferguson-Miller, S. and Gennis, R. B. (2002) A mutation in subunit I of cytochrome *c* oxidase from *Rhodobacter sphaeroides* results in an increase in steady-state activity but completely eliminates proton pumping. Biochemistry. **41**, 13417-13423

94 Rich, P. R. (1995) Towards an understanding of the chemistry of oxygen reduction and proton translocation in the iron-copper respiratory oxidases. Aust. Journ. Plant. Physiol. **22**, 479-486 doi:10.1071/PP9950479

95 Kaila, V. R. I., Sharma, V. and Wikström, M. (2011) The identity of the transient proton loading site of the proton-pumping mechanism of cytochrome *c* oxidase. Biochim. Biophys. Acta. **1807**, 80-84

96 Rich, P. R., Jünemann, S. and Breton, J. (2000) Protonation reactions of bovine cytochrome *c* oxidase in relation to coupling mechanism. Biochim. Biophys. Acta. **1459**, 475-480

97 Seibold, S. A., Mills, D. A., Ferguson-Miller, S. and Cukier, R. I. (2005) Water chain formation and possible proton pumping routes in *Rhodobacter sphaeroides* cytochrome *c* oxidase: A molecular dynamics comparison of the wild type and R481K mutant. Biochemistry. **44**, 10475-10485 doi:10.1021/bi0502902

98 Maréchal, A. and Rich, P. R. (2011) Water molecule reorganization in cytochrome *c* oxidase revealed by FTIR spectroscopy. Proc. Natl. Acad. Sci. USA. **108**, 8634-8638 doi:10.1073/pnas.1019419108

99 Shimokata, K., Katayama, Y., Murayama, H., Suematsu, M., Tsukihara, T., Muramoto, K., Aoyama, H., Yoshikawa, S. and Shimada, H. (2007) The proton pumping pathway of bovine heart cytochrome *c* oxidase. Proc. Natl. Acad. Sci. USA. **104**, 4200-4205 doi:10.1073/pnas.0611627104

100 Pfitzner, U., Odenwald, A., Ostermann, T., Weingard, L., Ludwig, B. and Richter, O.-M. H. (1998) Cytochrome *c* oxidase (heme aa_3) from *Paracoccus denitrificans:* analysis of mutations in putative proton channels of subunit I. J. Bioenerg. Biomemb. **30**, 89-97 doi:10.1023/A:1020515713103

101 Lee, H.-M., Das, T. K., Rousseau, D. L., Mills, D., Ferguson-Miller, S. and Gennis, R. B. (2000) Mutations in the putative H-channel in the cytochrome *c* oxidase from *Rhodobacter sphaeroides* show that this channel is not important for proton conduction but reveal modulation of the properties of heme *a*. Biochemistry. **39**, 2989-2996 doi:10.1021/bi9924821

102 McMahon, B. H., Fabian, M., Tomson, F., Causgrove, T. P., Bailey, J. A., Rein, F. N., Dyer, R. B., Palmer, G., Gennis, R. B. and Woodruff, W. H. (2004) FTIR studies of internal proton transfer reactions linked to inter-heme electron

transfer in bovine cytochrome *c* oxidase. Biochim. Biophys. Acta. **1655**, 321-331

103 Puustinen, A., Bailey, J. A., Dyer, R. B., Mecklenburg, S. L., Wikström, M. and Woodruff, W. H. (1997) Fourier transform infrared evidence for connectivity between Cu_B and glutamic acid 286 in cytochrome bo_3 from *E. coli*. Biochemistry. **36**, 13195-13200

104 Okuno, D., Iwase, T., Shinzawa-Itoh, K., Yoshikawa, S. and Kitagawa, T. (2003) FTIR detection of protonation/deprotonation of key carboxyl side chains caused by redox change of the Cu_A-heme *a* moiety and ligand dissociation from the heme a_3-Cu_B center of bovine heart cytochrome *c* oxidase. J. Am. Chem. Soc. **125**, 7209-7218

105 Rost, B., Behr, J., Hellwig, P., Richter, O. M. H., Ludwig, B., Michel, H. and Mäntele, W. (1999) Time-resolved FT-IR studies on the CO adduct of *Paracoccus denitrificans* cytochrome *c* oxidase: comparison of the fully reduced and the mixed valence form. Biochemistry. **38**, 7565-7571

106 Lübben, M., Prutsch, A., Mamat, B. and Gerwert, K. (1999) Electron transfer induces side-chain conformational changes of glutamate-286 from cytochrome bo_3. Biochemistry. **38**, 2048-2056

107 Yamazaki, Y., Kandori, H. and Mogi, T. (1999) Effects of subunit I mutations on redox-linked conformational changes of the *Escherichia coli bo*-type ubiquinol oxidase revealed by Fourier-transform infrared spectroscopy. J. Biochem. (Tokyo). **126**, 194-199

108 Hellwig, P., Pfitzner, U., Behr, J., Rost, B., Pesavento, P., Donk, W. V., Gennis, R. B., Michel, H., Ludwig, B. and Mäntele, W. (2002) Vibrational modes of tyrosine in cytochrome *c* oxidase from *Paracoccus denitrificans*: FTIR and electrochemical studies on Tyr-D4-labeled and on Tyr280His and Tyr35Phe mutant enzymes. Biochemistry. **41**, 9116-9125

109 Behr, J., Hellwig, P., Mäntele, W. and Michel, H. (1998) Redox dependent changes at the heme propionates in cytochrome *c* oxidase from *Paracoccus denitrificans*: Direct evidence from FTIR difference spectroscopy in combination with heme propionate ^{13}C labelling. Biochemistry. **37**, 7400-7406

110 Goormaghtigh, E., Raussens, V. and Ruysschaert, J.-M. (1999) Attenuated total reflection infrared spectroscopy of proteins and lipids in biological membranes. Biochim. Biophys. Acta. **1422**, 105-185

111 Nyquist, R. M., Heitbrink, D., Bolwien, C., Wells, T. A., Gennis, R. and Heberle, J. (2001) Perfusion-induced redox differences in cytochrome *c* oxidase: ATR/FT-IR spectroscopy. FEBS Lett. **505**, 63-67

112 Rich, P. R. and Iwaki, M. (2007) Methods to probe protein transitions with ATR infrared spectroscopy. Mol. Biosys. **3**, 398-407

113 Moss, D., Nabedryk, E., Breton, J. and Mäntele, W. (1990) Redox-linked conformational changes in proteins detected by a combination of IR spectroscopy and protein electrochemistry. Evaluation of the technique with cytochrome *c*. Eur. J. Biochem. **187**, 565-572

114 Mäntele, W. (1993) Reaction-induced infrared difference spectroscopy for the study of protein function and reaction mechanisms. Trends Biochem. Sci. **18**, 197-202

115 Rich, P. R. and Breton, J. (2002) Attenuated total reflection Fourier transform infrared studies of redox changes in bovine cytochrome *c* oxidase: Resolution of the redox Fourier transform infrared difference spectrum of heme a_3. Biochemistry. **41**, 967-973

116 Hellwig, P., Grzybek, S., Behr, J., Michel, H. and Mäntele, W. (1999) Electrochemical and ultraviolet/visible/Infrared spectroscopic analysis of heme *a* and a_3 redox reactions in the cytochrome *c* oxidase from *Paracoccus denitrificans*: separation of heme *a* and a_3 contributions and assignment of vibrational modes. Biochemistry. **38**, 1685-1694

117 Gorbikova, E. A., Vuorilehto, K., Wikström, M. and Verkhovsky, M. I. (2006) Redox titration of all electron carriers of cytochrome *c* oxidase by Fourier transform infrared spectroscopy. Biochemistry. **45**, 5641-5649

118 Meunier, B., Maréchal, A. and Rich, P. R. (2012) Construction of histidine-tagged yeast mitochondrial cytochrome *c* oxidase for facile purification of mutant forms. Biochem. J. **444**, 199-204 doi:10.1042/BJ20120116

119 Zimmer, C. (2009) Origins. On the origin of eukaryotes. Science. **325**, 666-668 doi: 10.1126/science.325_666

120 Richards, T. A. and Archibald, J. M. (2011) Cell evolution: gene transfer agents and the origin of mitochondria. Curr. Biol. **21**, R112-R114 doi:10.1016/j.cub.2010.12.036

121 Das, J., Miller, S. T. and Stern, D. L. (2004) Comparisons of diverse protein sequences of the nuclear-encoded subunits of cytochrome *c* oxidase suggests conservation of structure underlies evolving functional sites. Mol. Biol. Evol. **21**, 1572-1582

122 Arnold, S. and Kadenbach, B. (1997) Cell respiration is controlled by ATP, an allosteric inhibitor of cytochrome-*c* oxidase. Eur. J. Biochem. **249**, 350-354

123 Napiwotzki, J. and Kadenbach, B. (1998) Extramitochondrial ATP/ADP-ratios regulate cytochrome *c* oxidase activity via binding to the cytosolic domain of subunit IV. Biol. Chem. **379**, 335-339

124 Fang, J.-K., Prabu, S., Sepuri, N., Raza, H., Anandatheerthavarada, H., Gelati, D., Spear, J. and Avadhani, N. (2007) Site specific phosphorylation of cytochrome *c* oxidase subunits I, IVi1 and Vb in rabbit hearts subjected to ischemia/reperfusion. FEBS Lett. **581**, 1302-1310

125 Pierron, D., Wildman, D. E., Hüttemann, M., Markondapatnaikuni, G. C., Aras, S. and Grossman, L. I. (2012) Cytochrome *c* oxidase: evolution of control via nuclear subunit addition. Biochim. Biophys. Acta. **1817**, 590-597 doi:10.1016/j.bbabio.2011.07.007

126 Chance, B. and Williams, G. R. (1955) A method for the localization of sites for oxidative phosphorylation. Nature. **176**, 250-254

127 Hackenbrock, C. R., Chazotte, B. and Gupte, S. S. (1986) The random collision model and a critical assessment of diffusion and collision in mitochondrial electron transport. J. Bioenerg. Biomemb. **18**, 331-368

128 Schägger, H. and Pfeiffer, K. (2000) Supercomplexes in the respiratory chains of yeast and mammalian mitochondria. EMBO J. **19**, 1773-1783

129 Cruciat, C. M., Brunner, S., Baumann, F., Neupert, W. and Stuart, R. A. (2000) The cytochrome bc_1 and cytochrome *c* oxidase complexes associate to form a single supracomplex in yeast mitochondria. J. Biol. Chem. **275**, 18093-18098

130 Schägger, H. (2001) Respiratory chain supercomplexes. IUBMB Life. **52**, 119-128

131 Pfeiffer, K., Gohil, V., Stuart, R. A., Hunte, C., Brandt, U., Greenberg, M. L. and Schagger, H. (2003) Cardiolipin stabilises respiratory chain supercomplexes. J. Biol. Chem. **278**, 52873-52880

132 Heinemeyer, J., Braun, H.-P., Boekema, E. and Kouril, R. (2007) A structural model of the cytochrome c reductase/oxidase supercomplex from yeast mitochondria. J. Biol. Chem. **282**, 12240-12248

133 Wittig, I. and Schägger, H. (2009) Supramolecular organization of ATP synthase and respiratory chain in mitochondrial membranes. Biochim. Biophys. Acta. **1787**, 672-680 doi:10.1016/j.bbabio.2008.12.016

134 Althoff, T., Mills, D. J., Popot, J.-L. and Kühlbrandt, W. (2011) Arrangement of electron transport chain components in bovine mitochondrial supercomplex $I_1III_2IV_1$. EMBO J. **30**, 4652-4664 doi:10.1038/emboj.2011.324

135 Mileykovskaya, E., Penczek, P. A., Fang, J., Mallampalli, V. K., Sparagna, G. C. and Dowhan, W. (2012) Arrangement of the respiratory chain complexes in *Saccharomyces cerevisiae* supercomplex III_2IV_2 revealed by single particle cryo-electron microscopy. J. Biol. Chem. **287**, 23095-23103 doi:10.1074/jbc.M112.367888

136 Ramzan, R., Staniek, K., Kadenbach, B. and Vogt, S. (2010) Mitochondrial respiration and membrane potential are regulated by the allosteric ATP-inhibition of cytochrome *c* oxidase. Biochim. Biophys. Acta. **1797**, 1672-1680 doi:10.1016/j.bbabio.2010.06.005

137 Hüttemann, M., Lee, I., Gao, X., Pecina, P., Pecinova, A., Liu, J., Aras, S., Sommer, N., Sanderson, T. H., Tost, M., Neff, F., Aquilar-Pimentel, J. A., Becker, L., Naton, B., Rathkolb, B., Rozman, J., Favor, J., Hans, W., Prehn, C., Puk, O., Schrewe, A., Sun, M., Höfler, H., Adamski, J., Bekeredjian, R., Graw, J., Adler, T., Busch, D. H., Klingenspor, M., Klopstock, T., Ollert, M., Wolf, E., Fuchs, H., Gailus-Durner, V., Hrabe de Angelis, M., Weissmann, N., Doan, J. W., Bassett, D. J. and Grossman, L. I. (2012) Cytochrome *c* oxidase subunit 4 isoform 2-knockout mice show reduced enzyme activity, airway hyporeactivity, and lung pathology. FASEB J. **26**, 3916-3930 doi:10.1096/fj.11-203273

138 Ramzan, R., Weber, P., Kadenbach, B. and Vogt, S. (2012) Individual biochemical behaviour versus biological robustness: spotlight on the regulation of cytochrome *c* oxidase. Adv. Exp. Med. Biol. **748**, 265-281 doi:10.1007/978-1-4614-3573-0_11

139 Acin-Perez, R., Gatti, D. L., Bai, Y. and Manfredi, G. (2011) Protein phosphorylation and preventation of cytochrome *c* oxidase inhibition by ATP: coupled mechanisms of energy metabolism regulation. Cell Metab. **13**, 712-719 doi:10.1016/j.cmet.2011.03.024

140 Hüttemann, M., Kadenbach, B. and Grossman, L. I. (2001) Mammalian subunit IV isoforms of cytochrome *c* oxidase. Gene. **267**, 111-123 doi:10.1016/S0378-1119(01)00385-7

141 Horvat, S., Beyer, C. and Arnold, S. (2006) Effect of hypoxia on the transcription pattern of subunit isoforms and the kinetics of cytochrome *c* oxidase in cortical astrocytes and cerebellar neurons. J. Neurochem. **99**, 937-951 doi:10.1111/j.1471-4159.2006.04134.x

142 Aras, S., Pak, O., Sommer, N., Finley, R. Jr., Hüttemann, M., Weissman, N. and Grossman, L. I. (2013) Oxygen-dependent expression of cytochrome *c* oxidase subunit 4-2 gene expression is mediated by transcription factors RBPJ, CXXC5 and CHCHD2. Nucleic Acids Res. **41**, 2255-2266 doi:10.1093/nar/gks1454

143 Singh, S., Misiak, M., Beyer, C. and Arnold, S. (2009) Cytochrome *c* oxidase isoform IV-2 is involved in 3-nitropropionic acid-induced toxicity in striatal astrocytes. Glia. **57**, 1480-1491 doi:10.1002/glia.20864

144 Cumsky, M. G., Ko, C., Trueblood, C. E. and Poyton, R. O. (1985) Two nonidentical forms of subunit V are functional in yeast cytochrome *c* oxidase. Proc. Natl. Acad. Sci. USA. **82**, 2235-2239

145 Cumsky, M. G., Trueblood, C. E., Ko, C. and Poyton, R. O. (1987) Structural analysis of two genes encoding divergent forms of yeast cytochrome *c* oxidase subunit V. Mol. Cell. Biol. **7**, 3511-3519

146 Hodge, M. R., Kim, G., Singh, K. and Cumsky, M. G. (1989) Inverse regulation of the yeast *COX5* genes by oxygen and heme. Mol. Cell Biol. **9**, 1958-1964

147 Trueblood, C. E. and Poyton, R. O. (1988) Identification of *REO1*, a gene involved in negative regulation of *COX5b* and *ANB1* in aerobically grown *Saccharomyces cerevisiae*. Genetics. **120**, 671-680

148 Burke, P. V., Raitt, D. C., Allen, L. A., Kellog, E. A. and Poyton, R. O. (1997) Effects of oxygen concentration on the expression of cytochrome *c* and cytochrome *c* oxidase genes in yeast. J. Biol. Chem. **272**, 14705-14712

149 Zitomer, R. S., Carrico, P. and Deckert, J. (1997) Regulation of hypoxic gene expression in yeast. Kidney Int. **51**, 507-513

150 Kwast, K. E., Burke, P. V. and Poyton, R. O. (1998) Oxygen sensing and the transcriptional regulation of oxygen-responsive genes in yeast. J. Exp. Biol. **201**, 1177-1195

151 Allen, L. A., Zhao, X.-J., Caughey, W. and Poyton, R. O. (1995) Isoforms of yeast cytochrome *c* oxidase subunit V affect the binuclear reaction center and alter the kinetics of interaction with the isoforms of yeast cytochrome *c*. J. Biol. Chem. **270**, 110-118 doi:10.1074/jbc.270.1.110

152 Meunier, B. (2001) Site-direct mutations in the mitochondrially-encoded subunits I and III of yeast cytochrome oxidase. Biochem. J. **354**, 407-412

153 Johnston, S. A. and DiVit.M.J (1996) Biolistic Tranformation of yeasts. In Methods in molecular biology (Evans, ed.). pp. 147-153, Totowa, NJ

154 Rich, P. R. and Moody, A. J. (1997) Cytochrome *c* oxidase. In Bioelectrochemistry: principles and practice (Gräber, P. and Milazzo, G., eds.). pp. 419-456, Birkhäuser Verlag AG, Basel

155 Moody, A. J., Cooper, C. E. and Rich, P. R. (1991) Characterisation of 'fast' and 'slow' forms of bovine heart cytochrome-*c* oxidase. Biochim. Biophys. Acta. **1059**, 189-207

156 Kuboyama, M., Yong, F. K. and King, T. E. (1972) Studies on cytochrome oxidase VIII. Preparation and some properties of cardiac cytochrome oxidase. J. Biol. Chem. **247**, 6375-6383

157 Keilin, D. and Hartree, E. F. (1940) Succinic dehydrogenase-cytochrome system of cells intracellular respiratory system catalysing aerobic oxidation of succinic acid. Proc. Roy. Soc. Lond. B. **129**, 277-306

158 Dodia, R., Maréchal, A., Bettini, S., Iwaki, M. and Rich, P. R. (2013) IR signatures of the metal centres of bovine cytochrome *c* oxidase: assignments and redox-linkage. Biochem. Soc. Trans. **41**, 1242-1248

159 Moody, A. J. and Rich, P. R. (1990) The effect of pH on redox titrations of haem *a* in cyanide-liganded cytochrome-*c* oxidase: experimental and modelling studies. Biochim. Biophys. Acta. **1015**, 205-215 doi:10.1016/0005-2728(90)90022-V

160 Harmon, P. A., Hendler, R. W. and Levin, I. W. (1994) Resonance Raman and optical spectroscopic monitoring of heme A redox states in cytochrome *c* oxidase during potentiometric titrations. Biochemistry. **33**, 699-707

161 Lindsay, J. G. and Wilson, D. F. (1974) Reaction of cytochrome *c* oxidase with CO: involvement of the invisible copper. FEBS Lett. **48**, 45-49

162 Wilson, G. S. (1978) Determination of oxidation-reduction potentials. Methods Enzymol. **54**, 396-410

163 Viré, J.-C., Patriarche, J. and Christian, G. D. (1979) Electrochemical study of 1,2-naphthoquinone-4-sulphonate and 1,2-naphthoquinone. Fresenius Z. Anal. Chem. **299**, 197-201

164 Tsubaki, M. and Yoshikawa, S. (1993) Fourier-transform infrared study of cyanide binding to the Fe_{a3}-Cu_B binuclear site of bovine heart cytochrome *c* oxidase: Implication of the redox-linked conformational change at the binuclear site. Biochemistry. **32**, 164-173 doi:10.1021/bi00052a022

165 Caughey, W. S., Dong, A., Sampath, V., Yoshikawa, S. and Zhao, X.-J. (1993) Probing heart cytochrome *c* oxidase structure and function by infrared spectroscopy. J. Bioenerg. Biomemb. **25**, 81-91

166 Iwaki, M., Breton, J. and Rich, P. R. (2002) ATR-FTIR difference spectroscopy of the P_M intermediate of bovine cytochrome *c* oxidase. Biochim. Biophys. Acta. **1555**, 116-121

167 Frisch, M. J., Trucks, G. W., Schlegel, H. B., Scuseria, G. E., Robb, M. A., Cheeseman, J. R., Montgomery, J. A. Jnr., Vreven, T., Kudin, K. N., Burant, J. C., Millam, J. M., Iyengar, I. I., Tomasi, J., Barone, V., Mennucci, B., Cossi, M., Scalmani, G., Rega, N., Petersson, G. A., Nakasuji, H., Hada, M., Ehara, M., Toyota, K., Fukuda, R., Hasegawa, J., Ishida, M., Nakajima, T., Honda, Y., Kitao, O., Nakai, H., Klene, M., Li, X., Knox, J. E., Hratchian, H. P., Cross, J. B., Bakken, V., Adamo, C., Jaramillo, J., Gomperts, R., Stratmann, R. E., Yazyev, O., Austin, A. J., Cammi, R., Pomelli, C., Ochterski, J. W., Ayala, P. Y., Morokuma, K., Voth, G. A., Salvador, P., Dannenberg, J. J., Zakrzewski, G., Dapprich, S., Daniels, A. D., Strain, M. C., Farkas, O., Malick, D. K., Rabuck, A. D., Raghavachari, K., Foresman, J. B., Ortiz, J. V., Cui, Q., Baboul, A. G., Clifford, S., Cioslowski, J., Stefanov, B. B., Liu, G., Liashenko, A., Piskorz, P., Komaromi, I., Martin, R. L., Fox, D. J., Keith, T., Al-Laham, M. A., Peng, C. Y., Nanayakkara, A., Challacombe, M., Gill, P. M. W., Johnson, B., Chen, W., Wong, M. W., Gonzalez, C., and Pople, J. A. Gaussian 03. (2005). Wallingford, CT, USA, Gaussian, Inc.

168 Becke, A. D. (1993) Density-functional thermochemistry. III. The role of exact exchange. J. Chem. Phys. **98**, 5648-5652 doi:10.1063/1.464913

169 Lee, C., Yang, W. and Parr, R. G. (1988) Development of the Colle-Salvetti correlation-energy formula into a functional of the electron density. Phys. Rev. B. Condens Matter. **37**, 785-789

170 Rappoport, Z. (2004) The chemistry of phenols pp. 39-44, John Wiley & Sons, Surrey

171 Brown, S., Colson, A.-M., Meunier, B. and Rich, P. R. (1993) Rapid screening of cytochromes of respiratory mutants of *Saccharomyces cerevisiae* - application to the selection of strains containing novel forms of cytochrome *c* oxidase. Eur. J. Biochem. **213**, 137-145

172 Dutton, P. L. (1978) Redox potentiometry: determination of midpoint potentials of oxidation-reduction components of biological electron-transfer systems. Methods Enzymol. **54**, 411-435

173 Dutton, P. L., Wilson, D. F. and Lee, C.-P. (1970) Oxidation-reduction potentials of cytochromes in mitochondria. Biochemistry. **9**, 5077-5082

174 Coolidge, T. B. (1932) Cytochrome and yeast iron. J. Biol. Chem. **98**, 755-764

175 Bergersen, F. J. and Turner, G. L. (1979) Systems utilizing oxygenated leghemoglobin and myoglobin as sources of free dissolved O_2 at low concentrations for experiments with bacteria. Anal. Biochem. **96**, 165-174

176 Bowen, W. J. (1949) The absorption spectra and extinction coefficients of myoglobin. J. Biol. Chem. **179**, 235-245

177 Schenkman, K. A., Marble, D. R., Burns, D. H. and Feigl, E. O. (1997) Myoglobin oxygen dissociation by multiwavelength spectroscopy. J. Appl. Physiol. **82**, 86-92

178 Casey, R. P., Chappell, J. B. and Azzi, A. (1979) Limited-turnover studies on proton translocation in reconstituted cytochrome *c* oxidase-containing vesicles. Biochem. J. **182**, 149-156

179 Wrigglesworth, J. M., Cooper, C. E., Sharpe, M. A. and Nicholls, P. (1990) The proteoliposomal steady state. Effect of size, capacitance and membrane permeability on cytochrome-oxidase-induced ion gradients. Biochem. J. **270**, 109-118

180 Hosler, J. P., Fetter, J., Tecklenburg, M. M. J., Espe, M., Lerma, C. and Ferguson-Miller, S. (1992) Cytochrome aa_3 of *Rhodobacter sphaeroides* as a model for mitochondrial cytochrome *c* oxidase. Purification, kinetics, proton pumping, and spectral analysis. J. Biol. Chem. **267**, 24264-24272

181 Margoliash, E. and Frohwirt, N. (1959) Spectrum of horse-heart cytochrome c. Biochem. J. **71**, 570-572

182 Fisher, A. C. (1999) Electrode dynamics pp. 1-83, Oxford University Press, Oxford

183 Bard, A. J. and Faulkner, L. R. (2001) Electrochemical methods: fundamentals and applications pp. 1-864, John Wiley & Sons, Inc., New York

184 Barth, A. (2000) The infrared absorption of amino acid side chains. Prog. Biophys. Mol. Biol. **74**, 141-173

185 Rich, P. R. and Iwaki, M. (2005) Infrared protein spectroscopy as a tool to study protonation reactions within proteins. In Biophysical and Structural Aspects of Bioenergetics (Wikström, M., ed.). pp. 314-333, The Royal Society of Chemistry, Cambridge

186 Iwaki, M., Puustinen, A., Wikström, M. and Rich, P. R. (2006) Structural and chemical changes of the P_M intermediate of *Paracoccus denitrificans* cytochrome *c* oxidase revealed by IR spectroscopy with labeled tyrosines and histidines. Biochemistry. **45**, 10873-10885

187 Iwaki, M., Puustinen, A., Wikström, M. and Rich, P. R. (2004) ATR-FTIR spectroscopy and isotope labelling of the P_M intermediate of *Paracoccus denitrificans* cytochrome *c* oxidase. Biochemistry. **43**, 14370-14378

188 Yonetani, T. (1960) Studies on cytochrome oxidase. I Absolute and difference absorption spectra. J. Biol. Chem. **235**, 845-852

189 Horie, S. and Morrison, M. (1963) Cytochrome *c* oxidase components III spectral properties of cytochromes *a* and a_3. J. Biol. Chem. **238**, 2859-2865

190 Vanneste, W. H. (1966) The stoichiometry and absorption spectra of components *a* and a_3 in cytochrome *c* oxidase. Biochemistry. **5**, 838-848

191 Van Buuren, K. J. H., Nicholls, P. and van Gelder, B. F. (1972) Biochemical and biophysical studies on cytochrome aa_3. VI Reaction of cyanide with oxidised and reduced enzyme. Biochim. Biophys. Acta. **256**, 258-276

192 Yoshikawa, S., Mochizuki, M., Zhao, X.-J. and Caughey, W. S. (1995) Effects of overall oxidation state on infrared spectra of heme a_3 cyanide in bovine heart cytochrome *c* oxidase. Evidence of novel mechanistic roles for Cu_B. J. Biol. Chem. **270**, 4270-4279

193 Gibson, Q. H. and Greenwood, C. (1963) Reactions of cytochrome oxidase with oxygen and carbon monoxide. Biochem. J. **86**, 541-554

194 Orii, Y. and Okunuki, K. (1964) Studies on cytochrome *a* XI. Nature of the interaction between cytochrome *a* and cyanide. J. Biochem. **55**, 37-48

195 Van Buuren, K. J. H., van Gelder, B. F. and Eggelte, T. A. (1971) Biochemical and biophysical studies on cytochrome aa_3 I. Steady-state kinetics of cytochrome aa_3. Biochim. Biophys. Acta. **234**, 468-480

196 Hellwig, P., Soulimane, T., Buse, G. and Mäntele, W. (1999) Similarities and dissimilarities in the structure-function relation between the cytochrome *c* oxidase from bovine heart and from *Paracoccus denitrificans* as revealed by FT-IR difference spectroscopy. FEBS Lett. **458**, 83-86

197 Iwaki, M., Puustinen, A., Wikström, M. and Rich, P. R. (2003) ATR-FTIR spectroscopy of the P_M and F intermediates of bovine and *Paracoccus denitrificans* cytochrome *c* oxidase . Biochemistry. **42**, 8809-8817

198 Wilson, D. F., Lindsay, J. G. and Brocklehurst, E. S. (1972) Heme-heme interaction in cytochrome oxidase. Biochim. Biophys. Acta. **256**, 277-286

199 Nicholls, P. and Petersen, L. C. (1974) Haem-haem interactions in cytochrome aa_3 during the anaerobic-aerobic transition. Biochim. Biophys. Acta. **357**, 462-467

200 Wikström, M. K. F., Harmon, H. J., Ingledew, W. J. and Chance, B. (1976) A re-evaluation of the spectral potentiometric and energy-linked properties of cytochrome *c* oxidase in mitochondria. FEBS Lett. **65**, 259-277

201 Mason, M. G., Nicholls, P. and Cooper, C. E. (2009) The steady-state mechanism of cytochrome *c* oxidase: redox interactions between metal centres. Biochem. J. **422**, 237-246 doi:10.1042/BJ20082220

202 Yoshikawa, S., O'Keefe, D. H. and Caughey, W. S. (1985) Investigations of cyanide as an infrared probe of heme protein ligand binding sites. J. Biol. Chem. **260**, 3518-3528

203 Maréchal, A., Meunier, B. and Rich, P. R. (2012) Assignment of the CO-sensitive carboxyl group in mitochondrial forms of cytochrome *c* oxidase using yeast mutants. Biochim. Biophys. Acta. **1817**, 1921-1924 doi:10.1016/j.bbabio.2012.03.036

204 Kubo, M., Nakashima, S., Yamaguchi, S., Ogura, T., Mochizuki, M., Kang, J., Tateno, M., Shinzawa-Itoh, K., Kato, K. and Yoshikawa, S. (2013) Effective pumping proton collection facilitated by a copper site (Cu_B) of bovine heart cytochrome *c* oxidase, revealed by a newly developed time-resolved infrared system. J. Biol. Chem. **288**, 30259-30269 doi:10.1074/jbcM113.473983

205 Iwaki, M. and Rich, P. R. (2004) Direct detection of formate ligation in cytochrome *c* oxidase by ATR-FTIR spectroscopy. J. Am. Chem. Soc. **126**, 2386-2389

206 Rich, P. R. and Maréchal, A. (2008) Carboxyl group functions in the heme-copper oxidases: Information from mid-IR vibrational spectroscopy. Biochim. Biophys. Acta. **1777**, 912-918

207 Lubben, M., Prutsch, A., Mamat, B. and Gerwert, K. (1999) Electron transfer induces side-chain conformational changes of glutamate-286 from cytochrome bo_3. Biochemistry. **38**, 2048-2056 doi:10.1021/bi981859k

208 Iwaki, M. and Rich, P. R. (2007) An IR study of protonation changes associated with heme-heme electron transfer in bovine cytochrome *c* oxidase. J. Am. Chem. Soc. **129**, 2923-2929

209 Namslauer, A., Aagaard, A., Katsonouri, A. and Brzezinski, P. (2003) Intramolecular proton-transfer reactions in a membrane-bound proton pump: the effect of pH on the peroxy to ferryl transition in cytochrome *c* oxidase. Biochemistry. **42**, 1488-1498

210 Hellwig, P., Rost, B., Kaiser, U., Ostermeier, C., Michel, H. and Mäntele, W. (1996) Carboxyl group protonation upon reduction of the *Paracoccus denitrificans* cytochrome *c* oxidase: Direct evidence by FTIR spectroscopy. FEBS Lett. **385**, 53-57

211 Hellwig, P., Soulimane, T. and Mantele, W. (2002) Electrochemical, FT-IR and UV/VIS spectroscopic properties of the caa_3 oxidase from *T. thermophilus*. Eur. J. Biochem. **269**, 4830-4838 doi:10.1046/j.1432-1033.2002.03182.x

212 Vygodina, T., Kirichenko, A. and Konstantinov, A. A. (2013) Direct regulation of cytochrome *c* oxidase by calcium ions. PLoS One. **8**, e74436 doi:10.1371/journal.pone.0074436

213 Tomson, F. L., Morgan, J. E., Gu, G., Barquera, B., Vygodina, T. V. and Gennis, R. B. (2003) Substitutions for glutamate 101 in subunit II of cytochrome *c* oxidase from *Rhodobacter sphaeroides* result in blocking the proton-conducting K-channel. Biochemistry. **42**, 1711-1717

214 Gorbikova, E. A., Wikström, M. and Verkhovsky, M. I. (2008) The protonation state of the cross-linked tyrosine during the catalytic cycle of cytochrome *c* oxidase. J. Biol. Chem. **283**, 34907-34912 doi:10.1074/jbc.M803511200

215 Hulsebosch, R. J., van den Brink, J. S., Nieuwenhuis, S. A. M., Gast, P., Raap, J., Lugtenburg, J. and Hoff, A. J. (1997) Electronic structure of the neutral tyrosine radical in frozen solution. Selective ^{2}H-,^{13}C-, and ^{17}O-isotope labeling and EPR spectroscopy at 9 and 35 GHz. J. Am. Chem. Soc. **119**, 8685-8694

216 Dixon, W. T., Moghimi, M. and Murphy, D. (1974) Substituent effects in E.S.R. spectra of phenoxyl radicals. J. Chem. Soc. Faraday Trans. 2. **70**, 1713-1720

217 Dixon, W. T. and Murphy, D. (1976) Determination of the acidity constants of some phenol radical cations by means of electron spin resonance. J. Chem. Soc. Faraday Trans. 2. **72**, 1221-1230

218 Altwicker, E. R. (1967) The chemistry of stable phenoxyl radicals. Chem. Rev. **67**, 475-531

219 Mukherjee, A., McGlashen, M. L. and Spiro, T. G. (1995) Ultraviolet resonance Raman spectroscopy and general valence force field analysis of phenolate and phenoxyl radical. J. Phys. Chem. **99**, 4912-4917

220 Aki, M., Ogura, T., Naruta, Y., Le, T. H., Sato, T. and Kitagawa, T. (2002) UV resonance Raman characterization of model compounds of Tyr^{244} of bovine

cytochrome *c* oxidase in its neutral, deprotonated anionic, and deprotonated neutral radical forms: effects of covalent binding between tyrosine and histidine. J. Phys. Chem. A. **106**, 3436-3444

221 Berthomieu, C. and Boussac, A. (1995) FTIR and EPR study of radicals of aromatic amino acids 4-methylimidazole and phenol generated by UV irradiation. Biospectroscopy. **1**, 187-206

222 Cappuccio, J. A., Ayala, I., Elliot, G. I., Szundi, I., Lewis, J., Konopelski, J. P., Barry, B. A. and Einarsdóttir, Ó. (2002) Modeling the active site of cytochrome oxidase: synthesis and characterization of a cross-linked histidine-phenol. J. Am. Chem. Soc. **124**, 1750-1760

223 Barry, B. A. and Einarsdóttir, O. (2005) Insights into the structure and function of redox-active tyrosines from model compounds. J. Phys. Chem. B. **109**, 6972-6981

224 Webster, R. D. (2003) *In situ* electrochemical-ATR-FTIR spectroscopic studies on solution phase 2,4,6-tri-substituted phenoxyl radicals. Electrochem. Commun. 6-11

225 Richards, J. A., Whitson, P. E. and Evans, D. H. (1975) Electrochemical oxidation of 2,4,6-tri-tert-butylphenol. Electroanal. Chem. **63**, 311-327

226 Malfoy, B. and Reynaud, J. A. (1980) Electrochemical investigations of amino acids at solid electrodes. J. Electroanal. Chem. **114**, 213-223

227 Harriman, A. (1987) Further comments on redox potentials of tryptophan and tyrosine. J. Phys. Chem. **91**, 6102-6106

228 Shao, C., Wei, Y. and Jiang, L. (2008) Study on electrochemical behaviour of tyrosine at multi-wall carbon nanotubes modified glassy carbon electrode. J. New. Mat. Electrochem. Systems. **11**, 175-179

229 Moody, A. J. (1996) 'As prepared' forms of fully oxidised haem/Cu terminal oxidases. Biochim. Biophys. Acta. **1276**, 6-20

230 Berthomieu, C. and Hienerwadel, R. (2005) Vibrational spectroscopy to study the properties of redox-active tyrosines in photosystem II and other proteins. Biochim. Biophys. Acta. **1707**, 51-66

231 Nyquist, R. M., Heitbrink, D., Bolwien, C., Gennis, R. B. and Heberle, J. (2003) Direct observation of protonation reactions during the catalytic cycle of cytochrome *c* oxidase. Proc. Natl. Acad. Sci. USA. **100**, 8715-8720

232 Hasegawa, K., Ono, T.-A. and Noguchi, T. (2002) *Ab initio* density functional theory calculations and vibrational analysis of zinc-bound 4-methylimidazole as a model of a histidine ligand in metalloenzymes. J. Phys. Chem. A. **106**, 3377-3390

233 McCauley, K. M., Vrtis, J. M., Dupont, J. and van der Donk, W. A. (2000) Insights into the functional role of the tyrosine-histidine linkage in cytochrome *c* oxidase. J. Am. Chem. Soc. **122**, 2403-2404

234 Tomson, F., Bailey, J. A., Gennis, R. B., Unkefer, C. J., Li, Z., Silks, L. A., Martinez, R. A., Donohoe, R. J., Dyer, R. B. and Woodruff, W. H. (2002) Direct

infrared detection of the covalently ring linked His-Tyr structure in the active site of the heme-copper oxidases. Biochemistry. **41**, 14383-14390

235 Moore, G. F., Hambourger, M., Gervaldo, M., Poluektov, O. G., Rajh, T., Gust, D., Moore, T. A. and Moore, A. L. (2008) A bioinspired construct that mimics the proton coupled electron transfer between $P680^{\bullet+}$ and the Tyr(Z)-His190 pair of photosystem II. J. Am. Chem. Soc. **130**, 10466-10467 doi:10.1021/ja803015m

236 Moore, G. F., Hambourger, M., Kodis, G., Michl, W., Gust, D., Moore, T. A. and Moore, A. L. (2010) Effects of protonation state on a tyrosine-histidine bioinspired redox mediator. J. Phys. Chem. B. **114**, 14450-14457 doi:10.1021/jp101592m

237 Benisvy, L., Bill, E., Blake, A. J., Collison, D., Davies, E. S., Garner, C. D., Guindy, C. I., McInnes, E. J., McArdle, G., McMaster, J., Wilson, C. and Wolowska, J. (2004) Phenolate and phenoxyl radical complexes of Co(II) and Co(III). Dalton Trans. **21**, 3647-3653

238 Brabec, V. and Mornstein, V. (1980) Electrochemical behaviour of proteins at graphite electrodes. II. Electrooxidation of amino acids. Biophys. Chem. **12**, 159-165

239 Fotouhi, L., Ganjavi, M. and Nematollahi, D. (2004) Electrochemical study of iodine in the presence of phenol and o-cresol: Application to the catalytic determination of phenol and o-cresol. Sensors. **4**, 170-180

240 Yin, H., Zhou, Y., Ai, S., Han, R., Tang, T. and Zhu, L. (2010) Electrochemical behaviour of bisphenol A at glassy carbon electrode modified with gold nanoparticles, silk fibroin, and PAMAM dendrimers. Microchim Acta. **170**, 99-105

241 Phanthong, C. and Somasundrum, M. (2007) Enhanced sensitivity of 4-chlorophenol detection by use of nitrobenzene as a liquid membrane over a carbon nanotube-modified glassy carbon electrode. Electroanalysis. **20**, 1024-1027

242 Evans, D. H., Jimenez, P. J. and Kelly, M. J. (1984) Reversible dimerisation of phenoxyl radicals formed by anodic oxidation of phenolates: a quantitative study by cyclic voltammetry. J. Electroanal. Chem. **163**, 145-157 doi:10.1016/S0022-0728(84)80048-0

243 Cohen, L. and Jones, W. M. (1963) A study of free energy relationships in hindered phenols. Linear dependance for solvation effects in ionization. J. Amer. Chem. Soc. **85**, 3397-3402

244 Gorbikova, E. A., Belevich, I., Wikström, M. and Verkhovsky, M. I. (2008) The proton donor for O-O bond scission by cytochrome *c* oxidase. Proc. Natl. Acad. Sci. USA. **105**, 10733-10737 doi:10.1073/pnas.0802512105

245 Martin, H. B. and Morrison, Jr. (2001) Application of a diamond thin film as a transparent electrode for *in situ* infrared spectroelectrochemistry. Electrochem. Solid-State Lett. **4**, E17-E20 doi:10.1149/1.1353162

246 Jasaitis, A., Verkhovsky, M. I., Morgan, J. E., Verkhovskaya, M. L. and Wikström, M. (1999) Assignment and charge translocation stoichiometries of

the major electrogenic phases in the reaction of cytochrome *c* oxidase with dioxygen. Biochemistry. **38**, 2697-2706

247 Eytan, G. D., Matheson, M. J. and Racker, E. (1976) Incorporation of mitochondrial membrane proteins into liposomes containing acidic phospholipids. J. Biol. Chem. **251**, 6831-6837

248 Casey, R. P. (1984) Membrane reconstitution of the energy-conserving enzymes of oxidative phosphorylation. Biochim. Biophys. Acta. **768**, 319-347

249 Papa, S., Capitanio, N. and De Nitto, E. (1987) Characteristics of the redox-linked proton ejection in beef-heart cytochrome *c* oxidase reconstituted in liposomes. Eur. J. Biochem. **164**, 507-516

250 Casey, R. P., Ariano, B. H. and Azzi, A. (1982) Studies on the transmembrane orientation of cytochrome *c* oxidase in phospholipid vesicles. Eur. J. Biochem. **122**, 313-318

251 Krab, K. and Wikström, M. (1978) Proton-translocating cytochrome *c* oxidase in artificial phospholipid vesicles. Biochim. Biophys. Acta. **504**, 200-214

252 Sigel, E. and Carafoli, E. (1980) Quantitative analysis of the proton and charge stoichiometry of cytochrome *c* oxidase from beef heart reconstituted into phospholipid vesicles. Eur. J. Biochem. **111**, 299-306

253 Morin, P. E., Diggs, D. and Freire, E. (1990) Thermal stability of membrane-reconstituted yeast cytochrome *c* oxidase. Biochemistry. **29**, 781-788

254 VanAken, T., Foxall-VanAken, S., Castleman, S. and Ferguson-Miller, S. (1986) Alkyl glycoside detergents: synthesis and applications to the study of membrane proteins. Methods Enzymol. 27-35

255 Rigaud, J.-L., Pitard, B. and Levy, D. (1995) Reconstitution of membrane proteins into liposomes: application to energy-transducing membrane proteins. Biochim. Biophys. Acta. **1231**, 223-246

256 Stuart, R. A. (2008) Supercomplex organisation of the oxidative phosphorylation enzymes in yeast mitochondria. J. Bioenerg. Biomemb. **40**, 411-417

257 Vukotic, M., Oeljeklaus, S., Wiese, S., Vogtle, F., Meisinger, C., Meyer, H. E., Zieseniss, A., Katschinski, D. M., Jans, D. C., Jakobs, S., Warscheid, B., Rehling, P. and Deckers, M. (2012) Rcf1 mediates cytochrome oxidase assembly and respirasome formation, revealing heterogeneity of the enzyme complex. Cell Metabolism. **15**, 336-347 doi:10.1016/j.cmet.2012.01.016

258 Speck, S. H., Dye, D. and Margoliash, E. (1984) Single catalytic site model for the oxidation of ferrocytochrome *c* by mitochondrial cytochrome *c* oxidase. Proc. Natl. Acad. Sci. USA. **81**, 347-351

259 Dodia, R., Meunier, B., Kay, C. W. M. and Rich, P. R. (2014) Comparisons of subunit 5A and 5B isozymes of yeast cytochrome *c* oxidase. *In press* Biochem. J. doi:10.1042/BJ20140732

260 Grossman, L. I. and Lomax, M. I. (1997) Nuclear genes for cytochrome *c* oxidase. Biochim. Biophys. Acta. **1352**, 174-192

261 David, P. S. and Poyton, R. O. (2005) Effects of a transition from normoxia to anoxia on yeast cytochrome *c* oxidase and the mitochondrial respiratory chain: implications for hypoxic gene induction. Biochim. Biophys. Acta. **1709**, 169-180 doi:10.1016/j.bbabio.2005.07.002

262 Trueblood, C. E. and Poyton, R. O. (1987) Differential effectiveness of yeast cytochrome *c* oxidase subunit V genes results from differences in expression not function. Mol. Cell. Biol. **7**, 3520-3526

263 Hess, K. C., Liu, J., Manfredi, G., Muhlschlegel, F. A., Buck, J., Levin, L. R. and Barrientos, A. (2014) A mitochondrial CO_2-adenylyl cyclase-cAMP signalosome controls yeast normoxic cytochrome *c* oxidase activity. FASEB J. **ahead of print**, doi:10.1096/fj.14-252890

264 Massari, S., Bösel, A. and Wrigglesworth, J. M. (1996) The variation of K_m for oxygen of cytochrome oxidase with turnover under de-energized and energized conditions. Biochem. Soc. Trans. **24**, 464S

265 Petersen, L. C., Nicholls, P. and Degn, H. (1976) The effect of oxygen concentration on the steady-state kinetics of the solubilised cytochrome *c* oxidase. Biochim. Biophys. Acta. **452**, 59-65

266 Montgomery, D. L., Leung, D. W., Smith, M., Shalit, P., Fave, G. and Hall, B. D. (1980) Isolation and sequence of the gene for iso-2-cytochrome *c* in *Saccharomyces cerevisiae*. Proc. Natl. Acad. Sci. USA. **77**, 541-545

267 Osheroff, N., Koppenol, W. H., and Margoliash, E. (1978) From electrons to tissues. In Frontiers of Biological Energetics (Scarpa, A., Dutton, P. L., and Leigh, J. S., eds.). pp. 439-449, Academic Press, NY

268 Davies, H. C., Smith, L. and Wasserman, A. R. (1964) The influence of ionic strength and polycations on the oxidation of ferrocytochrome *c* by cytochrome *c* oxidase. Biochim. Biophys. Acta. **85**, 238-246

269 Rieder, R. and Bosshard, H. R. (1978) The cytochrome *c* oxidase binding site on cytochrome *c*. Differential chemical modification of lysine residues in free and oxidase-bound cytochrome *c*. J. Biol. Chem. **253**, 6045-6053

270 Bisson, R., Jacobs, B. and Capaldi, R. A. (1980) Binding of arylazidocytochrome *c* derivatives to beef heart cytochrome *c* oxidase: cross-linking in the high- and low-affinity binding sites. Biochemistry. **19**, 4173-4178

271 Zhen, Y., Hoganson, C. W., Babcock, G. T. and Ferguson-Miller, S. (1999) Definition of the interaction domain for cytochrome *c* on cytochrome *c* oxidase. I. Biochemical, spectral, and kinetic characterization of surface mutants in subunit II of *Rhodobacter sphaeroides* cytochrome aa_3. J. Biol. Chem. **274**, 38032-38041

272 Drosou, V., Malatesta, F. and Ludwig, B. (2002) Mutations in the docking site for cytochrome *c* on the *Paracoccus* heme aa_3 oxidase. Electron entry and kinetic phases of the reaction. Eur. J. Biochem. **269**, 2980-2988

273 Witt, H., Malatesta, F., Nicoletti, F., Brunori, M. and Ludwig, B. (1998) Tryptophan 121 of subunit II is the electron entry site to cytochrome *c* oxidase in *Paracoccus denitrificans*. Involvement of a hydrophobic patch in the docking reaction. J. Biol. Chem. **273**, 5132-5136

274 Ferguson-Miller, S., Brautigan, D. L. and Margoliash, E. (1976) Correlation of the kinetics of electron transfer activity of various eukaryotic cytochromes *c* with binding to mitochondrial cytochrome *c* oxidase. J. Biol. Chem. **251**, 1104-1115

275 Garber, E. A. E. and Margoliash, E. (1990) Interaction of cytochrome *c* with cytochrome *c* oxidase: An understanding of the high- to low-affinity transition. Biochim. Biophys. Acta. **1015**, 279-287

276 Wilms, J., Dekker, H. L., Boelens, R. and van Gelder, B. F. (1981) The effect of pH and ionic strength on the pre-steady-state reaction of cytochrome *c* and cytochrome aa_3. Biochim. Biophys. Acta. **637**, 168-176

277 Lin, M. T. and Gennis, R. B. (2012) Product-controlled steady-state kinetics between cytochrome aa_3 from *Rhodobacter sphaeroides* and equine ferrocytochrome *c* analyzed by a novel spectrophotometric approach. Biochim. Biophys. Acta. **1817**, 1894-1900

278 Kwast, K. E., Lai, L. C., Menda, N., James, D. T. 3., Aref, S. and Burke, P. V. (2002) Genomic analyses of anaerobically induced genes in *Saccharomyces cerevisiae*: Functional roles of Rox1 and other factors in mediating the anoxic response. J. Bacteriol. **184**, 250-265

279 Ter Linde, J. J. and Steensma, H. Y. (2002) A microarray-assisted screen for potential Hap1 and Rox1 target genes in *Saccharomyces cerevisiae*. Yeast. **19**, 825-840

280 Follmann, K., Arnold, S., Ferguson-Miller, S. and Kadenbach, B. (1998) Cytochrome *c* oxidase from eucaryotes but not from procaryotes is allosterically inhibited by ATP. Biochem. Mol. Biol. Int. **45**, 1047-1055

281 Bazán, S., Mileykovskaya, E., Mallampalli, V. K., Heacock, P., Sparagna, G. C. and Dowhan, W. (2013) Cardiolipin-dependent reconstitution of respiratory supercomplexes from purified *Saccharomyces cerevisiae* complexes III and IV. J. Biol. Chem. **288**, 401-411 doi:10.1074/jbc.M112.425876

10 Appendix

10.1 Publication

10.2 Iterative fit to estimate H^+/e^- stoichiometry

A fit to proton pumping profiles of COVs was calculated iteratively. The shape of the profile was then adjusted by varying the H^+/e^- stoichiometry (coupling ratio) to give a best fit to the measured data. The following LabTalk script was written on OriginPro 8.6 by Liberty Foreman with contributions from Raksha Dodia and Peter Rich.

[Proton to electron stoichiometry]

```
//User Defined Constants
CoupRatio=1;
CytCred=1.35;
K1=1.2;
K2=0.026;
Tinc=0.05;
K3=0.03

//Initial Fixed Conditions
Hout=0;
Hin=0;
ii=1;
CytCox=0;
IntialAcidPulse=0.36

range rData=[Book1]Sheet1!;

rData.nrows=1200;

for(T=0; T<=200; T=T+$(Tinc))
{
range rX=%(rData)col(1)[ii];
range rY=%(rData)col(2)[ii];
rX=T;
    Oxidation= (CytCred*$(Tinc)*K1);
    CytCred= CytCred - Oxidation;
    CytCox= CytCox + Oxidation;
    AcidPulseused= InitialAcidPulse*$(Tinc)*K3
    AcidPulseleft=InitialAcidPulse - AcidPulseused
    Hout= Hout + (Oxidation*CoupRatio)+AcidPulseleft;
    Hin= Hin - Oxidation - (Oxidation*CoupRatio)+AcidPulseleft;
    Hdecay=(Hout + CytCox)*K2*$(Tinc);
    Hout= Hout - Hdecay;
    Hin= Hin + Hdecay;
    rY=(Hout*-1);
    ii=ii+1;
        }
```

1.2.1 Description of script

'CytCred' is the initial concentration of cyt c^{2+} (µM) added to the reaction. **'Tinc'** is the time increment between data points and was defined as 0.05 s. **'Oxidation'** is the amount of cyt *c* oxidised in the defined time increment (0.05 s). **'CytCox'** is the cumulative amount of cyt *c* oxidised with each time increment. Although not significantly large, steps 4 and 5 takes into account the measured profile of the calibrating acid pulse (see Figure 6-7) where the added protons from HCl equilibrate into the vesicles at a measureable rate constant **'K3'**, thus the initial acidification burst from pumping must be compared to the initial size of the acid pulse and the final extent of reaction profile should be compared to the final extent of the acid pulse profile. **'InitialAcidPulse'** is the amount of protons that equilibrate into the vesicle (0.36 µM). **'AcidPulseused'** is the amount of protons entering the vesicle in a time increment based on the measured rate constant K3. **'AcidPulseleft'** is the cumulative amount of protons left to enter the vesicle which would soon become 0. **'Hout'** is the amount of protons pumped out of the vesicle by C*c*O. **'CoupRatio'** is the H^+/e^- stoichiometry that can be adjusted to obtain the best fit to the data. **'Hin'** is the amount of protons lost inside the vesicle due to pumping and consumption for H_2O formation. **'Hdecay'** is the extent by which the pumped protons re-enter the vesicle at the measured rate constant (**K2**) in the defined time increment. The pumping of protons is outcompeted by the opposing decay, and the re-entry of protons is increasing based on the decay.